

2013

An economic evaluation of the robotic tufting process considering the application of a novel composite wing rib post

Harman, David Edward

<http://hdl.handle.net/10026.1/10847>

<http://dx.doi.org/10.24382/3501>

University of Plymouth

All content in PEARL is protected by copyright law. Author manuscripts are made available in accordance with publisher policies. Please cite only the published version using the details provided on the item record or document. In the absence of an open licence (e.g. Creative Commons), permissions for further reuse of content should be sought from the publisher or author.

**An economic evaluation of the robotic tufting
process considering the application of a novel
composite wing rib post**

Harman D. E.

DOCTOR OF PHILOSOPHY

2013

This copy of the thesis has been supplied on condition that anyone who consults it is understood to recognise that its copyright rests with its author and that no quotation from the thesis and no information derived from it may be published without the author's prior consent

**An economic evaluation of the robotic tufting process considering the
application of a novel composite wing rib post**

by

David Edward Harman

A thesis submitted to the University of Plymouth
in partial fulfilment for the degree of

DOCTOR OF PHILOSOPHY

School of Marine Science and Engineering

Faculty of Technology

Funded by Great Western Research and QinetiQ Group Plc

March 2013

Abstract

This thesis aims to establish a greater understanding of the effects of the single-sided robotic tufting process on component manufacturing costs and weight, and subsequently determine whether potential economic benefits can be realised through its implementation. To complete this assessment, the study uses the novel composite rib post application of the Next Generation Composite Wing (NGCW) project as an example case, investigating the component's manufacturing cost, performance and weight relative to those of a non-tufted rib post with the same initial fabric layup, and a prepreg rib post with the same fibre orientation and fibre volume fraction.

Detailed analyses of the tufted composite rib post manufacturing process have established the relationships between its manufacturing activities and the consumed resources, facilitating the creation of a novel cost model incorporating algorithms defining the robotic tufting process, which may be adapted for different geometries and tuft parameters. In addition, novel permeability data for the considered tufted preform have been obtained experimentally allowing the simulation of the liquid composite manufacturing process. The insertion of tufting in the studied arrangement was shown to decrease the in-plane permeability of the preform, reducing the characteristic by a factor of 3.5 in the direction perpendicular to the tuft seams, and 1.8 in the direction parallel.

Completing structural analyses and further cost modelling, the study considers the manufacturing costs and weight of each of the studied components when performance is normalised. Implementing weight penalties including lifetime fuel consumption and lifetime revenue, appreciation is given to the potential lifetime costs generated by each of the structural solutions. Comparing the amalgamated costs of each component,

relative economy has been evaluated both when considering equipment amortisation and also the use of pre-amortised equipment. Considering lifetime fuel cost/kg as the weight penalty, the novel composite rib post has greater economy within the pure pull-off load case without tufting due to its lower manufacturing costs. However, with the consideration of a more significant weight penalty, such as potential increased lifetime revenue, the use of the novel composite rib post results in superior economy, its lifetime cost/part is estimated to be 14% less than the component without tufting and 61% less than the lifetime cost/part of the prepreg component.

Critical evaluations of the project's methodologies have highlighted the various assumptions made due to the limitations of available information and means to perform certain validations. Under these circumstances the assumptions are believed to be the best representations of what is experienced in reality. As far as possible, errors believed to be the result of assumptions have been accounted for in rigorous error analyses to establish their propagation through the various calculations performed. These analyses have provided confidence in the results of the study, ensuring the significance of the determined economical differences between the investigated components.

Table of contents

ABSTRACT	1
TABLE OF CONTENTS.....	3
FIGURES	7
TABLES	17
NOMENCLATURE	21
ABBREVIATIONS	25
ACKNOWLEDGEMENTS.....	27
AUTHOR’S DECLARATION.....	29
CHAPTER 1. INTRODUCTION	31
1.1 3D FIBRE REINFORCED COMPOSITES	37
1.2 PROJECT AIMS AND OBJECTIVES	40
CHAPTER 2. LITERATURE REVIEW OF STITCHING BASED THROUGH-THICKNESS REINFORCEMENT TECHNIQUES.....	43
2.1 THROUGH-THICKNESS REINFORCEMENT	43
2.1.1 <i>The stitching process</i>	46
2.1.2 <i>Mechanical properties of stitched composites</i>	51
2.1.2.1 In-plane mechanical properties of stitched composites.....	51
2.1.2.2 Out-of-plane mechanical properties and delamination behaviour of tufted composites ..	54
CHAPTER 3. TUFTED COMPOSITE MANUFACTURE AND EQUIPMENT ..	59
3.1 TUFTED PREFORM MORPHOLOGY.....	62
3.2 THE NOVEL COMPOSITE RIB POST MANUFACTURING PROCESS	66
3.2.1 <i>Fabric cutting and preform lay-up</i>	67

Table of contents

3.2.2	<i>The automated robotic tufting process</i>	69
3.2.3	<i>Preform de-moulding</i>	74
3.2.4	<i>Tufted preform RTM</i>	75
3.3	TUFTED FIBRE PREFORM PERMEABILITY	81
3.3.1	<i>Experimental apparatus</i>	85
3.3.2	<i>Experimental Procedures</i>	89
3.3.3	<i>Results and discussion</i>	95
3.3.3.1	Experimental errors	95
3.3.3.2	Permeability results	96
CHAPTER 4. NOVEL COMPOSITE RIB POST RTM SIMULATION		101
4.1	INTRODUCTION.....	101
4.2	PAM-RTM BENCHMARKING AND MESH DENSITY DEPENDENCY	103
4.3	MESH REFINEMENT AT THE SIMULATED INLETS OF THE COMPONENTS.....	107
4.4	EXPERIMENTAL PERMEABILITY VALIDATION.....	110
4.4.1	<i>The influence of the tuft seam on the permeability of the tufted preform in the K_1 and K_2 directions</i>	118
4.5	PAM-RTM SIMULATIONS FOR COMPONENT MANUFACTURING COST ESTIMATION	127
CHAPTER 5. COST MODELLING.....		135
5.1	COST ESTIMATION TECHNIQUES	136
5.2	COST ESTIMATION AND MODEL CREATION.....	142
5.3	TUFTED NOVEL COMPOSITE RIB POST COST MODEL	144
5.3.1	<i>Labour</i>	144
5.3.1.1	Fabric cutting and layup sub process labour estimate	145
5.3.1.2	Robotic tufting sub process	149
5.3.1.3	Preform de-moulding sub-rocess.....	150

Table of contents

5.3.1.4 RTM sub-process	151
5.3.1.5 Part de-moulding sub-process	154
5.3.2 Material.....	154
5.3.2.1 Consumed tuft thread length	155
5.3.2.2 Consumed non-crimp fabric.....	158
5.3.2.3 Noodle roving consumption.....	161
5.3.2.4 Resin consumption.....	161
5.3.2.5 Consumables	162
5.3.3 RTM tool costs	162
5.3.4 Equipment costs	163
5.3.5 Energy costs	164
5.4 TUFTED AND NON-TUFTED NOVEL COMPOSITE RIB POST MANUFACTURING COST ESTIMATES	166
5.4.1 Tufted novel composite rib post manufacturing cost estimates	167
5.4.2 Non-tufted novel composite rib post manufacturing cost estimates	169
CHAPTER 6. STRUCTURAL MODELLING OF THE COMPOSITE RIB POST COMPONENT	177
6.1 ESTIMATION OF ELASTIC PROPERTIES	177
6.1.1 Non-tufted composite elastic properties.....	179
6.1.2 Tufted composite elastic properties	181
6.1.2.1 Tuft component volume fraction estimation	182
6.1.2.2 Tufted composite elastic moduli estimation.....	185
6.1.3 Carbon fibre/epoxy prepreg elastic property estimation.....	189
6.1.4 Noodle elastic property estimation	190
6.2 RIB POST NUMERICAL MODEL	191
6.3 SIMULATION RESULTS	199
6.3.1 Rib post pull-off test element performance/weight.....	203

CHAPTER 7. INTEGRATION OF ANALYSES	207
7.1 AUTOCLAVE PREPREG RIB POST MANUFACTURING COST ESTIMATION	207
7.1.1 <i>Cost/part comparison of the considered composite rib posts</i>	215
7.2 RELATIVE COMPONENT ECONOMY.....	217
7.2.1 <i>Weight penalty variation</i>	223
CHAPTER 8. DISCUSSION AND FUTURE WORK	229
8.1.1 <i>Rib post manufacturing cost</i>	230
8.1.2 <i>Rib post performance and economy</i>	232
8.2 FUTURE WORK.....	236
CHAPTER 9. CONCLUSIONS.....	241
APPENDIX 1 - DIFFERENTIAL PRESSURE GAUGE ADAPTION.....	245
APPENDIX 2 – CORN OIL DYNAMIC VISCOSITY MEASUREMENT AND THERMOMETER CALIBRATION	247
APPENDIX 3 – CALCULATION OF VOLUMETRIC FLOW RATE	251
APPENDIX 4 – 3D FIBRE PREFORM INTERNAL ARCHITECTURE ANALYSIS WITH THE SKYSCAN 1174 MICRO-CT SCANNER.....	255
REFERENCES.....	275

Figures

Figure 1-1. Trade-off between acquisition and operating costs [18].	34
Figure 2-1. Stitching machine developed by NASA in association with Boeing to stitch composite wing panels [43].	46
Figure 2-2. Computer-controlled robotic one sided stitching head (courtesy of QinetiQ)	47
Figure 2-3. Schematic of the (a) lock stitch, (b) modified lock stitch and (c) chain stitch [44].	48
Figure 2-4. Schematic showing the stitching heads, needles, and stitching patterns of (a) Blind stitching, (b) tufting and (c) Two needle single sided stitching techniques. Adapted from KSL [48] and Tong et al [26].	49
Figure 2-5. Diagram demonstrating the arrangement of the thread in the tufted preform	50
Figure 2-6. Airbus A380 rear pressure bulkhead [72].	56
Figure 3-1. The design of the ALCAS lateral wing, including spars ribs and rib posts [20]	59
Figure 3-2. The design of the novel composite rib post (Courtesy of QinetiQ)	60
Figure 3-3. A schematic of the mounting of the rib post to the spar, noting load and bending moment directions (courtesy of QinetiQ)	61
Figure 3-4. A schematic of the square tuft arrangement of the investigated preform ...	63
Figure 3-5. The tuft form within a representative unit cell of the 4 x 4mm, $\pm 45^\circ$ tufted preform	64
Figure 3-6. Preform photos showing a) the measurement of tuft loop length, b) the spacing of the tuft heads and c) the spacing of the surface segment of the carbon tufts in the quasi-isotropic carbon NCF stack	65

Figures

Figure 3-7. The novel composite rib post manufacturing process chain	66
Figure 3-8. Visual summary of the fabric cutting and lay-up sub process	68
Figure 3-9. The KSL KL502 Linear axis robot unit and tufting head with the worktop and 390mm x 400mm work piece jig.....	69
Figure 3-10. Visual summary of the tufting sub process	72
Figure 3-11. The tufting foot and needle used by QinetiQ	73
Figure 3-12. Angled tuft insertion requiring the tufting foot to be removed	73
Figure 3-13. Visual summary of the tufted preform de-moulding.....	75
Figure 3-14. Visual summary of the RTM sub process	78
Figure 3-15. A visual summary of the part de-moulding sub process	80
Figure 3-16. Micro-CT images showing the influence of tufting on internal geometry, a) of through-thickness image from a carbon/epoxy composite panel made from a quasi-isotropic lay-up of non-crimp fibre, and b) of through-thickness image from a panel differing only in that has tufts pitched at 45° in a 4mm x 4mm arrangement.....	82
Figure 3-17. Diagram illustrating the experimental set-up	85
Figure 3-18. Acrylic mould insert.....	86
Figure 3-19. Mould sample cavity dimensions with insert in place	86
Figure 3-20. The dial gauge mounted to the mould surface	87
Figure 3-21. Video camera set up to capture temperature, differential pressure and flow front length data	88
Figure 3-22. The CNC ply cutter employed to cut the tufted preform samples at Pipex ltd [100].....	90
Figure 3-23. The experimental set-up of the video camera and liquid pump	92
Figure 3-24. An example of the observed liquid flow front during the measurement of the permeability of a tufted preform	94

Figures

Figure 3-25. Measured permeabilities of the tufted and non-tufted material samples with experimental error	96
Figure 4-1. Screenshots of the flat plate (a) and L (b) geometries used to benchmark PAM-RTM with Darcy's law, within the PAM-RTM environment.....	104
Figure 4-2. Fill times simulated by PAM-RTM for the flat panel geometry with various mesh densities compared to the fill time estimated by Darcy's law	105
Figure 4-3. Fill times simulated by PAM-RTM for the L geometry with various mesh densities compared to the fill time estimated by Darcy's law	106
Figure 4-4. Flat panel mesh with 1056 elements, refined at the simulated inlet.....	108
Figure 4-5. Flat panel mesh density vs. PAM-RTM simulated fill time for inlet refined meshes, compared to the fill time calculated with Darcy's equation	108
Figure 4-6. L component mesh density vs. PAM-RTM simulated fill time for inlet refined meshes, compared to the fill time calculated with Darcy's equation.....	109
Figure 4-7. The dimensions of the L geometry using symmetry to model the RTM of the manufactured T-component	111
Figure 4-8. The injection pressure/time profile of the flat panel RTM documented in process records	111
Figure 4-9. The simulated flat panel inlet and vents.....	112
Figure 4-10. The injection pressure/time profile of the T-component documented in process records	113
Figure 4-11. The simulated inlet and vents of the T-component, shown with the L geometry.....	114
Figure 4-12. The defined permeability directions of the T RTM simulation.	115
Figure 4-13. The simulated and observed fill times of the flat panel showing simulation error bars relating to the limits of the material permeability measurement	115

Figures

Figure 4-14. The simulated and observed fill times of the T-component showing simulation error bars relating to the limits of the material permeability measurement	116
Figure 4-15. The tuft seam created by the tufting process aligned in the tufting direction	118
Figure 4-16. The K_1 and K_2 directions of the tufted preform	119
Figure 4-17. A microscopy image of the tuft seam cross section at the surface of a composite made with the investigated tufted preform	120
Figure 4-18. An idealised cell of the tuft seam surface layer	122
Figure 4-19. The tufted preform layers considered within the mean permeabilities	124
Figure 4-20. The simulated fill times of the T-component modelling anisotropic and isotropic permeabilities compared to the documented fill time from the process record	125
Figure 4-21. A schematic of the composite rib post noting the dimensions used in the RTM simulations (courtesy of QinetiQ)	128
Figure 4-22. A schematic of the RTM tool and injection strategy of the T-component	129
Figure 4-23. The RTM simulation geometry of the rib post	129
Figure 5-1. A classification of product cost estimation techniques [118]	137
Figure 5-2. Diagram showing the geometrical terms of the idealised unit cell defined for the 4 x 4mm, $\pm 45^\circ$ tufted preform	156
Figure 5-3. The fabric roll edges and roll width edge of the NCF fabric rolls	159
Figure 5-4. The novel composite rib post aluminium RTM tool	163
Figure 5-5. A breakdown of the estimated tufted novel composite rib post manufacturing cost	169
Figure 5-6. A breakdown of the estimated non-tufted novel composite rib post manufacturing cost	171

Figures

Figure 5-7. SEER-DFM industrial extrapolation of tufted rib post MFG cost for 1000 parts.....	174
Figure 5-8. SEER-DFM industrial extrapolation of non-tufted rib post MFG cost for 100 parts.....	174
Figure 6-1. The idealised unit cell defined for the 4 x 4mm, $\pm 45^\circ$ tufted preform.....	183
Figure 6-2. A cross section of a pull-off test specimen with test fixtures.....	192
Figure 6-3. The dimensions of the pull-off test specimen model, dimensions in metres (m).....	192
Figure 6-4. An image the model face selected for the condition of symmetry, the face is highlighted in blue	193
Figure 6-5. Schematic showing; a) the dimensions (0.012x0.03m) of the fixed boundary and b) the distance (0.023m) of the fixed boundary from the component's radius	194
Figure 6-6. An illustration of the load application normal to the upper surface of the test element web, the upper surface of the specimen is highlighted in blue.....	195
Figure 6-7. The orientation of the material principal directions within the component	196
Figure 6-8. The principal directions of the material within the noodle	196
Figure 6-9. Rib post pull-off test element mesh.....	197
Figure 6-10. Structural model sensitivity to through-thickness elastic modulus variation	198
Figure 6-11. The first principal strain results of the non-tufted rib post pull-off test simulation, indicating the maximum strain.....	200
Figure 6-12. The first principal strain results of the tufted rib post pull-off test simulation, indicating the maximum strain.....	201
Figure 6-13. The first principal strain results of the prepreg rib post pull-off test simulation, indicating the maximum strain.....	201

Figures

Figure 7-1. SEER-DFM manufacturing cost estimates for the prepreg rib post. The standard deviation of the total manufacturing cost is 3%, and that of the cost/parts is £24	214
Figure 7-2. Prepreg rib post manufacturing cost breakdown with a production quantity of 1000 parts.....	214
Figure 7-3. Prepreg rib post manufacturing cost breakdown with a production quantity of 1000 parts, excluding equipment costs	215
Figure 7-4. Manufacturing cost driver comparison of the tufted, non-tufted and prepreg components at a production quantity of 1000 parts	216
Figure 7-5. A breakdown of rib post manufacturing cost/part when performance is normalised, including lifetime fuel cost.....	223
Figure 8-1. Comparison of component economies with increasing weight penalty	235
Figure 9-1. Differential pressure gauge arrangement	246
Figure 9-2. The RS Brookfield Rheometer employed to measure the dynamic viscosity of the experimental liquid.	247
Figure 9-3. Lowered C-50 rheometer cone	248
Figure 9-4. Corn oil dynamic viscosity / temperature profile.....	249
Figure 9-5. Thermometer calibration	249
Figure 9-6. Thermometer calibration with rheometer base plate.....	250
Figure 9-7. The separation of liquid flow into the sample cavity and the pressure gauge pipe.....	252
Figure 9-8. The Skyscan 1174 micro-CT scanner and the Thermo Fisher Scientific Mini 900 rate meter.....	256
Figure 9-9. The circular platform stage for the Skyscan 1174 micro-CT scanner, with and without spacer	258

Figures

Figure 9-10. The circular platform stage fixed inside the Skyscan 1174 micro-CT scanner.....	259
Figure 9-11. The material testing stage fixed inside the Skyscan 1174 micro-CT scanner with the dry Saertex NCF quasi 4x4 tufted fabric inserted.....	260
Figure 9-12. Micro-CT scans of dry fibre 3Tex 3D woven fabric a) view of warp binder b) view in warp direction c) visible distortion to surface weft rovings due to binder yarn d) through-thickness view of fabric's internal architecture	262
Figure 9-13. Micro-CT scans of dry fibre Saertex quasi NCF, 4x4 tufted fabric a) view in tuft row direction b) view perpendicular to tuft row direction c) through-thickness view of the fabric's internal architecture	262
Figure 9-14. Micro-CT scans of panel 12 – unstitched Saertex NCF quasi carbon and epoxy. a) a view of the internal architecture of the composite along y axis b)a through-thickness slice of the composite along the z axis.....	263
Figure 9-15. Micro-CT scans of panel 13 – 0,90 3Tex 3D woven carbon and epoxy. a)a view of the internal architecture of the composite along y axis b)a through-thickness slice of the composite along the z axis.....	263
Figure 9-16. Micro-CT scans of panel 15 – baseline 4x4 tufted Saertex quasi NCF carbon and epoxy. a) a view of the internal architecture of the composite along y axis b)a through- thickness slice of the composite along the z axis.....	264
Figure 9-17. Micro-CT scans of panel 29 – Carbon/Priiform soluble fibre and epoxy a) a view of the internal architecture of the composite along y axis b) a through-thickness slice of the composite along the z axis.....	264
Figure 9-18. Micro-CT scans of panel 36 – 4x4 tufted Saertex quasi NCF carbon with 45o tuft angle, and epoxy. a) a view of the internal architecture of the composite along y axis b) a through- thickness slice of the composite along the z axis.....	264

Figures

Figure 9-19. Micro-CT scans of panel 46 – 1k Sigmatex orthogonal 3D woven carbon and epoxy. a) a view of the internal architecture of the composite along y axis b) a through-thickness slice of the composite along the z axis 265

Figure 9-20. Micro-CT scans of panel 49 – 1k Sigmatex angle interlock 3D woven carbon and epoxy. a) a view of the internal architecture of the composite along y axis b) a through-thickness slice of the composite along the z axis 265

Figure 9-21. Micro-CT scans of panel 53 – 3k Sigmatex orthogonal 3D woven carbon and epoxy. a) a view of the internal architecture of the composite along y axis b) a through-thickness slice of the composite along the z axis 265

Figure 9-22. Micro-CT scans of panel 58 – 3k Sigmatex angle interlock 3D woven carbon and epoxy. a) a view of the internal architecture of the composite along y axis b) a through-thickness slice of the composite along the z axis 266

Figure 9-23. Micro-CT scans of the compression and release of the dry fibre 3Tex 3D woven fabric. a) the compression of the fabric specimen shown with cross section scans along the y axis and reconstructed images of a single point along the z axis b) the release of the fabric specimen shown with cross section scans along the y axis and reconstructed images of a single point along the z axis 267

Figure 9-24. Micro-CT scans of the compression and release of the dry fibre Saertex quasi NCF 4x4 tufted fabric. a) the compression of the fabric specimen shown with cross section scans along the y axis and reconstructed images of a single point along the z axis b) the release of the fabric specimen shown with cross section scans along the y axis and reconstructed images of a single point along the z axis 268

Figure 9-25. A graph plotting the load (N) and displacement (mm) data collated during the compression and release of the dry fibre 3Tex 3D woven fabric 269

Figure 9-26. A graph plotting the load (N) and displacement (mm) data collated during the compression and release of the dry fibre Saertex quasi NCF 4x4 tufted fabric 269

Figures

Figure 9-27. 3D visualization of the sample microstructure of a double layer fabric with two different types of glass fibre [149]	273
Figure 9-28. A 3D smooth volumetric mesh of an Aluminium auxetic foam, generated within the +ScanFE meshing module of Simpleware [150]	274

Tables

Table 1-1. ALCAS composite wing box weight and recurring costs compared to a state of the art metallic baseline[21].....	36
Table 3-1. The design loads and bending moment of the composite rib post.....	61
Table 3-2. Preform fabric characteristics	63
Table 3-3. Tuft thread characteristics.....	64
Table 3-4. Fabric cutting and lay-up manufacturing activities	67
Table 3-5. Robotic tufting manufacturing activities	71
Table 3-6. Tufted preform de-moulding manufacturing activities.....	74
Table 3-7. Rib post RTM manufacturing activities	77
Table 3-8. Component de-moulding and mould cleaning activities	79
Table 3-9. Sample in-mould fibre volume fraction and tuft number variation.....	90
Table 3-10. Random errors of experimental apparatus.....	95
Table 3-11. Possible systematic error range of experimental apparatus.....	95
Table 3-12. Mean permeabilities and standard deviations of the data sets.....	97
Table 4-1. The process parameters used for the benchmarking of PAM-RTM.....	105
Table 4-2. Flat panel RTM process parameters documented in process records and determined experimentally.....	112
Table 4-3. The T-component process parameters documented within process records and determined experimentally	114
Table 4-4. Tuft seam surface layer thickness measurements.....	120
Table 4-5. Tuft seam cross-section width measurements	121
Table 4-6. The process parameters used for the rib post RTM simulation.....	130
Table 4-7. Tufted rib post RTM simulation results	131

Tables

Table 4-8. The experimentally determined maximum and minimum possible values for the non-tufted preform material isotropic permeability	131
Table 4-9. Non-tufted rib post RTM results	132
Table 5-1. Fabric cutting and lay-up sub process labour time relationships.....	148
Table 5-2. Labour time relationships of the robotic tufting sub process	150
Table 5-3. Labour time relationships of the preform de-moulding sub-process.....	151
Table 5-4. Labour time relationships for the RTM sub-process	153
Table 5-5. Component de-moulding labour time relationships	154
Table 5-6. NCF fabric cost.....	161
Table 5-7. Carbon noodle roving specifications	161
Table 5-8. Consumable unit costs	162
Table 5-9. Equipment investment costs of the novel composite rib post manufacturing process.....	164
Table 5-10. Equipment power ratings and usage times/part.....	164
Table 5-11. Equipment energy costs/part generated during the tufted and non-tufted rib post manufacturing processes.	166
Table 5-12. Total and cost/part manufacturing cost estimates of the tufted novel composite rib post	168
Table 5-13. Total and cost/part manufacturing cost estimates of the non-tufted novel composite rib post	170
Table 5-14. Industrial manufacturing cost/part estimates for the tufted and non-tufted composite rib posts with a production volume of 1000 parts.	173
Table 6-1. The elastic properties and density of Toray T700 50C carbon fibre [139].	180
Table 6-2. The elastic properties and density of Advanced Composites Group's MVR-444 epoxy resin [111]	180

Tables

Table 6-3. The elastic properties of the non-tufted composite synthesised in CoDA at 0.60 V_f	181
Table 6-4. The volume fractions of the various tuft components within the tufted composite	185
Table 6-5. Fibre angle orientation factors [138]	185
Table 6-6. The longitudinal elastic modulus and density of the tuft thread of the tufted composite (Tenax carbon thread - HTA 40)	186
Table 6-7. The CoDA synthesised E_3 of the non-tufted composite at 0.64 V_f	187
Table 6-8. The orientation factors assumed for the components of the tuft in direction 1	187
Table 6-9. The orientation factors assumed for the fibre components of the composite in direction 2.....	188
Table 6-10. The estimated elastic properties of the 4 x 4mm, 45° tufted composite....	189
Table 6-11. The CoDA estimated elastic properties of the quasi-isotropic prepreg composite	190
Table 6-12. The CoDA synthesised elastic properties of the noodle materials	191
Table 6-13. Rib post pull-off test element mesh	197
Table 6-14. Structural model sensitivity to elastic property variation, excluding the through-thickness elastic modulus	198
Table 6-15. The simulated maximum strains of the rib post test element models. The error resulting from the estimation of elastic moduli are considered insignificant ($\sim \pm 6 \times 10^{-8}$).....	199
Table 6-16. The fibre volume fractions of the simulated composite materials.....	204
Table 6-17. The estimated densities of the simulated composite materials.....	204
Table 6-18. The weight and performance index of the rib post test element with each simulated material	205

Tables

Table 7-1. The power rating, usage time, energy consumption and energy cost/part of the prepreg rib post manufacturing equipment 209

Table 7-2. Consumable input costs assumed for the prepreg rib post manufacturing cost estimates..... 209

Table 7-3. SEER-DFM parameters for the prepreg rib post manufacturing cost estimate 211

Table 7-4. Costs/part of the prepreg, tufted, and non-tufted composite rib posts..... 216

Table 7-5. Estimated rib post weight and component performance index..... 217

Table 7-6. Corrected component weights for performance normalised to tufted rib post maximum strain..... 218

Table 7-7. Original non-tufted rib post constituent material weight fractions and subsequent weights within the component..... 219

Table 7-8. The additional material costs of the non-tufted rib post with normalised performance 220

Table 7-9. The costs/part and weights of the various rib posts when normalised to achieve the same maximum through-thickness strain as the tufted rib post, at a production quantity of 1000 parts 221

Table 7-10. Rib post cost/part considering manufacturing cost at a production quantity of 1000 parts and component lifetime fuel consumption..... 221

Table 9-1. Mean volumetric flow rates 253

Table 9-2. The specimens scanned with the Skyscan 1174 micro-CT scanner, the types of scan completed for each specimen and the type of image files collated during each scan..... 272

Nomenclature

A	...	Area (m^2)
b	...	Channel breadth (m)
c	...	Channel depth (m)
C_t	...	Cutting time (s)
CPT	...	Cured composite thickness (mm)
Cr	...	Ply cutting rate ($\text{mm}\cdot\text{s}^{-1}$)
d	...	Thickness (m)
dP	...	The pressure differential between the injection point and the liquid flow front
dx	...	The distance from the injection point to the liquid flow front (m)
E	...	Elastic modulus (GPa)
<i>Energy</i>	...	Energy cost (£)
<i>Equipment</i>	...	Equipment cost (£)
ETW_{pr}	...	The edge trim waste per ply row (m^2)
ftn	...	Number of different fabrics used (-)
G	...	Shear modulus (GPa)
h	...	Total depth of preform (m)
h_s	...	Preform section depth (m)
H_{sp}	...	Tufting head movement rate ($\text{m}\cdot\text{s}^{-1}$)
K	...	Permeability (m^2)
$[K]$...	Permeability tensor (m^2)

Nomenclature

K_s	...	Preform section permeability (m^2)
l	...	Inter-bundle pore space (m)
l_l	...	The length of the tuft loops (m)
L	...	Mould length in the direction of resin flow (m)
L_r	...	Labour rate (£/h)
L_t	...	Lay-up time (s)
Lt	...	Labour time (s)
M	...	Mass (kg)
<i>Material</i>	...	Material cost (£)
<i>MFG cost</i>	...	Manufacturing cost (£)
n	...	Production quantity (-)
n_s	...	Number of sections (-)
p_{pn}	...	Number of plies per preform (-)
ppd	...	Daily component manufacture capacity (-)
P_l	...	Ply length (m)
P_t	...	Part de-moulding time (s)
P_w	...	Ply width (m)
Pr_t	...	Preform de-moulding time (s)
Q	...	Volumetric flow rate ($m^3 \cdot s^{-1}$)
R_w	...	The fabric roll width (m)
R_{w2}	...	The fabric roll width that can be occupied by plies (disallowing zero wastage) (m)
R_{wpn}	...	Number of plies cut per fabric roll width (-)
Re	...	Reynolds number (-)

Nomenclature

RTM_t	...	RTM time (s)
s	...	Section number (-)
S_{tn}	...	The number of structural $\pm 45^\circ$ tufts (-)
S_x	...	Tuft row spacing (m)
S_y	...	Tuft spacing along seam (tuft pitch) (m)
t	...	Time (s)
T	...	Tuft thread linear density (g/m)
T_{sp}	...	Tufting speed ($\text{m}\cdot\text{s}^{-1}$)
T_t	...	Tufting time (s)
<i>Tooling</i>	...	Tooling cost (£)
u	...	Fluid velocity ($\text{m}\cdot\text{s}^{-1}$)
u_i	...	Volume averaged fluid velocity ($\text{m}\cdot\text{s}^{-1}$)
V	...	Volume fraction (-)
V_{tn}	...	The number of tufts within the vertex tufting (-)
Vol	...	Permeability mould cavity volume (m^3)
w	...	Tuft seam cross section width (m)
W_f	...	Fibre area weight ($\text{g}\cdot\text{m}^{-2}$)
W_{fr}	...	Fibre weight fraction (-)
W_m	...	Matrix weight fraction (-)
W_{pr}	...	Waste per ply row generated at the two edges of the fabric roll (m^2)
X	...	Stitching x axis length (m)
Y	...	Stitching y axis length (m)
η_o	...	Fibre orientation factor (-)

Nomenclature

ε	...	Strain (-)
θ	...	Through-thickness tuft angle ($^{\circ}$)
μ	...	Dynamic viscosity (Pa.s)
ν	...	Poisson's ratio (-)
ρ	...	Density (kg.m^{-3})
ϕ	...	Porosity (-)
∇P	...	Pressure gradient (Pa.m^{-1})

Subscripts

c	...	Composite constituent materials
f, m	...	Fibre and matrix
i	...	The principal composite direction
j	...	The tuft components within the tufted composite
$loops$...	The tuft loops
$non - tufted 0.64V_f$...	The non-tufted laminate at 64% fibre volume fraction
rr	...	Resin replaced by fibre in the tufted composite with respect to the non-tufted laminate
$seams$...	The tuft seams
$thread$...	The tuft thread
$tufts$...	The through-thickness portion of the tufts
$P1, P2, P3$...	Preforms 1- 3
x, y, z	...	Co-ordinates of the local unit cell
$1, 2, 3$...	In-plane, transverse and through-thickness
\parallel, \perp	...	Longitudinal and transverse directions

Abbreviations

ACEE	...	Aircraft Energy Efficiency
ABC	...	Activity Based Costing
ACCEM	...	Advanced Composite Cost Estimating Model
ALCAS	...	Advanced Low Cost Aircraft Structures
ATAG	...	Air Transport Action Group
BVID	...	Barely Visible Impact Damage
CAD	...	Computer Aided Design
CAI	...	Composites Affordability Initiative
CAPP	...	Computer Aided Process Planning
CER	...	Cost Estimation Relationship
CFD	...	Computational Fluid Dynamics
CNC	...	Computer Numerical Control
CoDA	...	Component Design and Analysis
CT	...	Computed Tomography
DLR	...	Deutsches Zentrum fuer Luft- und Raumfahrt
DOC	...	Direct Operating Cost
ENF	...	End-Notched Flexure
FBM	...	Feature Based Modelling
FE	...	Finite Element
FEM	...	Finite Element Methods
FRP	...	Fibre Reinforced Polymers
GT	...	Group Technology
HD	...	High Definition
LCM	...	Liquid Composite Moulding

Abbreviations

NASA	...	National Aeronautics and Space Administration
NCF	...	Non-crimp Fibre
NGCW	...	Next Generation Composite Wing
OoA	...	Out-of-Autoclave
RFI	...	Resin Film Infusion
RIFT	...	Resin Infusion under Flexible Tooling
RTM	...	Resin Transfer Moulding
SCRIMP	...	Seemann Composites Resin Infusion Molding Process
SD	...	Standard Deviation
UD	...	Uni-Directional
VACNT	...	Vertically Aligned Carbon Nanotubes

Acknowledgements

I would like to begin by expressing my gratitude to QinetiQ and Greater Western Research (GWR) for their sponsorship of this PhD. My decision to apply and accept this research project was based upon interests developed during my undergraduate studies, and I am very grateful to QinetiQ and GWR for providing me with an opportunity to continue working in these fields. I am especially indebted to Dr Linda Starink, Dr Robert West and Mr Andrew Drane of QinetiQ, who have provided invaluable supervision and support. I would also like to thank Simpleware Ltd for their employment prior to my completion of the PhD.

Great thanks must also go to my supervisory team, in particular Dr Stephen Grove for his tremendous advice, guidance and friendship, and Dr John Summerscales for his fantastic support whenever required. Thank you for giving me the opportunity to work with you, you have opened my eyes.

The technical support and advice provided by my friends and colleagues; Mr Terry Richards, Mr Greg Nash and Mr Richard Cullen has been the greatest of help and relief. I thank you all dearly and look forward to seeing you all again soon.

Thanks must also be given to Pipex px and Mr William Broom for allowing and organising the use of computer controlled cutting facilities at the Pipex headquarters. Thank you very much, this was extremely appreciated.

Finally and most especially, this PhD could not have been completed without the support of my wonderful fiancée Camille. I know it has been just as tough for you as it has been for me. Thank you so much for helping me through it all. I promise I'll be away from the desk soon. The never-ending encouragement of my parents Roger and Sue, and my brother Richard, has also helped me more than I can say. I will always be

Author's declaration

grateful. Thank you also to my lovely future parents in-law and of course the most honourable squire of Plymouth, Baker Adams. You are all there when I need you most.

You all deserve medals for putting up with me.

Author's declaration

At no time during the registration for the degree of Doctor of Philosophy has the author been registered for any other University award without prior agreement of the Graduate Committee.

This study was financed with the aid of a studentship from Greater Western Research (GWR) and sponsorship from QinetiQ.

In addition to the postgraduate level research undertaken for this project and attendance at a wide variety of skills courses provided by the Graduate School, the author has completed the general teaching associate's (GTA) course. Subsequently the author has undertaken extensive teaching opportunities. These have included casual teaching contracts for the Faculty of Technology and the provision of laboratory tours for new students.

The following subject specific commercial training courses have also been attended:

- Introduction to SEER-DFM, Airbus, Filton, Bristol, 7th-8th October 2008
- Skyscan 1174 Micro-CT scanner training, University of Plymouth, 21st August 2009
- Skyscan 1174 Micro-CT scanner advanced training, University of Plymouth, 5th April 2010

Relevant seminars and conferences were regularly attended at which work was presented; external institutions were visited for consultation purposes.

Oral presentations:

- 3D fibre reinforced composites – cost modelling and manufacture, ACMC seminar, University of Plymouth, 27th February 2009

Author's declaration

- Composite material costs and cost modelling, ACMC composites training course, University of Plymouth, 9th September 2009
- Cost modelling and manufacture of 3D fibre reinforced composites, GWR research symposium 2010, Bristol, 20th January 2010
- Cost modelling and manufacture of 3D fibre reinforced composites – Project progress, ACMC seminar, University of Plymouth, 18th October 2010

Presentation and Conferences Attended:

- 4th Annual ALCAS review, Airbus, Filton, 27th – 28th January 2009
- ICMAC 2009, Belfast, Ireland, 17th - 18th March 2009
- Galorath Conference 09, Manchester, 19th March 2009
- SEICO 09, Paris, 23rd – 24th March 2009
- JEC composites exhibition, Paris, 25th – 26th March 2009
- ACCIS annual conference, University of Bristol, 30th June 2009
- ICCM-17, Edinburgh, 26th – 31st July 2009
- SAMPE annual seminar, Nottingham, 24th February 2010
- ALCAS final review, Toulouse, 26th – 27th January 2011

Word count of main body of thesis: 43,386

Signed

Date

Chapter 1. Introduction

The completion of the Airbus A350XWB and the Boeing 787 Dreamliner will mark the introduction of commercial aircraft with approximately 50% of their structural weight made up by composite materials [1, 2]. The increasing use of composite materials in commercial aircraft, both in secondary and primary structures, has ultimately been driven by the prospect of reductions to fuel consumption, an area of profound interest for many years with notable efforts seeming to be initiated by the Aircraft Energy Efficiency (ACEE) program led by the National Aeronautics and Space Administration (NASA) [3]. Composite materials, by nature, consist of two or more materials which, when combined, demonstrate enhanced properties [4]. The use of composite materials can be traced back into the depths of human history. Straw reinforced mud brick [5], mentioned in Exodus 5: 6-8, cob [6] and wattle and daub [7] are all examples of our early use of composites, each consisting of a mixture of earthy and straw-like organic materials. These primitive composites proved to be very successful building materials, so successful in fact that they are still used to this day in developing parts of the world, and are currently experiencing a revival in developed countries following recent movements towards more sustainable building practices [8].

It may be a struggle to find an aeroplane made from mud and straw but there is certainly no shortage of those incorporating more advanced composite materials. Within the aerospace industry, high strength fibre reinforced polymers (FRP) are the composites of choice [9], delivering high specific strengths and specific stiffnesses (ratios of strength and stiffness to density respectively). In ideal circumstances (high V_f , tensile fibre alignment and pure tensile loading) composites have the potential to offer the stiffness of steel at one fifth the weight, the stiffness of aluminium at one half of the weight and specific strengths within the range of 3 to 5 times those of steel and aluminium alloys

[4], however in real world applications the likelihood of experiencing solely the conditions allowing these benefits are rare. To maximise upon their potential, the mechanical properties of composite materials can be tailored to individual applications with the strategic choice and design of their constituent materials. This capacity for mechanical property optimisation and the material's characteristically high specific strength and stiffness can facilitate weight savings over alternative aerospace materials. It is this reduction of surplus weight that offers to reduce the fuel consumption of aircraft incorporating composite structures.

The ability of composite materials to reduce structural weight has been demonstrated by their use in the Airbus A380, where they account for approximately 16% of the weight of the airframe. Compared to an all metal baseline, weight savings of approximately 15 tonnes (8%) were achieved [10]. The fuel saving facilitated by this reduction to weight can be estimated using fuel burn calculations similar to those used by Kaufmann [11]. The air transport action group (ATAG) [12], a global association representing all sectors of the air transport industry, state that the average fuel consumption of the Airbus A380 is less than 3 l/passenger/100km. Taking this figure as the worst case scenario fuel burn of the aircraft at full capacity, the fuel consumption of the typical 525 seat arrangement of the A380 [13] equates to 15.75 l/km.

According to Airbus [13], the daily range of the A380 is 15,400km. Assuming that the life of the aircraft is 25 years and that in this time it flies 300 days/year [11], the lifetime flown distance of the aircraft can be approximated as 115.5 million km. The lifetime fuel consumption of the A380 is therefore approximately 1.819×10^9 litres.

The maximum take-off weight of the A380 is stated by Airbus [13] to be 560 tonnes. Assuming that the average gross weight of the A380 is 500 tonnes, its lifetime fuel consumption equates to approximately 3638 l/kg flight mass. Applying this lifetime

fuel consumption/kg flight mass to the 15 tonne weight saving that the A380 provides compared to the all metal baseline [10, 14], the resultant lifetime fuel saving can be approximated to be 54.5 Mega litres (equivalent to approximately 3% of the A380's lifetime fuel burn). Taking into account the cost of jet fuel, \$0.78/l [15], and the US dollar/Euro exchange rate, \$1.43 [16], at the time of this writing the A380's approximate life time fuel saving as a result of the incorporation of composite materials equates to a saving of roughly €30 M.

Great efforts are made to reduce the fuel consumption of aircraft due to the large proportion of in service cost that this characteristic commands (the in service costs being those developed by the aircraft when it is in the possession of the operator). Kaufmann [17] states that up to 40% of an aircraft's direct operating cost (DOC), the cost associated with flying the aircraft, is fuel. Due to this influence, decreasing fuel consumption will lead to a significant reduction in the aircraft's operating cost.

Providing that the acquisition cost of an aircraft containing composite materials does not offset the cost savings resulting from its reduced weight, the aircraft should become more financially attractive to client airlines. However, at the present time, a recognised drawback of advanced composite materials, such as those suitable for aircraft, is their high manufacturing cost [17]. This is responsible for increasing the acquisition cost of aircraft with large quantities of advanced composite materials and diminishing the possible net monetary savings the client could make through the product's reduced fuel burn. The relationship between acquisition cost and fuel burn (essentially that between manufacturing cost and weight) is shown qualitatively in Figure 1-1. Plotting cost versus reliability (level of maintenance), Figure 1-1 depicts the trade-off between acquisition and operating costs. In the case of aircraft using large quantities of advanced composite materials, where substantial weight savings are made and therefore

operating costs are reduced through lower fuel consumption, for instance point A in Figure 1-1, the acquisition cost is significant enough to cause the life cycle cost to drift from its minimum. This greater acquisition cost is the result of the higher material and manufacturing costs that advanced composite materials demand.

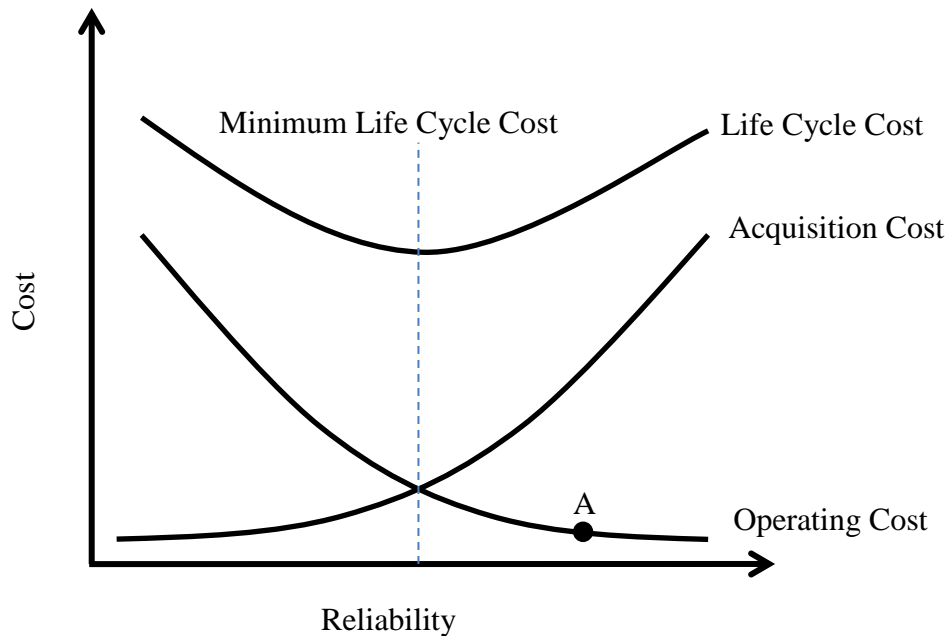


Figure 1-1. Trade-off between acquisition and operating costs [18].

The current high fuel prices and market competition have made it important for aircraft manufacturers to provide aircraft with both low weight and low manufacturing costs [11], in order to reduce operating and acquisition costs. Unlike weight reductions which reduce fuel consumption and benefit the aircraft operator, manufacturing cost reductions can directly benefit both the aircraft manufacturer and the operator. Manufacturing cost reductions allow the manufacturer to reduce the aircraft acquisition cost and also retain or slightly increase the profit margin.

Historically, when fuel prices have been low and weight saving was not so critical, metals were the materials of choice for the primary structures of commercial aircraft, achieving the optimum life cycle costs. Although they tend to be heavier, they are also less expensive than advanced composite materials and lend themselves to cheaper

manufacturing routes [19]. With low fuel prices, these attributes facilitate lower life time costs than those of more fuel efficient but more expensive advanced composite design. In the current climate however, where weight saving is critical (over an aircraft's life, €30,000 extra revenue [11] and life-time fuel savings in the region of €2000 could be made for every kilogram saved on structural weight – as per the calculations presented earlier), the optimum life cycle cost is most likely to be achieved by modifying the manufacturing routes used to produce light weight composite structures [17]. Cost saving developments are likely to consist of implementing much higher levels of automation.

The results of the Advanced Low Cost Aircraft Structures (ALCAS) European framework project support this argument. The aim of the project was to contribute to the reduction of the operating costs of relevant European aerospace products by 15% using the cost effective full application of carbon fibre composites to aircraft primary structures [20]. The project, divided into 4 work packages, targeted the cost and weight of airliner and business jet fuselages and wings. Using the work package focusing on the lateral wing box as an example it is evident that with the application of manufacturing cost reduction strategies, advanced composite solutions can successfully compete with state of the art metallic designs in terms of life cycle cost. The aims specific to the work package were to reduce weight by 20% while not affecting recurring costs compared to a state of the art metal baseline. The state of the art metal baseline was generated using 2004 economic conditions and represents an airbus long-range aircraft standard of technology [21].

Although contrary to the work package aim, recurring costs were increased, as indicated in Table 1-1, the composite solution did succeed in significantly reducing the life cycle

cost, when considering fuel consumption and manufacturing costs as the main contributors.

Table 1-1. ALCAS composite wing box weight and recurring costs compared to a state of the art metallic baseline[21]

Metallic weight	Target weight	Composite weight
3328kg	2600kg	2574kg
Metallic cost	Target cost	Composite cost
€ 387,322	€ 603,540	€ 594,390

Using the estimated fuel cost per kg of a metallic equivalent of the A380, discussed earlier in the chapter, it can be seen that the weight saving of the advanced composite solution allows a reduction of the life time fuel cost that overshadows the increase to the component's recurring costs. Using Table 1-1, the recurring cost increase resulting from the use of advanced composites can be calculated as €207,068. However, using the value of fuel saved per kg reduction of gross weight (calculated as ~ €2000/kg) it can be estimated that with a weight reduction of 754kg, a net monetary lifetime saving of approximately €1,508,000 will be made by the operator even when the inflated recurring cost is passed on to them in the form of a higher acquisition cost.

Addressing the commercial need for reduced fuel burn and cost, Airbus aim to be producing commercial aircraft with 40% less cost and 20% less fuel burn than those currently available, such as the Airbus A320 [22], by 2020. Successfully achieving these aims with advanced composites would almost certainly drive a design change in their favour, further distancing composite design from the 'black metal' approach that has been seen historically [11].

With Airbus and Boeing, the market leaders of the commercial aircraft industry [23], aiming to achieve high volume production with future aircraft (Airbus hope to achieve a production rate of 300 aircraft/year with the A30X [22, 24] and Boeing aim to produce 2 aircraft (737)/day in 2014 [25]), there is a great driving force behind the development of time and cost reduction strategies for the manufacture of advanced composites. If effective strategies are not successfully formed, it can be almost certain that there will be an increase in the use of more economical alternatives to composite materials, such as aluminium and titanium.

1.1 3D fibre reinforced composites

The movement towards high volume production will increase the cost benefits associated with the implementation of automated systems and decrease the influence of fixed costs, such as tooling investment, over the final aircraft acquisition cost. Under these circumstances 3D fibre reinforcements may provide part of the combined solution necessary to reduce the cost of advanced composite structures manufactured with autoclave processed prepregs. Other approaches include out-of-autoclave (OoA) processing, replacement of prepreg with infusion, automated tape lay-up and fibre placement.

3D fibre reinforcements and their composites are distinguished by the fact that fibres are not only aligned along the plane of the material in the x and y-directions, but also through the thickness of the material in the z-direction.

The development of 3D composites was driven by the need to overcome the inherent inadequacies of 2D laminates for certain applications. These inadequacies not only include shortfalls in through-thickness mechanical properties and impact damage resistance and tolerance but also high fabrication costs, which result from the need to

lay a number of individual thin plies to form a laminate with the required mechanical properties [26].

The manufacturing techniques used to produce 3D fibre reinforcements have the ability to manufacture net-shape preforms with high levels of automation [19]. With this capacity, a number of the 3D fibre reinforced composite manufacturing techniques; e.g. 3D weaving, 3D braiding and knitting, can avoid the labour intensive hand lay-up process, which is regularly used within the aerospace industry [17, 19] for the manufacture of prepreg components and fibre preforms for the resin transfer moulding (RTM) and resin infusion (e.g RIFT/SCRIMP) processes .

The hand lay-up process generally consists of cutting the fibre reinforcements and laying them down in the desired fibre orientation onto a tool [4]. Although the lay-up process can be semi-automated using tape lay-up machinery, the equipment is very expensive and is restricted to low complexity shapes, such as flat and slightly curved panels [26]. Through their avoidance of the labour intensive hand lay-up process, dry fibre preforms made by the stated 3D fibre reinforcement manufacturing techniques, remove the labour costs associated with hand lay-up. Although the 3D fibre reinforcement technique of structural stitching is fundamentally an additional process step to the manufacture of 2D laminated composites, and does not remove the labour cost of hand lay-up as the previously mentioned processes do, structural stitching can reduce the complexity of the hand lay-up process through the amalgamation of numerous stitched preforms [26]. This ability can alleviate some of the costs that would otherwise be experienced when laying individual plies into a highly complex tool or fabricating the complex component through the adhesive bonding or mechanical fastening of numerous previously cured parts.

The majority of 3D fibre reinforcements are processed with liquid composite moulding (LCM) techniques such as RTM, with the exception of Z-pinned prepregs which require autoclave processing [26]. The RTM process consists of placing a dry fibre preform in a matched tool and injecting a pressurised mixture of catalysed resin [4]. After a period of curing under heat and pressure, which is applied to the tool, the finished part is removed. In comparison to the prepreg/autoclave process regularly used within the aerospace industry, the RTM process does not require the use of an autoclave. However, the cost benefits associated with the avoidance of autoclave processing are often offset by the high cost tooling required by RTM, though this does depend on production volume and part complexity, with RTM becoming more economical at higher levels of production, and with increased part complexity lowering the volume production at which RTM becomes more profitable [27]. The high level of part integration capable with RTM can see the process's tooling costs falling below those of autoclave moulding several parts and bonding them together [27]. The prepreg/autoclave process uses fibre reinforcements, known as prepregs, which are pre-impregnated with catalysed resin. Within the process, the prepreg is cut, hand laid onto an open mould, vacuum bagged and then placed in an oven or autoclave to consolidate and cure [4].

Due to the presence of through-thickness reinforcement, the applications of 3D fibre reinforced composites are generally within structural components requiring improved through-thickness mechanical properties [28], such as those likely to encounter impact. However, the use of 3D fibre reinforced composites can also be seen where through-thickness stress is generated through an applied static load rather than impact, and where complex geometries or sheer volume limit the use of conventional hand lay-up manufacturing techniques [28]. The preferred use of 3D rather than 2D fibre reinforced composites in these areas can be associated not only with the reduction of labour but

also, in applications benefiting from improved delamination resistance and impact damage tolerance, with reductions in weight. As Tong et al [26] and Mouritz et al [29] observe, ‘to combat the problem of delamination damage, (conventional 2D) composite parts are often over-designed with extra thickness’, increasing their weight. This practice is also emphasised by Tai et al [30]. As 3D fibre reinforcements can be optimised in terms of their in-plane and through-thickness mechanical properties, they have the potential to improve upon the weight of 2D composites. This brings about a question that is at the heart of this research project. How does through-thickness fibre reinforcement, specifically single-side access robotic tufting, affect composite cost and weight?

1.2 Project aims and objectives

The overall aim of this thesis is to establish a greater understanding of the effects of the single-sided robotic tufting process, a form of structural stitching, on component manufacturing costs and weight, and subsequently determine whether potential economic benefits can be realised through its implementation. To complete this assessment the study uses the novel composite rib post component developed for the Airbus-led Next Generation Composite Wing (NGCW) programme as an example case.

This project focuses on using a variety of techniques, including process analysis, material analyses, process simulation, cost modelling and structural modelling in a concurrent manner to provide a novel understanding of the economic effects of the through-thickness fibre reinforcement technique. Novel aspects of the project also lie in the creation of a manufacturing cost model for the tuft reinforced novel composite rib post, incorporating algorithms defining the resources consumed by the robotic tufting process. In addition data are generated with regard to the permeability of the tufted fibre reinforcement, providing required values for the simulation of the material’s

consolidation and providing an early indication of the general effect of tufting on permeability.

For the successful completion of the project, the following objectives were made:

1. *Perform manufacturing process analyses to determine the resources consumed during the manufacture of the novel composite rib post.*
2. *Establish algorithms describing the relationships between the process's manufacturing activities and their consumption of resources.*
3. *Investigate the permeability of the tufted reinforcement to establish values for the completion of process simulation.*
4. *Complete modelling of the novel composite rib post's RTM process to establish mould fill times.*
5. *Develop a manufacturing cost model for the novel composite rib post based upon the established relationships between the process's manufacturing activities and the required resources.*
6. *Complete structural modelling simulating the pure pull-off load case to determine the relative performance of the novel composite rib post, a non-tufted rib post and a prepreg rib post.*
7. *Use known densities, measured fibre volume fractions and component volume to estimate the weight of the components.*
8. *Estimate comparative component manufacturing costs using the developed manufacturing cost model and available commercial manufacturing cost estimation facilities.*

9. *Compare the estimated manufacturing costs and weights of the components incorporating the use of a weight penalty to evaluate their relative economies.*

Chapter 2. Literature review of stitching based through-thickness reinforcement techniques

2.1 Through-thickness reinforcement

The susceptibility of 2D laminate composites to failure by delamination is well documented [26, 29, 31-34]. Delamination is initiated by interlaminar stress concentrations which can be caused by out of plane loading [35], manufacturing defects, geometric discontinuities and bonded and bolted joints [36]. Additionally, the significant interlaminar stress, and also damage, that can arise from encountering impact [36], such as barely visible impact damage (BVID) which is the occurrence of significant levels of delamination with barely visible surface indications, is of particular concern in composite applications likely to experience such an event. In aircraft structures, impact load may be generated by various circumstances. These can include; dropped hand tools, bird strike and hail and stone impacts, with the resultant damage being known to seriously degrade the in-plane mechanical properties of a laminate [26].

There are a number of techniques that incorporate what has been termed ‘material improvement’ [29] to increase delamination resistance and damage tolerance. Although these techniques are only effective for low energy impact, they can inhibit the manufacture of high quality laminates and are stated to vastly increase cost through their additions to material cost and direct labour time [26]. These techniques can include the use of thermoplastic films, the chemical and rubber toughening of resins and the treatment of fibres [26]. More recently, improvements to interlaminar fracture properties have been reported using carbon nanotube reinforced matrices [37], and also

vertically aligned carbon nanotubes (VACNT) [38] between prepreg plies. The objective of toughening the individual material components is to increase the fracture toughness of the matrix and fibre-matrix interface, where cracks are most likely to initiate and propagate [36].

Stitching is one of a variety of fibre-architecture modification techniques that have been developed to address the vulnerability of 2D laminate composites to delamination and improve upon the delamination resistance provided by material improvement techniques [36]. Along with techniques such as 3D weaving, 3D braiding, 3D knitting, z-pinning and z-anchoring, stitching focuses on manufacturing advanced fibre reinforcements with fibres aligned in-plane and through the thickness of the material. The characteristic fibre orientations of these reinforcements facilitate the production of composite materials with attractive mechanical properties, both in and out of plane. Whilst this provides enhanced interlaminar shear strength, delamination toughness and impact damage resistance [39], it also avoids some of the manufacturing pitfalls associated with material improvement strategies, such as; the uneven distribution of resin toughening particles due to their entrapment within the fabric during consolidation, labour intensive interleaving of toughening films and the use of expensive toughened resins [26].

Introduced over two decades ago [40], the stitching of advanced composites was first investigated by the aerospace industry for the reinforcement of composite joints [26]. Despite findings demonstrating the benefits of stitching in this area, the technique's improvements to impact damage resistance and tolerance have seen it attain greater popularity for the reinforcement of composite aircraft panels [26].

Stitching provides various manufacturing advantages over a number of its contemporary 3D fibre reinforcement techniques. These advantages relate to the fact that stitching is completed as a secondary process step to the lay-up of traditional 2D laminate stacks.

This characteristic allows stitching a great flexibility in terms of possible fabric lay-ups [26]. The fibre orientations that are possible with competing 3D textile processes can be limited by the capabilities of the manufacturing processes themselves, with out of plane fibres manufactured as integral aspects of the fibre reinforcement [26]. The stitching technique provides through-thickness fibre reinforcement as a secondary process step and hence allows a level of optimisation. Stitch densities can be varied according to the level of through-thickness reinforcement required and stitches can be placed only in areas benefitting from their presence [26, 28].

In addition to providing through-thickness reinforcement, stitching can be used to produce (a) simple preforms for improvements to handling and (b) complex 3D net-shape preforms to reduce labour times associated with fabric lay-up. A labour time reduction greater than 80% has been shown compared to the use of prepreg for a fuselage frame with a J-shaped cross section [41]. The more complex preforming is carried out by stitching several different components together, the end result being a net-shape preform containing through-thickness reinforcement in certain areas [26, 28]. Similar to many of the other 3D fibre reinforcement manufacturing processes, the ability of stitching to create complex net-shape dry fibre preforms gives the process additional commercial value, offering a potential cost advantage over the conventional preforming of prepreg materials.

The disadvantages of stitching, as with other 3D fibre reinforcement techniques, are mainly associated with the reductions to in-plane properties that can result from the damage caused by the process. In the case of stitching this can include; resin pockets, broken fibres, fibre kinking and misalignment [42].

2.1.1 The stitching process

In its simplest form, the stitching process consists of inserting a stitch thread through a stack of fabric layers with the use of a needle. To provide through-thickness reinforcement the stitch thread consists of a high performance yarn. Frequently this is made from glass, carbon or aramid fibres. The stitching of high performance fibres can be achieved using conventional industrial stitching equipment, but more complex machinery specifically designed for this purpose has been developed [26]. This machinery includes bespoke stitching machines with robotically controlled multi-needle sewing heads (Figure 2-1) and more recently, computer-controlled robotic one sided stitching heads (Figure 2-2). Being designed specifically for stitching high performance fibres, this equipment overcomes the drawbacks of conventional equipment, allowing stitching of curved structures and other complex shapes.

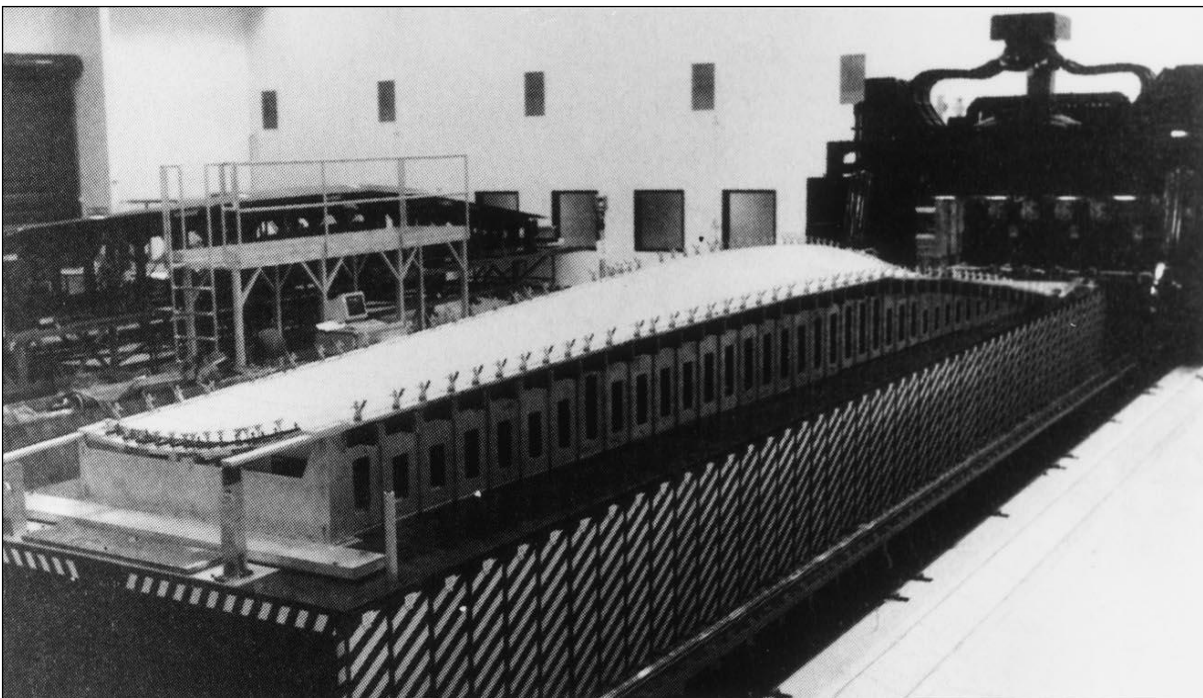


Figure 2-1. Stitching machine developed by NASA in association with Boeing to stitch composite wing panels [43].

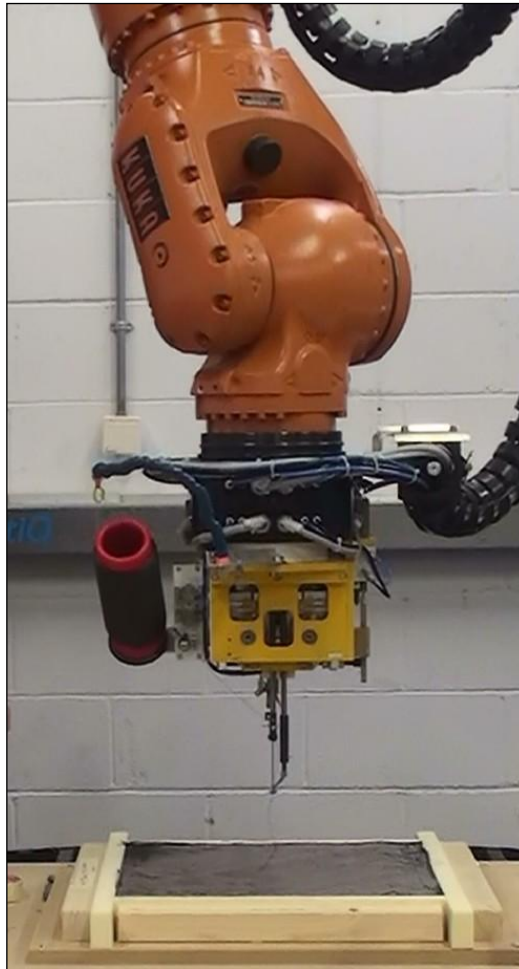


Figure 2-2. Computer-controlled robotic one sided stitching head (courtesy of QinetiQ)

According to Tong *et al* [26], Vinchery [44], Mouritz and Cox [45] and Mouritz *et al* [29], the most common stitching patterns used by double sided stitching machines, such as those conventionally used in industry and that pictured in Figure 2-1, are the lock stitch, modified lock stitch and the chain stitch (as shown in Figure 2-3). In order to create these interlocking stitch types and bind the fabric stack together, knots are used to link the needle and bobbin threads [45]. This requires access to both sides of the fabric stack [26]. Of the mentioned stitching patterns the modified lock stitch is often most popular as minimal in-plane fibre distortions are caused inside the material, the linking knots being formed at only one surface [26, 45].

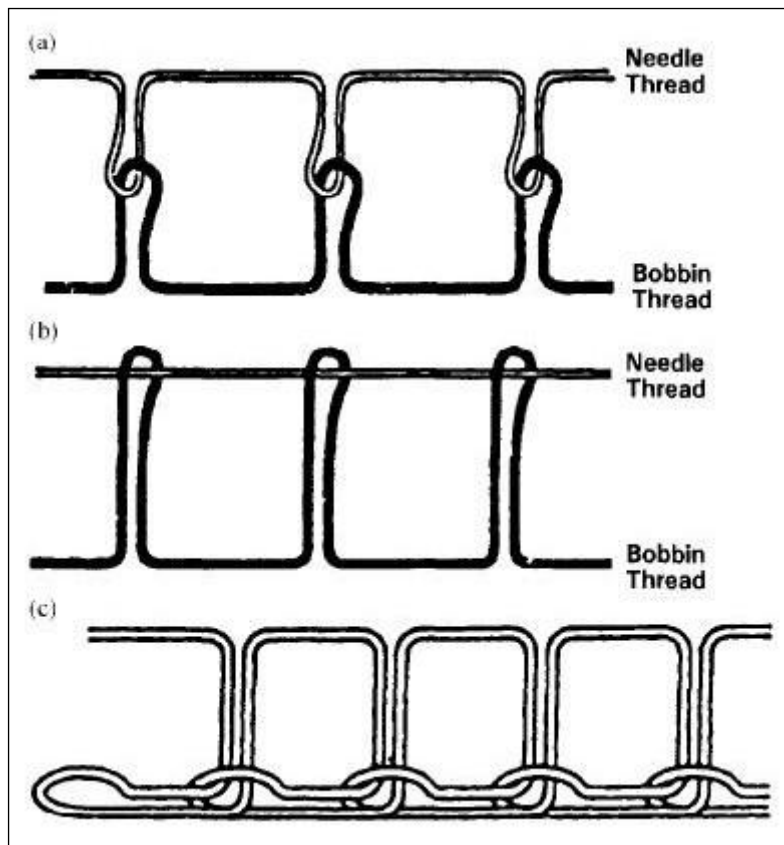


Figure 2-3. Schematic of the (a) lock stitch, (b) modified lock stitch and (c) chain stitch [44].

There are inherent limitations to the use of conventional stitching machines. The complexity, size and thickness of the resulting preforms can be constrained by the machine's requirement to access each side of the fabric stack, and the size of the machine itself [43]. These issues are overcome by robotic single-sided stitching. With this process a computer controlled stitching head, requiring access to only one side of the fabric stack, is supported by a robotic arm, as pictured in Figure 2-2. In contrast to conventional stitching machines, the robotic single-sided stitching process actively controls the movement of the stitching machine rather than the work piece, removing the dependence of the size of the resulting preform from the size of the stitching machine itself [46, 47].

Robotic single-sided stitching is capable of a number of stitching patterns through the use of interchangeable stitching heads. These stitch types can include two needle

stitching, blind stitching and tufting [48]. Each produces a different stitch pattern, as pictured in Figure 2-4.

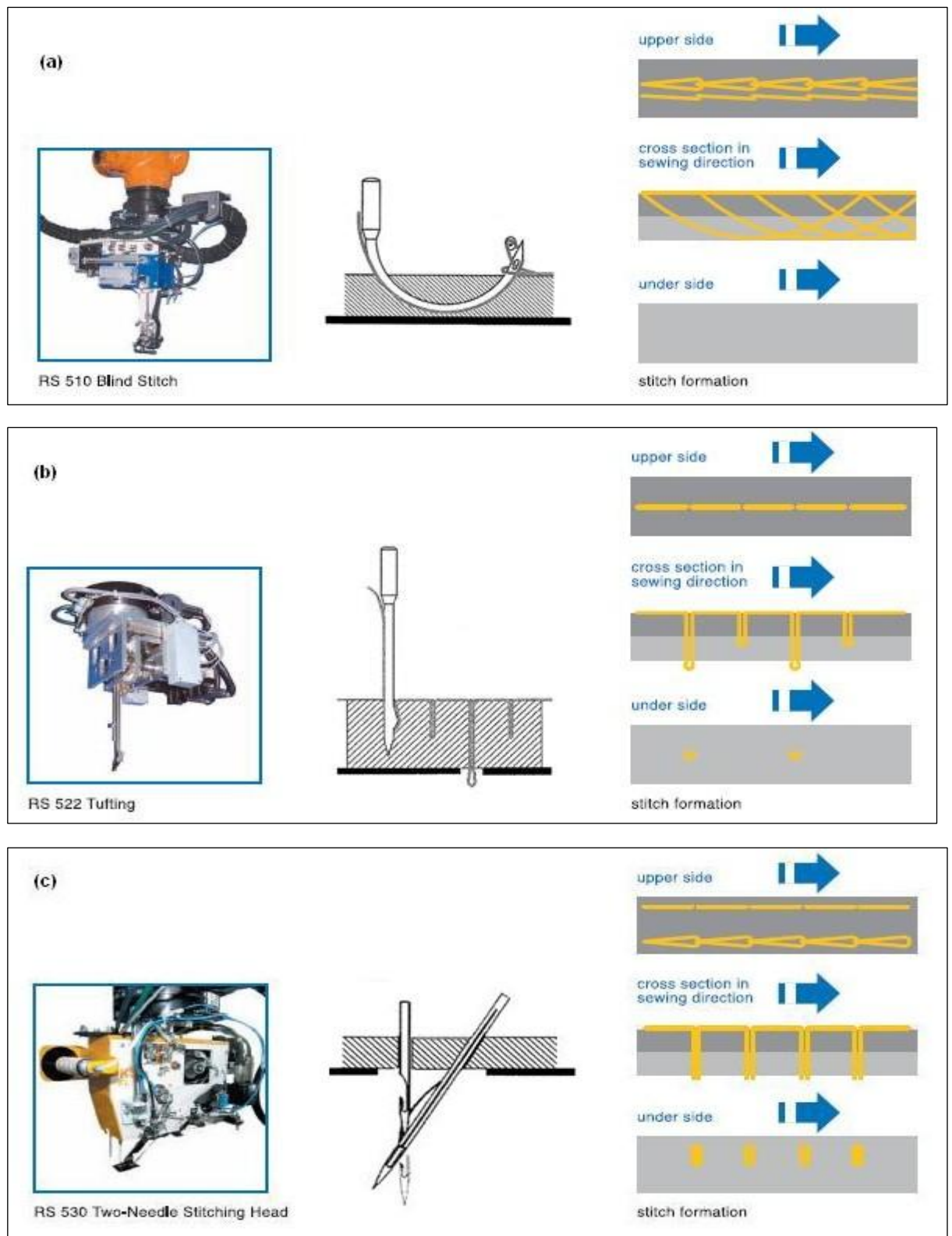


Figure 2-4. Schematic showing the stitching heads, needles, and stitching patterns of (a) Blind stitching, (b) tufting and (c) Two needle single sided stitching techniques. Adapted from KSL [48] and Tong et al [26].

It can be seen that similar to double sided stitching patterns, two needle stitching and blind stitching form interlocking stitches, binding the fabric stack together. On the other hand, tufting does not create an interlocking stitch structure (Figure 2-5). It is this characteristic that allows tufting to avoid the damaging effects of thread tensioning and knots typical of interlocking stitch types, which have been stated to considerably weaken mechanical properties [46].

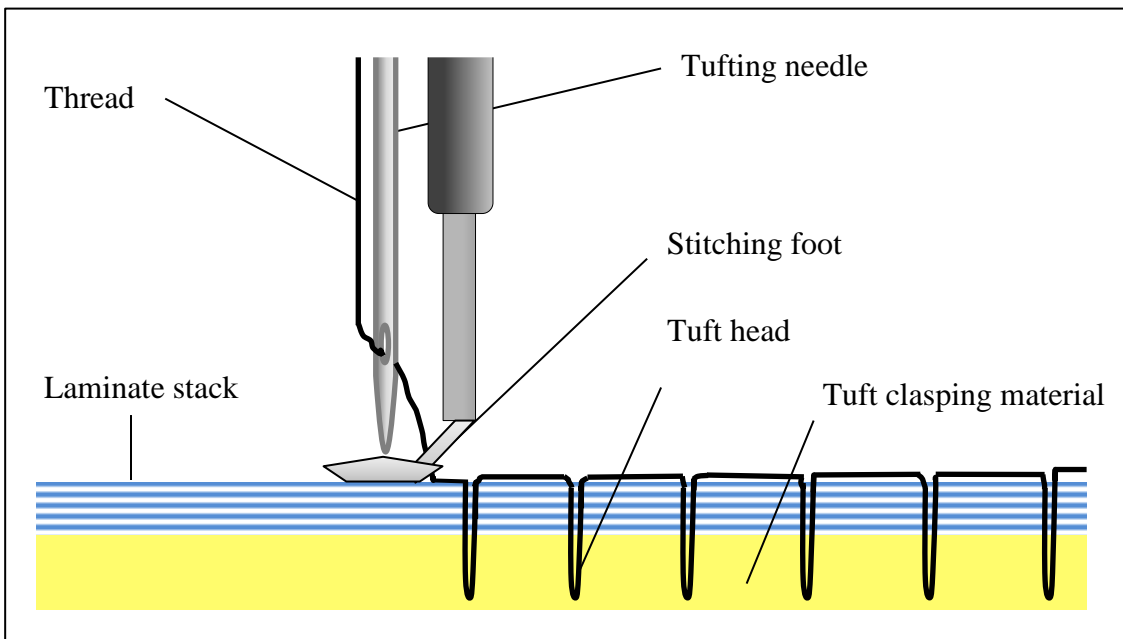


Figure 2-5. Diagram demonstrating the arrangement of the thread in the tufted preform

The single sided tufting process was developed by the DLR Institute of Structural Mechanics in Brunswick, Germany [46]. The process consists of the insertion of a single needle carrying a high performance thread into a stack of loose fabric plies and its removal along the same trajectory [49], as shown in Figure 2-5. Instead of the use of an interlocking stitch, tufting relies on friction between the plies and stitch thread or the use of an additional mould material, such as a foam, to keep the tuft in place during the process and avoid tuft pull out each time the tufting needle is removed [49]. Tufting does not have interlocking stitches and thus results in a preform that is slightly more fragile than those created by other forms of stitching [50], requiring more care when handling to avoid tuft pull out and disintegration of the preform.

The great flexibility offered by the tufting technique, which allows variation of stitch angle, low thread tension, and a maximum stitched material thickness of 40mm (limited by needle design) which is the greatest thickness of all the single-sided stitching techniques [47], has resulted in the technique being focused upon by the current project.

2.1.2 Mechanical properties of stitched composites

As expected, the placement of fibre in the through-thickness direction of a composite with a technique such as stitching, results in different properties to those achieved by conventional 2D laminates. The key objective of this technique, similar to other 3D fibre reinforcement methods, is to increase fibre volume fraction in the through-thickness direction and improve delamination resistance [26, 36], interlaminar shear strength [36, 43], impact damage resistance [45] and impact damage tolerance [45, 51]. Ideally, this would be achieved without affecting the in-plane mechanical properties of the composite but in reality this is not the case.

2.1.2.1 In-plane mechanical properties of stitched composites

Within this section the effect of stitching on the tensile, compressive and flexural behaviour of fibre reinforced thermoset composites is discussed.

Comprehensive reviews of the effect of conventional two-sided stitching on in-plane mechanical properties have been completed by Mouritz and Cox [39, 45] and Beier et al. [51]. Their reviews consider data for several types of stitch, yarn and fabric from a large number of studies. The findings show that there is a great deal of variability regarding the effects of stitching on the majority of the in-plane mechanical properties of composites. Tensile modulus is an example of such a property. In additional studies the variability is confirmed, stitching having been reported to have no effect on tensile modulus [51], to cause increases of 8% [52] and reductions of up to 17 % [52-55].

Kamiya et al [55] also highlight a correlation between axial modulus degradation and stitching thread thickness, with reductions of up to 10% when thread thickness is increased by a factor of 3. Reductions to tensile modulus are argued to be the result of in-plane fibre misalignment caused by the stitches, whereas improvements are thought to be associated with the effect of tensioned stitches increasing local fibre volume fraction [39].

Regarding tensile strength, stitching is documented to cause reductions of up to 36% [53-56] due to broken fibres resulting from stitch insertion [45], though it is also reported to result in improvements of up to 15 % [52, 57]. Studying the effect of stitch density on polymer thread stitched NCF carbon/epoxy composites, Yudhanto et al [57] show an initial tensile strength increase compared to the control of 10% with a stitch spacing of 3 x 3mm and then a decrease of 2% with a stitch spacing of 6 x 6mm. Treiber [58] also highlights several studies showing increases to tensile strength of up to 20%. Here causes are again speculated to be increased in-plane volume fraction.

Stitching is found by a number of studies to decrease compressive strength by up to 31% [53, 55] as a result of fibre misalignment initiating kink band failure [51]. However, increases of up to 14% have also been experienced [50, 53]. With findings reflecting those of Hess et al, Zheng [56] reports that when testing a Kevlar stitched specimen at 90° to the alignment of the stitch seams, an increase in compressive strength of approximately 10% is found, and general increases of approximately 40% are shown for 0°, 90°, and 45° stitch alignments with open hole tests. Though no reasoning is found for the occurrence of improved compressive strength of the stitched specimens, there may be similarities with the mechanisms associated with improvements to open hole compressive strength, such as the transformation of the failure mode from delamination to in-plane fibre failure.

As with the tensile behaviour of stitched composites, compressive modulus can be seen both to increase and decrease compared to a non-stitched control. Ranges of between +20% and – 8% have been noted [53], with the responsible mechanisms being argued to be increased delamination resistance, and in-plane fibre misalignment and reduced in-plane fibre volume fraction from fibre spreading respectively [39]. Reductions to flexural strength and modulus in stitched composites have been seen in the range of approximately 15% and 41% respectively, observations indicating that they arise due to a combination of the same factors responsible for the reductions seen in tensile and compressive strength and modulus [59].

The in-plane shear strength and modulus of stitched composites have received much less attention within literature, however a decrease in these properties is observed in work of Hess et al [53] compared to non-stitched quasi isotropic NCF carbon/epoxy composites. They report reductions of up to 15% and 22% for shear modulus and strength respectively. The noted correlation between the reduction to the shear properties and increasing thread thickness may suggest that fibre waviness around the stitches is responsible for the degradation.

Focusing on studies investigating the in-plane mechanical properties of tufted composites, similar variation in the behaviours can be seen. Tensile modulus is reported to remain unchanged in the majority of cases [49, 58, 60] but instances of degradation of 13% can also be found [42]. The improvements to tensile modulus seen when considering other varieties of stitching are possibly not observed with tufting due to the low thread tension resulting from the technique, and the subsequent reduction of comparative localized fibre volume fraction.

In terms of tensile strength, the majority of the considered studies concur that tufting causes degradation, with reductions of up to 19% [42, 49, 58], however Treiber [58]

also shows that tensile strength can remain un-affected in a twill woven fabric composite and Koissin et al [60] argue that improvements of approximately 14% can result. The studies detailing the effect of tufting on compressive modulus and strength show that the properties can remain unaffected or decreased by 11% and up to 25% respectively [42, 58].

Despite the varying results obtained for the effect of stitching on in plane compressive and tensile properties of various composites, Treiber [58] and Colin de Verdiere et al [42] agree that tufting has only positive influences over shear modulus and shear strength, reporting increases of up to 40% and 10% respectively. The findings of Treiber [58] suggest that the improvements correlate with stitch density, the increased shear modulus occurring from partial alignment of the tuft seams and loop ends with the load, and increased strength resulting from enhanced delamination suppression .

2.1.2.2 Out-of-plane mechanical properties and delamination behaviour of tufted composites

There is much agreement that structural stitching improves the interlaminar mechanical properties of laminated composites [52, 53, 60-69]. Delamination studies have shown stitching to increase Mode I and Mode II delamination toughness by up to 15 and 4 times respectively compared to unstitched laminated composites [67, 68]. This characteristic is argued to be the result of the ability of the stitches to bridge cracks and subsequently suppress delamination [35]. In Mode I delamination failure this attribute constrains crack propagation [56] and in Mode II delamination it suppresses failure by localised bucking [70]. These features provide stitched composites with greater capabilities in impact susceptible applications, having increased resistance to delamination damage from impact and maintaining greater integrity after impact events, showing increases in compression strength after impact of up to 48 % [50, 53].

Studies have shown stitching to provide more effective improvement to impact damage resistance at higher impact energies [62], approximately halving the projected damage area at impact energies of 3 J/mm but showing little reduction at energies of less than 1 [65]. Tan et al [62] show the damage resistance of stitched composites at these impact energy levels to be improved by increasing stitch density, a factor of two increase resulting in approximately half the delamination area when impacted with energies of between 4.1 and 10 J/mm.

Increasing stitching thread thickness is also reported to have extremely positive effects in Mode I delamination, with Plain and Tong [71] finding up to 100% increases in delamination toughness. No such improvements in Mode II delamination are reported, however substantial benefits are experienced when angling the stitches against the direction of crack propagation in end-notched flexure (ENF) tests, up to an 88% increase in fracture toughness in comparison to stitches being angled with the direction of crack propagation being shown [71]. Tan et al [69] investigate the extent to which stitching can reduce delamination damage, proposing that the reduction of delamination does not exceed 40%, and that additional reductions are not seen above a through-thickness stitch volume fraction of 0.4%.

Focusing again solely on the effects resulting from the addition of structural tufting to a composite, improved properties are seen. Treiber's [58] investigations show six fold increase in the Mode I delamination toughness and an increase in Mode II delamination toughness of 63% citing similar mechanisms for these improvements as those observed for conventional stitches. Comparable improvements are found by Colin de Verdier et al [42] who show a ten and threefold increase in the Mode I and Mode II delamination toughness respectively. As well as showing improvements to delamination resistance,

Dell'Anno et al [49] report subsequent decreases to delamination resulting from impact and improvements to compression after impact strength of up to 27%.

A recent high profile industrial application of stitching is the use of the technique to create a preform consisting of seven layers of carbon NCF and stiffeners for the rear pressure bulk head of Airbus's A380 [72, 73](Figure 2-6).



Figure 2-6. Airbus A380 rear pressure bulkhead [72].

Stitching has also been used to attach T-stiffener preforms to multi-axial fabric wing panels in research completed for Airbus, the stitched panel showing equivalent performance to the original prepreg component [41, 58]. With delamination being a frequent mode of failure in stiffened skins [74, 75], the use of stitching to provide a mechanical joint between the two structures can enhance performance. In studies examining the joints between T-stiffener and skin and also omega stiffener and skin, structural tufting has been shown to stop failure by delamination and increase the joint strength by a factor of two in pure pull-off tests [74, 76]. The use of tufting in the reinforcement of the T shaped composite rib post investigated within this project has been implemented to provide similar improvements, though in this case to resist delamination within the structure of the T resulting from the use of the component as a connection piece rather than a stiffener.

It is clear from published literature that there is a lack of consensus regarding the relationships between stitching and in-plane mechanical properties. The limited range of literature concerning the in-plane mechanical properties of tufted composites does however seem to highlight a trend in which the tensile and compressive modulus and strength do not experience improvements with tufting. A possible reason for this relationship compared to the positive correlations seen with some conventionally stitched composites is the reduced thread tension resulting from the technique, and the speculated lessening of higher localised fibre volume fraction and preform stabilisation. Interestingly, different again from the observations of conventionally stitched composites, improvements to the shear modulus and strength are seen to correlate with increased tuft density possibly as a result of the tuft seams and loops.

Much greater agreement is seen concerning the effect of stitching and tufting on out-of-plane mechanical properties, with widespread observations of significant improvements to mode I and mode II delamination toughness and the through-thickness strength of joints.

Chapter 3. Tufted composite manufacture and equipment

The manufacturing process and equipment used to produce tufted fibre preforms has developed over time. This study considers the automated robotic tufting process implemented by QinetiQ, the industrial sponsors of this project.

As part of the NGCW programme, a multidisciplinary technology programme aimed at developing technology for future aircraft wings, QinetiQ have investigated the automated robotic tufting process to evaluate its potential for high volume wing manufacture.

The specific case used to analyse the process is that of a wing rib post, designed to replace a typical metallic component already present in primary aircraft structures. Within an aircraft wing, rib posts form the connections between the front and rear spars and the ribs themselves (Figure 3-1), thus playing a major part in the transfer of load.

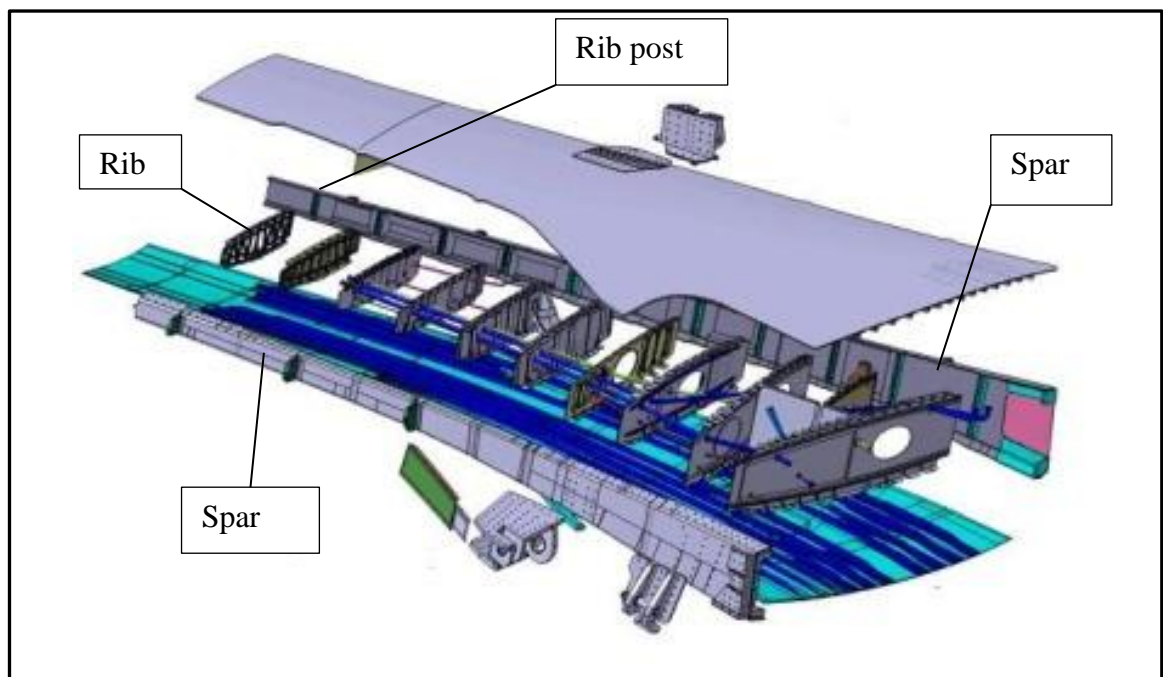


Figure 3-1. The design of the ALCAS lateral wing, including spars ribs and rib posts [20]

The rib post was designed and investigated in the NGCW work package concerned with composite manufacture. A diagram of the component is shown in Figure 3-2 labelling its dimensions and constituent preforms.

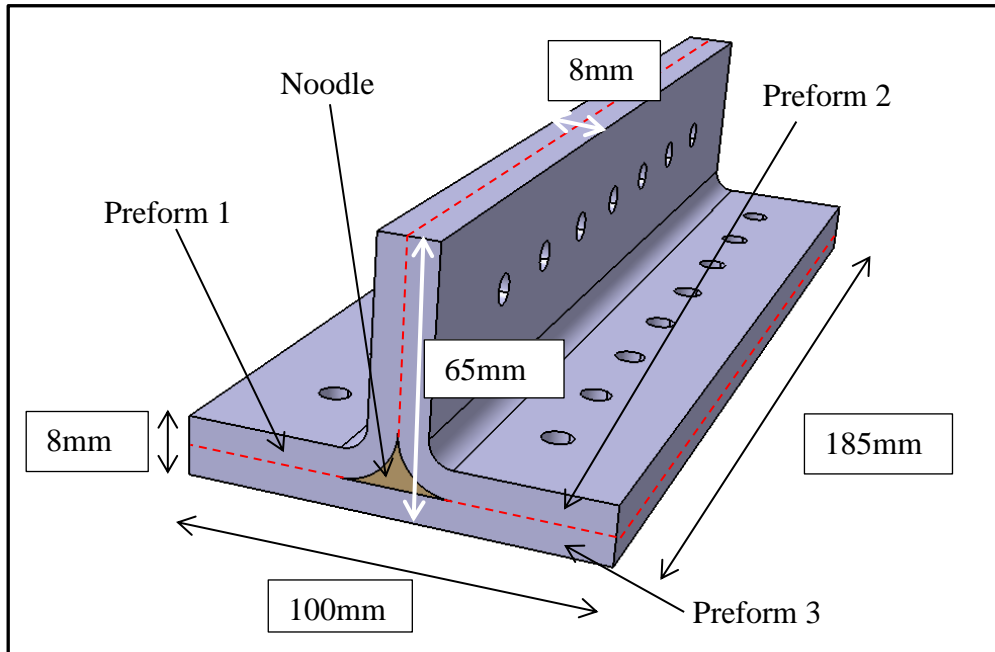


Figure 3-2. The design of the novel composite rib post (Courtesy of QinetiQ)

In order to be considered successful in the replacement of the metallic component, the composite equivalent was required to meet various criteria laid out within the programme. These conditions, parallel with those adopted in the ACEE programme run by NASA [3], required the composite rib post to:

- Meet the same design load as the current metallic solution.
- Meet or reduce the loads currently transferred into the adjoining structures, requiring no modification of these parts.
- Create little or no change to interfaces, with any change accommodating the current metallic solution as well as the composite part.
- Cause no significant change to the handling characteristics of the aircraft.

Within the wing, the rib post is mounted to the spar as shown in Figure 3-3, depicting the spar in its cross-section. The rib of the wing is then fixed to the rib post by way of

the web bolts shown in the diagram. Resulting from its role in connecting the spar and rib, the rib post is expected to experience combined loading in-service, experiencing a bending moment, shear and direct loads (Figure 3-3). The extent of these loads and the bending moment are noted in Table 3-1. The figures of the table refer to the failure loads of the metallic part, establishing the required minimum load and bending moment before failure of the novel composite solution.

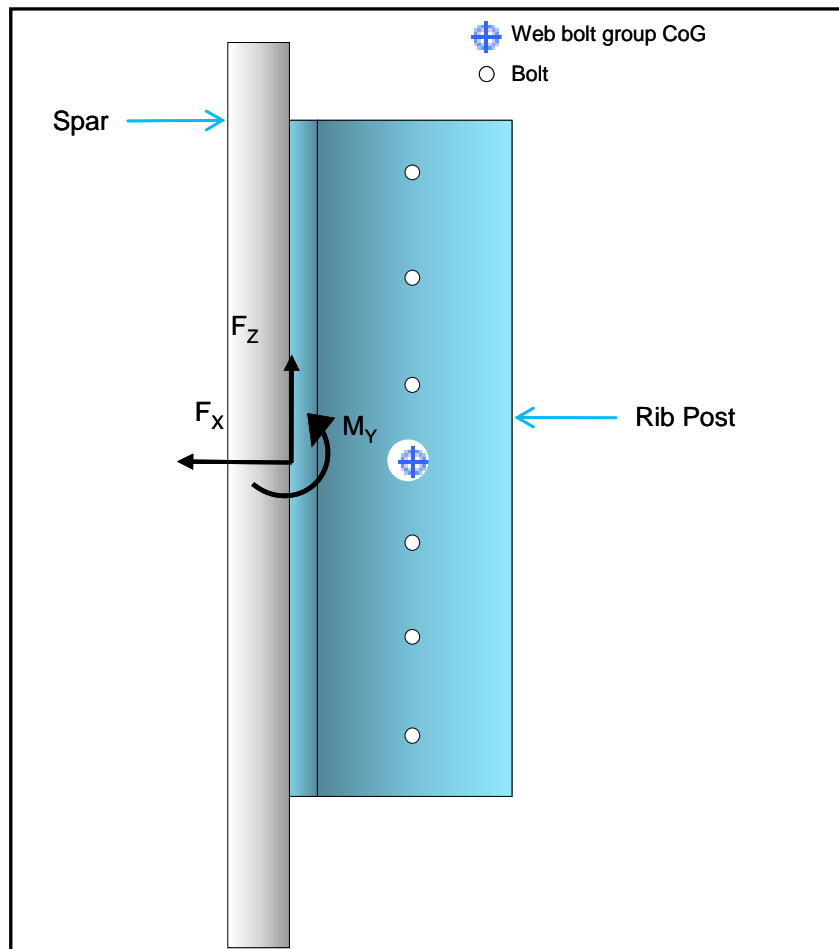


Figure 3-3. A schematic of the mounting of the rib post to the spar, noting load and bending moment directions (courtesy of QinetiQ)

Table 3-1. The design loads and bending moment of the composite rib post

Loading and Bending moment directions	Design Loads and Bending moment
F_x	-2.1 kN
F_z	-33.1 kN
M_y	-3.8 MN.m

The T-shaped composite rib post is constructed with three individually tufted rectangular preforms (forming a layer of tuft heads and resin mid-thickness of each limb) and a noodle, which fills the resin rich volume resulting from the transition between the flanges and the web of the structure (Figure 3-2). QinetiQ have explored various different forms of noodle in their investigation of the component, including glass and carbon rovings, stitched glass and carbon, braids and woven pyramids. The rib post is manufactured from a total of 24 plies of carbon non-crimp fabric (NCF), each of the 3 tufted preforms (Figure 3-2) consisting of 8 layers of 2 ply fabrics with a quasi-isotropic lay-up.

3.1 Tufted preform morphology

The tufting process produces typical characteristics in its resultant preforms. As with other stitching techniques, tufting produces a seam on the surface of the fabric where the tufts are inserted (Figure 2-5). The technique also characteristically produces a section of through-thickness reinforcement, the tuft, consisting of a doubled length of thread (Figure 2-5) which locally parts the ply fibres within the preform. In addition, this doubled section of thread also produces the tuft loop, (Figure 2-5), which protrudes from the bottom surface of the preform. Typically when the preform is closed within a mould, the tuft heads are forced to lie flat against the fabric.

The tufted material studied within this project is based on a quasi-isotropic lay-up of Saertex [77], non-structurally stitched, bi-axial carbon fibre NCF. The fabric stack consisted of eight layers and was laid up by hand in the following arrangement: $[\pm 45, 0/90]_{2s}$. The shared characteristics of the fabrics are provided in Table 3-2. The areal weights of the fabrics were 656g/m^2 and 411g/m^2 for the $0^\circ/90^\circ$ and $\pm 45^\circ$ respectively.

Table 3-2. Preform fabric characteristics

Manufacturer	Saertex
Fibre type	Toray T700 50C
Fibre density (kg/m ³)	1800 [78]
Stitch material	Polyester

The laminate stack was tufted in a square arrangement (Figure 3-4), with the tuft rows and subsequently the seams parallel to the fibres aligned in the 90° ply direction. The tufts were spaced 4mm x 4mm with an angle of $\pm 45^\circ$ in the 0° ply direction. In order to counter ply movement during the tufting process, two rows of vertical tufts (0° angled) with 4mm x 4mm spacing were placed along the perimeter of the preform.

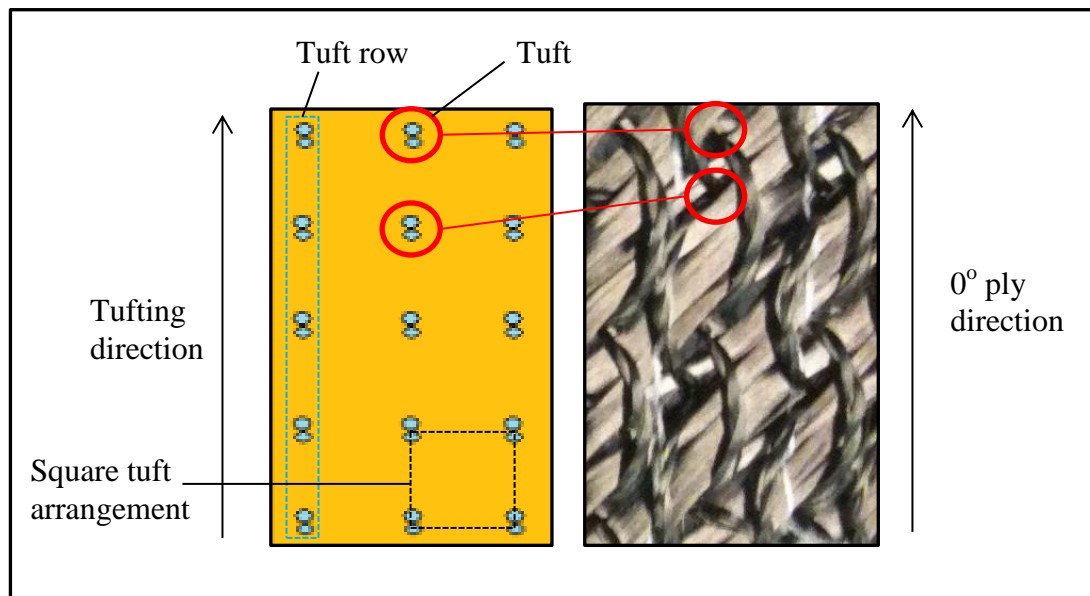


Figure 3-4. A schematic of the square tuft arrangement of the investigated preform

This arrangement is produced by first tufting each row with -45° angled tufts, with a tuft spacing of 8mm along the row. At the end of each row, the robotic tufting head then returns to the start of the same tuft row, is offset in the tufting direction by 4mm, and continues tufting with a tuft spacing of 8mm and a tuft angle of $+45^\circ$. This method is continued at every 4mm interval along the preform to produce a tuft spacing of 4mm x 4mm. The result of this procedure is that half of the tufts in each tuft row are angled at

+45°, and half are angled at -45°. A diagram showing the form of the tuft within a representative unit cell of the material is shown in Figure 3-5.

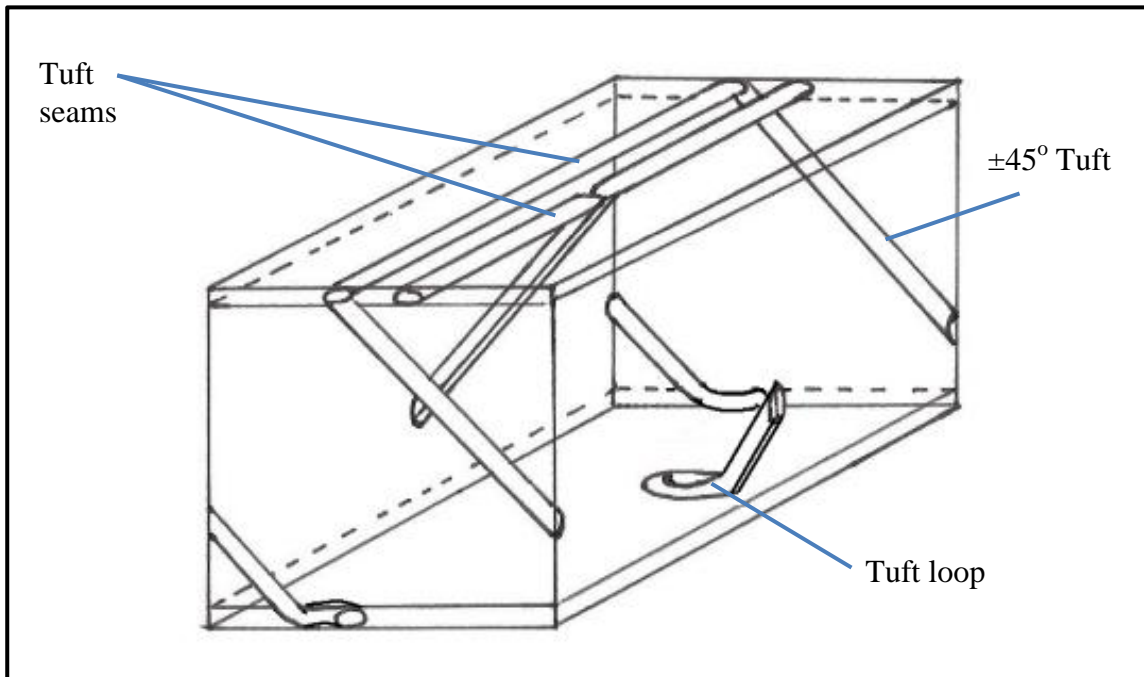


Figure 3-5. The tuft form within a representative unit cell of the 4 x 4mm, ±45° tufted preform

The tufting was completed using a carbon thread, the characteristics of which are provided in Table 3-3.

Table 3-3. Tuft thread characteristics

Thread type	Carbon
Manufacturer	Schappe Techniques®
Specification	Tenax® Carbon
Linear density (g/m)	0.14
Fibre Type	HTA 40
Fibre density (kg/m ³)	1780 [79]

The final weight per unit area of the tufted preform was 4494g/m². Detail of the preform's tufting can be seen in Figure 3-6.

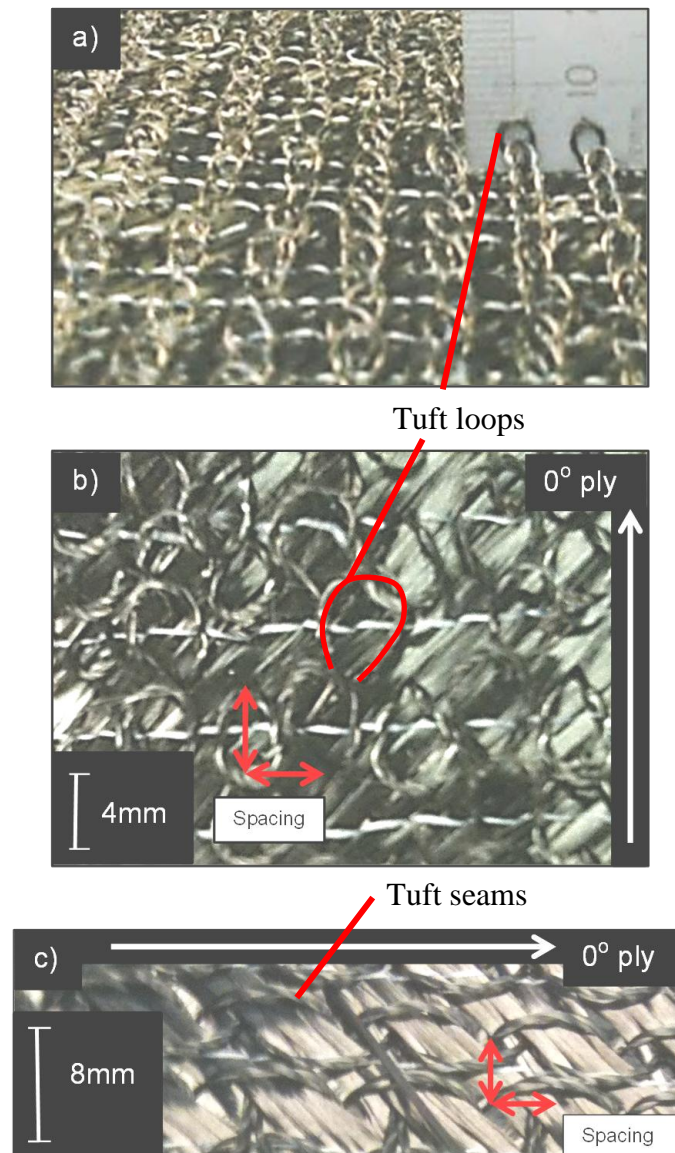


Figure 3-6. Preform photos showing a) the measurement of tuft loop length, b) the spacing of the tuft heads and c) the spacing of the surface segment of the carbon tufts in the quasi-isotropic carbon NCF stack

The tuft loops of the examined preform experience some variation in length, possibly the result of partial tuft pull-out during the tufting process and the de-moulding of the preform from the tufting foam used to clasp the tufts after their insertion. Due to this variation, an average tuft loop length was determined from 25 measurements of tuft length made at different regions of the preform. The average tuft loop length was determined to be 6mm with a standard deviation of 1mm.

3.2 The novel composite rib post manufacturing process

To properly characterise the tufted composite manufacturing process and facilitate the generation of a manufacturing cost model for the novel composite rib post, several periods were spent at QinetiQ, Farnborough, to determine and record each of the activities carried out within the implemented manufacturing process.

Initially, the complete manufacturing process was analysed during the manufacture of a tufted flat panel manufactured for testing, consisting of the same material as the novel composite rib post. Subsequently, analyses were performed to capture aspects of the novel composite rib manufacturing process differing from that of the previously manufactured flat panel. Each of the analyses was completed using a video camera to record the activities.

The manufacture of the novel composite rib post consisted of four sub-processes; fabric cutting and lay-up, tufting, preform demoulding, RTM, and component de-moulding and tool cleaning. A schematic of the manufacturing process chain consisting of these sub-processes is shown in Figure 3-7.

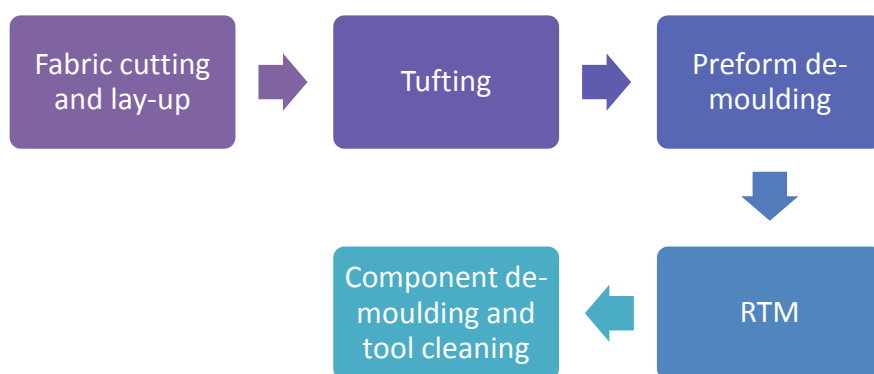


Figure 3-7. The novel composite rib post manufacturing process chain

Each of the sub-processes shown in Figure 3-7 can in turn be sub-divided into numerous manufacturing activities.

3.2.1 *Fabric cutting and preform lay-up*

The fabric cutting and the lay-up of the fibre preforms constituting the novel composite rib post was completed by hand. Individual fabric plies were cut from rolls of the two bi-axial NCF fabrics ($0/90^\circ$ and $\pm 45^\circ$), using steel templates and a rotary cutting knife. A detailed list of the manufacturing activities completed within this sub-process is provided in Table 3-4, and a visual summary is provided by Figure 3-8.

Table 3-4. Fabric cutting and lay-up manufacturing activities

Process step	Manufacturing activity
1.	Fabric collection
2.	Unboxing
3.	Placement on cutting table
4.	Unwrapping
5.	Unravel fabric
6.	Check for damage
7.	Collect set edge, rules and cutter
8.	Place set edge on fabric
9.	Trim fabric edge
10.	Dispose of trimmed fabric
11.	Collect template and return set edge
12.	Place template
13.	Manually cut row of plies and pack
14.	Unravel fabric for cutting of next row of plies
15.	Place template
16.	Manually cut row of plies and pack
17.	Change fibre alignment (turn fabric role over/rotate 90°)
18.	Place template
19.	Manually cut row of plies and pack
20.	Unravel fabric for cutting of next row of plies
21.	Place template
22.	Manually cut row of plies and pack

23.	Return tools
24.	Return fabric to roll
25.	Collect and position wrap
26.	Re-wrap
27.	Collect and prepare box
28.	Re-box
29.	Return Fabric to storage
30.	Repeat for next fabric orientation
31.	Lay-up preforms

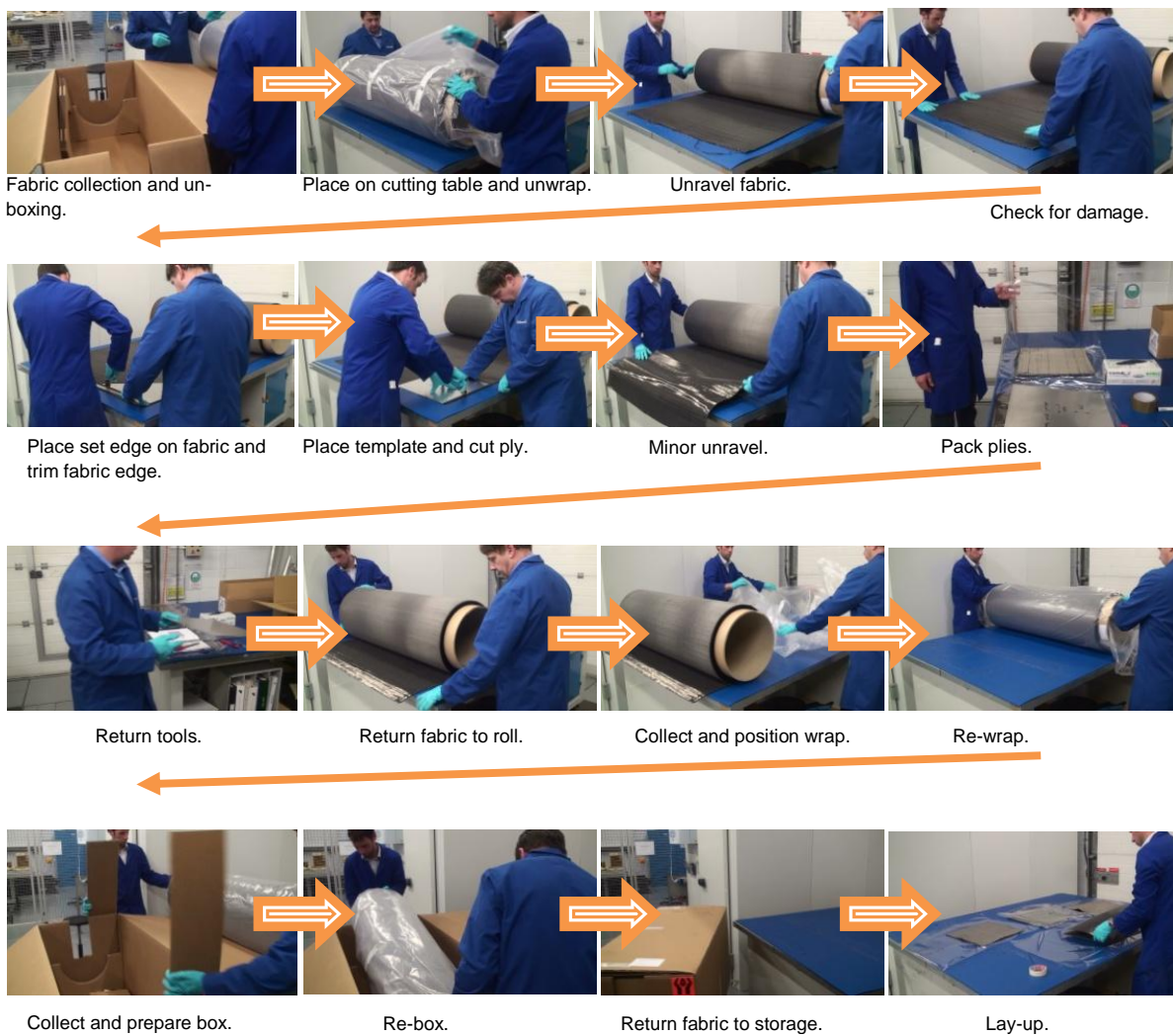


Figure 3-8. Visual summary of the fabric cutting and lay-up sub process

3.2.2 The automated robotic tufting process

At QinetiQ this particular process is completed with a KL 502 linear axis robot unit developed by KSL. This unit consists of a KUKA industrial KR 100 HA robotic arm, which in conjunction with a running track provides 7 axes of movement. Attached upon this robotic arm is a RS522 tufting head that is also manufactured by KSL. The robotic equipment is used in conjunction with a worktop, the position of which is known to the robot control software, and a jig mounted to its surface which supports the work piece (Figure 3-9).

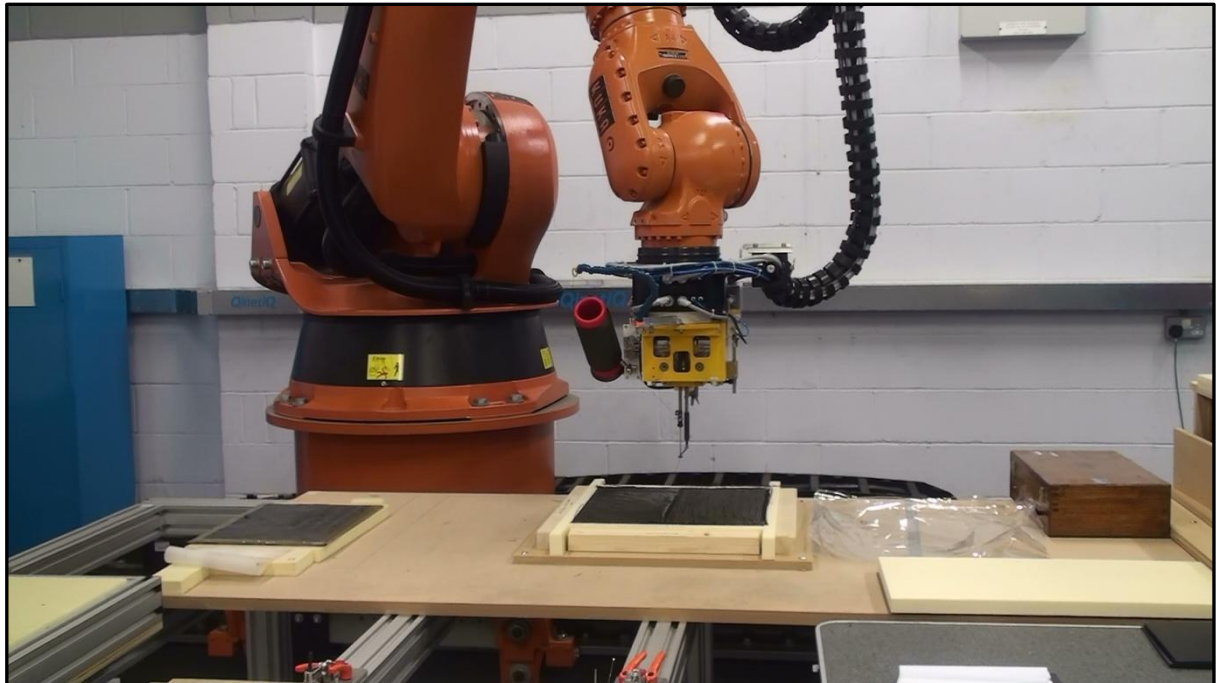


Figure 3-9. The KSL KL502 Linear axis robot unit and tufting head with the worktop and 390mm x 400mm work piece jig

Components of the fabric preform are then secured within the jig on top of an extruded polystyrene foam support material (25mm Yelofam X2i produced by Celecta Ltd). The foam support carries out an important role within the process. As discussed earlier, unlike other types of single sided stitching, tufting produces a stitch that does not interlock and is virtually tension free. As a result, friction alone stops the inserted tufts unravelling during the tufting process. The use of the foam support material not only increases this friction, clasping the tuft heads and ensuring that the tufts are not

unravelling during the process, but also facilitates the full insertion of the tuft through the thickness of the work piece. The foam provides a surface that can support the fabric but also be pierced by the tufting needle, allowing the tuft to pass through the bottom layer of the fabric and into the foam itself. The piercing of the foam requires it to be replaced after the tufting of each preform.

Several different materials are documented to have been used for this purpose including silicone foam [49], brush-like materials [80] and conventional sandwich core foams [58]. Much like the method employed by Treiber [58], the process implemented by QinetiQ makes use of a fine grain foam (extruded polystyrene). The use of this foam allowed its machining to various thicknesses and provided a rigid and resilient stitching mould material that had the ability to clasp the tufts as they were inserted and also retain its shape during the tufting process.

The tufting of the preforms begins once the head carrying the tufting needle and the stitching foot has been moved to the tuft starting position programmed using the robot control software. At this point the tufting foot is lowered, compressing the lay-up, and the first tuft is inserted by the needle. Whilst the needle is removed, the surrounding fabric layers and the foam mould clasp the tuft, allowing the progression of the needle and the foot to the next tufting position defined by the required tuft spacing. As the tufts are inserted, the robotic arm moves continuously forward, the foot and needle being driven by a separate oscillating mechanism. This mechanism keeps these components stationary whilst the needle is inserted and extracted, moving them forward to the next tufting position when the needle is removed in a separate motion from that of the robotic arm. Tufts can be inserted within this process at a rate of up to 500 tufts per minute.

When the programmed end of the tuft row is reached, the needle completes the final tuft of this row. The tuft head is then raised, allowing the trailing tuft thread to be cut by mechanical scissors integrated with the tufting head. At this stage of the tufting process the head is moved to the next programmed starting point, and the tufting of the next row begins.

The manufacturing activities of the tufting process are detailed in Table 3-5.

Table 3-5. Robotic tufting manufacturing activities

Process step	Manufacturing activity
1.	Stitching head attached to robotic arm
2.	Needle and stitching foot calibration
3.	Needle threaded
4.	Laminate stack placed in mould
5.	Program selected and initiated
6.	Tufting completed
7.	Robot returned to home position
8.	Equipment set down

The following figure provides a visual representation of the manufacturing activities of the tufting sub process.

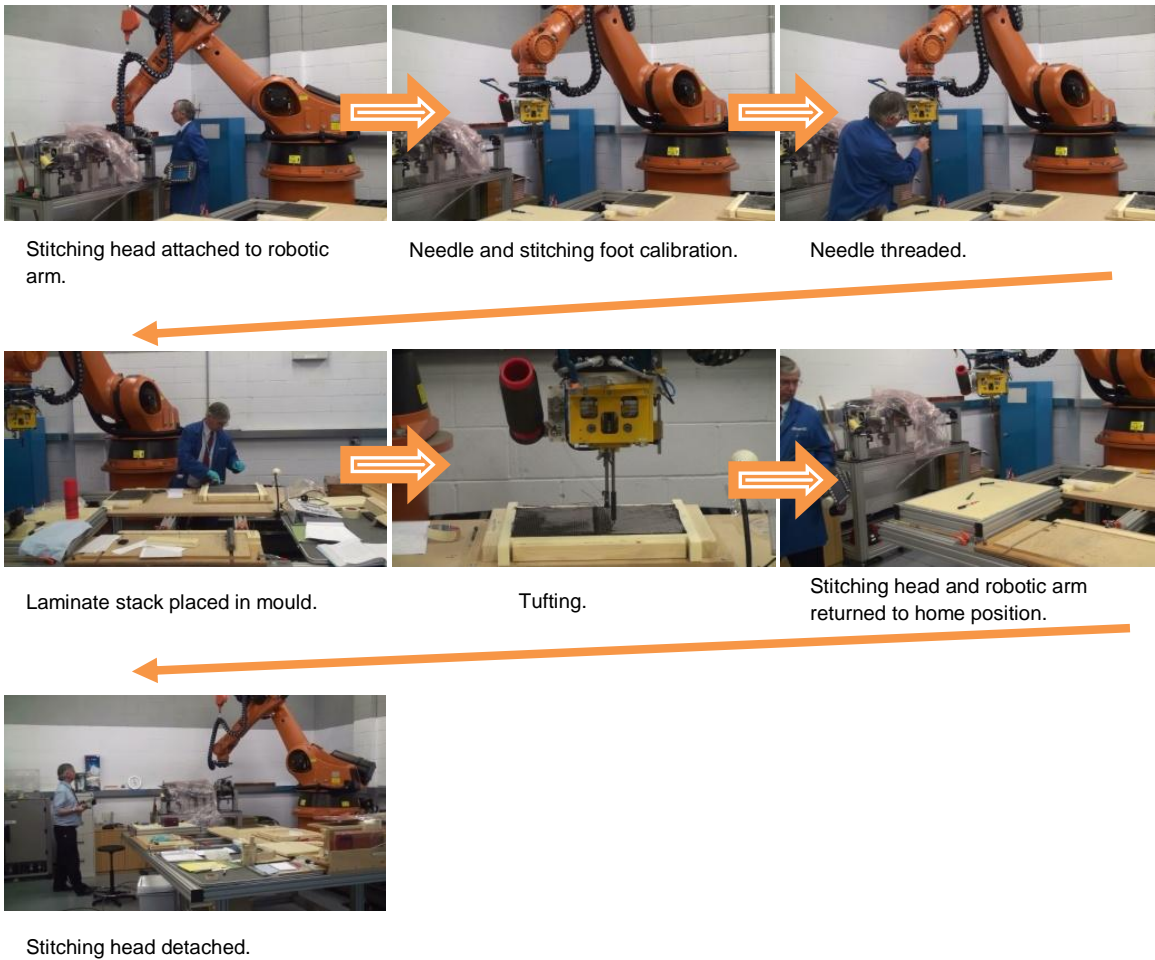


Figure 3-10. Visual summary of the tufting sub process

The needle and stitching foot carried by the tufting head have been specifically developed for the tufting process. The needle used within the tufting process at QinetiQ was a bespoke tufting needle provided by KSL. The eye of the needle is inclined and inset within a channel on one side, ensuring a minimal possibility of the tuft becoming caught in the needle itself and being removed as the needle is retracted from the fabric. The tufting foot (Figure 3-11) is designed to direct the needle during its insertion and ensure that deviation from the required tuft position does not occur as a result of resistance from the fabric plies. The base of the foot is also curved upwards to minimise the possibility of it catching and subsequently damaging the fibres of the fabric.

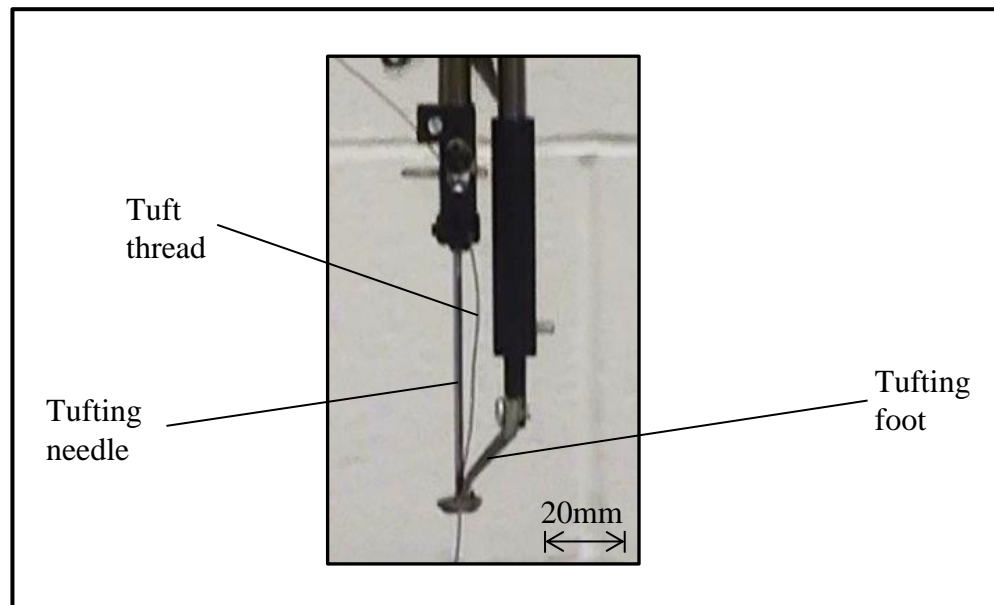


Figure 3-11. The tufting foot and needle used by QinetiQ

As well as tufting normal to the surface of the work piece, tufts can also be inserted at an angle. This angle is currently limited to a range of $\pm 45^\circ$ from the angle normal to the plane of the preform, due to the set-up of the tuft head. When tufts are inserted at an angle it is not possible to use the tuft foot due to its interference with the work piece, a current limitation of the tuft head design.

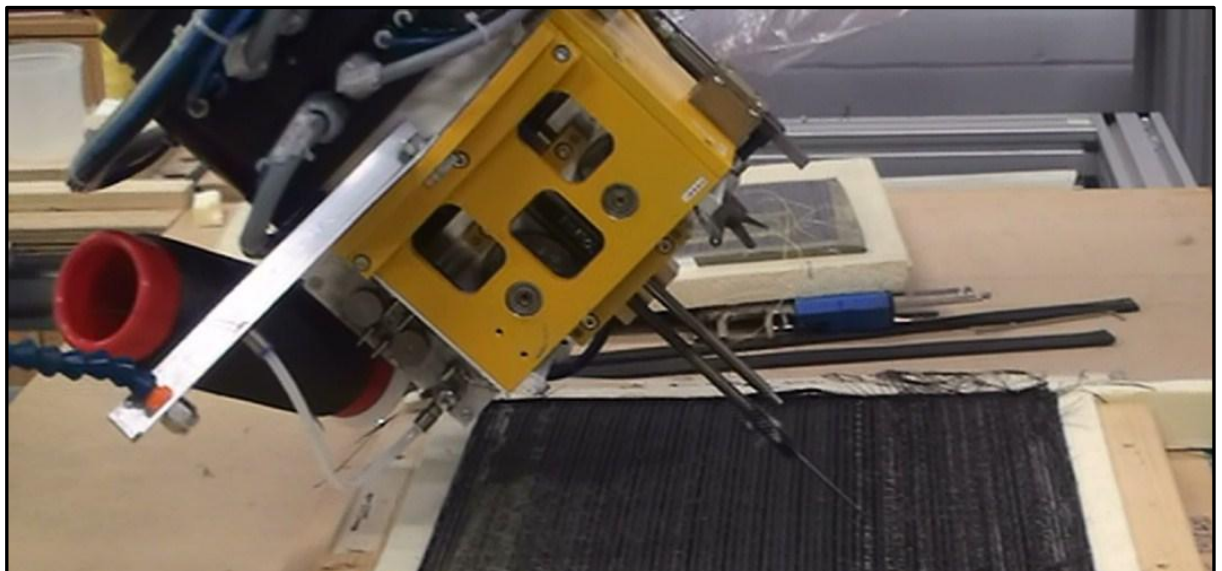


Figure 3-12. Angled tuft insertion requiring the tufting foot to be removed

3.2.3 *Preform de-moulding*

Subsequent to the tufting of the preform, it is necessary for it to be de-moulded from the tuft mould material. The activities completed within this sub process are documented in Table 3-6. Figure 3-13 provides a visual summary of these activities.

Table 3-6. Tufted preform de-moulding manufacturing activities

Process step	Manufacturing activity
1.	Trim loose fibres/threads
2.	Dispose of trimmings
3.	Remove foam mould from stitching jig
4.	Collect steel rule (de-moulding tool)
5.	Place foam mould & packing material on workshop table
6.	Preform de-moulding
7.	Preform straightening and check
8.	Collect hand needle for tuft tidy
9.	Tidy tufts & remove flakes of foam
10.	Dispose of trimmings, loose fibres and waste

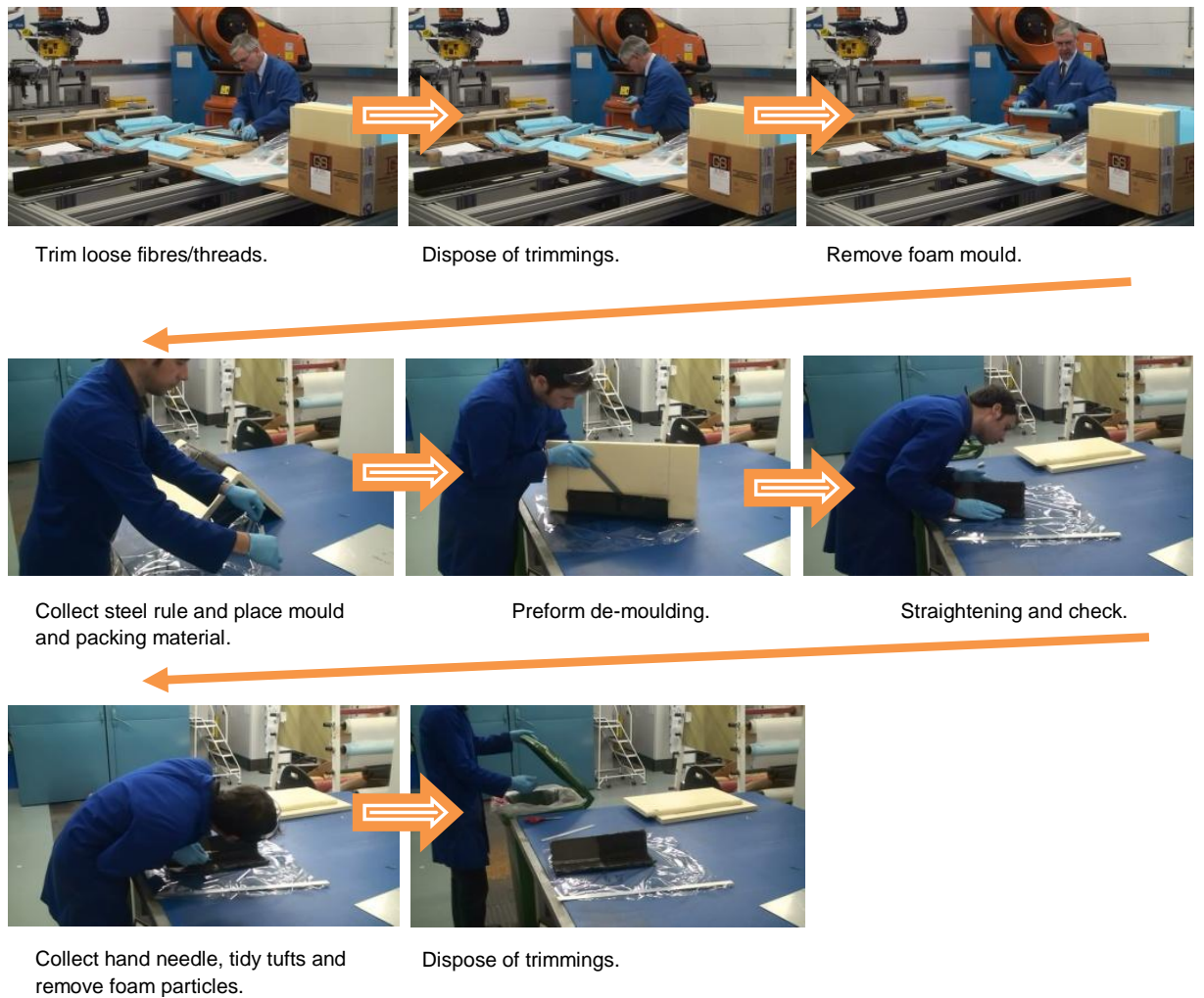


Figure 3-13. Visual summary of the tufted preform de-moulding

3.2.4 Tufted preform RTM

The RTM process was used by QinetiQ to manufacture the composite component using the tufted carbon fibre preform, the manufacturing route providing high dimensional tolerances and process control. An oil heated Aluminium mould tool was used in conjunction with a vacuum pump and a bespoke injection machine manufactured by Composite Integration [81], which allowed the control of injection pressure and resin temperature. To ensure that the component would release from the surfaces of the mould cavity, release agent (Frekote) was applied prior to inserting the preform. Subsequent to the placement of the preform in the mould, the chosen resin was brought to its specified injection temperature (70°C) within an oven. The resin selected was the single part epoxy resin system MVR-444, developed by Advanced Composites Group.

After reaching the required temperature, the resin was placed within the pressure chamber of the injection machine and degassed for 10 minutes under 5 mbar residual pressure. Following the degassing, vacuum pressure was used to inject the resin into the mould, which was pre-heated to 80°C. Once filled, the mould was pressurised for the duration of the cure cycle to reduce the formation of voids within the composite component. The implemented cure cycle was that suggested by the resin manufacturer, ramping the temperature from 80°C at 2°C/ minute to 180°C and holding the mould at this temperature for two hours, with no postcure. A detailed breakdown of the RTM process into its constitutive manufacturing activities is provided in Table 3-7. A visual representation of the completed RTM process is shown in Figure 3-14.

Table 3-7. Rib post RTM manufacturing activities

Process step	Manufacturing activity
1.	Oven switched on, res defrost and heats to 80
2.	Open tool
3.	Place inserts and preform
4.	Tool closed
5.	resin port attachments attached to tool
6.	Placement of tool rig
7.	Resin pipes attached
8.	Oil pipes attached to tool oil inlets
9.	Thermal couples inserted
10.	Leak test (includes switch on rtm machine)
11.	Inlet and outlet clamps fitted
12.	Oil heaters switched on and program chosen
13.	tool and resin left to heat (about 1hr with the Al tool)
14.	Resin temp checked
15.	Resin placed in infusion resin chamber
16.	de-gas / resin re-heat
17.	Infusion (inlets to outlets)
18.	outlet clamping
19.	Technician notes
20.	Tool ramped up to 180 for cure (pressure on)
21.	Pressure released from resin chamber
22.	Resin chamber and resin pipes cleaned
23.	Oil heaters switched off
24.	Tool left to cool overnight

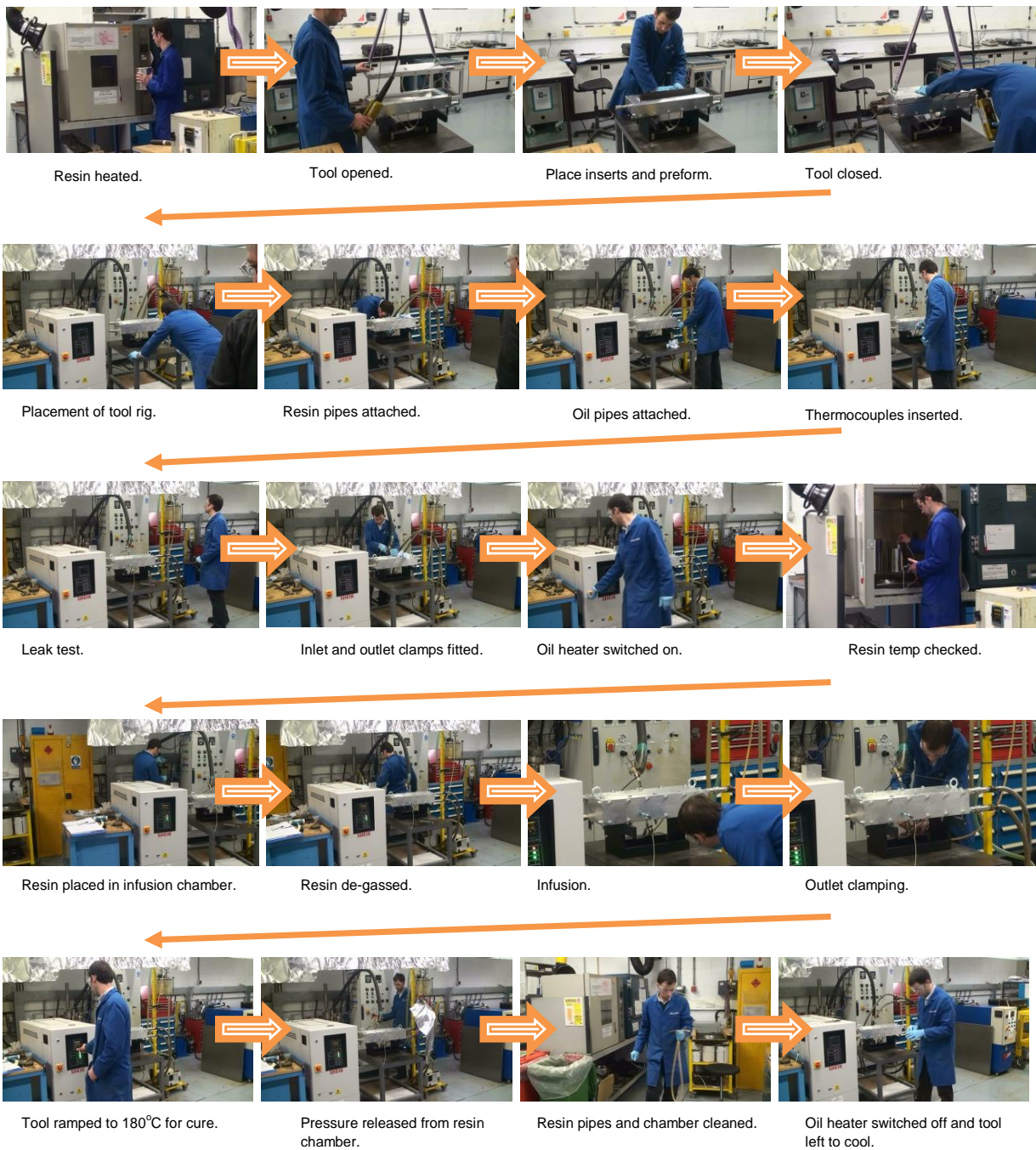


Figure 3-14. Visual summary of the RTM sub process

Once the cure cycle of the component has completed and the tool has cooled (left to cool overnight), the component is de-moulded following the steps documented in Table 3-8.

Table 3-8. Component de-moulding and mould cleaning activities

Process step	Manufacturing activity
1.	Removal of thermocouples (2)
2.	Removal of inlet clamps
3.	Removal of oil pipes
4.	Placement of tool rig
5.	Removal of outlet clamps
6.	Removal of tool bolts (10)
7.	Removal and placement of tool top surface
8.	Removal of cured resin from flow channel
9.	Insertion of part lifting points
10.	Attachment of crain
11.	Removal of part
12.	Removal of excess cured resin
13.	Apply release agent to tool bottom, top and inserts

Images of the part de-moulding manufacturing activities are shown in Figure 3-15.

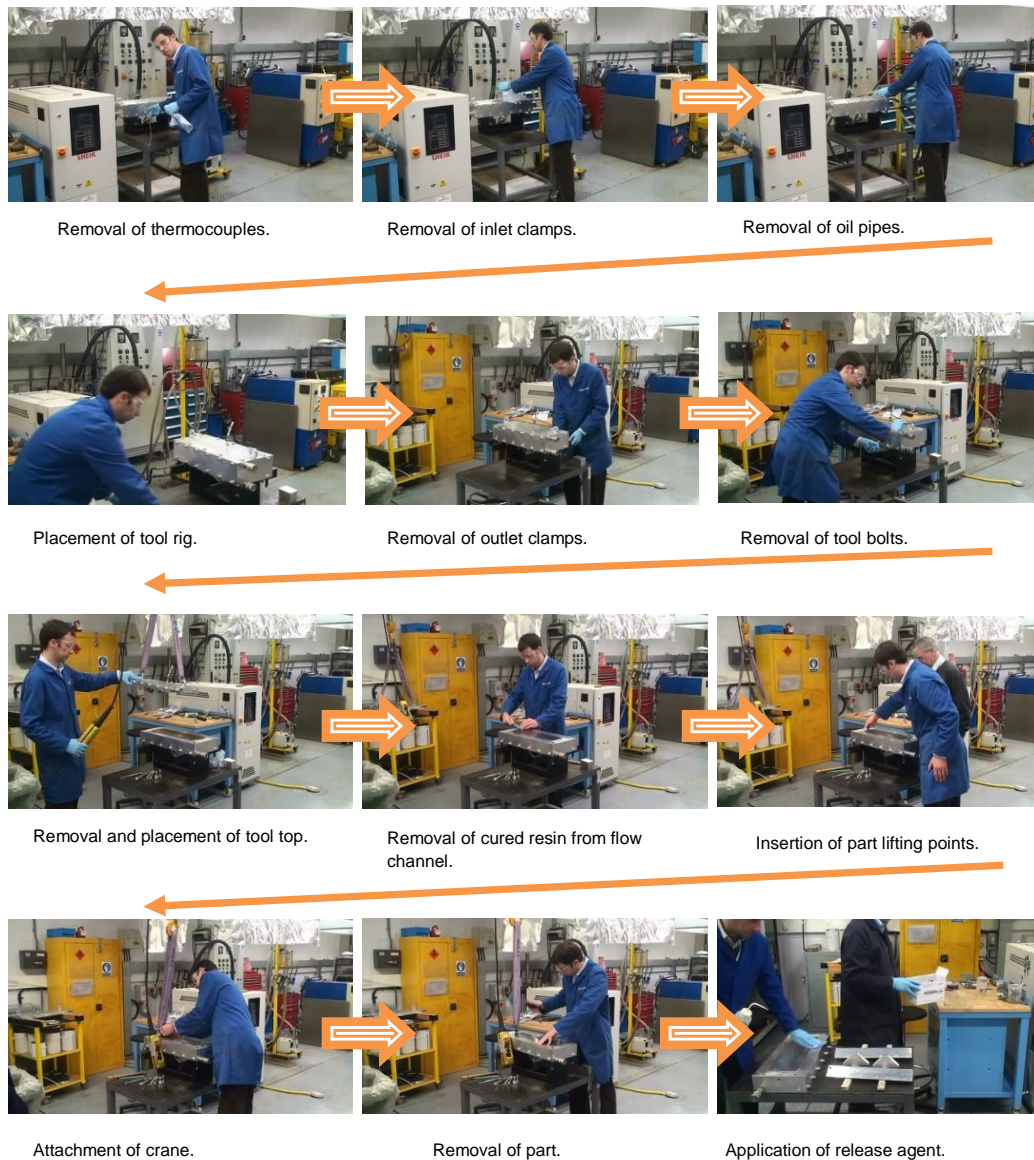


Figure 3-15. A visual summary of the part de-moulding sub process

With the sum of the time consumed by the activities in each of the sub-processes of the novel composite rib post, derived from the recorded video footage, total labour times and machine times can be calculated and used in conjunction with corresponding rates to estimate the manufacturing cost of the rib post, forming an operation based cost model for the manufacturing process. However, due to the fact that some of the rib post manufacturing activities could not be captured, the result of material delivery hold-ups, it was necessary to extrapolate the data from the manufacture of various test components. This in addition to the dependence of component fill time on the permeability of the material, favoured the use of the ABC cost model framework which

requires the formation of cost estimation relationships (CERs) (algorithms relating each manufacturing activity to the cost it generates) for each of the manufacturing activities, as the model is required to account for different fibre preforms. In order to do this, the permeabilities of the materials must therefore be determined and the relationship between the material permeability and the fill time of the component must be modelled.

3.3 Tufted fibre preform permeability

The permeability of a fibre preform is a fundamental processing characteristic of LCM manufacturing processes. LCM techniques used in conjunction with tufted dry fibre preforms include RTM [27, 45, 82] and RIFT [49, 83-85]. In order to determine how tufting affects the cost of these composite manufacturing techniques, it is important to develop an understanding of how the addition of tufts affects permeability and therefore the flow of resin through a fibre reinforcement.

It is well established that the flow of resin through the fibres of a reinforcement during liquid resin infusion manufacturing processes follows Darcy's law [86]. Darcy's law for three dimensional flow in an anisotropic porous medium, such as a tufted fibre preform, is given as follows:

$$\begin{bmatrix} u_x \\ u_y \\ u_z \end{bmatrix} = -\frac{1}{\mu} \begin{bmatrix} K_{xx} & K_{xy} & K_{xz} \\ K_{yx} & K_{yy} & K_{yz} \\ K_{zx} & K_{zy} & K_{zz} \end{bmatrix} [\nabla P]$$

Equation 3-1[87]

In permeability measurements, flow is usually constrained to one dimension. Darcy's law is then:

$$u_x = \frac{Q}{A} = \frac{K_x}{\mu} \cdot \frac{dP}{dx}$$

Equation 3-2[82]

Permeability is the measure of a materials ability to accommodate fluid flow [88]. It is sensitive to variations in the materials geometry [86, 89]. It follows that disruption to the fabric structure caused by tufting will influence a fibre reinforcement's in-plane and through-thickness permeability, as is the case with geometric variations caused by other forms of stitch [86, 89, 90]. An indication of the effect of tufting on fabric structure is provided by Figure 3-16, where through-thickness images acquired by Micro-CT show a non-crimp fibre (NCF) composite in its original form (a) and with tufting (b). It can be seen that the tufts create large resin rich eyelets, causing a significant geometrical changes to the fabric.

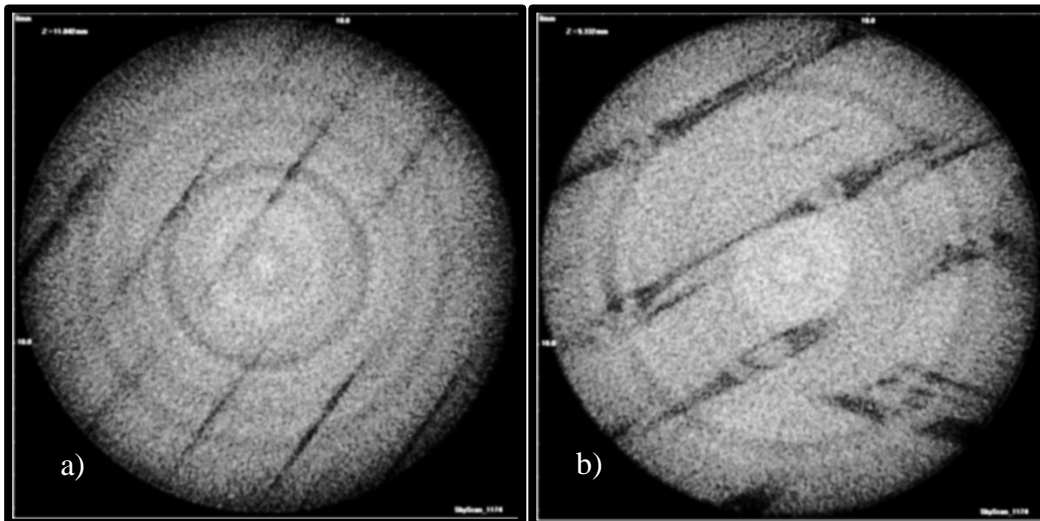


Figure 3-16. Micro-CT images showing the influence of tufting on internal geometry, a) of through-thickness image from a carbon/epoxy composite panel made from a quasi-isotropic lay-up of non-crimp fibre, and b) of through-thickness image from a panel differing only in that has tufts pitched at 45° in a 4mm x 4mm arrangement

Drapier et al [91] have documented that the stitching used in NCF also has an effect on the through-thickness permeability of the material. Their findings indicate that the through-thickness permeability of the fabric increases linearly with stitch density. The calculations of Han et al [92] suggest that the two-sided structural stitching also enhances this characteristic. It is therefore very likely that tufting leads to an increased through-thickness permeability, providing advantages in LCM techniques such as RIFT and vacuum infusion where through-thickness resin flow can be significant, though there is currently no data to corroborate this theory. Within the RTM manufacturing

process however, fluid flow often takes place primarily in the plane of the material and thus through-thickness permeability may not have a significant influence over the manufacturing process [93, 94]. It is in cases where there are through-thickness flow gradients, such as resin film infusion (RFI) or the RTM of very thick complex preforms [94, 95], that through-thickness permeability becomes a parameter by which to optimise the manufacturing process.

As the volumetric flow rate of a fluid travelling through a material is dependent on the material's permeability, it follows that if all other parameters remain constant, altering permeability will consequently affect process time and therefore process cost.

The clustering of fibres in some fabric reinforcements used in resin infusion results in two types of liquid flow [86]. These flow types can be defined as pressure-driven macroscopic flow (the inter-fibre bundle flow of liquid) and capillary force microscopic flow (the intra-fibre bundle flow of liquid) [82]. These distinct flow types result in one global permeability but two different local permeabilities. Lundström [86] and various other authors [96, 97] have found that of the two types of flow, macroscopic flow is predominant in commercial processes, and suggest that the effects of micro scale flow may be neglected. Thus, to calculate the macroscopic permeability of the material in the direction of interest, the macroscopic fluid velocity (v) must be determined. This is achieved through the division of the fluid velocity (u_x), given in Equation 3-2, by the material's porosity (ϕ), as shown in Equation 3-3.

$$v_x = \frac{u_x}{\phi} = \frac{Q}{\phi A} = \frac{K_x}{\phi \mu} \frac{dP}{dx}$$

Equation 3-3

Porosity is a factor defined as the volume of pore space available to fluid flow as a fraction of the total volume of the material compressed in the mould. As the

macroscopic fluid velocity is calculated in just one dimension, the porosity is used to determine the average cross sectional area available to fluid flow, as shown in Equation 3-3. When considering fibre reinforcements, porosity is given as:

$$\phi = 1 - V_f$$

Equation 3-4

If volumetric flow rate (Q) is constant, permeability in the primary direction of liquid flow can be calculated by rearranging Equation 3-3 [82]:

$$K_x = \frac{Q\mu}{A} \bigg/ \frac{dP}{dx}$$

Equation 3-5

Due to the fact that subsequent to tufting, the preform is generally removed from constraints before being placed in the mould, it is allowed to swell in the directions perpendicular to the plane of the fibres. In order to accommodate the tufts, much like Z-pins [39], the in-plane fibres are spread, changing the local in-plane fibre volume fraction. Due to in-plane fibre spreading, additional trimming of the preform is completed to fit the swollen preform into the mould tooling, reducing the global fibre volume fraction of the preform. To determine the influence of tufting on fibre volume fraction, each sample is accurately weighed, highlighting any volume fraction variation.

To provide data for RTM simulations, and subsequently facilitate cost estimates, this investigation aims to establish the global in-plane permeability of a tufted preform. Here the in-plane permeability is defined as that of the material in the direction of the predominant resin flow. The permeability of the tufted preform is assumed to be globally isotropic in the x and y directions due to the quasi-isotropic nature of the lay-up

studied. The through-thickness permeability of the preform is not investigated due to the in-plane directions of fluid flow dominating the manufacture of the component for which the preform was composed.

Examining the permeabilities of both tufted and un-tufted preforms with the same quasi-isotropic lay-up, the study will also establish the extent to which tufting influences permeability and therefore processing times and cost.

Within this study the permeabilities of the various fibre reinforcements are calculated from in-plane flow front measurements using Darcy's law as shown in Equation 3-5.

3.3.1 *Experimental apparatus*

The investigation of the in-plane permeability of the tufted preforms was carried out using a one-dimensional flow permeability rig. The arrangement of this equipment can be seen in Figure 3-17.

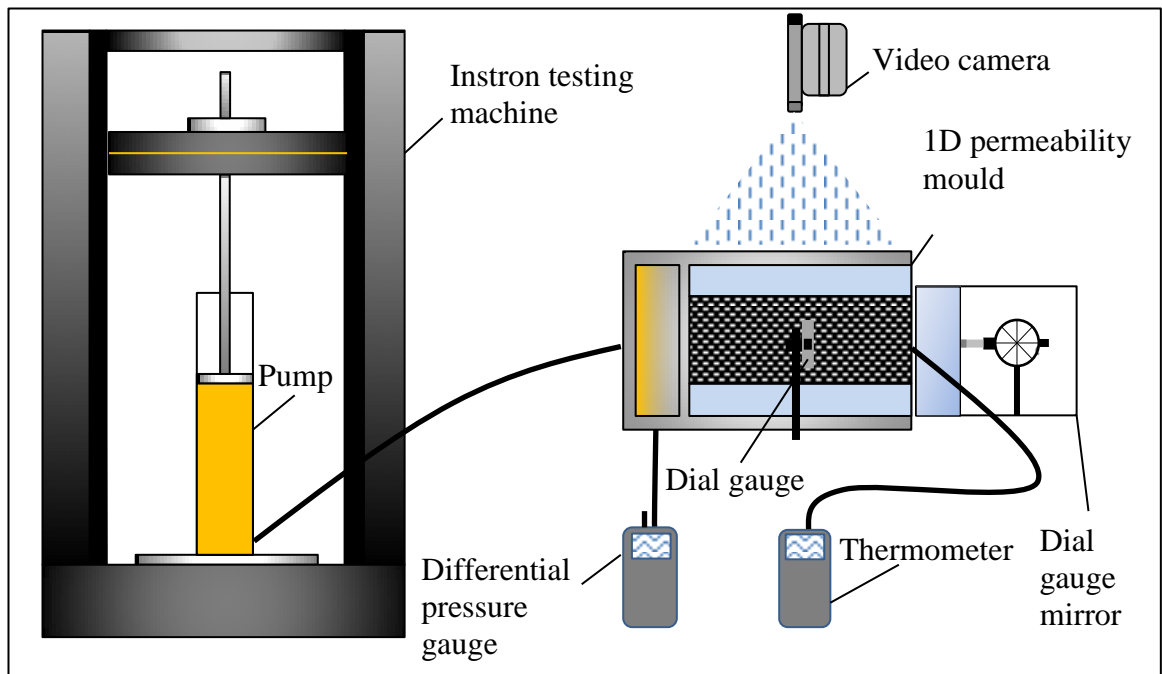


Figure 3-17. Diagram illustrating the experimental set-up

The main component of the permeability rig consisted of a glass topped aluminium matched mould, adapted from previous work carried out by Pomeroy [98]. The

dimensions of the mould cavity were 100mm x 170mm x 10mm. The aluminium base thickness was 25mm and the glass top thickness was 35mm.

In order to achieve the fibre volume fraction of interest, an acrylic insert was manufactured to reduce the depth and width of the tool cavity (Figure 3-18). Width was reduced to avoid edge effects that may have arisen due to the damaged internal surfaces of the glass mould top. The final cavity dimensions with the insert in place were 65mm x 170mm x 4mm. The acrylic insert can be seen inside the mould in Figure 3-19.

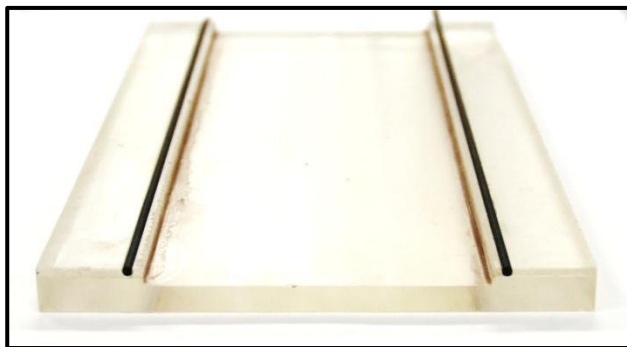


Figure 3-18. Acrylic mould insert

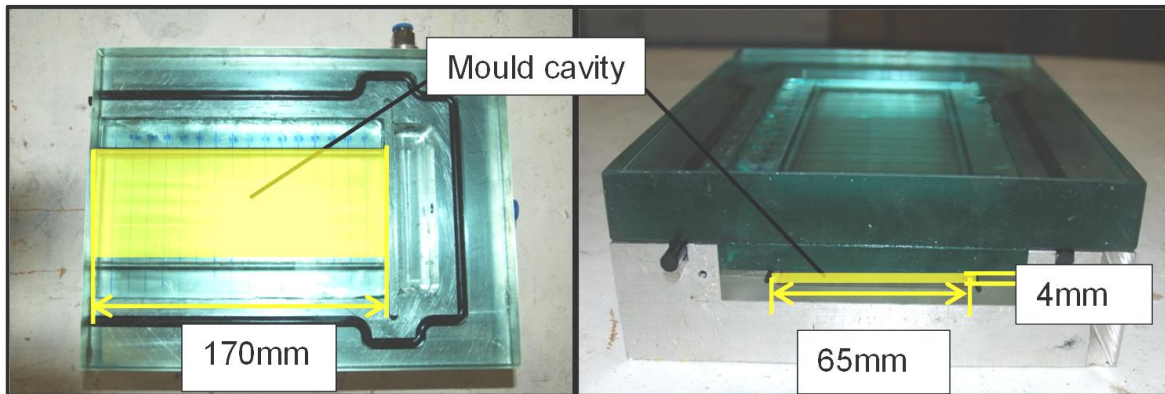


Figure 3-19. Mould sample cavity dimensions with insert in place

To account for any changes to fibre volume fraction that may have resulted from mould deflections caused by the pressure generated by the liquid injection, an in-house calibrated dial gauge was mounted on the tool's surface in the manner shown in Figure 3-20.

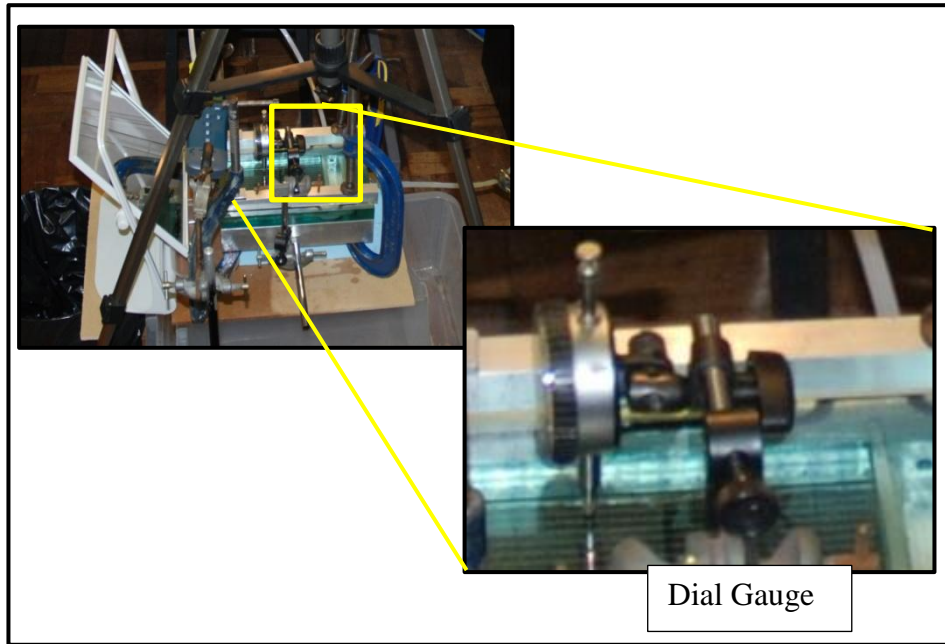


Figure 3-20. The dial gauge mounted to the mould surface

In addition to the mould, equipment was required to supply a flow of liquid to the experiment. This equipment consisted of a limited volume pump also from previous studies completed by Pomeroy [98]. The pump consisted of a 50mm diameter Festo piston (Standard Cylinder-DNCB-50-250-PPV-A (532758)) mounted in an Instron Universal Testing Machine (Serial number 5582). With this pump a constant liquid flow rate could be achieved. The liquid chosen was corn oil. This decision was made based on the incompressible nature of the liquid, its ready availability, Newtonian behaviour and its relatively low viscosity, which provided manageable pressures and flow times within the experiment. As only comparative data are sought this choice of permeant fluid is not compromised by the controversy over permeant dependence of permeabilities [99].

In order to capture the data required to calculate the permeability of the tufted fabric, a Sony HD video camera was mounted above the glass topped mould (Figure 3-21). This was used in conjunction with a Digitron 2022P differential pressure gauge to measure the pressure gradient across the mould cavity, and a K-series thermocouple attached to a Digitron 2022T thermometer (Figure 3-21) to measure the temperature of the

incompressible fluid used in the investigation. In addition, a mirror was placed at the open mould exit to enable the camera to record the output of the dial gauge measuring mould deflections.

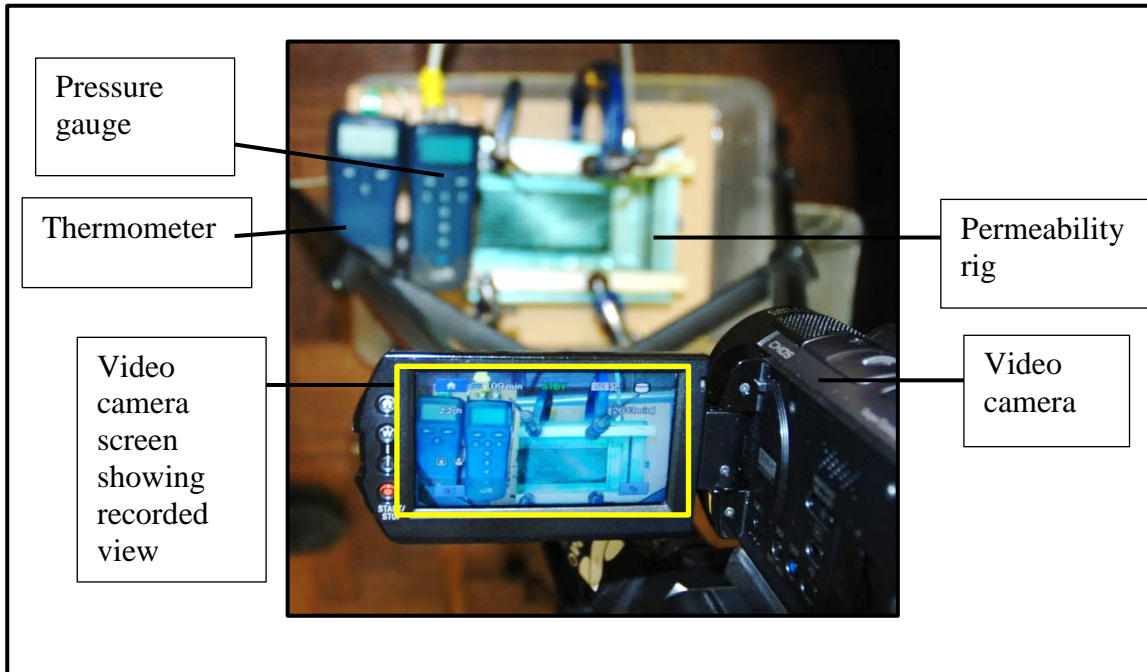


Figure 3-21. Video camera set up to capture temperature, differential pressure and flow front length data

Having been made to measure differential pressure in air, it was necessary to adapt the Digitron 2022P differential pressure gauge to measure the pressure differential between the liquid at injection and atmospheric pressure, the assumed pressure at the liquid flow front. This adaptation is described in Appendix 1.

The completion of this adaptation subsequently affected the flow rate within the experiment. Effectively, the constant flow of liquid supplied by the pump was divided between that flowing through the material sample and the increasing volume within the pressure gauge pipe caused by the constant pressure increase at the inlet point. In order to complete calculations of the permeabilities of the various materials it was necessary to define the constant rate of liquid flow through the material sample. This was done by measuring the time taken for each sample to fill with liquid to a length of 0.12m and

therefore also a defined volume, providing the liquid flow rate. The flow rate calculated for each sample was then used in the calculation of the materials permeability.

The use of the equipment described allowed all required data to be logged by the video camera and analysed after the experiment. Having marked the inner side of the glass mould top at every 10mm increment along its length, the video camera could capture the distance travelled by the resin whilst simultaneously logging the differential pressure and fluid temperature through recording the digital output of the various gauges used.

3.3.2 Experimental Procedures

Prior to carrying out the permeability experiment, it was necessary to cut a number of samples from the original tufted and non-tufted panel preforms to the dimensions of the permeability rig cavity. With the material available, five 170mm x 65mm samples were cut from the tufted preform and four 170mm x 65mm samples were cut from the non-tufted material. The non-tufted preform was cut into samples ply by ply using a bespoke cutting block and a rotary hand cutting knife. The cutting of the 4mm thick tufted preform was performed using a CNC ply cutter (XTC1800x2200 – O21) fitted with a rotary cutting tool (Figure 3-22) at the headquarters of Pipex px [100]. The use of a single large preform cut into several samples meant that the effect of the perimeter stitching used with the individual preforms of the novel composite rib post could not be considered. Once fabric samples were cut, the number of tuft heads in each sample was determined and each sample was weighed to determine its fibre volume fraction within the mould cavity. This information is presented in Table 3-9.



Figure 3-22. The CNC ply cutter employed to cut the tufted preform samples at Pipex ltd [100]

Table 3-9. Sample in-mould fibre volume fraction and tuft number variation

Sample	Fibre volume fraction	Tuft number
NCF 1	0.600	-
NCF 2	0.598	-
NCF 3	0.605	-
NCF 4	0.603	-
Mean	0.60	-
Tufted 1	0.639	564
Tufted 2	0.646	600
Tufted 3	0.645	*
Tufted 4	0.631	547
Tufted 5	0.635	490
Mean	0.64	550

*Tuft pull-out occurred when removing sample from mould, inhibiting the counting of tuft heads.

Having weighed each of the samples, their individual fibre volume fractions were calculated using Equation 3-6 [101].

$$CPT(mm) = \frac{W_f}{\rho_f \cdot V_f}$$

Equation 3-6

With the composite consisting of a single preform and with its final thickness known, the equation is re-arranged to make fibre volume fraction the subject.

Prior to the experiment it was also necessary to determine the temperature/dynamic viscosity relationship of the corn oil employed. This was completed with the use of a Brookfield RS rheometer. A description of the rheometer's use is given in Appendix 2.

Following the fabric cutting, the samples were carefully placed in the cavity of the permeability rig. The thermocouple was placed beneath the fabric inside the tool insert. The glass mould top was then put in place and sealed in compression with four G-clamps to obtain the correct cavity depth. To ensure even compression and avoid distorting the glass mould top, aluminium stiffeners were used. These were placed between the tool top and the G-clamps, with strips of 6mm thick plywood protecting the glass surface from damage.

Once the mould had been closed, the dial gauge was mounted on the tool surface and the dial gauge mirror was arranged. The dial gauge was used twice within the study, once during the test of the first un-tufted NCF sample and once again in the test of the first tufted NCF sample. For the remainder of the material samples the dial gauge was removed. For the tufted and un-tufted samples tested without the use of the dial gauge, the assumption was made that as the same range of pressures generated by the constant liquid flow rate would be experienced, mould deflections (if any) would remain constant.

Following the set-up of the differential pressure gauge and the arrangement of the permeability rig, the HD video camera was arranged with a tripod to face the surface of

the permeability rig and record both the propagation of resin and the values from the sensors (Figure 3-23).

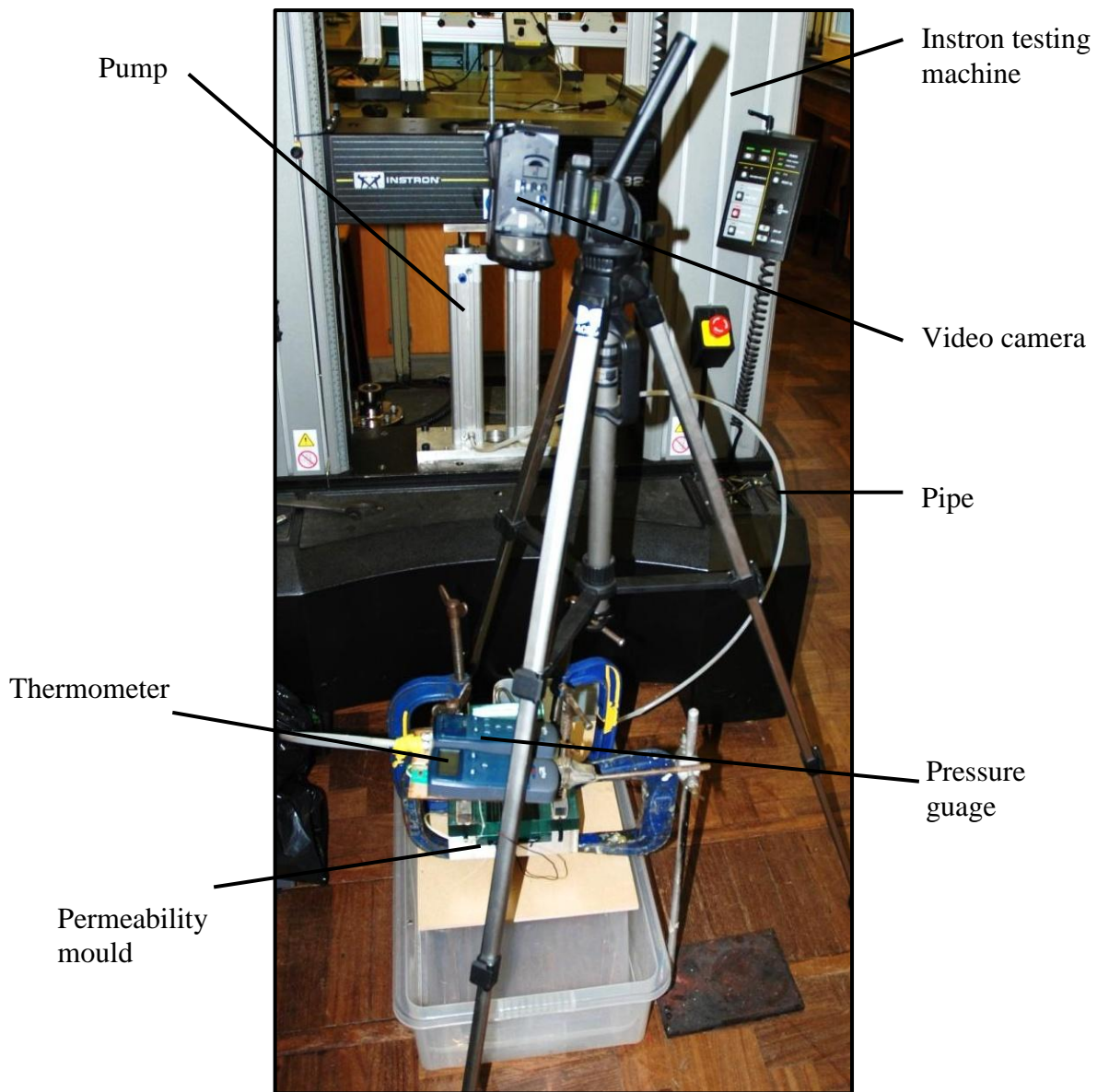


Figure 3-23. The experimental set-up of the video camera and liquid pump

It was then necessary to fill the limited flow volume pump that would supply the permeability rig with the relevant liquid. The pump itself was mounted inside the Instron Universal Testing Machine (Figure 3-23), which controlled the flow rate of the liquid supplied to the permeability mould tool by maintaining a constant downward cross-head displacement rate, and therefore piston compression rate. Due to the adaptation of the pressure gauge to measure liquid pressure, the constant flow rate of liquid through the material sample was not equal to the flow rate entering the mould

from the pump. Subsequently, the flow rate through the material was calculated through observation. Greater detail of this process is given in Appendix 3.

It is argued [91, 102] that Darcy's law may only be used to describe laminar or creeping flow. To address this constraint, the flow of liquid through the various samples studied had to be characterised. This was completed using the equation for the Reynolds number (Re) of a fluid. The number produced by this equation describes the type of flow, with values of less than one being considered as valid to be used with Darcy's law [91].

The Reynolds number of a fluid is given as [103]:

$$Re = \frac{\rho lu}{\mu}$$

Equation 3-7

The flow velocity (u) is given as [98]:

$$u = \frac{Q}{A\phi}$$

Equation 3-8

Within this study the flow rate of the fluid and the porosity of the medium are shown to vary between the samples. Due to the dependency of the Reynolds number of the fluid on these parameters, the maximum flow rate experienced and the minimum porosity within the sample groups were used to calculate a maximum Reynolds number. This ensured that in the remainder of the studied cases, the Reynolds number would be below this value. The result of this calculation was a Reynolds number of 0.01, assuming l to be an arbitrary maximum of 5mm, confirming that Darcy's law could be used to calculate the permeabilities of all of the samples investigated.

To ensure that the allowable pressure range of the Digitron 2022P differential pressure gauge was not exceeded, the flow rate at which the liquid entered the mould from the pump, and the corresponding cross-head depression rate of the Instron was calculated using Darcy's law. These parameters were calculated using a minimum permeability determined with existing process records from the RTM of the tufted preform. The cross-head compression rate was kept constant throughout the investigation, providing a constant liquid flow rate.

During the experiment, as a result of its placement, the HD video camera was then able to record the propagation of the liquid through the preform, whilst also recording time and the values provided by the differential pressure gauge and the thermometer (as can be seen in Figure 3-24), facilitating the calculation of permeability. Each sample was tested once in unsaturated flow.

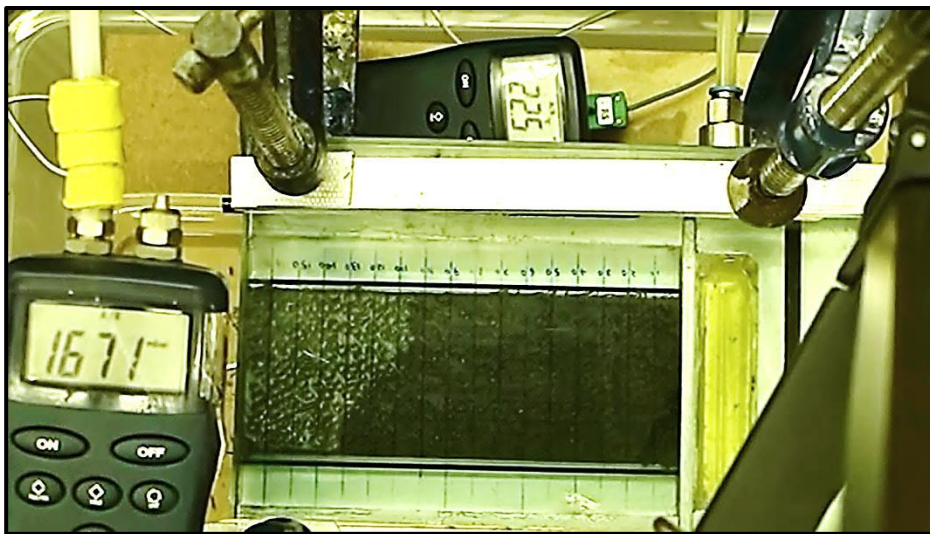


Figure 3-24. An example of the observed liquid flow front during the measurement of the permeability of a tufted preform

3.3.3 *Results and discussion*

3.3.3.1 *Experimental errors*

The random experimental errors experienced by apparatus used within this study were accounted for in the calculation of permeability through the use of error propagation equations documented by Taylor [104]. These allowed the error in the calculation of permeability to be quantified. The apparatus random errors considered are shown in Table 3-10.

Table 3-10. Random errors of experimental apparatus

Apparatus	Random error
Thermometer	$\pm 0.2\%$ reading
Brookfield RS temperature controlled baseplate	$\pm 0.05^\circ\text{C}$
Brookfield RS Rheometer	$\pm 5 \times 10^{-4}$ Pa.s
Flow length observation	$\pm 1\text{mm}$
Differential pressure gauge	$\pm 200\text{Pa}$
Instron crosshead	$\pm 0.1\%$ rate
Digital scales	$\pm 5 \times 10^{-5}$ kg
Cutting equipment	$\pm 1\text{mm}$

Systematic errors were also considered within this study. These known tolerances were used to estimate the possible maximum and minimum permeability values of the experiment. The tolerances considered are shown in Table 3-11.

Table 3-11. Possible systematic error range of experimental apparatus

Apparatus	Systematic error
Mould cavity width	$\pm 0.1\text{mm}$
Mould cavity depth	$+0.7\text{mm} / -0.2\text{mm}$
Machining tolerances	$\pm 0.1\text{mm}$

3.3.3.2 Permeability results

The permeability results obtained for the tufted and un-tufted material samples are shown in Figure 3-25. The input data for the calculation of the permeabilities was obtained when the liquid flow front reached 120mm.

As can be seen in Figure 3-24, linear flow did not occur consistently across the samples width. Race-tracking regularly caused flow to propagate along the lower edge of the cavity more quickly than the top. In order to determine flow front distances to be used in calculations, an average linear distance was estimated by eye, assuming that there was no occurrence of 2D flow. In the case of Figure 3-24 the flow front distance was estimated to be 120mm.

Measurements were made at this point as the flow front in each sample consistently reached this length without experiencing overwhelming edge effects or the maximum pressure of the pressure gauge used. In addition, using the greatest length of liquid propagation consistent in all samples allowed experimental error to be minimised. The error bars plotted in Figure 3-25 represent the experimental error experienced in the measurement of each permeability.

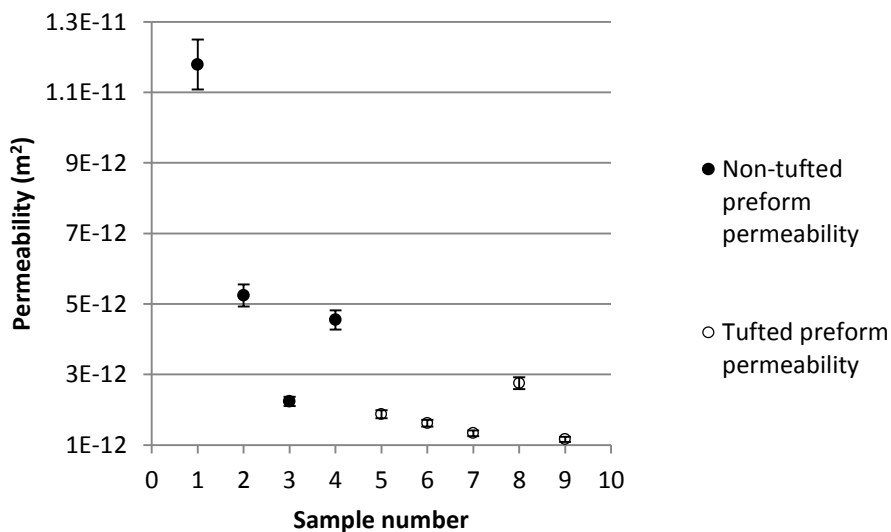


Figure 3-25. Measured permeabilities of the tufted and non-tufted material samples with experimental error

The mean permeabilities of the two materials, are provided in Table 3-12 alongside the standard deviation of each of the data sets. The non-tufted and tufted mean permeabilities were calculated using the total four values for the non-tufted preform and the five measured values of the tufted preform including the outliers Sample 1 and Sample 3.

Table 3-12. Mean permeabilities and standard deviations of the data sets

Material	Mean permeability (m²)	Standard deviation
Non-tufted NCF	5.95 x 10 ⁻¹²	60%
Tufted NCF	1.75 x 10 ⁻¹²	32%

The recorded standard deviations may result from a number of factors. Slight variations in fibre volume fraction between samples caused by loss of tows during cutting and also sample tuft number differences are likely to have resulted in discrepancies between the pressure differentials recorded when the flow front in each sample reached the defined 0.12m. The variations in fibre volume fraction are shown in Table 3-9. This effect is likely to have exacerbated variations caused by slight sample to sample cavity depth variation, resulting from a combination of the utilised clamping equipment and human error, which is thought to be responsible for the majority of the resulting (standard) deviation.

The standard deviation of the un-tufted sample permeabilities is much greater than that of the tufted preform permeabilities. This could suggest that the un-tufted samples are very susceptible to geometry variations, and subsequently permeability variations, when being handled and placed in the mould. The smaller standard deviation of the tufted sample permeabilities may indicate a stabilising effect of the tufts, their presence inhibiting the geometry variation that may occur with the un-tufted samples during handling.

It is interesting to note that the scatter of permeability measurements for both sample groups is approximately the same as that argued by Loendersloot [94] to be the result of random variation of the dimensions of openings caused by stitching threads in NCF. It is suggested that a difference of up to a factor of 2.5 may be seen between permeability measurements of the same reinforcement with the same fibre volume fractions. This agreement implies that the observed scatter within the results may be partially due to this variability. Though the scatter of the tufted sample permeabilities show good agreement with this factor of 2.5 difference, the scatter of the un-tufted sample permeabilities is slightly greater. This may be accounted for in part by the issues discussed.

Studying the results presented in Figure 3-25 and Table 3-12, it can be seen that the permeabilities of the un-tufted and tufted preforms are significantly different as the mean permeability of each data set lies outside the region covered by the standard deviations.

The results indicate that the permeability of the NCF preform in the examined direction is reduced by approximately a factor of 3.5 by the presence of the 4x4, 45° angled tufts. These results concur with trends suggested by RTM process records for the two materials and with the effect of stitching on permeability proposed by Lundström [86] and Hu and Liu [89].

In addition to indicating a difference between the permeabilities of preforms with and without 4x4, 45° tufting, the experiment has also provided an absolute value for the permeability of the 4x4, 45° tufted preform that may be used to carry out simulations of the material's processing during LCM.

Though the experiment itself does not have a calibration to determine the extent of systematic error, maximum and minimum permeability values resulting from the known

possible causes of systematic error have been estimated using the tolerances noted in Table 3-11. The estimates for the maximum permeabilities of the tufted and un-tufted preforms respectively are $2.32 \times 10^{-12} \text{m}^2 \pm 0.08 \times 10^{-12} \text{m}^2$ and $7.70 \times 10^{-12} \text{m}^2 \pm 0.26 \times 10^{-12} \text{m}^2$. The estimates for the minimum permeabilities of the tufted and un-tufted preforms respectively are $1.35 \times 10^{-12} \text{m}^2 \pm 0.05 \times 10^{-12} \text{m}^2$ and $4.65 \times 10^{-12} \text{m}^2 \pm 0.16 \times 10^{-12} \text{m}^2$. Divergence from these maximum and minimum points shown in the standard deviation of the measured permeability values must arise either from additional systematic errors that have not been considered or actual permeability variation within the sample groups. Suggested future work includes the calibration of the permeability experiment to facilitate more accurate measurement of material permeability.

An error that is not accounted for within the experiment is that arising from non-linear flow. That experienced within the experiment was the result of edge effects from the interaction of the material sample with the edges of the mould cavity. In order to complete calculations of the permeability, the non-linear flow front occurring as a result of the race-tracking had to be resolved. This was completed by estimating the average flow front distance by eye. Using this method caused the calculated permeabilities to account for the regions of high permeability occurring at the edges of the sample. This in turn makes it likely that the calculated permeabilities slightly overestimate the actual values of the constant in each sample.

Having employed a constant flow rate within the experiment, this issue could have been resolved if data of the filled length of the pressure gauge pipe had been collated. This data would have allowed the volume of liquid with the sample cavity, and therefore the equivalent flow front distance to be calculated. Unfortunately, due to the limitations of the single camera used, this was not possible.

With the completion of this study, the experimentally determined permeability of the tufted preform is used to simulate the RTM of the novel composite rib post to subsequently provide data for the estimation of the manufacturing costs associated with the filling of the mould.

Chapter 4. Novel composite rib post RTM simulation

4.1 Introduction

To generate manufacturing cost estimates for composite components made with RTM, a mould fill time is required. With this information, costs directly related to the mould fill time, such as those associated with labour and energy consumption may be estimated.

Mould fill time in LCM is a function of a number of parameters, including characteristics of the fibre preform, the viscosity of the resin and the pressure gradient within the mould. As has been discussed in Chapter 3, Darcy's law may be used to model the flow of resin in LCM. With simple geometries in which linear or two dimensional flow is experienced, the time required for resin to fill a given length may be calculated using simple solutions to Darcy's law, however when more complex geometries are encountered with similarly intricate injection strategies, the calculation becomes intractable.

In these situations it is beneficial to use computational fluid dynamics (CFD) software. There are several methods of implementing CFD. In general, these methods consist of the discretization of a geometry, in this case the mould cavity, into volumes or two dimensional elements within which the governing equations of the model (for instance Darcy's law) are solved. In each of the cells the input of the equation is based on the outcomes of the calculations made for neighbouring cells, and the boundary conditions defined for the simulation (such as inlet and outlet pressures, or resin flow rates). Using this method the propagation of fluid through a complex mould geometry can be modelled.

Within this project CFD has been employed for a number of reasons. Its use, in conjunction with the availability of RTM process records, has allowed the validation of the experimentally-determined permeability of the tufted preform studied. The main reason for employing CFD, however, was to allow the manufacturing cost model to consider component and injection complexity within its estimates of RTM injection costs.

Several CFD software packages specifically made for the simulation of LCM manufacture are available commercially. These include PAM-RTM, developed by the ESI group [105], RTM-Worx developed by Polyworx [106] and LIMS, developed at the University of Delaware [107]. Each of these packages is based upon the use of finite element methods (FEM) to solve Darcy's law over the specified geometry. The open source software myRTM [108] is based on alternative methods. Using cellular automats, the model boasts a more efficient use of computational time. Similarly to FEM, the program requires geometries to be discretized, but it differs in the fact that the governing equations of the modelled phenomena are not calculated over each of the created elements. Instead, each of the cells is ruled by an algorithm that defines its state, which, in the case of myRTM, is either wetted with resin or dry. The cell state is in turn dependent on the state of a defined neighbourhood of cells. By defining a cell where the phenomenon, such as filling, is to begin and adjusting its parameters (such as pressure) accordingly, the state of each of the cells within the model can be calculated over numerous time steps. In this way, the filling of a mould with resin can be simulated. With this software being freely available, much thought was given to its use, and the program was evaluated thoroughly. However, despite its potential benefits, the software was unable to provide accurate fill time data, its results failing to converge with analytical solutions to Darcy's law. This software was therefore not considered further.

PAM-RTM was finally chosen to complete the required CFD, its user interface being sufficiently intuitive to reduce the learning curve. As the software does not have an integrated meshing facility, the open source meshing program Gmsh [109] was used to create the component meshes required to run the PAM-RTM software.

Prior to using the package to validate permeability results and complete simulations on which resin injection costs would be based, benchmarking was carried out to increase confidence in the model's results and ensure that no fundamental errors were being made by the user. Whilst completing the benchmark studies, investigations were also carried out to determine the dependency of the results on mesh density. This also provided an opportunity to establish the optimum mesh density for the simulations, considering both estimate accuracy and computation time.

4.2 PAM-RTM benchmarking and mesh density dependency

Benchmarking consisted of comparisons of calculated mould fill time results with estimates made using Darcy's law for one dimensional flow (Equation 4-1).

$$t = \frac{\phi\mu L^2}{2K\Delta P}$$

Equation 4-1

The geometries used for this comparison included a flat plate and an L-shaped component, two geometries manufactured by the project sponsors using the tufted preform material to create test specimens. Figure 4-1 shows the geometries within the PAM-RTM work environment, labelled with their dimensions.

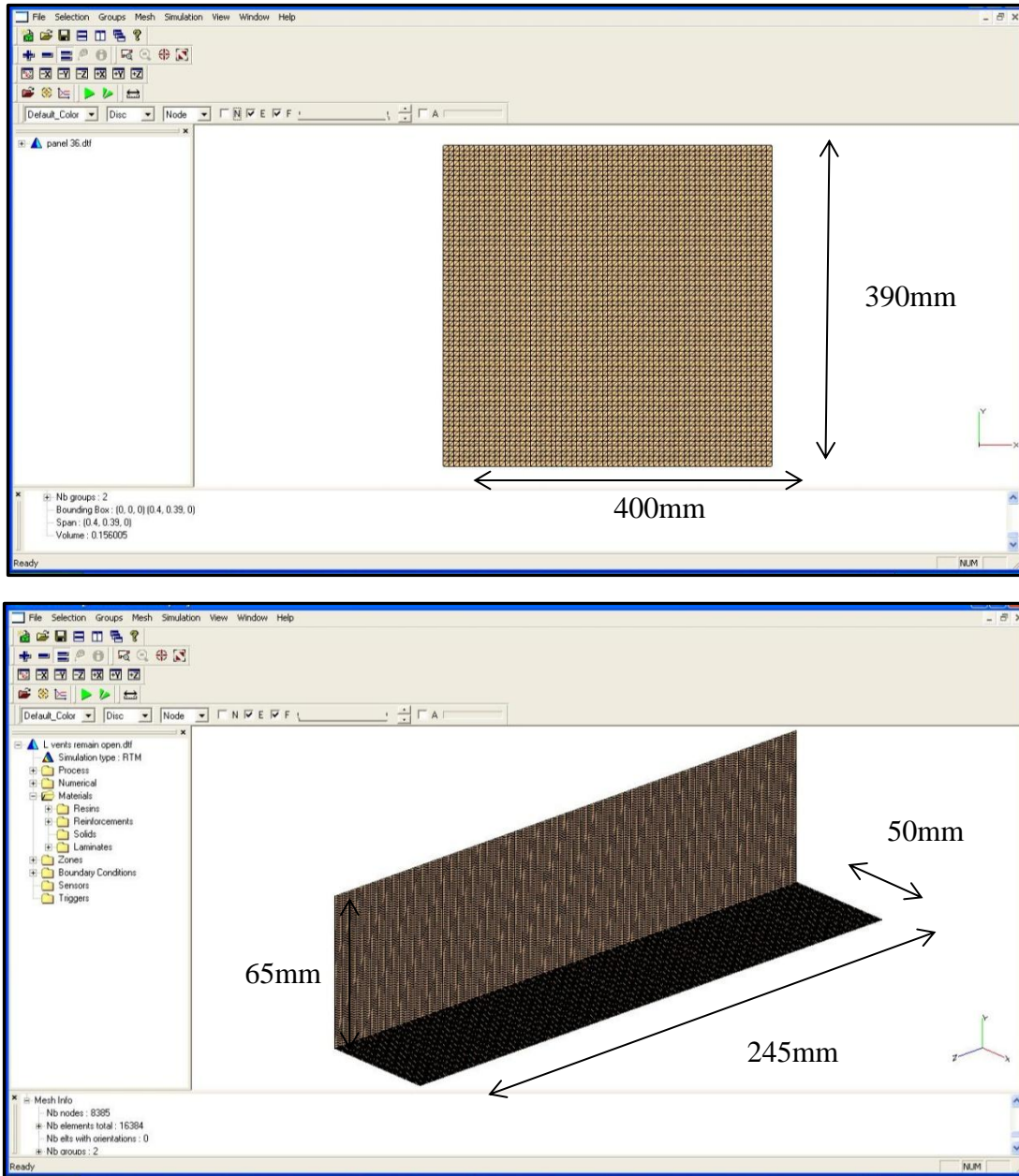


Figure 4-1. Screenshots of the flat plate (a) and L (b) geometries used to benchmark PAM-RTM with Darcy's law, within the PAM-RTM environment

Each of the geometries consisted of 2D shell type structures, meshed with linear triangular elements. In order to simulate one dimensional fluid flow and provide results that could be compared with those calculated with Darcy's law in one dimension, the geometries were modelled with line injection.

The parameters used for the simulations are documented in Table 4-1. These values refer to the measured processing characteristics of the tufted preform and the process parameters used in the documented RTM of test components manufactured at QinetiQ.

Table 4-1. The process parameters used for the benchmarking of PAM-RTM

Parameter	Flat panel	L component
Permeability (m²)	1.75 x 10 ⁻¹²	1.75 x 10 ⁻¹²
Porosity	0.376	0.376
Dynamic resin viscosity (Pa.s)	0.05	0.05
Differential pressure (Pa)	3.15 x10 ⁵	3.01x10 ⁵
Flow length (mm)	390	115

Using Darcy's law, a single fill time was calculated for each of the scenarios. These were then used to benchmark the results of the PAM-RTM simulations using meshes of various densities, the aim being to determine the mesh densities providing an accuracy within 1% of the Darcy solutions. For each of the geometries, five meshes were created, ranging from a density of approximately 10 to 100,000 triangle elements, increasing in an approximately exponential manner. To retain ordered meshes, the mesh densities could not be defined to meet the specified range exactly. This was prevented by the dimensions of the meshed geometries. The results of the simulations completed with the various meshes can be seen compared to the corresponding results of the Darcy equation in Figure 4-2 and Figure 4-3.

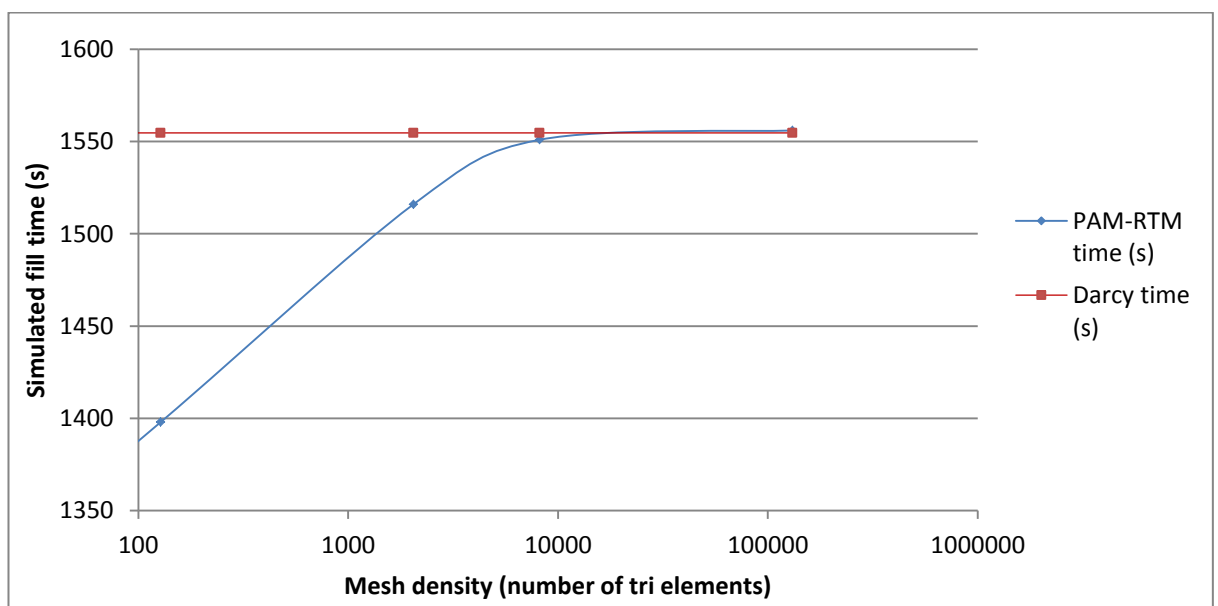


Figure 4-2. Fill times simulated by PAM-RTM for the flat panel geometry with various mesh densities compared to the fill time estimated by Darcy's law

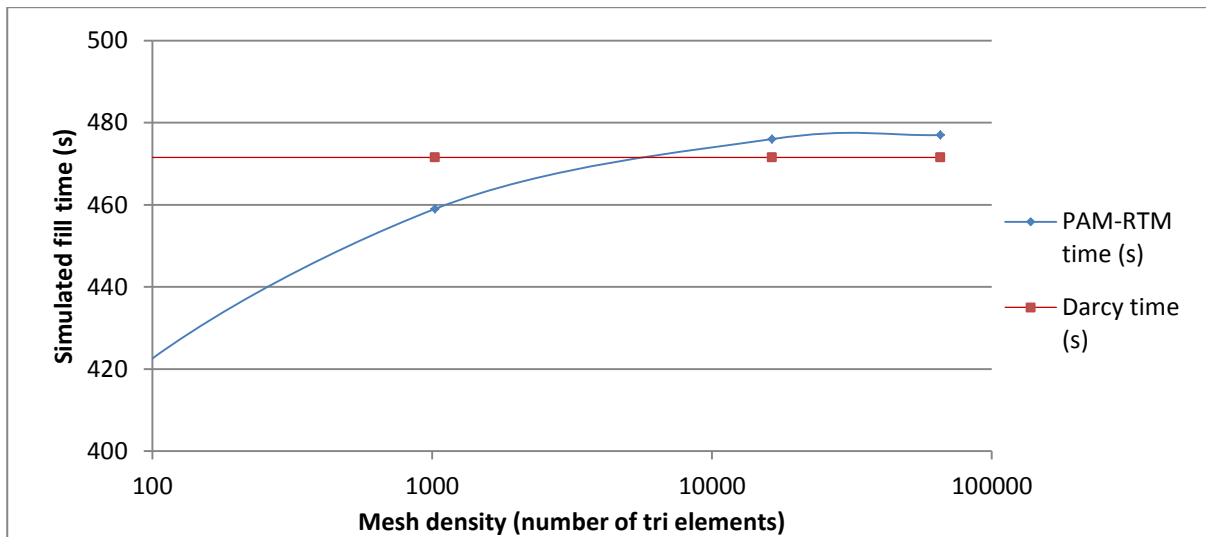


Figure 4-3. Fill times simulated by PAM-RTM for the L geometry with various mesh densities compared to the fill time estimated by Darcy's law

As Figure 4-2 and Figure 4-3 show, increasing the mesh densities increases the accuracy of the PAM-RTM simulations. The results of the simulations using the finer meshes can be seen to converge with the estimates of the Darcy equation. The difference between the simulated results generated by the meshes converging with Darcy's law was very small in each case. For the flat panel, the simulation with the finest mesh showed an increase in accuracy of just 0.2% over that completed with the preceding mesh density. For the L component a decrease in accuracy of 0.21% was observed. This small increase in the accuracy for the flat panel and the apparent decrease in accuracy for the L geometry were accompanied by increases of computation time of approximately an hour. Taking this into consideration, it was decided that the optimum mesh density was that of approximately 10,000 elements, resulting in a percentage error of +0.85% for the L component and -0.26% for the flat panel. More specifically, the optimal mesh densities were 16384 elements for the L component and 8192 elements for the flat panel. With these meshes numerous simulations were completed in a relatively short time.

4.3 Mesh refinement at the simulated inlets of the components

In addition to establishing an optimum mesh density, the effect of refining the meshes around the simulated inlets of the benchmark geometries was also investigated. Using a mesh of consistently sized elements in simulations employing Darcy's law as the governing equation, errors can be generated at the inlet of the simulation that propagate through the model and cause inaccuracies in the simulated results. These errors result from the initial calculation of the pressure gradient within the process. At the start of the simulation, the pressure gradient is calculated using the flow length occupied by the initial elements of the mesh. Depending on the mesh density, the length occupied by the initial elements in the simulation may be a significant proportion of the flow length. Refining the mesh in this region increases the accuracy of the pressure gradient calculation early in the simulation. Local refinement also avoids making the entire mesh too dense, increasing computational time unnecessarily. In this situation rounding errors within the differential equations solved over each element would also reduce the accuracy of the simulation, as the errors propagate through the model.

Mesh refinement at the simulated inlets of the geometries was completed using Gmsh. By specifying the required element size at each of the geometries' points, the mesh could be refined in specific areas. For both the L and flat panel, the geometric points corresponding to the simulated line injection inlet were given an element size factor of 0.01, and the remainder of the points were given an element size factor of 1. The element size factor related to the size of the element to the dimensions of the component. In specifying these size factors, the lengths of the elements at the inlets of the components were consistently two orders of magnitude smaller than those at the outlets. To subsequently refine the global mesh density, the option to 'refine by mesh splitting' was used. An example of the completed inlet mesh refinement is provided in Figure 4-4.

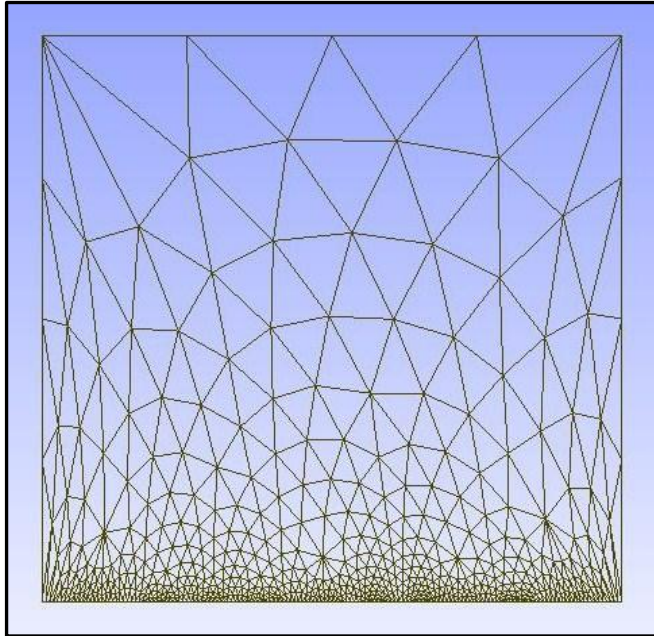


Figure 4-4. Flat panel mesh with 1056 elements, refined at the simulated inlet

Several meshes of different density with refined inlet elements were created for each component. One dimensional flow was then modelled with each of these meshes for comparison with Darcy's law. The parameters used for the simulations were again those documented in Table 4-1. The simulated fill times using these meshes can be seen compared to the estimates of the Darcy equation in Figure 4-5 for the flat panel and Figure 4-6 for the L component.

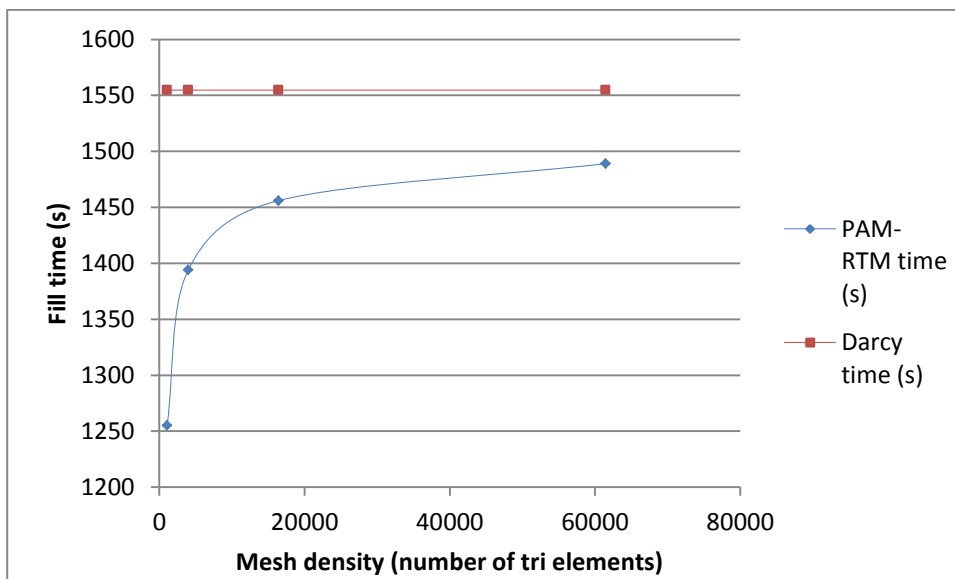


Figure 4-5. Flat panel mesh density vs. PAM-RTM simulated fill time for inlet refined meshes, compared to the fill time calculated with Darcy's equation

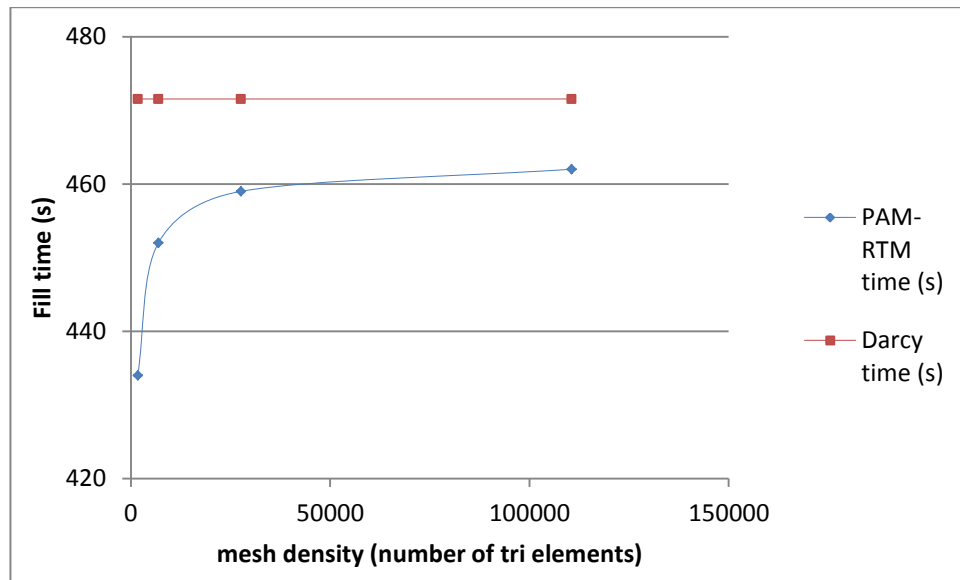


Figure 4-6. L component mesh density vs. PAM-RTM simulated fill time for inlet refined meshes, compared to the fill time calculated with Darcy's equation

As the results plotted in Figure 4-5 and Figure 4-6 show, though the simulations indicate that they are beginning to converge with the results of Darcy's law, this convergence will occur at a much higher mesh density than was observed with the simulations employing meshes of consistent element size (Figure 4-2 and Figure 4-3). As a consequence of the requirement for higher mesh densities to generate a converging result, it is expected that computation time at convergence will be unmanageable, the highest mesh densities used already taking in the region of thirty minutes and two hours for the flat panel and the L component respectively. It is for this reason that inlet mesh refinement was decided not to be used in subsequent PAM-RTM fill time simulations. The increased error is most likely to be the result of elements being too large away from the inlet and also errors caused by elements with poor aspect ratio. Due to time requirements, the decision was made not to manually rectify these issues and to continue using the suitably refined meshes with uniform element size.

4.4 Experimental permeability validation

Prior to being used to estimate component fill time with the tufted preform material, PAM-RTM was initially employed to validate the material's experimentally determined permeability. Using the software to simulate the RTM of components manufactured by the project sponsors, comparisons were made between the recorded and simulated fill times. With the RTM process parameters being modelled as boundary conditions in PAM-RTM, the comparisons of the fill times provided an indication of the accuracy of the experimentally determined permeability. This comparison provided only an indication of the accuracy of the measurement rather than a definitive specification, as the results are dependent on the accuracy of the process records, in which mould fill times were determined by observation of the resin exits. When resin was present at each of the exits, the mould was presumed to have filled. Due to the fact that the resin flow front within the mould could not be seen, it is possible that race-tracking occurred, causing inaccurate fill times to be recorded.

The components used for this validation were a flat panel of the same dimensions as that used within earlier benchmarking exercises (Figure 4-1 (a)), and also a T-component, again manufactured for testing. The mesh used for the simulation of the flat panel's RTM was the same as that created for the benchmark studies, consisting of exactly the same mesh density. Due to the symmetric nature of the T-component's injection, resin flow within the T was modelled assuming symmetric boundary conditions about the component's cross sectional line of symmetry. This allowed the resin flow within the T to be simulated using an L geometry. The L geometry is shown in Figure 4-7, labelled with its dimensions. The density of the mesh created with this geometry was kept as close to the determined optimum as possible, producing a mesh of 19,346 elements.

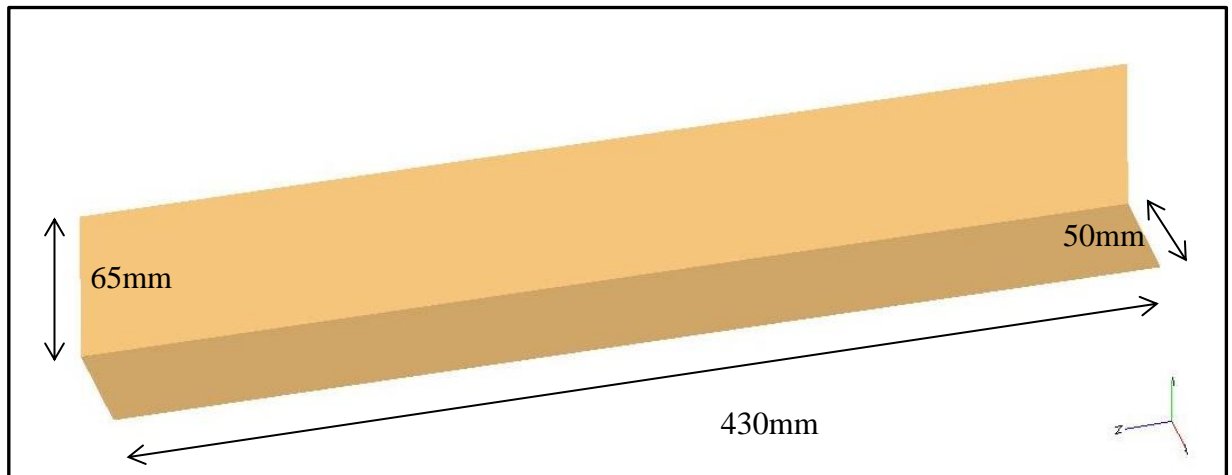


Figure 4-7. The dimensions of the L geometry using symmetry to model the RTM of the manufactured T-component

The process parameters used in the simulations varied for each of the components in accordance with the process records. For the flat panel the injection pressure was modelled to vary throughout the process (as documented within the process records) following the pressure/time profile shown in Figure 4-8, using PAM-RTM's user interface to achieve this. This profile was generated by the manual control of the technician, who adjusted the injection pressures in order to optimise the quality of the component.

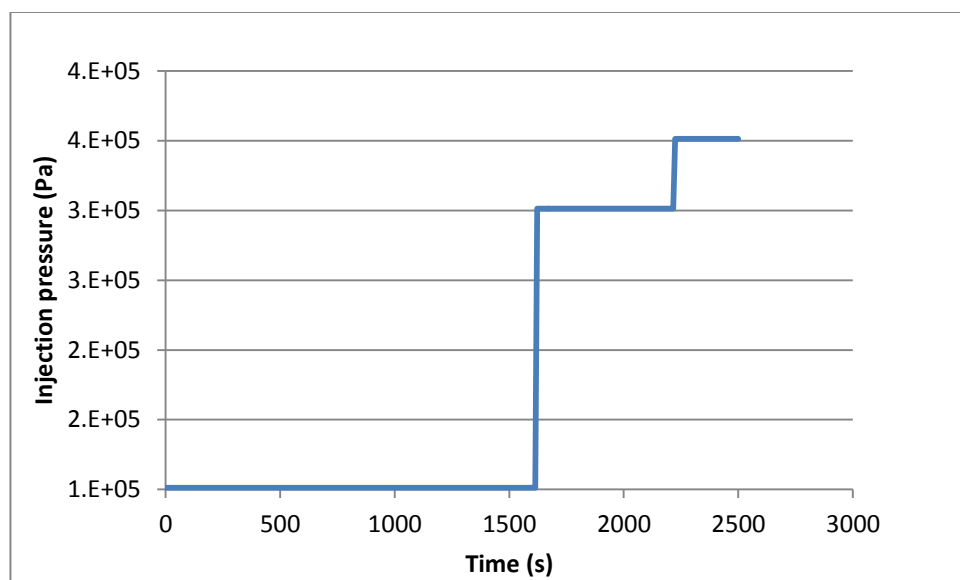


Figure 4-8. The injection pressure/time profile of the flat panel RTM documented in process records

The inlets and vents modelled with the flat panel can be seen in Figure 4-9. The nodes corresponding to the inlet are highlighted in blue, and those corresponding to the vents in green.

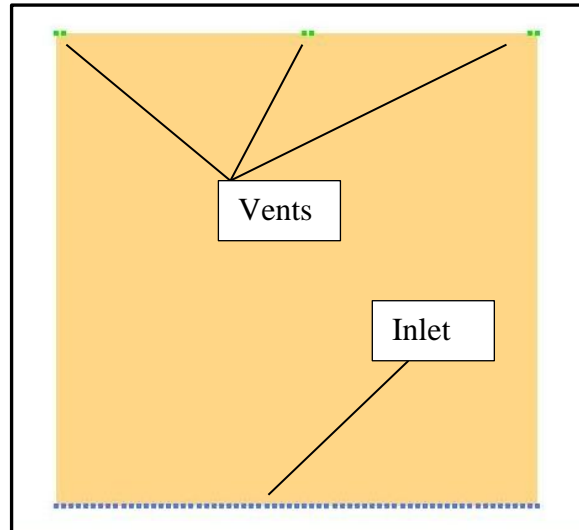


Figure 4-9. The simulated flat panel inlet and vents

The remainder of the flat panel process parameters are summarised in Table 4-2.

Table 4-2. Flat panel RTM process parameters documented in process records and determined experimentally

Process parameter	Parameter value
Vent pressure (Pa)	3600
Resin dynamic viscosity (Pa.s)	0.03
Porosity	0.36
Isotropic Permeability (m²)	1.75×10^{-12}

The dynamic resin viscosity stated in Table 4-2 corresponds to the single component epoxy resin system RTM6 at a temperature of 120°C [110], provided by the resin datasheet. The porosity and permeability values stated are those determined experimentally. The permeability used is that determined for the primary direction of resin flow through the tufted preform in the flat panel manufacture. In addition to the measured permeability documented in Table 4-2, minimum and maximum possible permeability values, resulting from a combination of potential systematic and random

experimental error within the permeability measurement, were also used. These limits were used to establish the bounds of the possible fill time, within which the value observed within process records should be encompassed.

The documented process parameters of the T-component, modelled in PAM-RTM, consisted of an injection pressure which again varied throughout the process due to manipulation by the technician. The pressure/time profile is given in Figure 4-10.

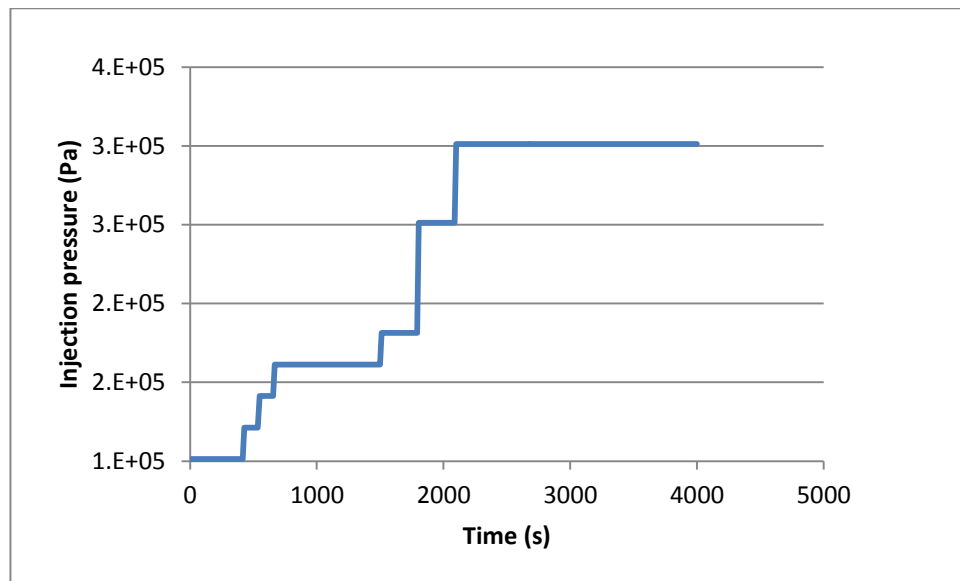


Figure 4-10. The injection pressure/time profile of the T-component documented in process records

The simulated inlet and vents of the T-component are pictured in Figure 4-11. Again the nodes corresponding to the inlet are highlighted in blue, and those corresponding to the vents are highlighted in green.

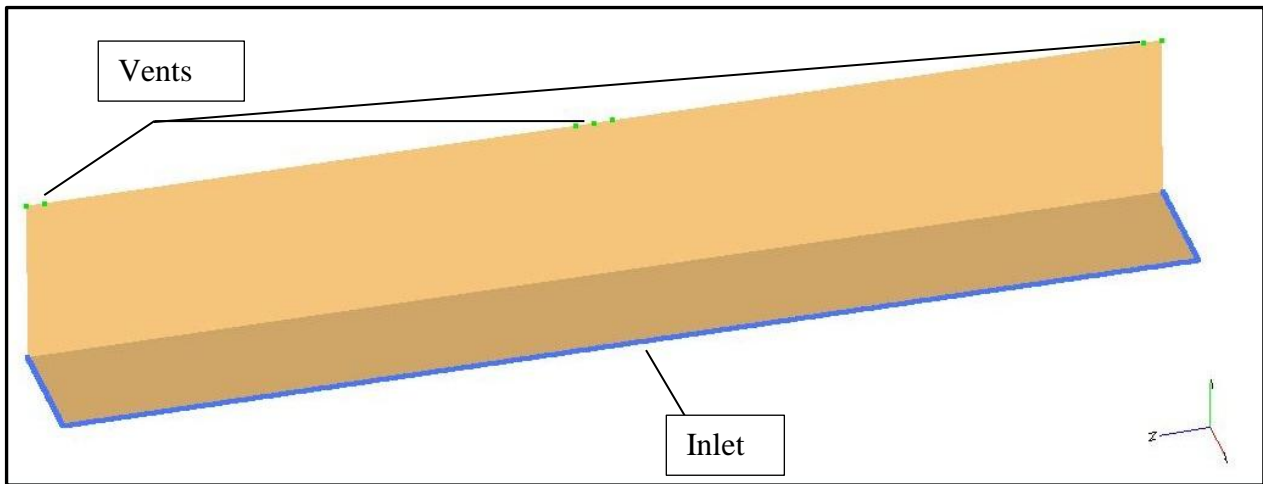


Figure 4-11. The simulated inlet and vents of the T-component, shown with the L geometry.

The remainder of the process parameters are summarised in Table 4-3.

Table 4-3. The T-component process parameters documented within process records and determined experimentally

Process parameter	Parameter value
Vent pressure (Pa)	3750
Resin dynamic viscosity (Pa.s)	0.1
Porosity	0.36
Permeability (m²)	1.75×10^{-12}

Similarly to the simulations of the flat panel RTM, the calculated maximum and minimum permeabilities were again used to determine the possible range of simulated fill times resulting from uncertainty in the experimentally measured permeability. As a result of the two dimensional nature of the T-component's injection, the stated permeability of the tufted preform was modelled as isotropic in the two directions of resin flow (Figure 4-12). The tufted preform is aligned so that the experimentally determined permeability corresponds to the K_1 direction, marked in Figure 4-12. The assumption of isotropic permeability was justified by the quasi-isotropic lay-up of the preform plies, and the limited alignment of the tuft thread in these directions. In the case of the T-component, the documented dynamic resin viscosity corresponds to the single component epoxy resin system MVR444 at a temperature of 80°C [111].

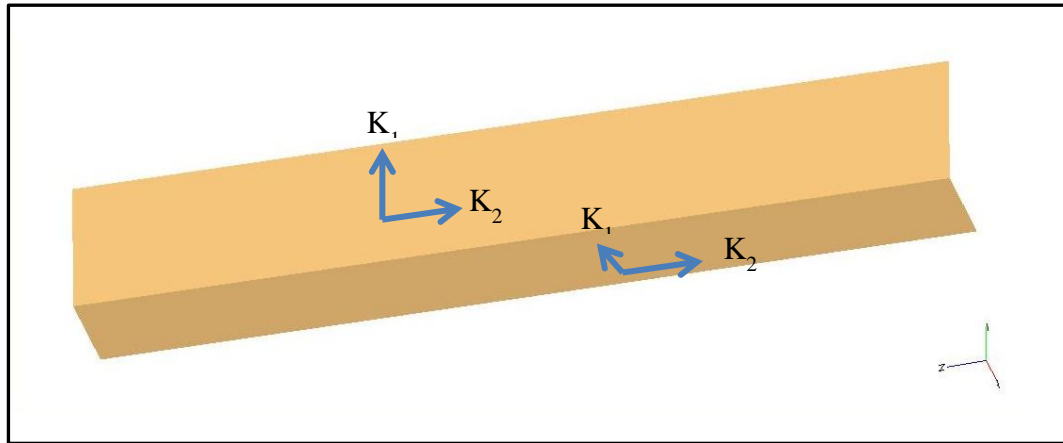


Figure 4-12. The defined permeability directions of the T RTM simulation.

The simulated fill times of the manufactured flat panel and T-component are shown respectively in Figure 4-13 and Figure 4-14, plotted with the corresponding fill times documented in the process records.

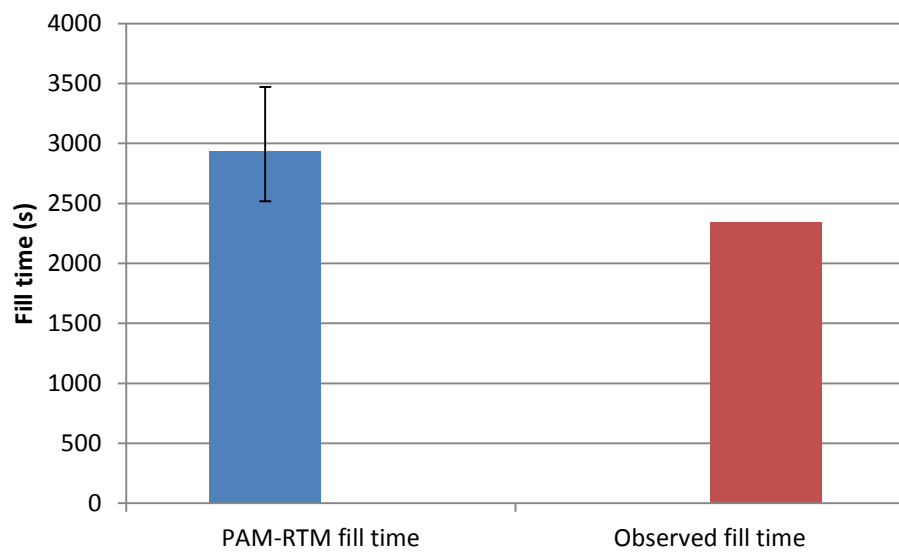


Figure 4-13. The simulated and observed fill times of the flat panel showing simulation error bars relating to the limits of the material permeability measurement

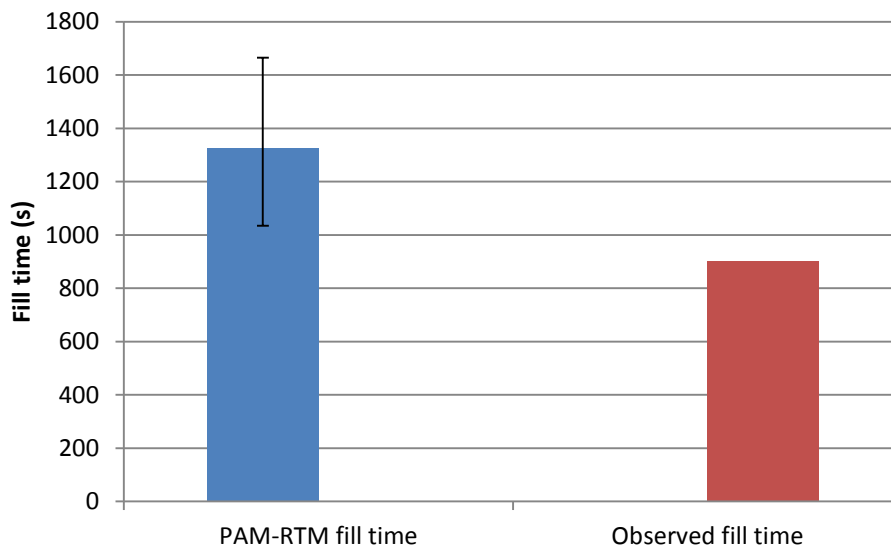


Figure 4-14. The simulated and observed fill times of the T-component showing simulation error bars relating to the limits of the material permeability measurement

Studying Figure 4-13 and Figure 4-14, it can be seen that the fill times estimated using the maximum possible permeability provide the closest estimates to the fill times documented within the process records. The fact that the simulated fill times are consistently more accurate using the maximum possible permeability provides some evidence to suggest that, due to the presence of systematic error within the experiments, the permeability of the material is greater than that indicated by the experimentally measured values.

In the cases of both of the components, Figure 4-13 and Figure 4-14 show that despite accounting for the range of possible material permeability within the simulations, the fill times documented in the process records do not lie within the simulated fill time bounds. The simulated minimum fill time of the flat panel overestimates the documented fill time by approximately 8%. That simulated for the T-component overestimates the recorded time by approximately 15%. As well as resulting from the possibility that the experimentally measured permeability may be lower than reality as a result of systematic errors, these discrepancies may in part be due to inherent errors generated by the meshes employed within the simulations (as discussed earlier within the chapter), errors within the documented fill times resulting from issues such as race-

tracking or the assumption that through-thickness flow is negligible. In addition, the fact that the discrepancy between the observed and simulated fill times is greater in the case of the T-component than that of the flat panel suggests that the preform's permeability is not isotropic in the K_1 and K_2 directions. This is because the flat panel experiences resin flow in just the K_1 direction, the direction in which permeability has been measured, whereas the T-component experiences resin flow in both the K_1 and K_2 directions. The greater error in the case of the T-component suggests that the K_2 permeability is not the same as the K_1 permeability, as has been assumed.

Anisotropy within the tufted preform material would, depending on the ratio of the permeabilities in the K_1 and K_2 directions, either increase or decrease the fill time of the component. Having modelled the RTM of the T-component with isotropic permeability, as determined experimentally for the K_1 direction of the material (Figure 4-12), the finding that the documented fill time was smaller than that simulated indicates that the material must be more permeable in the K_2 direction.

Acknowledging the fact that the lay-up of the plies within the tufted preform is quasi-isotropic, the proposed anisotropy can only be the result of directionality caused by the tufting. The single aspect of the tufting that contains directionality in either the K_1 or K_2 directions are the tuft seams. The fact that this component of the tuft is aligned in the K_2 direction leads to the hypothesis that the tuft seams are responsible for the material's higher permeability in this direction. This hypothesis has been examined theoretically in order to estimate the anisotropy ratio that is generated by the alignment of the tuft seams.

4.4.1 The influence of the tuft seam on the permeability of the tufted preform in the K_1 and K_2 directions

As well as creating the tell-tale tuft on the lower surface of a fibre preform, tufting also creates a seam on its upper surface (Figure 4-15). The tuft seam is the result of the continuous thread used to create the tufts. After the stitching needle inserts a tuft, the thread remains intact and trails to the next insertion, forming the seam. Due to the nature in which the surface geometry is formed, the thread forming the seam is aligned with the tufting direction.

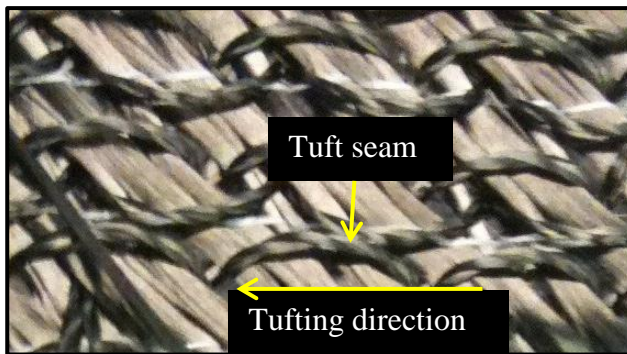


Figure 4-15. The tuft seam created by the tufting process aligned in the tufting direction

In a quasi-isotropic lay-up, such as that of the NCF fabric within the tufted preform examined, the permeability in the K_1 and K_2 directions should be equal. However, it is hypothesised that the directionality caused by the alignment of the tuft seams will result in anisotropy between the K_1 and K_2 permeabilities.

Due to limitations regarding available material, permeability was measured in the K_1 direction. As a result, the effect of the directionality on permeability in the K_2 direction has been evaluated theoretically.

The K_1 and K_2 directions of the tufted preform are defined as respectively perpendicular and parallel to the alignment of the tuft seams (Figure 4-16).

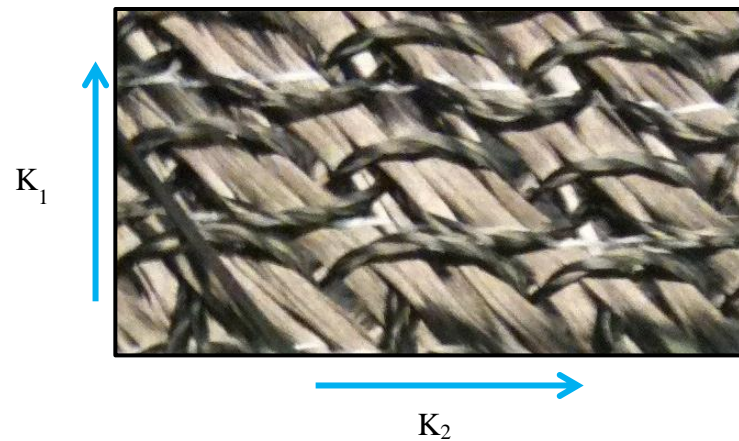


Figure 4-16. The K_1 and K_2 directions of the tufted preform

In order to estimate the effect of the directionality on the permeabilities of the preform, dimensions of the section containing the tuft seams, and of the seams themselves, in the preform compressed to its final height were determined. The required dimensions consisted of the section thickness and the width of the tuft seam cross-section. Measurements of these dimensions were made using computer controlled digital (optical) microscopy to analyse a composite sample composed of the same tufted preform material, compressed to the same final thickness as that within the permeability experiments. Analysing the cross-section of the sample around the tuft seams, the thickness of this section was averaged from twelve measurements made using the microscope control software. A similar approach was used to measure the cross-section width of the tuft seams, averaging from six measurements. Figure 4-17 shows an example of one of the microscopy images of the surface tuft seam cross sections used to measure the surface layer thickness and seam cross section width. The recorded surface layer thicknesses and tuft seam cross-section widths are provided in Table 4-4 and

Table 4-5 respectively, each with their average values.

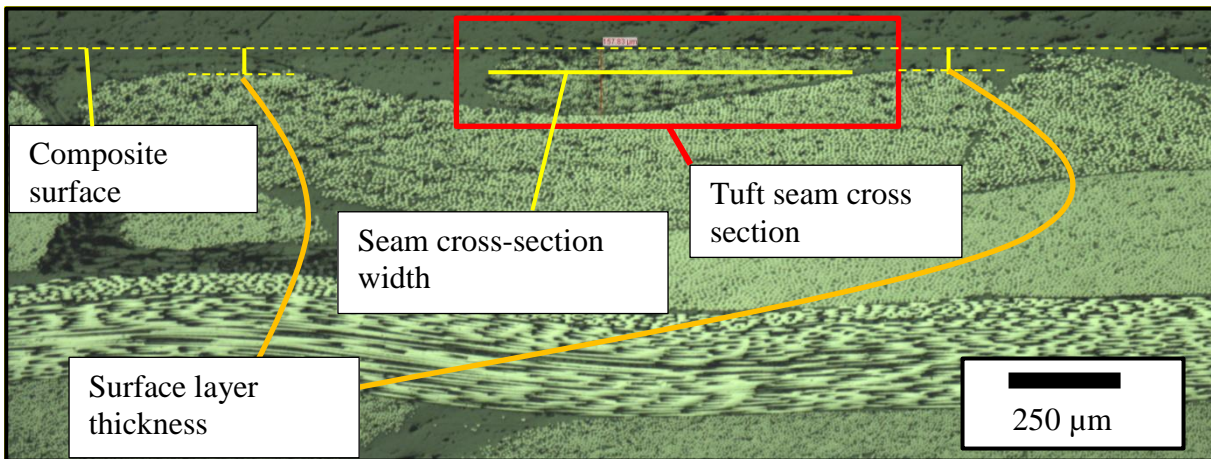


Figure 4-17. A microscopy image of the tuft seam cross section at the surface of a composite made with the investigated tufted preform

Table 4-4. Tuft seam surface layer thickness measurements

Layer thickness (μm)	
	96
	29
	54
	42
	39
	43
	27
	44
	35
	37
	45
	141
Mean	53
Standard deviation	32

Table 4-5. Tuft seam cross-section width measurements

Tuft seam cross-section width (μm)	
800	
902	
697	
1117	
1577	
925	
Mean	1003
Standard deviation	287

Subsequent to the measurement of the surface layer thickness and the tuft seam cross-section width, an idealised cell of the surface layer containing the tuft seams (Figure 4-18) was made to estimate the permeabilities of the layer in the $K_{1 \text{ surface}}$ and $K_{2 \text{ surface}}$ directions. It is assumed that the layer thickness does not deviate from the average determined with the microscopy measurements. Also, the tuft seams are assumed to be compressed to the same thickness as the layer, and their compressed cross-sections are assumed to be rectangular.

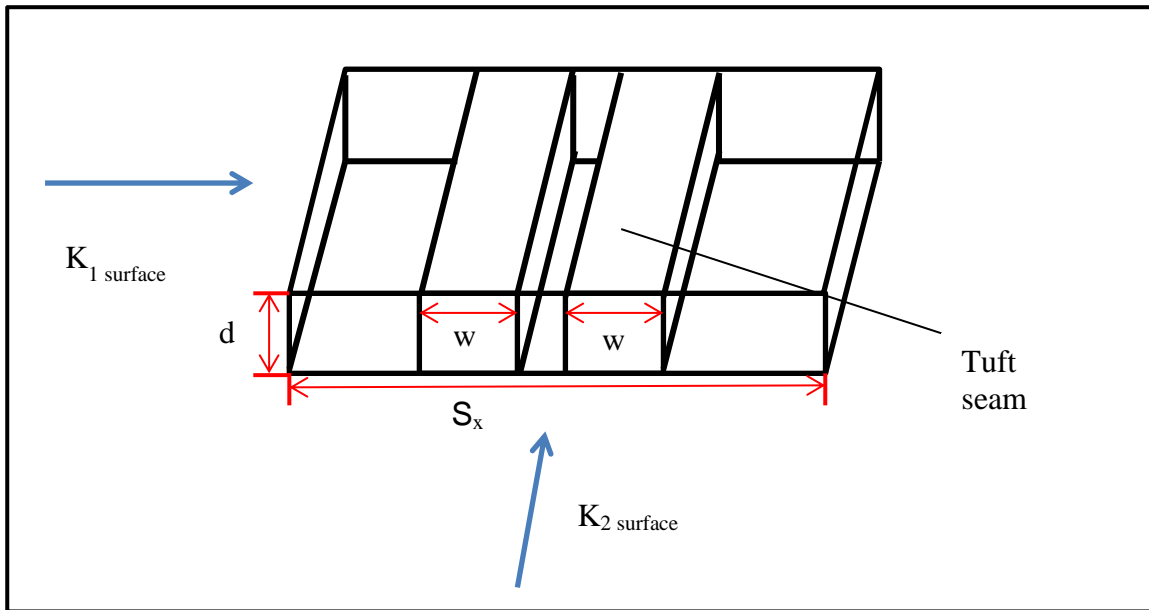


Figure 4-18. An idealised cell of the tuft seam surface layer

The minimum permeability of the tuft seam surface layer was assumed to be in the $K_{1 \text{ surface}}$ direction, where the tufts are aligned perpendicular to the flow direction. Within the idealised arrangement of the layer (Figure 4-18), the tuft seams can be seen to occupy the height of the layer throughout their width in the $K_{1 \text{ surface}}$ plane. In this instance there is no space in the cross section for any liquid flow to pass. It follows that the extreme arrangement of the layer was assumed to be impermeable in the $K_{1 \text{ surface}}$ direction.

As suggested, the permeability in the $K_{2 \text{ surface}}$ direction was assumed to be the greater of the two permeabilities, due to the much greater level of space within the cross section available to fluid flow. To estimate the permeability in this direction it was necessary to characterise this porosity. As defined earlier in Chapter 3, the porosity of a fibre reinforcement is a function of the fibre volume fraction. Using the idealised unit cell depicted in Figure 4-18, it was possible to estimate the fibre volume fraction in the $K_{2 \text{ surface}}$ direction assuming it to be the same as the fibre area fraction:

$$V_f = \frac{2wd}{S_x d} = \frac{2w}{S_x}$$

Equation 4-2

Where, in the case of the tufted preform the tuft row spacing (S_x) is 4mm, the fibre volume fraction for the $K_{2 \text{ surface}}$ direction of the preform was calculated to be 0.5, giving a porosity ($1 - V_f$) equal to 0.5.

With a value for the porosity in the $K_{2 \text{ surface}}$ direction, the permeability was estimated by applying the porosity to the term for the volumetric flow rate between two parallel planes given by Massey [103], as follows:

$$Q = \frac{\Delta P b c^3 \phi}{12 \mu L}$$

Equation 4-3

Substituting this term into Darcy's law, the following equation for the permeability of the channel between two parallel planes, with a known fibre volume fraction, is derived:

$$K = \frac{c^2 \phi}{12}$$

Equation 4-4

Using Equation 4-4 the tuft seam layer permeability in the $K_{2 \text{ surface}}$ direction is calculated to be $1.17 \times 10^{-10} \text{ m}^2$.

With the estimates of the permeability of the tuft seam surface layer in the $K_{1 \text{ surface}}$ and $K_{2 \text{ surface}}$ directions, their effect on the permeability of the whole preform in the K_1 and K_2 directions may also be estimated. This is achieved using a term defining the average directional permeability of a material as a function of the directional permeabilities of its constituent layers:

$$\bar{K} = \frac{1}{h} \sum_{s=1}^{n_s} K_s h_s$$

Equation 4-5 [82]

In the case of the tufted quasi isotropic preform, two layers are considered. These are the layer containing the tuft seams (layer 1), and the layer containing the remainder of the preform (layer 2). These layers are depicted in Figure 4-19.

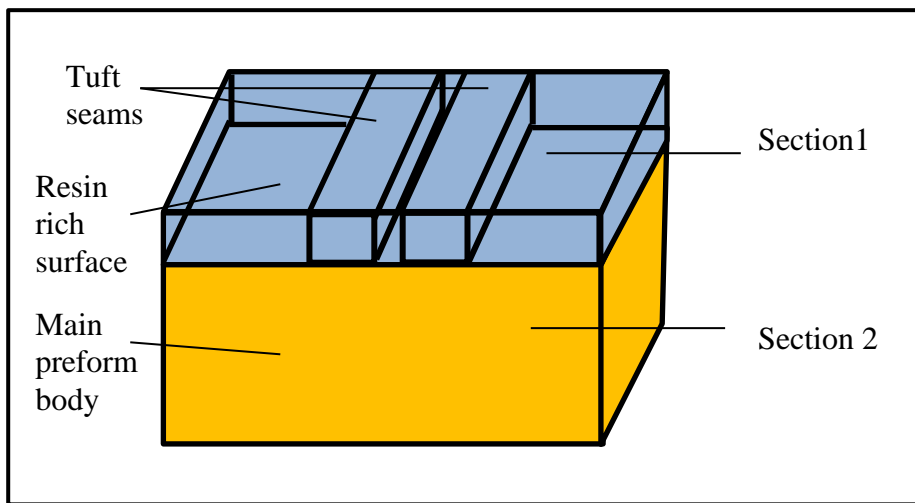


Figure 4-19. The tufted preform layers considered within the mean permeabilities

As the second layer is quasi-isotropic, its permeability in the K_2 direction can be assumed to be the same as that of the permeability in K_1 , which was determined experimentally. This allows the mean permeability of the preform in the K_2 direction to be estimated using Equation 4-5 as follows,

$$\bar{K} = \frac{[(1.17 \times 10^{-10} m^2) \times (5.3 \times 10^{-5} m)] + [(1.75 \times 10^{-12} m^2) \times (3.95 \times 10^{-3} m)]}{0.004 m}$$

$$\therefore \bar{K} = 3.28 \times 10^{-12} m^2$$

Equation 4-6

This suggests that the permeability of the preform is influenced by the tuft seams and supports the hypothesis that it is increased with their alignment parallel to the permeability direction.

The resultant anisotropy ratio between the measured K_1 and the estimated K_2 permeability was estimated to be 1:1.87. This ratio indicates that the permeability of the preform is almost doubled when the tuft seams are aligned with the permeability direction rather than perpendicular to it.

To assess the anisotropy ratio, PAM-RTM was again used to re-simulate the RTM of the T-component, modelling the estimated anisotropic permeabilities. In addition to using the experimentally determined K_1 permeability, simulations were completed with the maximum and minimum possible permeabilities resulting from the potential error in the permeability experiment. This method provided a range of possible results. A comparison of the simulated fill time of the T-component modelling the anisotropic permeability and the fill time taken from the component's process record can be seen in Figure 4-20.

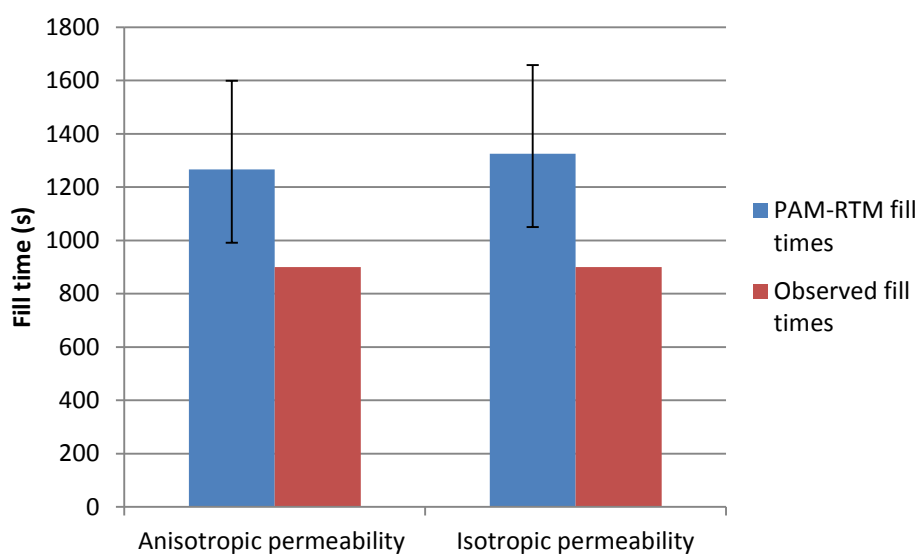


Figure 4-20. The simulated fill times of the T-component modelling anisotropic and isotropic permeabilities compared to the documented fill time from the process record

Studying Figure 4-20, it is evident that including the anisotropy ratio shifts the possible range of fill time values closer to the observed process time, indicating an increase in accuracy. Within the T-component simulations where the experimentally determined permeability was modelled isotropically, the observed fill time documented in the process record lay outside the simulated range by approximately 15% (Figure 4-14). Modelling the estimated anisotropic permeability, this discrepancy is reduced to approximately 10%.

Despite the increased accuracy, the shorter observed fill time remains outside of the simulated range. This discrepancy may be due to error generated by the mesh used within the simulations, the underestimation of the permeability in the K_2 direction or any other inadvertent differences between the model and reality (e.g resin temperature and viscosity), but it is most likely to be due to the underestimation of the observed fill time as a result of race-tracking (which was noted due to resin not reaching each of the vents at the same time in some observations). If as assumed, the 10% discrepancy is a result of the presence of race tracking, this issue is much more significant than the effect of modelling the materials estimated anisotropy.

The proportion of the discrepancy due to underestimation of the K_2 permeability is likely to be small. This is evident as within the results of the simulation of the flat panel RTM (Figure 4-13), the K_2 permeability does not influence the component's fill time. The discrepancy between the range of simulated fill times and that documented in the process record is still approximately 8%, only 2% less than that identified for the simulations of the T-component modelled with anisotropic permeabilities.

In the case of the flat panel, where only one dimensional flow in the K_1 direction was generated, the 8% discrepancy must be due to the inaccuracy of the model and the observed fill time. With the RTM of the T-component, where two dimensional flow

was experienced, it is therefore likely that the additional 2% discrepancy results from error in the estimation of the tufted preform's anisotropy.

As the evidence suggests that due to systematic error, the permeability of the tufted preform is greater than that indicated by the experimentally measured values, the possible fill times in subsequent simulations are accounted for using the maximum possible permeability in conjunction with the experimentally determined permeability to generate a reduced range of fill time values. An exact calibration cannot be performed as a result of uncertainty regarding the fill times documented within the process records, which are used for the permeability validation.

The approximate 10% error between the fill time simulated with the maximum possible permeability and the fill time observed is thought to result largely from error within the observation. This conclusion is made due to the much smaller levels of error generated by the simulation meshes, and the possible underestimation of the preform anisotropy ratio. In turn, the error in the simulated fill time is assumed to be less than 10% and is considered to be acceptable for the intended use of the values.

4.5 PAM-RTM simulations for component manufacturing cost estimation

The rib post geometry is similar in every way to the T-component analysed within the validation of the tufted preform's experimentally determined permeability, differing only in its length. A diagram of the rib post is provided in Figure 4-21, noting the dimensions used within RTM simulations and also the position of fixing holes drilled post moulding.

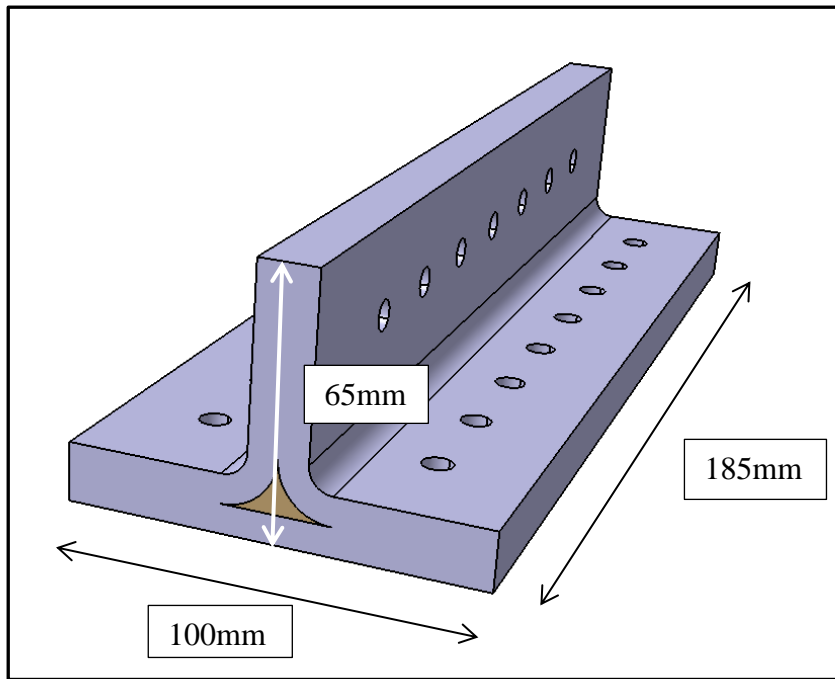


Figure 4-21. A schematic of the composite rib post noting the dimensions used in the RTM simulations (courtesy of QinetiQ)

The component is assumed to be manufactured net-shape, using the same injection strategy as that employed for the manufacture of the T-component analysed in section 4.4. This strategy consists of injecting pre-heated resin into a runner within the heated mould. A runner is a channel of high permeability surrounding the mould cavity that is connected to the resin inlet. The resin enters the runner, which follows the perimeter of the T flange, from a single injection point. Due to its high permeability, the runner fills prior to the mould cavity which contains the fibre reinforcement. Once the runner is filled the resin permeates the fibre preform from each of its edges simultaneously, as shown in Figure 4-22.

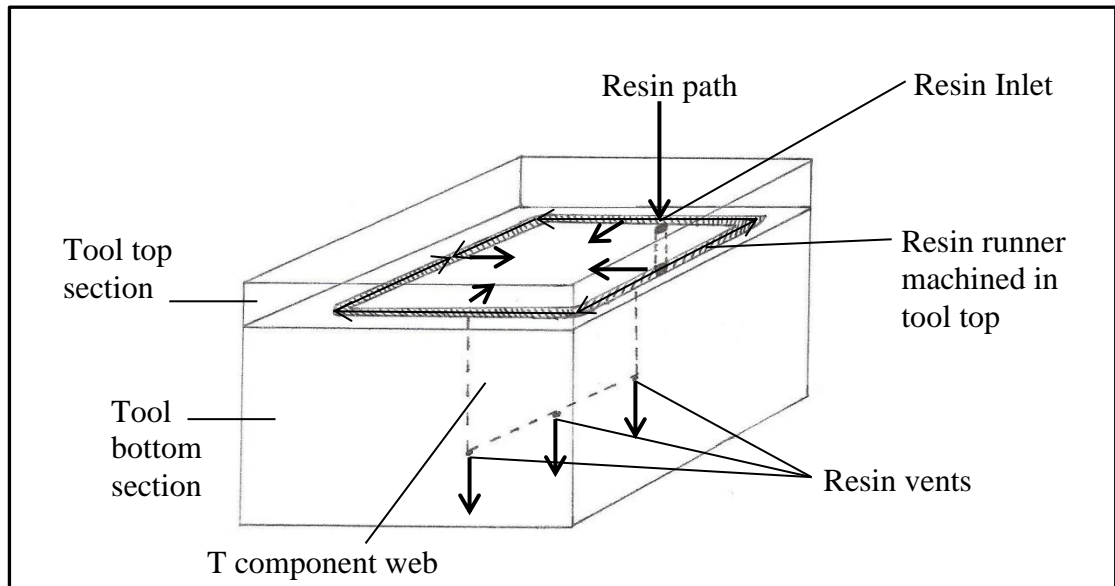


Figure 4-22. A schematic of the RTM tool and injection strategy of the T-component

The process employs three vents which are located at the outer edges of the T-component's web (Figure 4-22). Similarly to the T-component analysed within the permeability validation, the symmetry of the component's injection strategy allowed the RTM of the rib post to be modelled in just half of the structure, which took the form of an L geometry. The simulation geometry is shown in Figure 4-23.

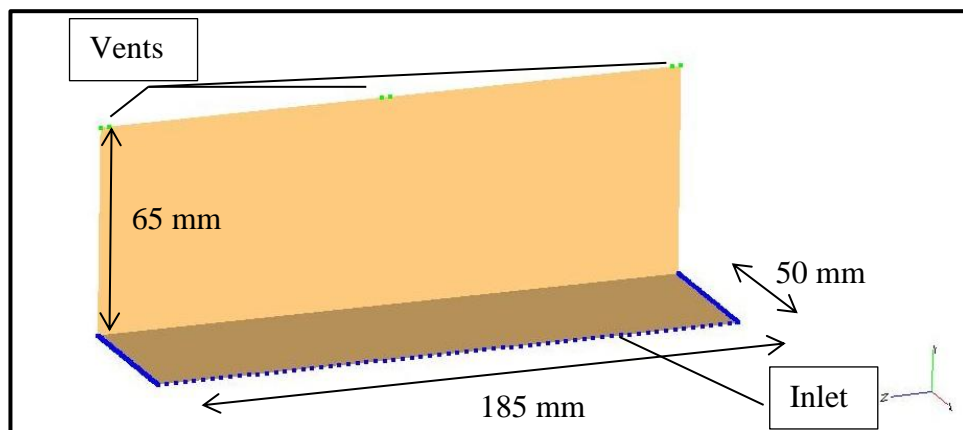


Figure 4-23. The RTM simulation geometry of the rib post.

The RTM of the T-component, as with previous simulations was modelled in two dimensions, assuming the through-thickness flow of resin resulting from the implemented infusion strategy to be negligible. The inlets and vents were defined to be in the same positions as those of the simulations completed for the validation of the determined permeability (Figure 4-11). Subsequently the permeability directions were

defined as those shown in Figure 4-12. The process parameters assumed for the RTM simulation are documented in Table 4-6.

Table 4-6. The process parameters used for the rib post RTM simulation

Parameter	Value
K₁ permeability (m²)	1.75 x 10 ⁻¹²
K₂ permeability (m²)	3.28 x 10 ⁻¹²
Differential pressure (Pa)	1.01x10 ⁵
Porosity	0.36
Resin dynamic viscosity (Pa.s)	0.1

As a result of the linear relationship between the differential pressure, the fluid dynamic viscosity and the simulated fill time, which obeys the relationship defined by Darcy's law, the process parameters can be altered subsequent to the simulation to determine the fill times resulting from different resin viscosities and pressure conditions.

The permeabilities documented in Table 4-6 consist of the experimentally determined permeability of the preform in the K₁ direction, and the K₂ permeability estimated in section 4.4.1. As well as using these permeabilities, the maximum possible permeabilities occurring as a result of error within the permeability experimentation were also modelled, providing a range of possible fill times. The differential pressure given in Table 4-6 relates to vacuum pressure and was assumed to remain constant. The documented dynamic resin viscosity corresponds to the single component epoxy resin system MVR444 at a temperature of 80°C [111], and the porosity relates to the average determined for the tufted preform samples analysed within the permeability experiment.

The results of the simulations completed for the RTM of the rib post are provided in Table 4-7.

Table 4-7. Tufted rib post RTM simulation results

Simulation	Fill time (s)
Maximum permeability	653
Measured permeability	907

As a result of evidence provided by the permeability validation study, it is concluded that the fill time that would be experienced in reality is closest to that simulated with the maximum possible permeability. It follows that the range of fill times between that modelled with the maximum permeability and that modelled with the experimental permeability should encompass the fill time which would be experienced in reality. Subsequently it is this range that is used to estimate the costs for the RTM of the rib post.

For comparison purposes with regard to manufacturing costs, the fill time of the component manufactured without tufting was also simulated. This was made possible through the experimental measurement of the isotropic permeability of a non-tufted preform material with the same lay-up and fabric as the tufted preform. The simulation was completed using two values for the material's permeability, that determined to be the maximum possible and that determined to be the minimum possible within experimentation (Table 4-8).

Table 4-8. The experimentally determined maximum and minimum possible values for the non-tufted preform material isotropic permeability

Maximum permeability	$9.72 \times 10^{-12} \text{ m}^2$
Minimum permeability	$2.18 \times 10^{-12} \text{ m}^2$

Using these values to simulate the fill time with the non-tufted preform, a range of possible values are again provided, the range being used within the estimate of the non-tufted rib post RTM costs. Other than the permeability and porosity, the parameters

used within the simulation were kept the same as those documented in Table 4-6. From fibre volume fraction calculations (Chapter 3) porosity of the non-tufted preform was given to be 0.4. The simulated maximum and minimum fill times of the non-tufted rib post are shown in Table 4-9.

Table 4-9. Non-tufted rib post RTM results

Simulation	Fill time (s)
Maximum permeability	228
Minimum permeability	404

The simulation of the RTM process completed during the manufacture of the novel composite rib post has facilitated the validation of the experimentally determined values for the permeability of the tufted preform material, and also the simulation of component fill times for the estimation of manufacturing costs. Comparisons of observed and simulated fill times of benchmark components manufactured using the tufted preform material have indicated that the maximum possible material permeability, considering experimental error and the material's theoretically determined anisotropic permeability ratio, provide fill times most representative of observations. The simulated fill times using these parameters are approximately 10% greater than the observed values, proving more significant than the difference resulting from the consideration of the material's theoretical anisotropic permeability. The discrepancy between the simulated and observed values is most likely to be the result of race tracking occurring during the observed processes but may also suggest that through-thickness flow is not negligible as was assumed. If the latter is true, the assumption would form a major limitation of the RTM simulation and would subsequently affect the manufacturing cost estimates of the component.

As well as simulating the RTM of the composite rib post with the tufted material, the process was also completed considering the experimentally determined permeability of the non-tufted material. With values for the fill times of the component considering both materials, manufacturing cost estimates could be made for the composite rib post with and without tufting, providing the facility to estimate the additional manufacturing costs attributed to the tufting technique. In the case of the investigated rib post application, the difference between the fill times of the component with the tufted preform and the non-tufted preform will not result in a great difference to overall manufacturing cost due to the small resulting fill times, reducing the effect of any error resulting from the assumption of negligible through-thickness flow. However, in the case of larger components this difference could well become more significant, having a much greater effect on component manufacturing costs.

Chapter 5. Cost modelling

The purpose of the cost modelling within this project has been to facilitate comparisons of the costs of manufacturing the NGCW's novel composite rib post with a number of different manufacturing techniques. The processes considered consist of robotic tufting with RTM, used within the NGCW project, RTM without tufting for benchmarking purposes and also the prepreg/autoclave process, chosen for comparison due to its favoured use within the aerospace industry [4, 112, 113]. In each of the processes, to allow for comparison, the component dimensions remain the same. Variations in structural performance resulting from the use of different manufacturing processes (and consequently different material feedstock) are accommodated later using structural analyses to generate a performance index. This index compares the critical structural response and weight of the component resulting from each manufacturing process. Combining this index with the estimated manufacturing costs of the various manufacturing processes, conclusions can be made as to whether the tufted composite provides an economic advantage over the alternative material considerations.

Manufacturing costs are widely accepted to include the labour, material, tooling, equipment and overhead costs. These costs are a combination of both recurring and non-recurring costs, defined respectively as those which recur for every part within the production quantity (labour, material etc.) and those independent of production rate, usually occurring as start-up costs (tooling, equipment etc) [4]. It may or may not be the case that the cost of the equipment has been amortised over its previous use, and if equipment is purchased for a particular production run, it will almost certainly be used in subsequent productions. This results in equipment costs being amortised over the production quantity [114-116], sometimes additionally over future business projections [117], and also in some cases being considered as non-contributory [11]. Within this

project two possibilities are examined. Manufacturing cost estimates are made assuming equipment capital costs to have been amortised over previous equipment use, and also assuming that they are amortised over the production quantity. This decision allows additional conclusions to be made about the economy of the material when equipment has been paid for, as may be the case in the production of various components within the aerospace industry. Plant overheads are also assumed to be the same for each process, removing the requirement for their inclusion within cost estimates when providing a relative appreciation of process costs.

5.1 Cost estimation techniques

A wide range of cost modelling techniques are available to generate manufacturing cost estimates. Generally the techniques are split into two main branches, which are given a variety of names in literature. Niazi *et al* [118] refer to the two groups as qualitative and quantitative techniques whereas Rush and Roy [119] name them ‘first sight’ and ‘detailed’ estimates. The initial group (qualitative/first sight) encompasses techniques using past data to generate estimates for new products, whereas the later (quantitative/detailed) includes techniques which focus on the detailed analysis of product design, features and manufacturing processes, relating these to the resources consumed during production. It can be argued that through creating a direct link between the product and the resources consumed within its production, quantitative/detailed techniques provide a greater understanding of how individual product features affect the final product cost and therefore the product’s cost drivers. The various techniques defined by Niazi *et al* [118] are shown in Figure 5-1.

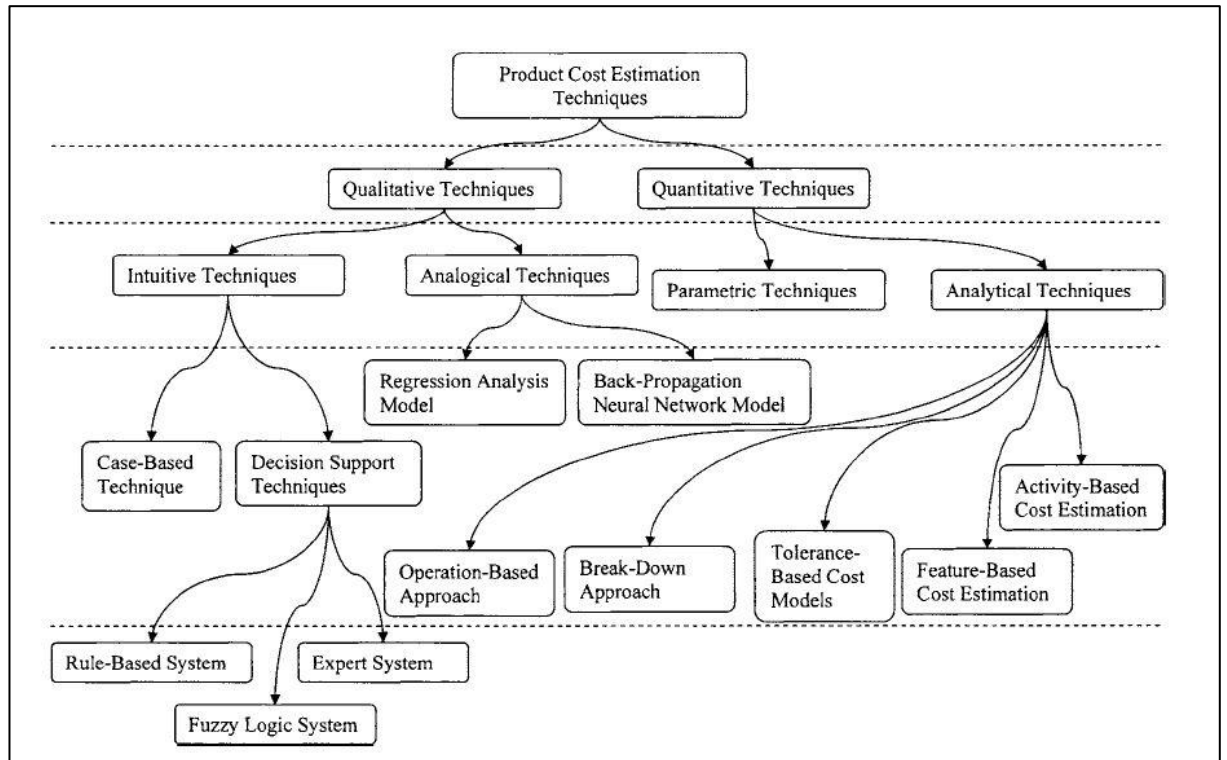


Figure 5-1. A classification of product cost estimation techniques [118]

According to Niazi *et al* [118], the qualitative cost estimation group includes both ‘intuitive’ and ‘analogical’ techniques. Where ‘intuitive’ cost estimation is based upon the use of past expert experience in the form of rules or decisions that relate to a database and therefore improve the decision making ability of the user, ‘analogical’ techniques also make use of similarity criteria [120]. The similarity between past and new designs is assessed and relationships between the costs of past designs and the value of product features are developed, allowing the cost of new design to be estimated.

Quantitative cost estimation techniques are based on detailed analyses of the product and can also be divided into two methods. These are known as parametric and analytical cost estimation [118]. As suggested by Geiger and Dilts [121], and succinctly described by Kauffmann [11], parametric techniques are based on cost relevant design parameters known as cost drivers, and mathematical functions that relate the cost drivers to the final product cost. In contrast, analytical cost estimation techniques,

referred to elsewhere as generative cost estimation [120, 122], incorporate the division of the product into its basic features or the operations and activities required within its production. These individual aspects are then related to their consumption of resources during the product's manufacture. The product cost is then expressed by the sum of the costs of each of the operations.

A variety of analytical cost estimation techniques are mentioned by Geiger and Dilts [121]. Among these are activity-based costing (ABC), also discussed by Ashby [123], and feature-based modelling (FBM). Each of these methods can be classed as analytical cost estimation techniques within the quantitative estimation group. FBM determines the costs associated with the product's cost related features, relating the features to the resources consumed during their creation. These features may be aspects of the product's design or its manufacturing process. On the other hand, ABC techniques focus on the product's manufacturing process by identifying the major cost driving activities and forming algorithms known as CERs [124]. The sum of these CERs provides the estimate for the product's manufacturing cost. A much simpler analytical cost estimation approach, but one that requires a great deal of process information is the operation-based technique [118]. This technique is based upon the summation of the costs of all of the operations completed in order to manufacture the product. Due to the level of process detail this approach requires it is often only used in the final design stages, its simple cumulative nature also restricting its estimation capabilities to the component for which it was designed.

Other relevant cost estimation methods discussed by Geiger and Dilts [121] include; group technology (GT) and computer aided process planning (CAPP). GT is defined as a classification system capable of recognising part similarities, and therefore old products that are similar to new designs. In this way, GT can provide cost estimates for

new designs that are based upon the historical costs of past products. Under the definitions of Niazi *et al* [118], this method would be classed as a ‘qualitative analogical’ cost estimation technique. Geiger and Dilts’ [121] description of CAPP suggests that it is also very much part of an ‘analogical’ cost estimation technique, but that it also contains features of ‘intuitive’ cost estimation. Numerous variations of CAPP exist [121], though all share common ground in the fact that they assess the similarities of new designs to old products, in the manner of an ‘analogical’ technique, to retrieve stored expert knowledge about the product’s preferred manufacturing routes and potential costs, in the same way as an ‘intuitive’ cost estimation.

The commercial cost estimation software SEER-MFG [125] also shares similarities with intuitive cost estimation. As Kaufmann [11] states, SEER-MFG is a very popular commercial tool for the estimation of manufacturing costs. The model combines feature-based techniques with those of parametric estimation and also incorporates the ability to provide quantitative early design phase estimates, with an intuitive cost estimation technique. The exact technique used is defined by Niazi *et al* [118] as a case-based methodology. The technique is achieved through the adaptation of similar past design cases that are stored within a database. SEER-MFG incorporates this technique with a wide-ranging library of what it calls ‘knowledge-base templates’. These knowledge-base templates contain all of the parameters required to form an estimate of the manufacturing cost of the past design case. Individual parameters within these templates can be altered to estimate the cost of a new design, whilst using any chosen amount of parameter information from the past design case. The altered template may then also be saved within the SEER-MFG library, allowing it to be continuously updated.

Another commercial cost estimation tool that Kaufmann [11] states is equally as popular as SEER-MFG is Price systems' Trueplanning [126]. This is similar to SEER-DFM in that it makes use of quantitative parametric cost estimation methods to provide cost estimates when all of the details of the design are finalised, and that it also facilitates early design phase estimates when the product's features have not been determined. The model's early design phase estimates are again completed using intuitive techniques, the model utilising benchmarks based upon knowledge bases of past industrial project data.

Similarly to the commercial tools described above, an important feature of the composite structure cost model proposed by Zhao *et al* [127] is its ability to estimate costs in the early design phase. To achieve this the model has to account for uncertainty regarding final design decisions, known as epistemic uncertainty [128], using the fuzzy-logic approach. The technique considers the 'fuzziness' of various design parameters using expert knowledge in the form of part descriptions or 'linguistic expressions' [118]. These expressions may consist of descriptions of part complexity, for example, 'complex' or 'very complex'. Each of the expressions is related to the final cost estimate, their effect on the estimate being defined by the expert knowledge held by the model. The user can then assign a truth value to this expression within the model, which defines how well it describes the part [127]. The choice of the truth value is then reflected in the cost estimate provided.

Scanlan *et al* [122] also make use of the fuzzy-logic approach within a cost model proposed for aircraft design optimisation. The authors' use of this technique differs from Zhao *et al* [127] in that it was used to account for uncertainty experienced at any point during the design, be it in the early stages or much closer to the end of the process. Within the cost model, the fuzzy-logic approach was used in combination with both

parametric and feature-based techniques to provide the different levels of cost estimation. Progressively more accurate estimates could be made as design details were finalised.

As well as uncertainty in design definition, the difficulty in validating cost models requires uncertainties in the relationships estimating resource consumption to be acknowledged. The Monte Carlo method [129] is ideally suited to account for the stochastic nature of various rates and activity times, often being employed to simulate statistical uncertainty in cost estimates [120, 128]. Within Monte Carlo simulation, statistical distributions between defined ranges replace absolute values for uncertain variables, and relationships are formed between statistical distributions for dependent variables. Once these steps are in place, the Monte Carlo method iterates the cost totalling procedure, creating a distribution of total costs from which overall error is estimated.

Cost models based on individual cost estimation techniques are discussed by Bao and Samareh [130], Barton [131] and Mazumder [4]. Unlike the multi-level estimation techniques described earlier, these cannot provide early design phase cost estimates. The methods proposed by these authors take the form of feature-based cost estimation techniques, relating component features to the resources consumed during their creation. The authors [4, 130, 131] describe what are known as first order cost models. This costing method originated from the observation that many manual and automated manufacturing processes can be represented as dynamic systems with first order velocity responses to a step input [130, 131]. The first order velocity responses basically describe how process time is affected by the process velocity, which is in turn driven by the major geometric dimensions of the part. It therefore follows that the

process time, and subsequently the process cost, can be estimated using the process velocity and the major process time driving part geometry.

Another cost model that may be considered simpler than the multi-estimation techniques of the models described earlier is the Advanced Composite Cost Estimating Model (ACCEM) [132]. Noted as one of the first major attempts to develop cost estimating methods for advanced composites [133], the ACCEM model again uses a feature-based cost estimation technique, formulating time estimates as a function of part geometry using power law relationships [131], and estimating cost through the multiplication of these estimated process times by the relevant rates.

As can be seen in this review, there are a wide range of established cost estimation techniques that may be used at various stages during the design process. Each of these methods varies in complexity and in the type of data required in order to form the cost estimates. Some of the methods can be seen to be only slight variations upon each other, whereas some are fundamentally different. It is evident that this is dependent on whether the technique is intended for early design phase or detailed design phase cost estimates. A combination of both of these estimation techniques, as with the commercial estimation models mentioned earlier, can be seen to be advantageous, providing the ability to form cost estimates at any stage during the design process. However, if design details are known quantitative methods will be favoured.

5.2 Cost estimation and model creation

During this project a manufacturing cost model has been developed for the NGCW's novel composite rib post, which provides estimates relative to those developed for other composite processes. The nature of this cost model also allows it to estimate the manufacturing cost of a non-tufted component, allowing the additional cost attributed to the tufting step used in the manufacture of the novel composite rib post to be evaluated.

To estimate the cost of the component if it were fabricated from prepreg carbon fibre and autoclave processed, enabling the evaluation of the cost differences and the assessment of whether the use of tufting provides advantages over the well-established high performance composite manufacturing technique, the commercial cost model SEER-DFM (now SEER-MFG) was implemented. The reason for the use of costing software rather than the generation of a customised cost model for this manufacturing process was the lack of data and opportunity to collate the required information. SEER-DFM was chosen due to the fact that its composite cost models were developed by industry members from leading aerospace companies under the US Air force funded composites affordability initiative (CAI) [134], providing a level of confidence in the model's data. SEER-DFM was not used for the cost estimation of the robotic tufted composite manufacturing process due to the fact that the model does not account for the specific type of stitching or equipment used in the tufting process. In addition, as the manufacturing process completed at QinetiQ is developmental it differs in time and method from the industrially calibrated processes available in SEER-DFM.

For the development of an additional comparison, based on processes adapted for full production, SEER-DFM was used with the developed cost model for the tufted composite rib post to extrapolate cost estimates for a more efficient 'industrialised' process. Taking into account that the process used by QinetiQ was still in the development stages, where possible, aspects of the manufacturing process such as fabric cutting, layup and tool cleaning were additionally modelled in SEER-DFM to provide what could be described as an industrial cost extrapolation. The costs provided by SEER-DFM were then summed with the estimates of the costs relating to the robotic tufting and parts of the RTM process formed by the developed novel composite rib post cost model. The purpose of such an estimate is to provide a speculative idea of what the

process's costs may look like in a high volume production environment rather than remaining in an R&D phase.

5.3 Tufted novel composite rib post cost model

The developed manufacturing cost model for the robotically tufted composite rib post consists of the sum of labour, material, equipment and tooling costs, as indicated by Equation 5-1.

$$\begin{aligned} MFG\ cost = & (C_t + L_t + T_t + Pr_t + RTM_t + P_t) L_r + Energy + Material \\ & + Tooling + Equipment \end{aligned}$$

Equation 5-1

Where the manufacturing cost is *MFG cost*, C_t is the fabric cutting sub process time, L_t is the fabric layup time, T_t is the robotic tufting time, Pr_t is the preform de-moulding time, RTM_t is the RTM time, P_t is the finished part de-moulding time, L_r is the labour rate, and Material, Tooling, Energy and Equipment refer to their specific costs.

The methods used by the generated cost model to estimate the costs of each of the manufacturing cost drivers are described in the following sections.

5.3.1 Labour

To estimate labour costs the cost model utilises the framework of the ABC approach, separating the manufacturing process into its main sub processes (as documented in Chapter 3); fabric cutting and lay-up, robotic tufting, preform de-moulding, RTM and de-moulding. These sub-processes are then divided into their constituent activities, each of which is related to production quantity and rate. Resulting from the completion of detailed process analyses (Chapter 3), the durations of various activities were recorded and therefore accounted for using the operation based approach. In some cases, it was not possible to capture complete activities and in these circumstances their

durations were accounted for using the feature based method. For this technique activity times were calculated as a function of the component's dimensions and material characteristics. Examples of sub process activities making use of this technique are the robotic tufting and the RTM mould fill time, each depending on the arrangement of the inserted tufts. To calculate the total labour costs of the manufacturing process, the activity times of the sub processes were summed and then multiplied by a labour rate.

To achieve an appreciation of the uncertainty within the recorded values, variation was simulated using the Monte Carlo method within Microsoft Excel. To complete this simulation, minimum and maximum values, estimated using the recorded values and the author's experience, were set for each of the activity durations and rates. The values between these bounds were assumed to be uniformly distributed, facilitating random values within these bounds to be determined each time the simulation was iterated. The simulation was then run numerous times to emulate the recording of multiple completions of the process. 200 simulations were completed in order to provide substantial data with which to estimate the uncertainty of the total labour time consumed. A slight disadvantage of the use of the Monte Carlo method is that due to its use of defined variable bounds, it is incapable of predicting highly unlikely events.

Further detail of the relationships developed to calculate the labour times consumed by the activities in each of the sub processes is provided in the following sections.

5.3.1.1 Fabric cutting and layup sub process labour estimate

As documented in Chapter 3 the fabric cutting and layup sub process of the rib post manufacture consisted of a number of different manufacturing activities (Table 5-1).

The activities documented in Table 5-1 differ slightly from the steps discussed in Chapter 3. The reason for this is that within the cost model, repeated activities are

accounted for in the relationships relating the activities to the total time consumed by their completion during the entire manufacturing process. The relationships modelling the consumption of labour time take the form of either operation based or feature based techniques, simply consisting of measured activity durations or using algorithms which relate the relevant features of the ply to the duration of the activity.

The inputs the model requires in order to estimate the labour time of the sub process include;

- Component production quantity (n)
- Daily component manufacture capacity (ppd)
- Number of plies per preform (p_{pn})
- Ply width (P_w)
- Ply length (P_l)
- Number of plies cut per fabric roll width ($R_{w_{pn}}$)
- Number of different fabrics used ($ft\ n$)
- Ply cutting rate (Cr)
- Labour time simulated from measured values with Monte Carlo methods (Lt)

With these inputs the durations of the sub process's activities were calculated using the developed relationships. In general the operation based relationships are the simplest, the simulated activity times requiring multiplication by the number of times the activity is completed during the production run. The feature based relationships however are slightly more complex, with the relevant features driving the estimate. The relationships developed for each of the activities of the fabric cutting and layup sub process are documented in Table 5-1 . Due to the fact that the novel composite rib post comprises several different sized preforms, the calculation of the fabric cutting and labour time had to include the cutting of the different sized plies making up these

preforms. This was achieved using a modular approach, calculating the time required to cut the plies of each sized preform and then summing these estimates. Due to the identical layups of the preforms it was assumed that the plies from the different preforms were cut simultaneously. This assumption was made in the time estimate by ensuring that the activities relating to the setup of the sub process were only accounted for once for the number of plies cut per day.

Table 5-1. Fabric cutting and lay-up sub process labour time relationships

	Labour time relationships
Fabric collection	$(L_t \cdot ft n) \cdot [n/ppd]$
Unboxing	$(L_t \cdot ft n) \cdot [n/ppd]$
Place on cutting table	$(L_t \cdot ft n) \cdot [n/ppd]$
Unwrap	$(L_t \cdot ft n) \cdot [n/ppd]$
Unravel fabric	$(L_t \cdot ft n) \cdot [n/ppd]$
Check for damage	$(L_t \cdot ft n) \cdot [n/ppd]$
Collect set edge, rules and cutter	$(L_t \cdot ft n) \cdot [n/ppd]$
Place set edge on fabric	$(L_t \cdot ft n) \cdot [n/ppd]$
Place rule to check edge	$L_t \cdot (n [P_{pn}/R_{wpn}])$
Trim fabric edge	$L_t \cdot (n [P_{pn}/R_{wpn}])$
Dispose of trimmed fabric	$L_t \cdot (n [P_{pn}/R_{wpn}])$
Collect template and return set edge	$L_t \cdot (n [P_{pn}/R_{wpn}])$
Place template	$L_t \cdot (n \cdot P_{pn})$
Manually cut ply	$\frac{\left(n \left((P_l (R_{wpn} + 1)) + (P_w \cdot R_{wpn}) \right) \cdot ([P_{pn}, R_{wpn}]) \right)}{Cr}$
Minor unravel	$L_t \cdot (n [pn/R_{wpn}])$
Pack ply	$(L_t \cdot ft n) \cdot [n/ppd]$
Return tools	$(L_t \cdot ft n) \cdot [n/ppd]$
Return fabric to roll	$(L_t \cdot ft n) \cdot [n/ppd]$
Collect and position wrap	$(L_t \cdot ft n) \cdot [n/ppd]$
Re-wrap	$(L_t \cdot ft n) \cdot [n/ppd]$
Collect and prepare box	$(L_t \cdot ft n) \cdot [n/ppd]$
Re-box	$(L_t \cdot ft n) \cdot [n/ppd]$
Return Fabric to storage	$(L_t \cdot ft n) \cdot [n/ppd]$
Lay-up	$L_t \cdot (n \cdot P_{pn})$

NB. The bottomless brackets ($[\]$) indicate the use of the ceiling function. Here the enclosed value is rounded up to the nearest integer, unless an additional value preceded by a comma is present. In this case, unless already a multiple, the initial value is rounded up to the nearest multiple of the second (i.e. $[5,2] = 6$).

5.3.1.2 Robotic tufting sub process

The labour times of the robotic tufting sub process activities are also described using a mixture of operation based and feature based techniques. The Inputs used by the model to estimate the labour time of this sub process include;

- Labour time simulated from measured values with Monte Carlo methods (Lt)
- Component production quantity (n)
- Daily component manufacture capacity (ppd)
- Tufting x axis length (X)
- Tufting y axis length (Y)
- Tuft spacing on x axis (S_x)
- Tuft spacing along seam (S_y)
- Tufting speed (T_{sp})
- Tufting head movement rate (H_{sp})

The relationships developed to estimate the labour time consumed by each manufacturing activity within the sub process are documented in Table 5-2. As in the case of the fabric cutting and lay-up sub process, due to the fact that each of the rectangular preforms constituting the rib post was tufted individually, the complete labour time of the robotic tufting process was estimated by summing the times required to tuft each of the preforms.

Table 5-2. Labour time relationships of the robotic tufting sub process

	Labour time relationship
Stitching head attached to robotic arm	$L_t \cdot [n/ppd]$
Needle and stitching foot calibration	$L_t \cdot (n \cdot 3)$
Needle threaded	$L_t \cdot (n \cdot 3)$
Laminate stack placed in mould	$L_t \cdot n$
Programme chosen and run	$L_t \cdot n$
Movement from home position to tuft row start	$L_t \cdot 5$
Movement from -45° to +45°	$n \cdot L_t \cdot \left(\left(\frac{X}{S_x} \right) + 1 \right)$
Tufting	$2 \cdot n \cdot \left(\frac{Y}{S_y} \right) \cdot \left(\left(\frac{X}{S_x} \right) + 1 \right) + \left(4 \cdot \left(\frac{Y}{S_y} \right) \right) + \left(4 \cdot \left(\frac{X}{S_x} \right) \right)$
Thread cutting	$n \cdot L_t \cdot \left(\left(\frac{X}{S_x} \right) + 1 \right)$
Head movement to tuft row start	$n \cdot \left(\frac{Y}{H_{sp}} \right) \cdot \left(\left(\frac{X}{S_x} \right) + 1 \right)$
Robot returned to home position	$L_t \cdot n$
Set down	$L_t \cdot [n/ppd]$

5.3.1.3 Preform de-moulding sub-process

Based entirely on operation based techniques, the relationships within the cost model estimating the activity times of the preform de-moulding sub process require only the simulated labour times for each activity (L_t) and the component production quantity (n). Again due to the fact that each preform is tufted individually, the sub process is repeated for each of the three preforms. This is accounted for within the cost model by the addition of labour times required to de-mould each preform. The relationships

describing the labour time consumed by each activity within the sub-process is documented in Table 5-3.

Table 5-3. Labour time relationships of the preform de-moulding sub-process

	Labour time relationship
Trim loose fibres/threads	$L_t \cdot n$
Dispose of trimmings	$L_t \cdot n$
Remove foam mould from stitching jig	$L_t \cdot n$
Collect steel rule (de-moulding tool)	$L_t \cdot n$
Place foam mould & packing material on workshop table	$L_t \cdot n$
Preform de-moulding	$L_t \cdot n$
Preform straightening and check	$L_t \cdot n$
Collect hand needle for tuft tidy	$L_t \cdot n$
Tidy tufts & remove flakes of foam	$L_t \cdot n$
Dispose of trimmings, loose fibres and waste	$L_t \cdot n$

5.3.1.4 RTM sub-process

The labour time relationships developed for this sub-process are almost entirely operation based, estimating the sub process labour time with the multiplication of recorded activity times by the frequency the activity is completed within the production run. The exception to this is the relationship developed for the labour time consumed during the filling of the mould. Though the relationship describing the labour time of this activity is seemingly operation based, the labour time is not derived from process recordings but from process simulations (Chapter 4) which consider the processing characteristics of the material derived in Chapter 3, and the various process parameters. The estimate of mould fill time was based on simulation rather than process analyses, allowing for the direct comparison of the labour time consumed by this activity for different materials, i.e. the tufted and non-tufted preforms. This could not be achieved

using the process recordings as within the studied RTM process, different processing parameters were used (i.e. for processing pressures and material permeabilities).

Table 5-4 documents the labour time relationship of each sub process activities completed within the RTM sub process.

Table 5-4. Labour time relationships for the RTM sub-process

	Labour time relationships
Oven switched on, resin defrosted heated to 80°	$L_t \cdot n$
Open tool	$L_t \cdot n$
Place inserts and preform	$L_t \cdot n$
Tool closed	$L_t \cdot n$
Resin port attachments attached to tool	$L_t \cdot n$
Placement of tool rig	$L_t \cdot n$
Resin pipes attached	$L_t \cdot n$
Oil pipes attached to tool oil inlets	$L_t \cdot n$
Thermal couples inserted	$L_t \cdot n$
Leak test (includes switch on RTM machine)	$L_t \cdot n$
Inlet and outlet clamps fitted	$L_t \cdot n$
Oil heaters switched on and program chosen	$L_t \cdot n$
Tool and resin left to heat (1hr with the Al tool)	<i>Not included in labour</i>
Resin temp checked	$L_t \cdot n$
Resin placed in infusion resin chamber	$L_t \cdot n$
De-gas / resin re-heat	$L_t \cdot n$
Infusion (resin from chamber to outlets)	$L_t \cdot n$
Outlet clamping	$L_t \cdot n$
Technician notes	$L_t \cdot n$
Tool ramped up to 180 for cure (pressure on)	$L_t \cdot n$
Pressure released from resin chamber	$L_t \cdot n$
Resin chamber and resin pipes cleaned	$L_t \cdot n$
Oil heaters switched off	$L_t \cdot n$
Tool left to cool overnight	<i>Not included in labour</i>

 5.3.1.5 *Part de-moulding sub-process*

The labour time relationships of this sub process are entirely operation based, requiring the input of the simulated labour time (L_t) and the production quantity (n). These relationships are shown in (Table 5-5).

Table 5-5. Component de-moulding labour time relationships

	Labour time relationships
Removal of thermocouples (2)	$L_t \cdot n$
Removal of inlet clamps	$L_t \cdot n$
Removal of oil pipes	$L_t \cdot n$
Placement of tool rig	$L_t \cdot n$
Removal of outlet clamps	$L_t \cdot n$
Removal of tool bolts (10)	$L_t \cdot n$
Removal and placement of tool top surface	$L_t \cdot n$
Removal of cured resin from flow channel	$L_t \cdot n$
Insertion of part lifting points	$L_t \cdot n$
Attachment of crane	$L_t \cdot n$
Removal of part	$L_t \cdot n$
Removal of excess cured resin	$L_t \cdot n$
Apply release agent to tool bottom, top and inserts	$L_t \cdot n$

 5.3.2 Material

The estimate of material cost within the process cost model was based upon the amount of raw material within the final component and the amount of material scrapped during its manufacture, including consumables. The calculation of the quantity of raw material within the rib post used estimates of the area of fabric (m^2), grams of resin and metres of tufting yarn and noodle roving used. The calculation of the scrapped material used similar estimates, but in addition included estimates of the consumable material

consumption. The consumable materials considered were the closed cell polystyrene stitching foam, mould release and acetone used during tool cleaning.

5.3.2.1 Consumed tuft thread length

The calculation of the quantity of tuft thread used during the manufacture of the novel composite rib post uses a similar algorithm to that used for the time consumed during the tufting process, taking into account vertical perimeter tufting, tuft spacing on the x and y axes of the preform, and the number of tuft rows to establish the length of thread made up by the tuft seams. However this calculation also considers the depth of the preform, the tuft loop length and the tufting angle to determine the length of thread placed through the thickness of the preform, that occupied by the tuft loops, and that attributed to waste.

The tuft thread consumed within the manufacture of each of the novel composite rib post's preforms is given by the following equation:

$$T_{total} = T_{vertex} + T_{structural} + T_{waste}$$

Equation 5-2

Where the total thread length consumed in the tufting of each preform (T_{total}) is the sum of the length of thread used within the perimeter tufting (T_{vertex}), the structural $\pm 45^\circ$ tufting ($T_{structural}$) and the wasted thread length (T_{waste}). The total thread length used within the manufacture of the novel composite rib post could then be determined by summing the T_{total} calculated for the three preforms.

The perimeter tufting thread length was calculated using Equation 5-3.

$$T_{vertex} = (V_{tn} \cdot 2d) + (V_{tn} \cdot 2l_l) + 4X + 4Y$$

Equation 5-3

Where V_{tn} is the number of tufts within the vertex tufting. V_{tn} was calculated as follows;

$$V_{tn} = \left[\left(4 \left(\frac{X}{S_x} + 1 \right) \right) + \left(4 \left(\frac{Y}{S_y} + 1 \right) \right) \right]$$

Equation 5-4

Here the brackets without tops ($\lfloor \]$) represent the floor function, where the value inside the brackets is rounded down to the nearest integer. The division of the tufting axes length by the spacing provides the number of spaces between tufts in that length. This value is increased by one as the number of tufts in the same length is always one greater. Each value is multiplied by 4 to account for the fact that each edge contains two rows of tufts. The terms of these equations relating to the tufting parameters used to manufacture the preform are given in Figure 5-2.

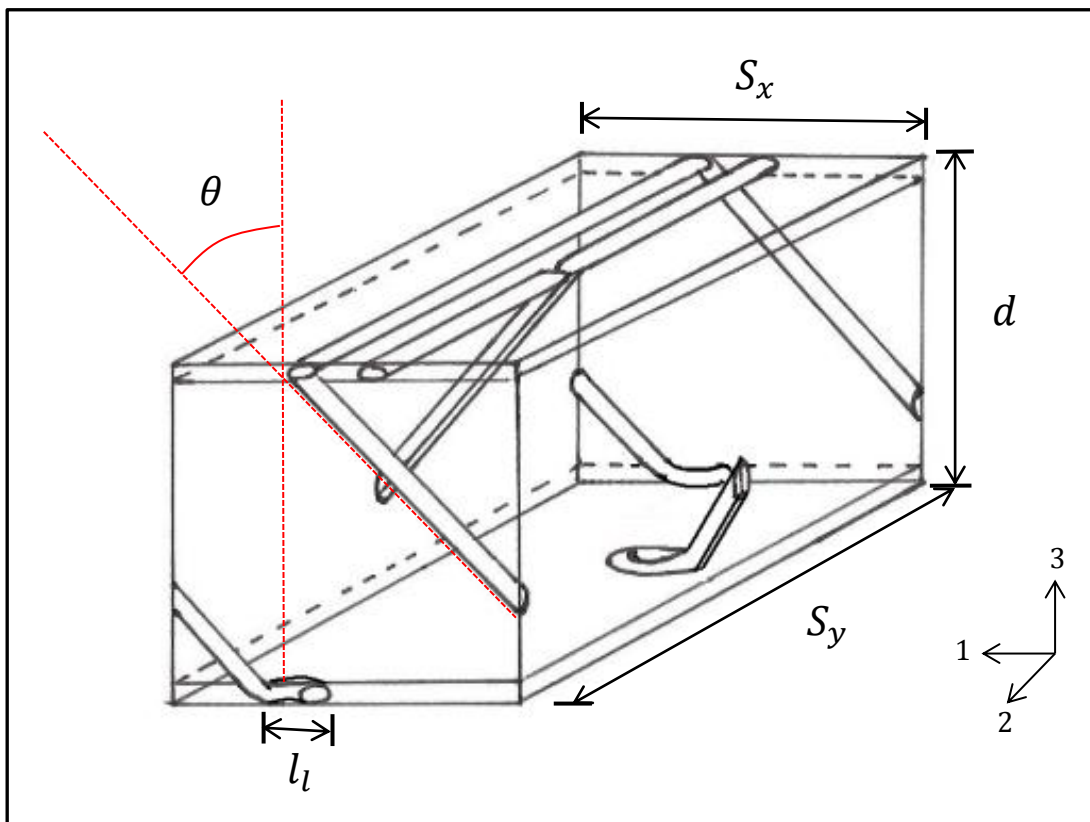


Figure 5-2. Diagram showing the geometrical terms of the idealised unit cell defined for the 4 x 4mm, $\pm 45^\circ$ tufted preform

The structural $\pm 45^\circ$ tuft thread length was calculated using Equation 5-5.

$$T_{structural} = 2 \left(\frac{X}{S_x} + 1 \right) + S_{tn} \left(2 \left(\frac{d}{\cos(45^\circ)} \right) \right) + (S_{tn} \cdot 2l_l)$$

Equation 5-5

Where S_{tn} is the number of structural $\pm 45^\circ$ tufts, calculated using Equation 5-6. Here the function $S_{tn} \left(2 \left(\frac{d}{\cos(45^\circ)} \right) \right)$ provides the length of thread angled at 45° within the preform. Each part of the equation includes a multiplication factor of 2 to account for the length of thread doubling within the geometry of the tuft. This also occurs in the tuft seams described by the first term of the equation, taking place as a result of the method used to produce $\pm 45^\circ$ tufting.

$$S_{tn} = \left[\left(\frac{X}{S_x} + 1 \right) \cdot \left(\frac{Y}{S_y} + 1 \right) \right]$$

Equation 5-6

The tuft thread length wasted within the tufting process resulted from the automated thread cutting process. In order to avoid damaging the preform when cutting the tuft thread, the tufting head was raised to allow a safe distance to cut the tufting thread. Due to this mechanism, an excess of tuft thread, estimated to be 100mm, was left at the end and start of the tuft rows which was subsequently removed. The waste tuft thread length was therefore calculated by multiplying the excess length by the number of tuft rows in each preform (Equation 5-7).

$$T_{waste} = 2 \cdot 100mm \cdot \left(\frac{X}{S_x} + 1 \right)$$

Equation 5-7

The cost of the consumed thread length was calculated by multiplying the length by the cost/m provided by manufacturer (£00.06/m - 04/09/12).

5.3.2.2 Consumed non-crimp fabric

The total quantity of non-crimp fabric consumed during the manufacture of the novel composite rib post was again calculated as the sum of that used within the final component and that scrapped during the process. The amount of fabric used within the rib post was calculated quite simply by summing the areas of the plies cut for each of the three preforms used to produce the rib post, and multiplying this total by the production quantity (Equation 5-8).

$$NCF_{used} = n \left(P_{pn}(A_{P1}) \right) + \left(P_{pn}(A_{P2}) \right) + \left(P_{pn}(A_{P3}) \right)$$

Equation 5-8

The quantity of fabric wasted during the manufacture of each preform is made up by the offcuts created during the ply cutting process, ensuring that each of the ply edges is cut from the fabric rather than relying on the edges of the roll which may be damaged. The algorithm used to calculate the waste generated in the cutting of the plies for each preform is provided in Equation 5-9, the total fabric waste is then calculated by summing the results determined for each of the preforms used in the novel composite rib post.

$$NCF_{waste} = n \left(\left(W_{pr} \left\lfloor \frac{P_{pn}}{R_{wpr}} \right\rfloor \right) + \left(IF \left(\left(\frac{P_{pn}}{R_{wpr}} \right) = \left\lfloor \frac{P_{pn}}{R_{wpr}} \right\rfloor, 0, \left(\frac{W_{pr}}{2} \right) \right) \right) \right. \\ \left. + \left(ETW_{pr} \left\lfloor \frac{P_{pn}}{R_{wpr}} \right\rfloor \right) \right)$$

Equation 5-9

Where W_{pr} is the waste per ply row generated at the two edges of the fabric roll, and ETW_{pr} is the edge trim waste per ply row which ensures the next row of plies is cut from a clean edge. Within this algorithm, the initial term; $W_{pr} \left\lfloor \frac{P_{pn}}{R_{wpn}} \right\rfloor$ calculates the waste generated at the edges of the fabric roll in all of the rows from which the maximum number of plies are cut. The second term; $IF \left(\frac{P_{pn}}{R_{wpn}} = \left\lfloor \frac{P_{pn}}{R_{wpn}} \right\rfloor, 0, \frac{W_{pr}}{2} \right)$ then uses the Excel IF function (IF(logical_test, value_if_true, value_if_false)) to determine if another row from which a lesser number of plies will be cut is required. If it is the case, a fabric waste value of half of the W_{pr} is added. The third term: $ETW_{pr} \left\lfloor \frac{P_{pn}}{R_{wpn}} \right\rfloor$ finally calculates the waste that is generated by trimming the fabric roll width edge, which ensures each of the plies is cut from a clean edge. The locations of the fabric roll width edge and the fabric roll edge are shown in Figure 5-3.

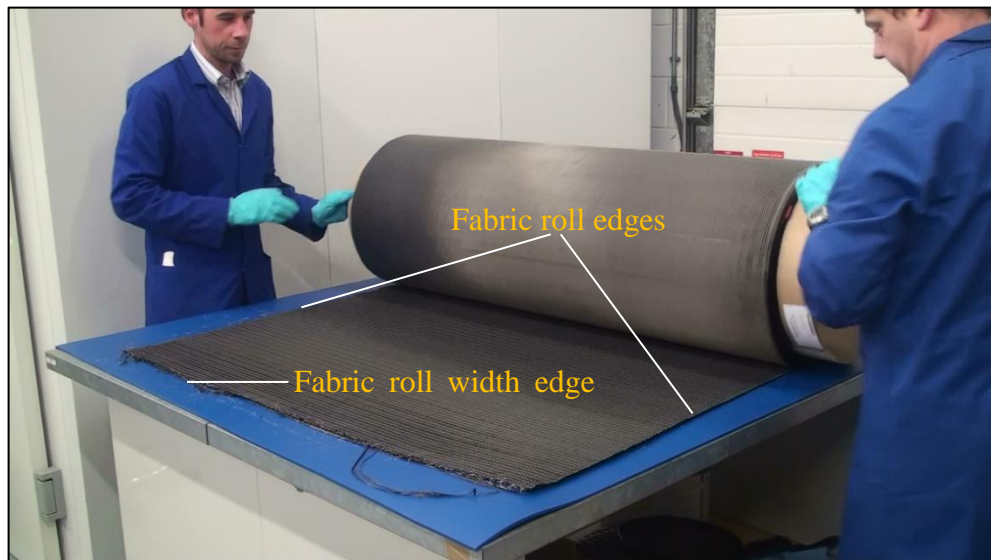


Figure 5-3. The fabric roll edges and roll width edge of the NCF fabric rolls.

The waste per ply row generated at the two edges of the fabric roll (W_{pr}), the term of which is used in Equation 5-9, is calculated using the following algorithm;

$$W_{pr} = P_l \left(R_w - \left(P_w \left[\frac{R_{w2}}{P_w} \right] \right) \right)$$

Equation 5-10

Where R_w is the fabric roll width and R_{w2} is the fabric roll width that can be occupied by plies (disallowing zero wastage). Within this equation, the required R_{w2} term is calculated using the following condition:

$$R_{w2} = IF(W_{pr} = 0, (R_w - P_w), R_w)$$

Equation 5-11

Here the fabric roll width that can be occupied by plies is equal to the fabric roll width minus a single ply width if the waste per ply row is zero. If W_{pr} does not equal zero, the fabric roll width that can be occupied by plies (R_{w2}) is kept equal to the fabric roll width (R_w).

The term ETW_{pr} , used in Equation 5-9 to denote the edge trim waste per ply row, is calculated as shown in Equation 5-12. The fabric roll width is multiplied by a 10mm length of the fabric, an area that removes any damage and fabric disturbance caused by the cutting of the plies in the previous row.

$$ETW_{pr} = R_w \cdot 10mm$$

Equation 5-12

The cost of the material feedstock from which the plies were cut was acquired through contact with the suppliers of the material (Table 5-6).

Table 5-6. NCF fabric cost

Fabric type	0°/90° bi-axial NCF	±45° bi-axial NCF
Manufacturer	Sigmatex	Sigmatex
Specification	V101896-00650-01270- 000000	S32CX010-00414-T1270- 250000
Cost (£/m ²)	<u>18.90 (04/09/12)</u>	<u>13.85 (04/09/12)</u>

5.3.2.3 Noodle roving consumption

The material used to fill the triangular resin rich volume of the T shaped rib post, formed during the placement of the fibre reinforcement into the RTM tool, consisted of carbon roving. The specifications of the roving used, including the cost provided by the manufacturer, are given in Table 5-7.

Table 5-7. Carbon noodle roving specifications

Manufacturer	Toray
Carbon fibre type	T700S
Number of filaments	24000
Fibre density (kg/m ³)	1800
Roving linear density (g/m)	1.6
Cost (£/kg)	18.96 (22/10/12)

Twenty three lengths of the roving were used to create the noodle, providing a fibre volume fraction of approximately 0.6 in the noodle region. The material cost was established using the linear density to quantify the consumption in kg, which was then multiplied by the cost per kg.

5.3.2.4 Resin consumption

The quantity of MVR-444 resin used as the matrix in the manufacture of the rib post was determined with the aid of the process records. In the case of each of the recorded

processes, 700g of resin was measured and placed in the pressure vessel of the RTM machine. This value incorporates the resin waste due to resin pipe and channel filling, and also that within the final component. The unit cost of the resin provided by the manufacturer was £63.53/kg (06/09/12).

5.3.2.5 Consumables

The main consumables considered within the calculation of material costs included the extruded polystyrene stitching foam requiring replacement after each use, the Frekote mould release used to coat the inside of the mould prior to its use and the acetone used to clean the uncured resin from RTM equipment such as the resin pressure chamber and the resin pipes. All other equipment used within the manufacturing process, including resin pipes and tool seals, were assumed to be re-used throughout the production run. The unit costs of the consumables were obtained from communication with their suppliers and manufacturers. These were then multiplied by the volumes used during the production run to determine the total cost. The unit costs of the consumables are provided in Table 5-8.

Table 5-8. Consumable unit costs

Consumable	Cost per unit
Tufting foam	<u>£3.81/m² (17/10/12)</u>
Frekote	<u>£15.85/l (18/10/12)</u>
Acetone	<u>£1.36/l (18/10/12)</u>

5.3.3 RTM tool costs

The RTM tool used for the manufacture of the novel composite rib post consisted of an oil heated, matched aluminium tool with four inserts (Figure 5-4). The tool was purchased from Composite Integration Ltd, costing £5660.00 (06/09/10).



Figure 5-4. The novel composite rib post aluminium RTM tool

5.3.4 Equipment costs

The equipment costs, primarily those of the RTM machine, the tool oil heater, the stitching robot, the oven and the vacuum pump used during the RTM process, were also obtained through contact with the manufacturers of the equipment. These investment costs are given in Table 5-9.

Table 5-9. Equipment investment costs of the novel composite rib post manufacturing process

Equipment piece	Cost (£)
50L lab oven (Genlab Ltd)	<u>£800.00 (19/10/12)</u>
Edwards E1M18 vacuum pump [135]	<u>£2458.00 (03/11/12)</u>
Tool oil heater (Tricool HTF350 48kw)	<u>£11000.00 (01/11/12)</u>
RTM Machine (Composite integration - Ciject one)	<u>£11150.00 (06/12/12)</u>
Stitching robot (KSL KL 502 5m linear axis robot unit)	<u>£216871.29 (10/02/06)</u>

5.3.5 *Energy costs*

The cost of the energy consumed by the equipment during the manufacture of the novel composite rib post and the non-tufted rib post was estimated using calculations of equipment usage time (originating from earlier process analyses) and the documented equipment power ratings (Table 5-10).

Table 5-10. Equipment power ratings and usage times/part

Equipment piece	Power rating (kW)	Usage time/part – Tufted (hrs)	Usage time/part – Non-tufted (hrs)
50L lab oven (Genlab Ltd – MINO/50)	0.75	2	2
Edwards E1M18 vacuum pump [135]	0.55	0.53	0.4
Tool oil heater (Tricool HTF350 48kw)	48	4.4	4.26
RTM Machine (Composite integration - Ciject one)	0.1	2.6	2.46
Tufting robot (KSL KL 502 5m linear axis robot unit)	2.35	1.6	-

The documented power ratings state the maximum energy consumption of each piece of equipment other than the tufting robot. Here the average energy consumption is given.

This value was estimated with the guidance of a technical support engineer from KUKA robotics, the supplier of the robot which forms the KSL 502 robot unit. The energy consumption of the RTM machine was also determined through conversation with the manufacturer, however the consumption values of the remaining pieces of equipment were provided within their documentation.

All of the equipment other than the tool oil heater and the RTM machine were assumed to run at their documented power rating for the duration of their use. Utilising the estimates made by Witik et al [113] and Scelsi et al [136] for the percentage of an autoclave's energy rating used during a curing cycle for guidance, the tool oil heater was assumed to use 60% of the energy rating during its ramping stages and 20% during dwell. The RTM machine was estimated to use 5% of its power rating when idle and 60% when in use. Multiplying the usage time of each piece of equipment by its power rating, the consumed energy in kilowatt hours was estimated. The cost of the consumed energy was calculated using the average UK manufacturing industry purchased electricity price from the first quarter of 2012, stated to be 7.25 pence/kWh [137]. The energy cost/part generated by the manufacturing equipment is provided in Table 5-11.

Table 5-11. Equipment energy costs/part generated during the tufted and non-tufted rib post manufacturing processes.

Equipment piece	Energy cost/part – Tufted (£)	Energy cost/part – Non-tufted (£)
50L lab oven (Genlab Ltd – MINO/50)	0.11	0.11
Edwards E1M18 vacuum pump [135]	0.02	0.02
Tool oil heater (Tricoool HTF350 48kw)	5.80	5.70
RTM Machine (Composite integration - Ciject one)	0.01	0.01
Tufting robot (KSL KL 502 5m linear axis robot unit)	0.28	-

5.4 Tufted and non-tufted novel composite rib post manufacturing cost estimates

The manufacturing cost estimates of these components include two estimates for each component; that assuming the equipment costs to have been amortised prior to the component's manufacture, and that assuming these to be amortised over the production quantity. These estimates have been generated to allow a variety of scenarios to be considered when comparing the costs of the manufacturing processes, particularly the costs of the tufted rib post and the rib post hypothetically manufactured with autoclave processed prepreg. Completing these comparisons, conclusions could be made about the economy of the component were it to be manufactured with an amortised autoclave and how this compared to that of the component manufactured using robotic tufting and RTM. This in turn has allowed a conclusion as to whether it is economically favourable to invest in the equipment required to produce the novel composite rib post rather than use an existing amortised autoclave.

In order to facilitate relative comparison of the component manufacturing costs, the labour rate used within the estimates was held at £50/hour in each case. Mould tool replacement has not been considered within these estimates. The mould tools would be replaced most likely at the same frequency, resulting in no change to the relative manufacturing cost estimates.

5.4.1 Tufted novel composite rib post manufacturing cost estimates

To appreciate the amortisation of various non-recurring costs, such as those arising from equipment and tooling, and to therefore determine the production number at which the component's manufacturing cost per part plateaus due to the recurring costs becoming the cost drivers, a number of cost estimates were made over a range of production quantities. This range includes production numbers of 10, 100, 1000, 10000, and 100000. The total estimated manufacturing cost for the novel tufted composite rib post is shown with the cost per part in Table 5-12. The table also documents the costs per part estimate with equipment costs removed from the calculation. These values provide an understanding of the manufacturing costs generated when using equipment that has been amortised in previous use. In addition, once the estimate excluding equipment costs plateaus at the higher production quantities due to tooling costs becoming insignificant, the estimate provides an additional benchmark for the minimum cost per part when including equipment.

Table 5-12. Total and cost/part manufacturing cost estimates of the tufted novel composite rib post

Production number	10	100	1000	10000	100000
Total Manufacturing cost (£)	251,610	284,574	614,192	3,910,844	36,819,452
SD	40	402	4,349	41,274	396,735
Cost/part (£)	25,161	2,846	614	391	368
SD	4	4	4	4	4
Cost/part – equipment (£)	933	423	372	367	366
SD	4	4	4	4	4

The standard deviations presented in Table 5-12 represent the uncertainty within the cost estimates originating from the uncertainty regarding the measured labour time of the component's manufacturing activities. The standard deviation of the total manufacturing cost was calculated using the Monte Carlo method. This standard deviation is that of the estimated labour cost after 200 iterations of the estimate. In each iteration, a random value between fixed bounds is chosen for each of the manufacturing activity labour times. The summing of the estimated labour cost with the contributors to the total manufacturing cost, which do not have any attributed uncertainty, allows the standard deviation to propagate through to the total manufacturing cost estimate without changing. The standard deviation of the cost per part estimates, both those including and those not including equipment cost, is based on the propagation of the total manufacturing cost standard deviation after it is divided by the production quantity. The total manufacturing cost presented is the sum of the costs of the contributing drivers, including labour, energy, tooling, equipment and material. Due to the uncertainty regarding the measured activity labour times, labour cost was determined as the average of the 200 iterated values of the Monte Carlo simulation.

A break-down of the cost estimates made for each of the considered production quantities is provided in Figure 5-5. Within this histogram the fixed tooling and equipment costs can be seen to remain constant with increasing production quantity, and the recurring costs can be seen to increase as is expected with the two types of manufacturing cost. It is this mechanism which leads to the fixed costs having a near negligible contribution to manufacturing cost per part at very high production volumes, as is shown with the 10,000 and 100,000 part production quantities within the figure.

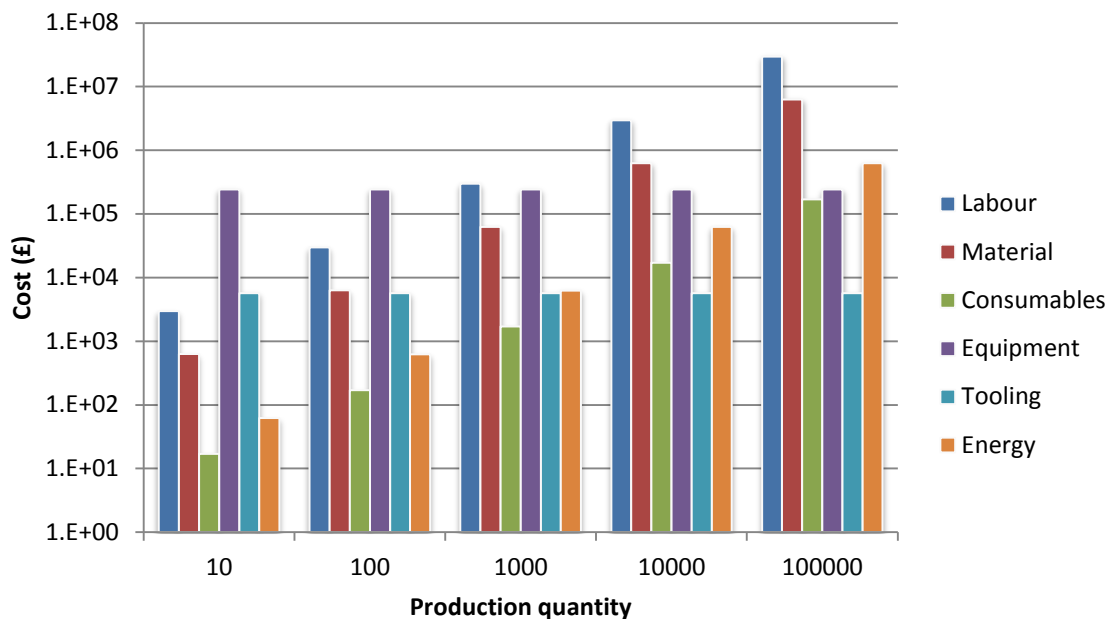


Figure 5-5. A breakdown of the estimated tufted novel composite rib post manufacturing cost

5.4.2 Non-tufted novel composite rib post manufacturing cost estimates

Emulating the estimates provided for the tufted rib post, manufacturing cost estimates were also generated for a non-tufted version.

The nature of the cost model allowed estimates of the non-tufted component to be made by accounting for the changes to the consumed materials and energy, removing various labour sub processes such as tufting and preform de-moulding from the estimate, and providing a measured preform insertion time and modelled mould fill time for the non-

tufted preform in RTM sub-process. In addition the tufting equipment cost was also removed from the equipment cost calculation. The estimated total manufacturing costs of the non-tufted rib post and the estimated costs per part are presented in Table 5-13.

Table 5-13. Total and cost/part manufacturing cost estimates of the non-tufted novel composite rib post

Production number	10	100	1000	10000	100000
Total Manufacturing cost (£)	33,347	53,846	259,204	2,307,147	22,786,846
SD	35	365	3,675	33,904	351,731
Cost/part (£)	3,335	538	259	231	228
SD	3	4	4	3	4
Cost/part – equipment (£)	794	284	234	228	228
SD	3	4	4	3	4

A breakdown of each of the total manufacturing cost estimates for various production quantities is presented in Figure 5-6.

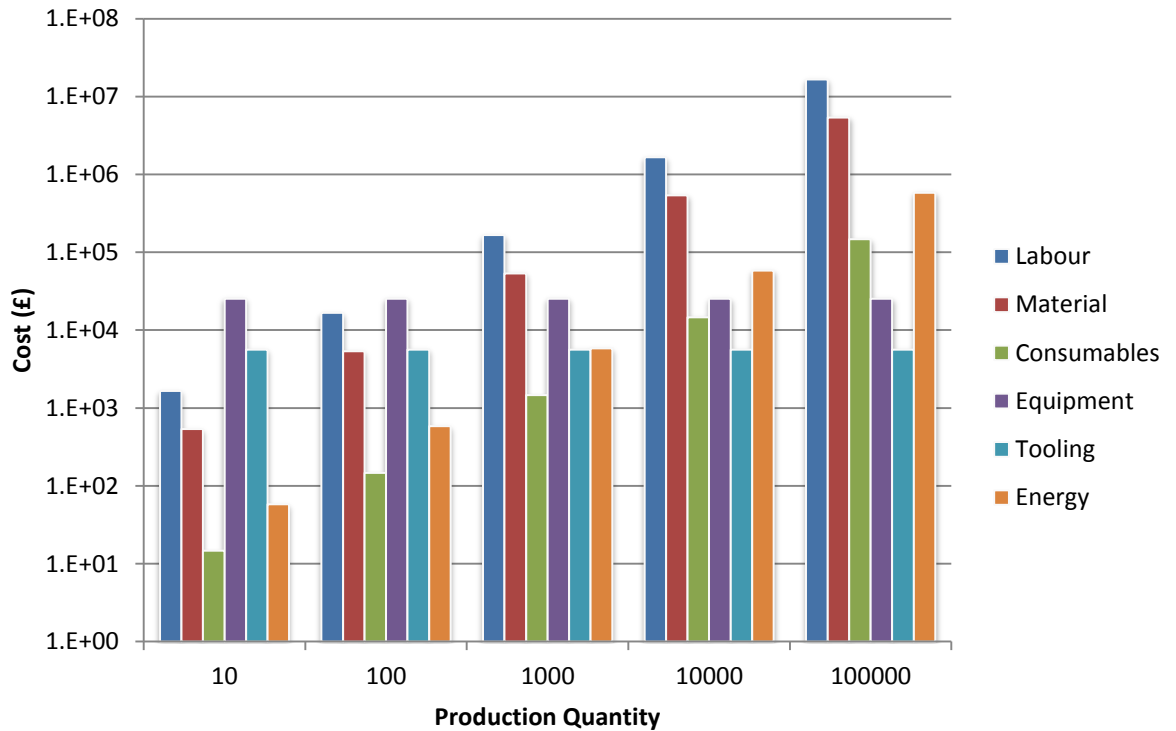


Figure 5-6. A breakdown of the estimated non-tufted novel composite rib post manufacturing cost

Comparing these results with those estimates generated for the tufted rib post, it can be seen that with the exception of tooling, all of the contributing costs are smaller leading to a reduced cost per part at all of the analysed production volumes (Table 5-13). Analysing the costs/part of the non-tufted rib post, it is noticeable that as a result of its lower investment costs, the cost/part inclusive of equipment costs plateaus at its minimum cost at a much lower production volume than the tufted rib post. The tufted composite rib post cost per part stabilises at approximately 100,000 parts, where the non-tufted composite rib post stabilises at its minimum cost per part at a production volume of approximately 10,000 parts. This in turn would make the non-tufted rib post manufacturing process more viable than that of the tufted form at lower production volumes if considering only manufacturing cost, but in order to achieve a more holistic appreciation of the economy of the components, weight and performance must also be considered, as they are in the following chapters.

Taking into account the high production volume targets of Airbus and Boeing for the production of 300 aircraft per year and 2 aircraft per day respectively, as discussed within the introduction of this thesis, and also the number of rib posts (22) within the ALCAS lateral wing pictured at the start of Chapter 3, a production volume of 100,000 parts equates to production runs of approximately eight and three years in the case of the Airbus and Boeing targets respectively. In order to achieve this production rate, more than one set of equipment, tooling and technicians would be required, the total labour requirements estimated by the cost model for the tufted and non-tufted rib post being approximately 212 and 121 working years respectively (taking a working year to be 235 days with day and night shifts equating to 12 hours of production per day). A much more realistic production volume for one set of equipment and tooling when considering the analysed manufacturing process is a production quantity of 1,000, for which the generated cost model estimates the tufted rib post labour requirement to be approximately two working years (6,096 hours), and the non-tufted rib post labour requirement to be approximately one year (taking 2820 $((52 \times 5 - 25) \times 12)$ to be the number of working hours in 1 year).

At a production volume of 1000 parts the cost/part of the tufted composite rib post is £355±6 greater than that of the non-tufted rib post, indicating the cost of adding tufting to the rib post structure. However, if the additional equipment required to perform the tufting process is assumed to have been amortised previously, the additional cost of the tufted composite rib post is reduced to £138 ±6.

Using the commercial cost model SEER-DFM, the manufacturing cost estimates made for the tufted and non-tufted composite rib posts, manufactured within a research and development environment, were extrapolated for more industrial oriented production. This was completed using SEER-DFM's labour estimates, for several labour time

drivers within the manufacture of the composite rib post in place of the same estimates made with the manufacturing cost model generated within this project. The labour time drivers included ply cutting, layup, part removal from the RTM tool and the tool cleaning. The entire manufacturing process was not modelled in SEER-DFM for two reasons, the first being that the commercial model does not have the facility to model all aspects of the different processes, and secondly, in the case of the RTM, it does not consider the processing characteristics of the material.

In the case of the tufted composite rib post, the labour time estimates of SEER-DFM were summed with those of the generated model for the robotic tufting, preform demoulding and component RTM sub processes. For the non-tufted rib post, the SEER-DFM estimates were summed with just that of the component RTM sub process. The manufacturing costs per part generated with the extrapolated labour times, for a production volume of 1000 parts, are shown in Table 5-14.

Table 5-14. Industrial manufacturing cost/part estimates for the tufted and non-tufted composite rib posts with a production volume of 1000 parts.

Component	Tufted rib post	Non-tufted rib post
Cost/part (£)	592	232
SD	3	2
Cost/part – equipment (£)	349	207
SD	3	2

Manufacturing cost breakdowns for the tufted rib post industrial manufacturing cost extrapolation and the non-tufted rib post industrial manufacturing cost extrapolation are given in Figure 5-7 and Figure 5-8 respectively.

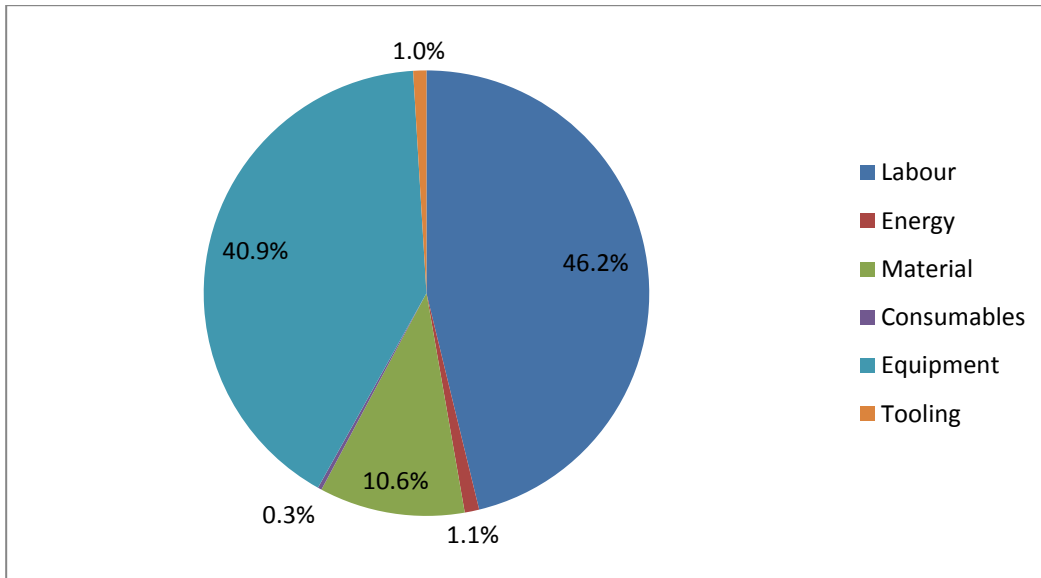


Figure 5-7. SEER-DFM industrial extrapolation of tufted rib post MFG cost for 1000 parts

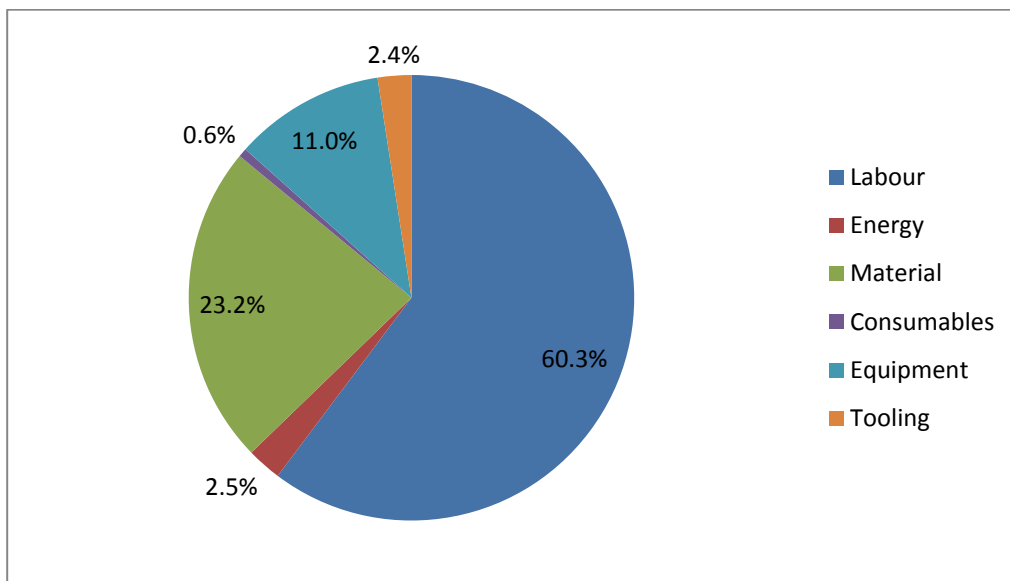


Figure 5-8. SEER-DFM industrial extrapolation of non-tufted rib post MFG cost for 100 parts

With the industrially extrapolated manufacturing cost estimates made with the additional use of SEER-DFM, the cost per part attributed to the addition of the tufts is $£360 \pm 3$ assuming a production quantity of 1000 parts. If equipment costs are assumed to have been amortised, the additional cost becomes $£143 \pm 3$.

The cost modelling completed within this project has consisted of the formation of a manufacturing cost model for the analysed tufted composite rib post, capable of also

generating estimates for a non-tufted version of the component. The model has used algorithms developed to describe the time consumption of each of the manufacturing activities and their material consumption, multiplying the estimated values by the appropriate rates to determine labour, energy and material costs. These estimates have been combined with documented tooling and equipment costs to generate total manufacturing cost estimates. In addition, uncertainty has been modelled using the Monte Carlo method and the commercial cost model SEER-DFM has been implemented to facilitate estimates of a more industrialised version of the developmental manufacturing process analysed.

In summary of the main findings of the cost modelling, the industrially extrapolated manufacturing cost estimates have been shown to be within the error of the manufacturing costs of the developmental process, indicating that the considered techniques do not differ greatly within a more commercial environment. These estimates indicate that when considering arguably the most realistic approximate production quantity of 1000 parts, the manufacturing cost/part of the tufted rib post is $£592 \pm 3$, $£360 \pm 3$ greater than that of the non-tufted component. When considering equipment costs to have been previously amortised the manufacturing cost/part of the tufted rib post is reduced to $£349 \pm 3$ and that of the non-tufted component is reduced to $£207 \pm 3$. In subsequent chapters, the cost increase associated with the tufting process is weighed against its potential benefits with regard to the component's performance and weight over a hypothetical alternative material for the rib post component.

Chapter 6. Structural modelling of the composite rib post component

The structural modelling carried out within this project served to determine the relative performance of the tufted composite material within the wing rib post application of the NGCW project compared with a non-tufted composite consisting of the same fabric, lay-up and resin, and an equivalent prepreg laminate made with the same lay-up and fibre volume fraction (64%) as the tufted composite. Resulting from the available data with which the modelling was completed, performance is considered in terms of the maximum experienced strain during pure pull-off test simulations. These simulations emulate physical tests completed during the component's testing program to determine the strength and stiffness of the structure's noodle region, and its delamination behaviour in a pure failure state.

6.1 Estimation of elastic properties

The complex geometry of the tufted composite's fibre reinforcement has led to the assumption of homogenous material properties within the completed structural modelling. Due to the absence of validated mechanical property data, this strategy required the elastic properties of the material to be estimated. Specifically, these properties consisted of the elastic moduli, the shear moduli and the Poisson's ratios. Modelling the elastic properties, the maximum strains experienced by the investigated component could be estimated and subsequently compared to those generated by different composite materials.

Rules of mixtures calculations can be used to estimate the required elastic properties of the composite materials, deriving them from the elastic properties of their constituent

materials. Equation 6-1 and Equation 6-2 show the well-known rules of mixture for the longitudinal and transverse tensile moduli of a composite respectively [138].

$$E_{\parallel} = \eta_0 E_f V_f + E_m V_m$$

Equation 6-1

$$\frac{1}{E_{\perp}} = \frac{V_f}{E_f} + \frac{1 - V_f}{E_m}$$

Equation 6-2

Different forms of the rules of mixtures can be used for the various shear moduli and Poisson's ratios, however, the rules of mixtures can involve assumptions that lessen their accuracy. The rule of mixtures for the longitudinal tensile modulus for example assumes the fibre length distribution factor to be 1 corresponding to continuous fibres. Despite this, the rule of mixtures for the longitudinal tensile modulus fits well with experimental data [138], however, the rule of mixtures for the transverse tensile modulus is less accurate. The assumptions made by the rule of mixtures for the transverse tensile modulus are that there is perfect bonding between the fibre and the matrix, the effects of Poisson's contractions are negligible and also that all fibres within the composite are uni-directional. The primary cause of its lesser accuracy is the assumption that the stress distribution in the transverse plane is uniform, an assumption that is more accurate in the longitudinal case. Realistically, in transverse tension where the force is applied normal to the alignment of the fibres, the distribution is inhomogeneous in the transverse plane, leading to non-linear behaviour [138].

To account for the inconsistencies of the rules of mixtures, the National Physics Laboratory (NPL) has carried out extensive tests to establish correlation factors with which corrections to the rules can be made. These correlation factors are implemented in the component design and analysis program (CoDA) [139] developed by NPL.

Consequently the material property estimates of CoDA are considered to be more reliable than those produced by the rules of mixtures alone.

CoDA has therefore been used in this work to aid estimates of the elastic properties. With the input of the fibre, resin and lay-up data, it was possible to synthesize the elastic properties of the non-tufted composite and the prepreg laminate. Using the fibre related terms of the rule of mixtures for longitudinal tensile modulus, the synthesized properties of the non-tufted composite could then be adjusted to account for the additional fibre volume fraction of the tuft thread within the tufted composite.

6.1.1 Non-tufted composite elastic properties

The elastic properties of the non-tufted composite were synthesised by CoDA, using details of the laminate's average fibre volume fraction (determined in Chapter 3 (Table 3-9)), lay-up and constituent material elastic properties. As mentioned previously, the lay-up of the non-tufted preform was the same as that of the tufted preform, consisting of 8 layers of bi-axial carbon NCF fabric laid in $[\pm 45, 0/90]_{2s}$. Details of the NCF fabrics are given in Table 3-2. As a result of CoDA's limitation in synthesizing properties for unidirectional (UD) fibre plies, it was necessary to model the lay-up of bi-axial plies as individual plies of UD fabric. The ply thickness, required by CoDA, was determined as an average, dividing the composite thickness by the number of plies within the laminate. For the individual UD plies modelled in CoDA, this was calculated to be 0.25mm.

The elastic properties of the Toray T700 50C carbon fibre composing the plies of the non-tufted composite, other than the tensile modulus, were modelled as those defined by CoDA for the standard carbon fibre within the software's database (Table 6-1) resulting from the lack of manufacturing data for these properties. The longitudinal tensile modulus of the Toray T700 50C carbon fibre [78] provided by the manufacturer

was the same as that of CoDA's standard carbon fibre, and thus the fibres were assumed to be the same.

Table 6-1. The elastic properties and density of Toray T700 50C carbon fibre [139].

Property	
E₁ (GPa)	230.0±0.1
E₂ (GPa)	20.9±0.1
G₁₂ (GPa)	27.6±0.1
ν₁₂	0.2±0.005
ρ (kg/m³)	1800

The elastic modulus and Poisson's ratio of the MVR-444 epoxy resin used within the composite were modelled in CoDA as those defined by the manufacturer [111] (Table 6-2).

Table 6-2. The elastic properties and density of Advanced Composites Group's MVR-444 epoxy resin [111]

Property	
E (GPa)	3.1±0.1
ν	0.35±0.005
ρ (kg/m³)	1140

Using this information, the elastic properties of the non-tufted composite documented were synthesised (Table 6-3).

Table 6-3. The elastic properties of the non-tufted composite synthesised in CoDA at 0.60 V_f

Elastic Property	
E_1 (GPa)	49.8±0.1
E_2 (GPa)	49.8±0.1
E_3 (GPa)	8.2±0.1
G_{12} (GPa)	18.9±0.1
G_{13} (GPa)	3.2±0.1
G_{23} (GPa)	3.2±0.1
ν_{12}	0.32±0.005
ν_{13}	0.22±0.005
ν_{23}	0.22±0.005
ν_{21}	0.32±0.005
ν_{31}	0.04±0.005
ν_{32}	0.04±0.005

6.1.2 Tufted composite elastic properties

The elastic properties of the tufted composite were estimated adapting those of the non-tufted laminate. This route was used as both composites contained the same initial fabric lay-up. The estimation of the elastic moduli consisted of the addition of the stiffness provided by the tuft thread, in the various principal directions, to the corresponding elastic moduli of the non-tufted composite. As a result of the tufted composite containing a higher global fibre volume fraction than the non-tufted composite due to the addition of the tuft thread, the adaptation also required the reduced contribution of the resin to be accounted for. In the case of the through-thickness elastic modulus, due to the dominance of the resin, this property of the non-tufted composite was recalculated using CoDA to model the non-tufted composite with a fibre volume fraction of 0.64, the average measured fibre volume fraction of the tufted composite (Table 3-9). The synthesised through-thickness elastic modulus was subsequently added to the contribution of the tuft thread. To account for the effect of the tufted composite's reduced resin content on its in-plane elastic moduli, the proportion of the

elastic modulus of the resin replaced by the increased fibre content was subtracted from the non-tufted composite's synthesised in-plane moduli. The shear moduli and Poisson's ratios used for the tufted material were estimated to be the same as those used for the non-tufted composite.

In the calculation of the tufted composite's elastic properties, the assumption is made that the addition of tufting has only an enhancing effect, differing somewhat from published findings for the in-plane moduli of tufted composites suggesting that this property is un-affected by the process [58], however, this did not raise concern as the purpose of these estimates was not to characterise the tufted material, but provide data for the structural model, which showed little sensitivity to these properties. The positive effect of the tufts on the through-thickness elastic modulus does, however, agree with literature [58] and is therefore assumed to be more representative than the estimates of the in-plane elastic moduli.

The additional stiffness provided by the tuft thread in the principal directions was determined by calculating the longitudinal tensile moduli of each of the components of the tuft (including the tuft seam, the through-thickness portion and the tuft loops, defined earlier in Figure 3-5 in each of the principal directions. This consisted of multiplying the volume fractions of the tuft components by the longitudinal elastic moduli of the thread material, and an orientation factor, correcting the elastic modulus according to the angle at which the thread is oriented in the principal direction.

6.1.2.1 Tuft component volume fraction estimation

To establish the volume fractions and orientations of each of the geometries formed by the tuft thread, an idealised unit cell of the tufted composite was formed. As described earlier, the tufted preform material consists of a lay-up of carbon NCF ($[\pm 45^\circ, 0^\circ/90^\circ]_{2s}$), tufted with a carbon thread. The tufting within the preforms consists of a square

arrangement of tufts, spaced $4 \times 4\text{mm}$ and angled at $\pm 45^\circ$. Perimeter tufting was also used during the manufacture of the preform, but due to its small proportion compared to the structural tufting and its incompatibility with consideration within a unit cell, it was assumed to have an insignificant influence over the preform material component volume fractions.

The idealised unit cell of the tufted composite produced by this tuft arrangement is presented in Figure 6-1.

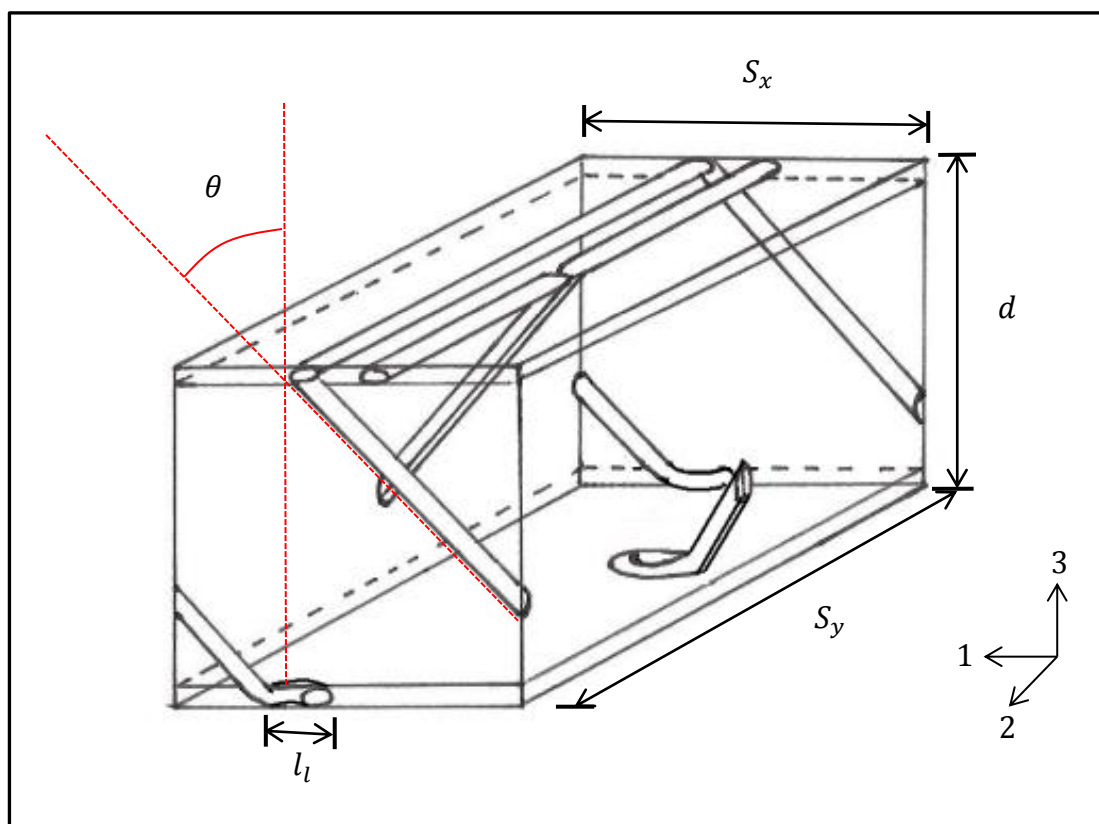


Figure 6-1. The idealised unit cell defined for the $4 \times 4\text{mm}$, $\pm 45^\circ$ tufted preform

In Figure 6-1, using similar notation to Treiber [58], l_l is $6 \pm 1\text{mm}$, S_y is 8mm , S_x is 4mm , d is 4mm , and θ is 45° .

In this unit cell it is assumed that each of the components of the tuft remain undistorted within the fabric lay-up. The assumption is also made that the length of the thread within each tuft loop is twice that of the loop length.

The volume fraction of the composite occupied by the tuft seams ($V_{f\ seams}$) was calculated using the following equation:

$$V_{f\ seams} = \frac{2}{S_x \cdot d} \cdot \frac{T}{\rho_f}$$

Equation 6-3

Here the division of the thread's linear density by the fibre density provides the thread's cross sectional area [58].

The volume fraction of the through-thickness portion of the tufts ($V_{f\ tufts}$) was calculated as shown below:

$$V_{f\ tufts} = \frac{4 \left(\frac{d}{\cos \theta} \right)}{S_y \cdot S_x \cdot d} \cdot \frac{T}{\rho_f}$$

Equation 6-4

The volume fraction occupied by the final tuft component, the tuft loops, was determined using Equation 6-5;

$$V_{f\ loops} = \frac{4l_l}{S_y \cdot S_x \cdot d} \cdot \frac{T}{\rho_f}$$

Equation 6-5

Using the linear thread density provided by the manufacturer (Table 3-3), the measured loop length (6 ± 1 mm) and the HTA40 carbon fibre density provided by the manufacturer (1780kg/m^3) [79], the tuft component volume fractions summarised in Table 6-4 were calculated.

Table 6-4. The volume fractions of the various tuft components within the tufted composite

Tuft component	Volume fraction
Tuft seams	0.01
Tuft	0.01
Tuft loops	0.02±0.003
Tuft thread (total)	0.04±0.003

Note that these volume fractions are validated by the fact that their sum is equal to the difference between the fibre volume fractions of the tufted and non-tufted composites, established in Chapter 3.

6.1.2.2 Tufted composite elastic moduli estimation

Within the defined unit cell of the tufted preform (Figure 6-1), in the principal directions, fibre is either aligned parallel, 90° or 45° to the relevant direction or, as is assumed for the tuft loops in 1 and 2 directions, randomly aligned. The orientation factors used to correct the elastic moduli provided by the tuft thread in the principal directions consist of the orientation factors that are normally used in conjunction with the rule of mixtures calculation of longitudinal tensile modulus. These orientation factors originate from laminate analysis, being $\cos^4\theta$, and are noted in Table 6-5.

Table 6-5. Fibre angle orientation factors [138]

Fibre angle	Orientation factor (η_o)
0°	1
±45°	0.25
90°	0
Random in-plane	0.375

As well as the orientation factors of the tuft components, their volume fractions, the elastic moduli of the non-tufted composite and the longitudinal elastic modulus of the tuft thread (Table 6-6) and the resin (Table 6-2), it was also necessary to calculate the

volume fraction of the resin replaced by fibre within the tufted composite. This allowed the reduced contribution of the resin to the in-plane elastic moduli of the tufted composite to be estimated.

Table 6-6. The longitudinal elastic modulus and density of the tuft thread of the tufted composite (Tenax carbon thread - HTA 40)

Property	
Elastic modulus (GPa)	195 ± 9 [58]
ρ (kg/m³)	1780 [58]

The volume fraction of the resin replaced by fibre within the tufted composite (V_{frr}) compared to the non-tufted composite was estimated to be equal to the total volume fraction of the tuft thread (Table 6-4). Using these data the elastic moduli of the tufted composite in the 1st and 2nd principal directions were calculated using Equation 6-6.

Here the in-plane elastic moduli of the tufted composite are taken as the sum of the elastic moduli of the tuft components, accounting for orientation and volume fraction, and the elastic moduli of the non-tufted composite in the principal directions, minus the elastic modulus contributed by the resin volume that is occupied by the increased fibre content.

$$E_i = \left(\sum_j E_{fj} \cdot V_{fj} \cdot \eta_{oji} \right) + E_{non-tufted\ i} - E_m \cdot V_{frr}$$

Equation 6-6

The elastic modulus of the tufted composite in the 3rd principal direction was estimated, as discussed, with the sum of the elastic modulus synthesised by CoDA for the non-tufted composite with a fibre volume fraction equal to that of the tufted composite, and the elastic modulus contribution of the tuft. The through-thickness elastic modulus synthesised by CoDA is given in Table 6-7.

Table 6-7. The CoDA synthesised E_3 of the non-tufted composite at $0.64 V_f$

Material	E_3 (GPa)
Non-tufted laminate at $0.64V_f$	8.8 ± 0.1

The through-thickness elastic modulus of the tufted composite was therefore calculated using

$$E_3 = E_{3 \text{ non-tufted } 0.64V_f} + (E_{\text{thread}} V_{\text{tuft}} \eta_{\text{lo tuft}})$$

Equation 6-7

In direction 1 defined by Figure 6-1, the orientation factors noted in Table 6-8 are assumed for various components of the tuft.

Table 6-8. The orientation factors assumed for the components of the tuft in direction 1

Tuft component	Orientation factor (η_o)
Tuft seams	0
Tuft	0.25
Tuft loops	0.375

The in plane elastic modulus of the composite is therefore:

$$E_1 = (195GPa \times 0.01 \times 0.25) + (195GPa \times 0.02 \times 0.375) + (195GPa \times 0.01 \times 0) \\ + (49.8GPa - (3.1GPa \times 0.04))$$

$$\therefore E_1 = 52 \pm 0.1 GPa$$

Equation 6-8

In direction 2 defined by Figure 6-1, the orientation factors noted in Table 6-9 are assumed for the various components of the tuft.

Table 6-9. The orientation factors assumed for the fibre components of the composite in direction 2

Tuft component	Orientation factor (η_o)
Tuft seams	1
Tuft	0
Tuft loops	0.375

The elastic modulus of the composite in the 2 direction was calculated as follows:

$$E_2 = (195GPa \times 0.01 \times 0) + (195GPa \times 0.02 \times 0.375) + (195GPa \times 0.01 \times 1) + (49.8GPa - (3.1GPa \times 0.04))$$

$$\therefore E_2 = 53 \pm 0.1 GPa$$

Equation 6-9

The only fibre component of the tufted composite aligned in the 3 direction (Figure 6-1), is the tuft itself. Due to the $\pm 45^\circ$ pitch angle of the tufts, the 0.25 orientation factor noted in Table 6-5 was assumed for this fibre component.

The elastic modulus of the composite in the 3 direction was calculated as shown in Equation 6-10;

$$E_3 = 8.8GPa + (195GPa \times 0.01 \times 0.25)$$

$$\therefore E_3 = 9 \pm 0.1 GPa$$

Equation 6-10

As indicated previously, the shear moduli and Poisson's ratios used for the structural analysis were estimated using CoDA. The same values were used for the tufted composite due to the model's insensitivity to these elastic properties. The estimated elastic properties of the tufted composite are summarised in Table 6-10.

Table 6-10. The estimated elastic properties of the 4 x 4mm, 45° tufted composite

Elastic Property	
E₁ (GPa)	52±0.1
E₂ (GPa)	53±0.1
E₃ (GPa)	9±0.1
G₁₂ (GPa)	18.9±0.1
G₁₃ (GPa)	3.2±0.1
G₂₃ (GPa)	3.2±0.1
v₁₂	0.32±0.005
v₁₃	0.22±0.005
v₂₃	0.22±0.005
v₂₁	0.32±0.005
v₃₁	0.04±0.005
v₃₂	0.04±0.005

6.1.3 Carbon fibre/epoxy prepreg elastic property estimation

The elastic properties of the comparative pre-preg component were estimated using the CoDA database for a carbon/epoxy composite with continuous, aligned fibres, and the same fibre volume fraction and lay-up as the tufted composite. The lay-up was synthesised in CoDA by layering individual uni-directional plies (bi-axial plies could not be modelled due to the limitations of the programme). To enable a comparison of the performance (and subsequently costs) arising from the chosen manufacturing techniques rather than the constituent materials themselves, the same fibre and matrix properties as those of the tufted composite were used in the synthesis of the prepreg composite. These properties consisted of the carbon fibre properties documented in Table 6-1, and the epoxy resin properties documented in Table 6-2.

The synthesised elastic properties of the prepreg composite are presented in Table 6-11.

Table 6-11. The CoDA estimated elastic properties of the quasi-isotropic prepreg composite

Elastic property	
E₁ (GPa)	53.2±0.1
E₂ (GPa)	53.2±0.1
E₃ (GPa)	8.8±0.1
G₁₂ (GPa)	20.2±0.1
G₁₃ (GPa)	3.5±0.1
G₂₃ (GPa)	3.5±0.1
v₁₂	0.31±0.005
v₁₃	0.22±0.005
v₂₃	0.22±0.005
v₂₁	0.31±0.005
v₃₁	0.04±0.005
v₃₂	0.04±0.005

6.1.4 Noodle elastic property estimation

In order to successfully model the composite rib post structurally, it was also necessary to estimate the elastic properties of the noodle material used to fill the triangular resin rich region formed in the T shaped component, where the web and the flanges meet. In each of the modelled cases, the noodle material was assumed to take the form of a uni-directional carbon roving with an epoxy matrix, its fibre volume fraction being estimated to be 60%. The elastic properties of this material were again estimated using CoDA with the fibre and matrix properties in Table 6-1 and Table 6-2. The synthesised properties are noted in Table 6-12.

Table 6-12. The CoDA synthesised elastic properties of the noodle materials

Elastic property	Composite noodle properties
E₁ (GPa)	132.3±0.1
E₂ (GPa)	7.8±0.1
E₃ (GPa)	7.8±0.1
G₁₂ (GPa)	3.9±0.1
G₁₃(GPa)	3.8±0.1
G₂₃(GPa)	2.7±0.1
v₁₂	0.31±0.005
v₁₃	0.31±0.005
v₂₃	0.25±0.005
v₂₁	0.02±0.005
v₃₁	0.02±0.005
v₃₂	0.25±0.005

6.2 Rib post numerical model

As has been discussed in Chapter 3, the in-service loading of the wing rib post includes a pull-off and shear load. To understand the performance of the component in this loading scenario, a variety of pure and mixed loading tests have been completed within the NGCW project. The numerical modelling completed within this work reproduces pull-off tests carried out to examine the through-thickness strength and stiffness of the component.

The geometric model created for the numerical modelling was therefore based upon the test specimens manufactured for the pull-off tests. Figure 6-2 shows a diagram of the cross section of a pull-off test specimen within test fixtures. The geometry and dimensions of the model created in Solidworks [140] and used for simulation can be seen in Figure 6-3.

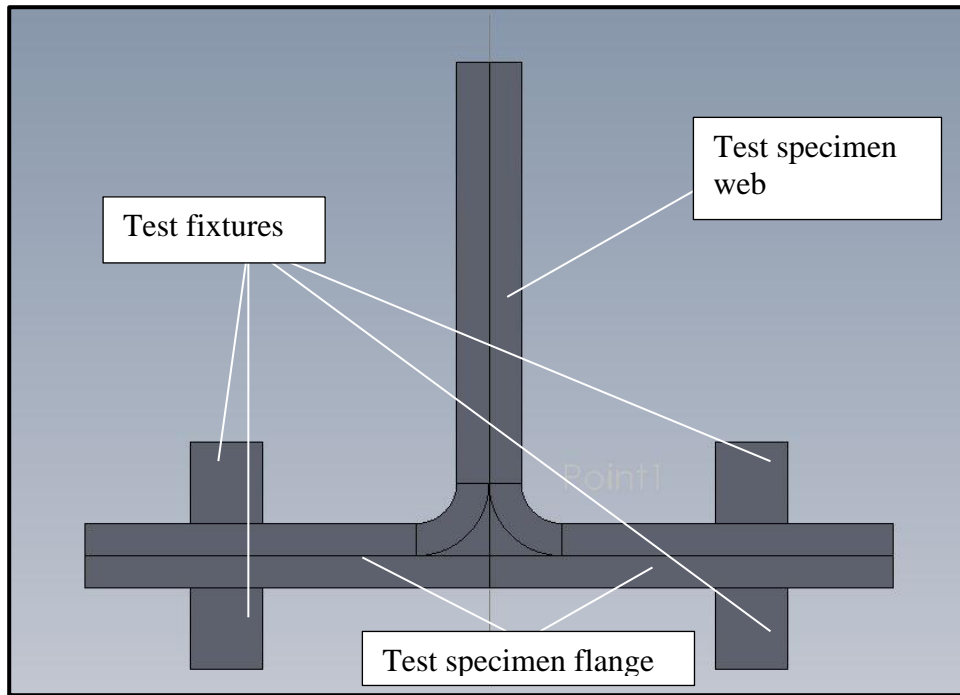


Figure 6-2. A cross section of a pull-off test specimen with test fixtures

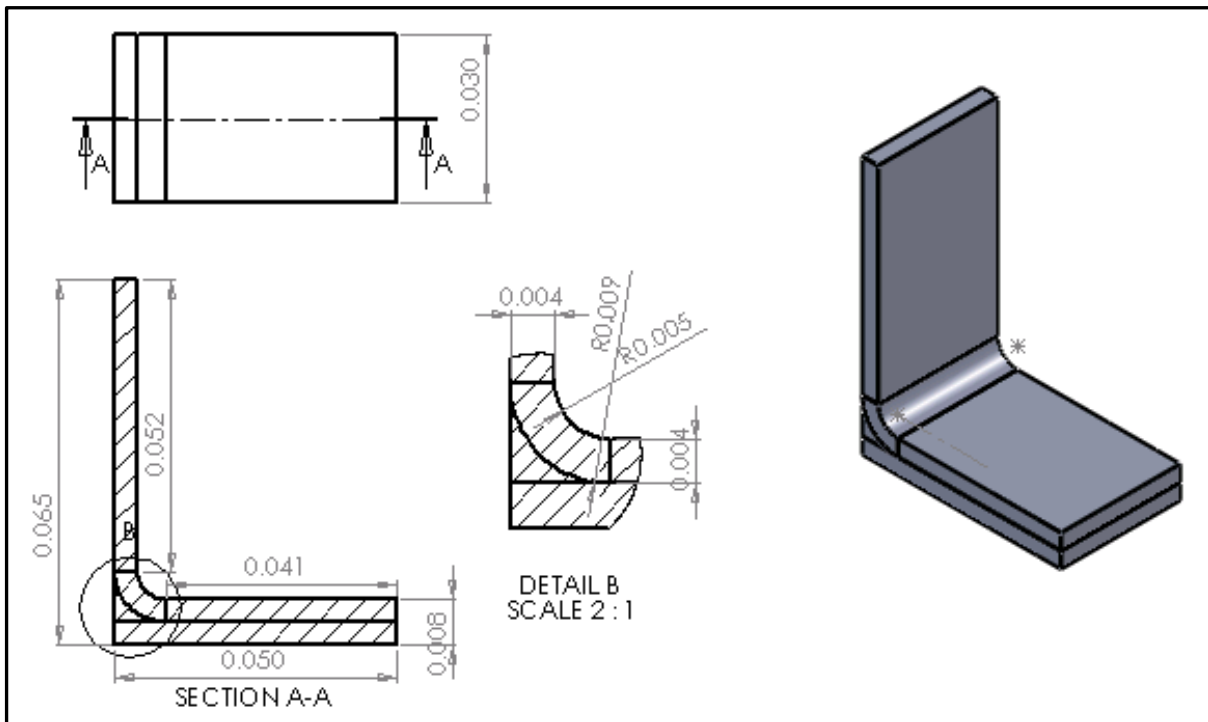


Figure 6-3. The dimensions of the pull-off test specimen model, dimensions in metres (m)

As a result of its symmetric nature, it was possible to model half of the test specimen, applying a boundary condition of symmetry to the face indicated in Figure 6-4. This results in a reduction of computational time.

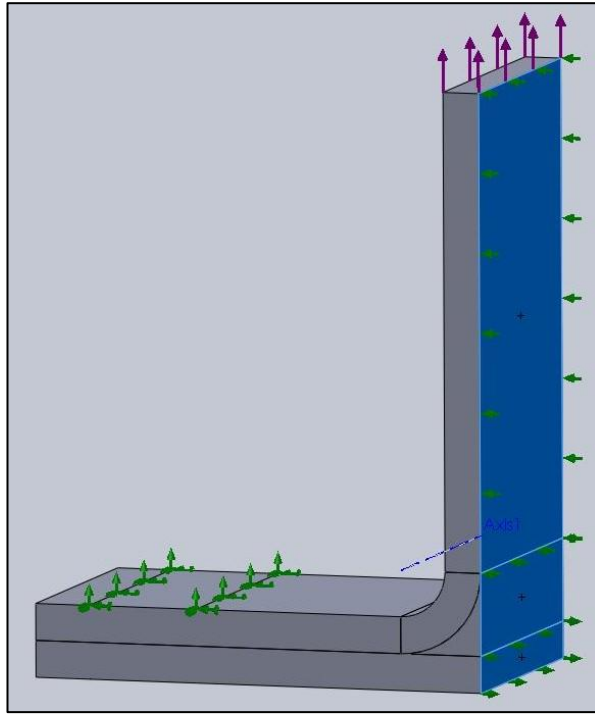


Figure 6-4. An image the model face selected for the condition of symmetry, the face is highlighted in blue

A fixed boundary condition was also applied to a section of the upper face of the rib post's flange, emulating the fixtures of the pull-off test arrangement. The dimensions and distance of this boundary from the start of the component's radius are documented in Figure 6-5.

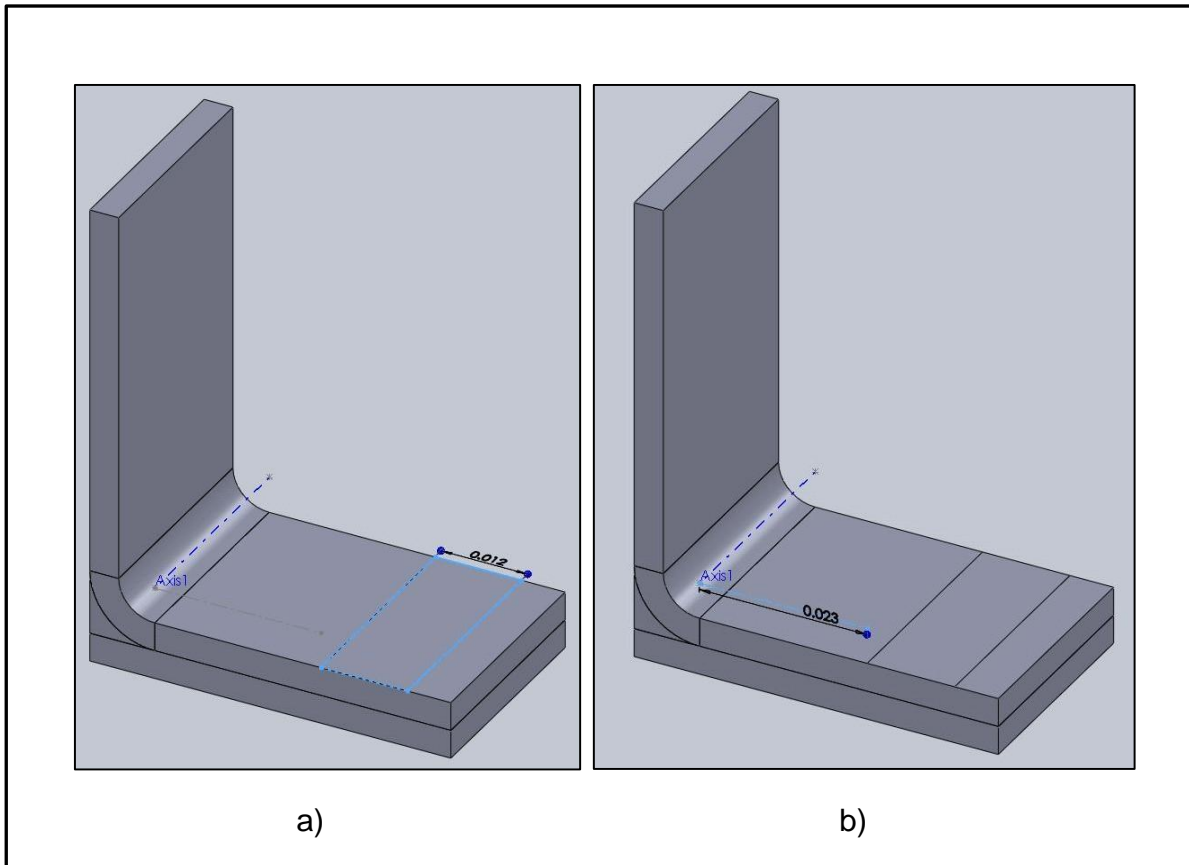


Figure 6-5. Schematic showing; a) the dimensions (0.012x0.03m) of the fixed boundary and b) the distance (0.023m) of the fixed boundary from the component's radius

The simulated pull-off load was determined by scaling down the in-service pull-off load for the 30mm long test piece. The service load for a 185mm long component is 2140 N. The load applied to the model was therefore calculated to be 347N. This load was applied normal to the upper surface of the web, as shown in Figure 6-6.

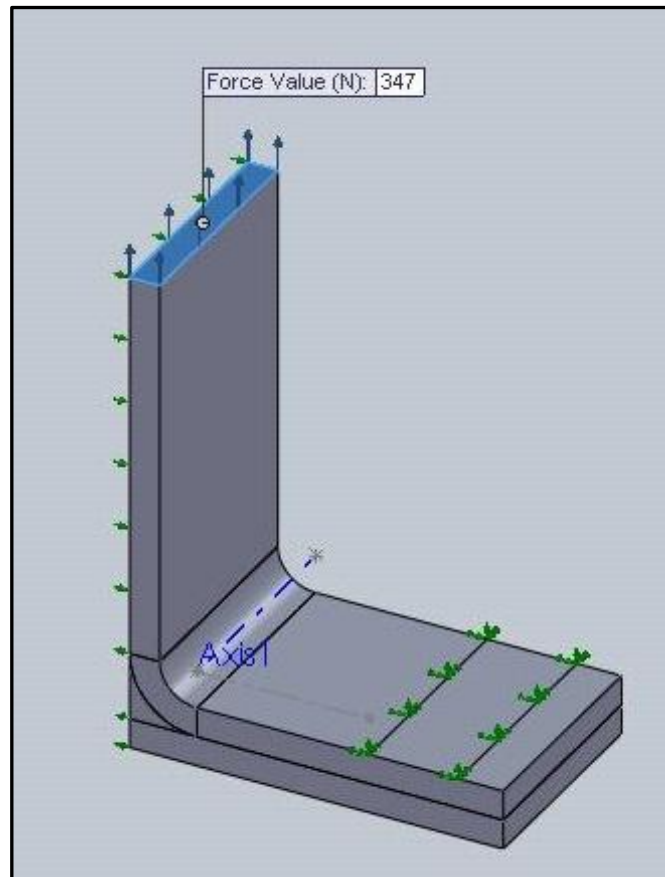


Figure 6-6. An illustration of the load application normal to the upper surface of the test element web, the upper surface of the specimen is highlighted in blue

In the absence of empirical interlaminar property data for the tufted composite studied, the composite materials were modelled homogeneously rather than on a ply by ply basis. Although this method did not permit a failure analysis and subsequently an appreciation of the effect of tufting on failure, an analysis of the relative performance of the different materials in terms of stiffness and strains was possible.

To represent the orthotropic elastic properties within the rib post test specimen, and in the instance of the noodle, model entirely different elastic properties, the numerical model was built with a number of sections, in each of which the elastic properties could be defined separately. This ensured that the principal directions of the materials could be oriented correctly within the component (Figure 6-7).

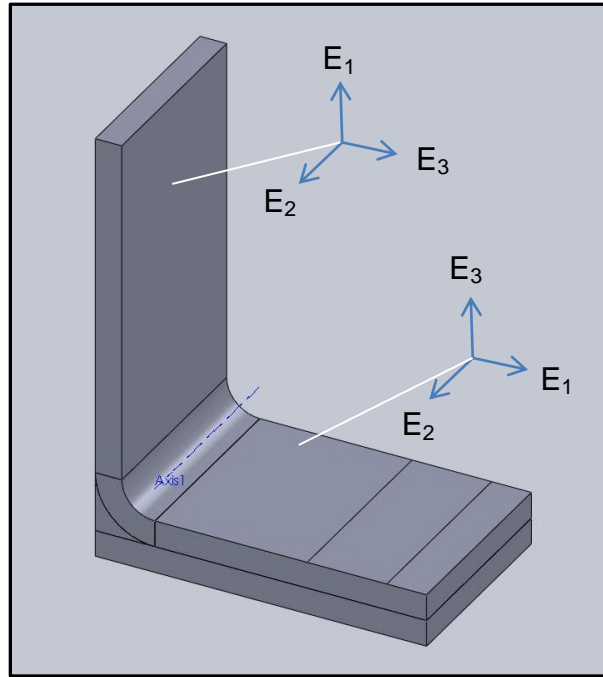


Figure 6-7. The orientation of the material principal directions within the component

The principal directions of the noodle differed slightly due to its alignment along the length of the component (Figure 6-8).

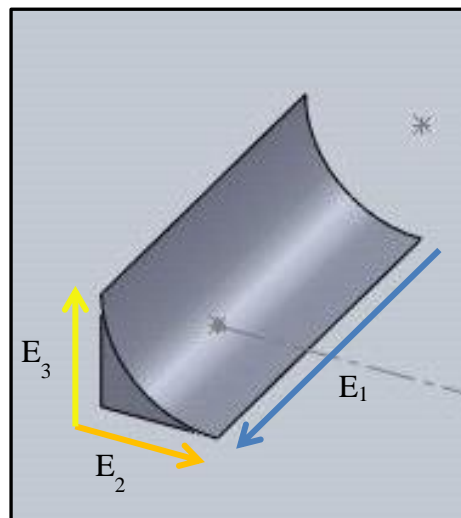
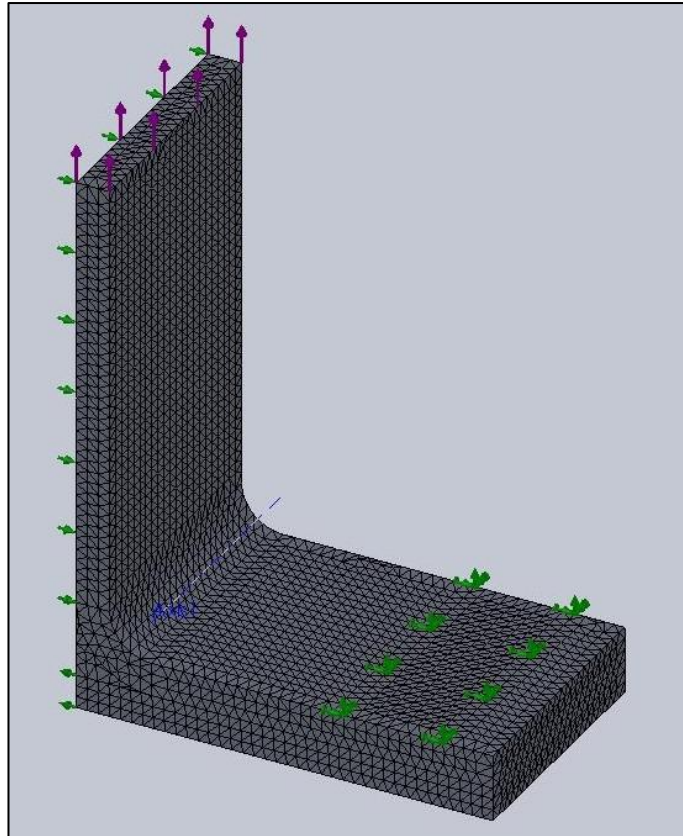


Figure 6-8. The principal directions of the material within the noodle

The density of the mesh generated to complete the simulations along with the size and aspect ratios of its elements, the defaults generated by the software, are noted in Table 6-13. The mesh itself is shown in Figure 6-9. Mesh sensitivity analysis concluded that refinement had no significant effect on the results of the simulation.

Table 6-13. Rib post pull-off test element mesh

Mesh parameters	
Element aspect ratio	28.38
Element size	1.33mm
Element density	50328 elements

*Figure 6-9. Rib post pull-off test element mesh*

The completion of analyses investigating the effect of the elastic properties on the maximum strain experienced within the structural model, varying each of the elastic properties independently, established that in the modelled loading scenario, the in-plane elastic moduli, shear moduli and Poisson's ratios have very little or no effect on the maximum strain (Table 6-14).

Table 6-14. Structural model sensitivity to elastic property variation, excluding the through-thickness elastic modulus

Elastic property variation	Max ϵ_1
Baseline estimated properties	2.128×10^{-3}
0.5 x E_1	2.120×10^{-3}
0.5 x E_2	2.130×10^{-3}
0.5 x G_{12}	2.127×10^{-3}
0.5 x G_{23}	2.134×10^{-3}
0.5 x G_{31}	2.213×10^{-3}
2 x ν_{12}	2.128×10^{-3}
2 x ν_{23}	2.128×10^{-3}
2 x ν_{31}	2.128×10^{-3}

In contrast the maximum strain was very sensitive to changes in through-thickness stiffness (E_3), suggesting that in the modelled case E_3 is the most significant elastic property, and in turn that the maximum strain is generated through the thickness of the component. The sensitivity of the simulated maximum strain to through-thickness elastic modulus variation is shown in Figure 6-10.

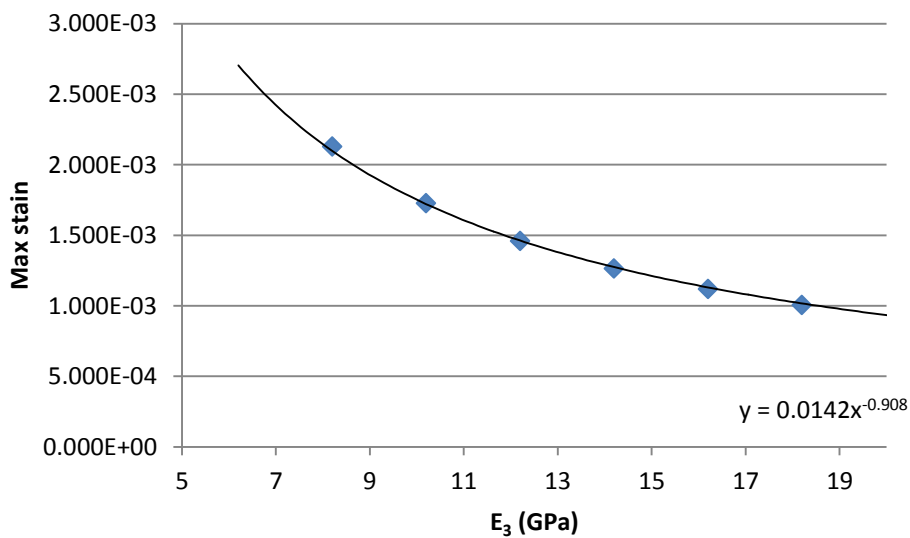


Figure 6-10. Structural model sensitivity to through-thickness elastic modulus variation

The results of the sensitivity analysis suggest that in the modelled load case, it is only necessary to represent the through-thickness elastic modulus accurately to determine the maximum strain.

6.3 Simulation results

The pull off test simulations were completed within Simulation, the integrated finite element package of Solidworks. The maximum strains of the material models in each axis are provided in Table 6-15.

Table 6-15. The simulated maximum strains of the rib post test element models. The error resulting from the estimation of elastic moduli are considered insignificant ($\sim \pm 6 \times 10^{-3}$)

Principal strain	Prepreg	Non-Tufted	Tufted
Max ϵ_1	1.982×10^{-3}	2.128×10^{-3}	1.957×10^{-3}
Max ϵ_2	-2.598×10^{-4}	-2.787×10^{-4}	1.972×10^{-4}
Max ϵ_3	-1.347×10^{-3}	1.437×10^{-3}	-1.336×10^{-3}
Max ϵ_{12}	1.661×10^{-3}	-1.920×10^{-3}	-1.627×10^{-3}
Max ϵ_{23}	3.241×10^{-4}	3.511×10^{-4}	3.430×10^{-4}
Max ϵ_{13}	-4.697×10^{-4}	-5.135×10^{-4}	-4.865×10^{-4}

These results indicate that in all of the material cases, the maximum strain experienced by the modelled rib post test element is generated in the 1st principal strain direction. Analysis of the 1st principal strain plots for each of the models (Figure 6-11 to Figure 6-13) shows that the maximum strain consistently occurs through the thickness of the constituent material, at the surface of the component's radius, indicating that the maximum strain is experienced within the composite laminate and not within the noodle region.

Figure 6-11 depicts the simulated maximum strain of the test element modelled with the non-tufted composite. The region of maximum strain is highlighted in red.

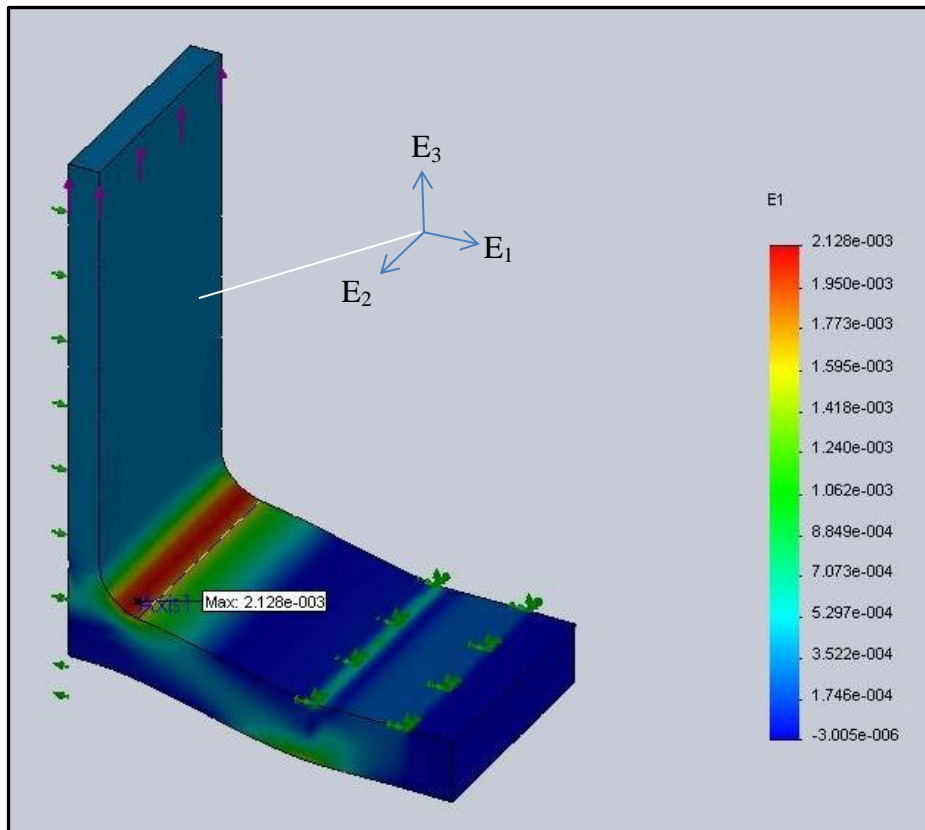


Figure 6-11. The first principal strain results of the non-tufted rib post pull-off test simulation, indicating the maximum strain.

Due to the required use of Cartesian and cylindrical co-ordinate systems within the definition of the material properties, the first principal direction is not consistent throughout the model. For this reason the strain shown in the component's radius, noodle region and web is that occurring through the thickness of the material (the radial direction), and the strain shown in the flange of the component is that occurring in the plane of the material (E_1).

As can be seen in Figure 6-12 and Figure 6-13, first principal strain plots for the tufted and prepreg components respectively, the strain distributions are practically identical to that of the non-tufted component (Figure 6-11), the difference between the results being the magnitude of the strain.

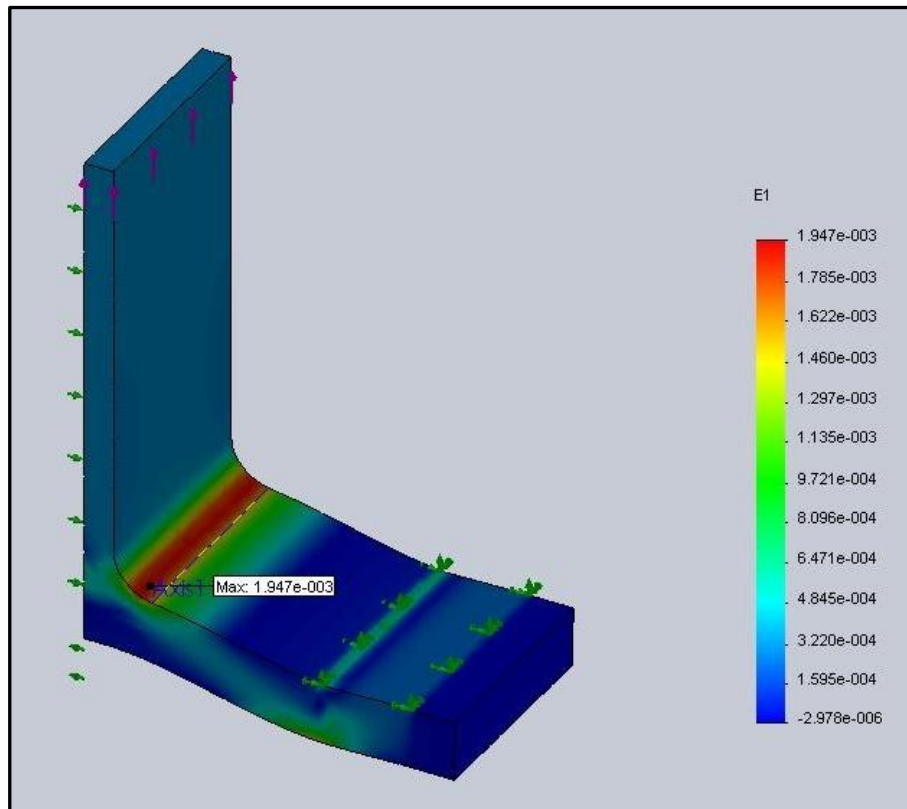


Figure 6-12. The first principal strain results of the tufted rib post pull-off test simulation, indicating the maximum strain.

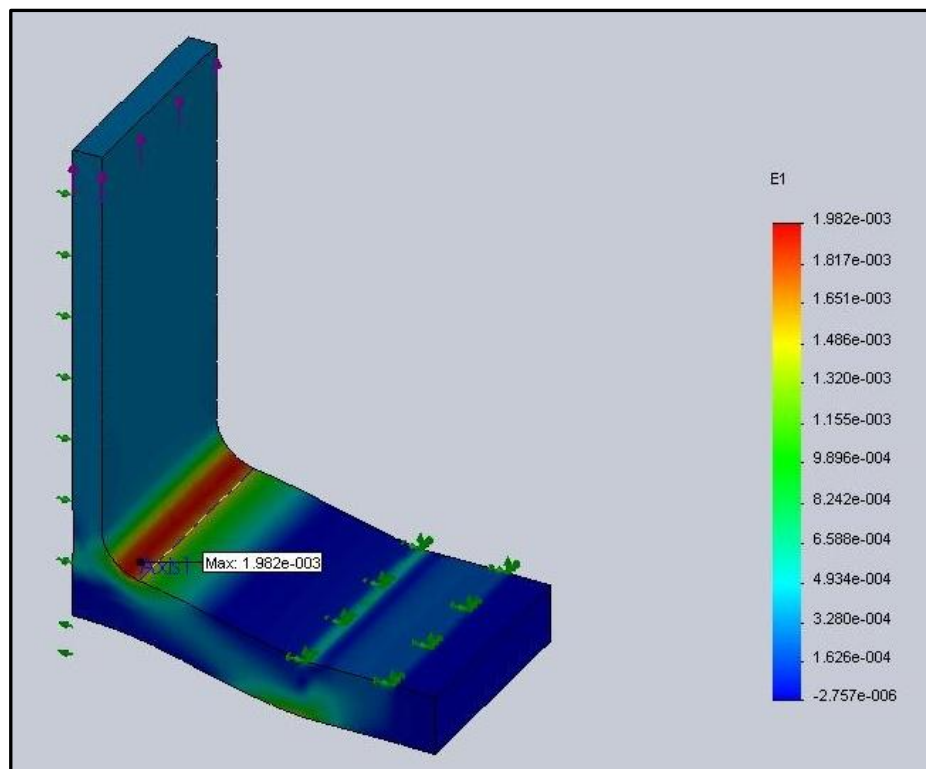


Figure 6-13. The first principal strain results of the prepreg rib post pull-off test simulation, indicating the maximum strain.

The maximum strain results (Table 6-15) indicate that in this specific loading scenario, the tufted material provides the best performance as far as stiffness is concerned,

resulting from its enhanced through-thickness elastic modulus (E_3). Comparing the results of the tufted and non-tufted materials, it can be seen that the tufting reduces the maximum strain by 8.0%. The strain reduction made by the tufted material over the prepreg is however smaller, the strain being reduced by only 1.3%.

Even with these modest reductions to the maximum strain, for the simulated load case it can be argued that due to the tufted component's increased stiffness the same performance as the non-tufted and the prepreg components could be achieved with a reduced material volume and therefore weight, using lighter fabrics or altering the layup. This would of course have positive implications for both the reduction of material costs and life cycle costs such as those associated with fuel burn.

Assuming the removal of material corresponds equally to the reduction of the component's cross section, there is an inverse linear relationship between the component's weight and the generated strain. It can therefore be approximated that as the tufted component experiences a maximum strain that is ~8% less than that of the non-tufted component, the tufted component could be made ~8% lighter and achieve the same performance. Using this approach, to provide the same maximum strain as the prepreg component with MVR-444 resin properties, the tufted component could be made ~1% lighter. These estimates of course make the assumption that the strain experienced by the prepreg and non-tufted components does not exceed the applications allowable strain.

Normalising the weights of the simulated components, and in doing so altering their performance, a simple comparison of the materials in terms of their performance/weight in the investigated load case can be made. This comparison provides an indication of the relative weight efficiencies of the composite materials within the rib post application.

6.3.1 Rib post pull-off test element performance/weight

In order to make comparisons of the performance/weight of the components simulated with different composite materials, the weight of each component must be estimated, requiring the volume of the simulated rib post test element and the densities of the simulated composite materials. The rib post test element volume is calculated automatically within Solidworks as $1.9 \times 10^{-5} \text{ m}^3$.

The densities of the various composite materials were estimated using the Rule of Mixtures for density, which takes the form of Equation 6-11.

$$\rho = \sum_c V_c \cdot \rho_c$$

Equation 6-11

Where the density of the composite is calculated as the sum of the products of the volume fraction and the density of each of the composite's constituent materials.

The densities of the constituent materials of the composites are given in Table 6-1, Table 6-2 and Table 6-6. Due to the fact that the same carbon fibre (Toray T700) is assumed for the prepreg composite as that which constitutes the NCF of the tufted and non-tufted composites, the fibre densities are also assumed to be the same. The total fibre volume fractions of the simulated composite materials are given in Table 6-16. As the fibre reinforcement of the tufted composite comprises of two different types of carbon fibre, that of the tuft thread and that of the NCF, it is treated as two different constituent materials. With the volume fraction of the tuft thread known (Table 6-4), the volume fraction of the NCF is calculated by subtracting the volume fraction of the tuft thread from the total volume fraction of the tufted composite (Table 6-8). The volume fractions of tufted composite's fibre constituents are also given in Table 6-16. It is

assumed that there is zero void content within the simulated composites and that the sum of the fibre volume fraction and the matrix volume fraction equal 1.

Table 6-16. The fibre volume fractions of the simulated composite materials

Material	Fibre volume fraction (V_f)
Non-tufted composite	0.60
Tufted composite	0.64
Tuft thread	0.04
NCF	0.60
Prepreg composite	0.64

Using the documented fibre and resin densities in conjunction with the corresponding volume fractions, the density of each of the composite materials was calculated (Table 6-17).

Table 6-17. The estimated densities of the simulated composite materials

Material	Density (kg/m ³)
Non-tufted composite	1536
Tufted composite	1562
Prepreg composite – MVR-444 epoxy resin	1562

Multiplying the calculated densities by the component volume, the weight of the component made with each of the composite materials is calculated. Using this information in conjunction with the maximum strains experienced by the component simulated with the tufted and non-tufted composites, and the Prepreg with MVR-444 epoxy resin (Table 6-15), a performance index for each material simulated within the rib post application can be calculated. Due to the fact that both low weight and low strain are desirable, the performance index is calculated as the inverse of component mass multiplied by its maximum strain, $(M\varepsilon)^{-1}$. This calculation provides a unique

performance value resulting from the component's unique combination of mass and maximum strain. The component providing the best weight efficiency is therefore indicated by the highest performance index value. Table 6-18 documents the mass of the component when made with each of the composite materials, and the calculated performance index.

Table 6-18. The weight and performance index of the rib post test element with each simulated material

Material	Mass (kg)	Performance index (kg.ε) ⁻¹
Non-tufted composite	0.029	16189
Tufted composite	0.030	17007
Prepreg composite	0.030	16835

The results indicate that with a performance value of 17007(kg.ε)⁻¹, the tufted composite is the most weight efficient material of those investigated within the rib post application in the pull-off load case. It can be argued that as the tufted composite component test element's performance value is approximately 1% greater than that of the prepreg component test element, it could be made 1% lighter and achieve the same strain. In this case the weight of the tufted rib post test element would be reduced to 29.7g. Naturally the same conclusion can also be made for the entire rib post, where the weight saving would be more significant.

Considering the arrangement of the tufts within the tufted composite, there is room for argument that the performance of the rib post made with this material, in terms of maximum strain in the pull-off load case, could be improved. Angled at ±45°, the tufts within the composite are not fully aligned in the through-thickness direction of the material, the direction in which the maximum strain is experienced. Changing the tuft angle to 0°, a much greater alignment of the tuft fibre in the through-thickness direction

would be achieved, thereby enhancing the through-thickness elastic modulus and reducing the maximum strain.

It is assumed that the tufts are not arranged in this manner as the rib post is not solely designed for the pull-off scenario, experiencing mixed loading in-service. Additionally, it is also thought that the tufting has been arranged to enhance energy absorption during failure, an area that is not within the scope of the completed structural modelling.

In addition to the analyses of performance/weight, the performance per unit manufacturing cost of each of the composite materials within the simulated load case can also be determined. This is achieved using the estimates of the developed manufacturing cost model and also the commercial cost model SEER-DFM, in conjunction with the simulated maximum strains. With this information, additional conclusions can be made about the economy of the materials within the studied application, in terms of their manufacturing cost efficiency with regard to performance. These evaluations are made in the following chapter, where the findings of the project are integrated.

Chapter 7. Integration of analyses

The purpose of this chapter is to bring together the findings of the work completed within this thesis and facilitate an economic evaluation of the NGCW novel composite rib post, using a non-tufted RTM processed NCF composite and an autoclave processed prepreg part as comparative benchmarks. The effectiveness of each component is judged by its balance of manufacturing cost, weight and through-thickness strain within the rib post application, established within the contributing chapters of the thesis.

The economic evaluation determines the increased cost of the implementation of tufting and also establishes whether there is any financial benefit regarding the use of tuft reinforced preforms over autoclave processed prepregs for this application.

Having completed structural analyses to estimate the through-thickness strain experienced by the components in pure pull off, estimated final component weights, and also modelled the manufacturing costs of the tufted and non-tufted configurations, the final parameter required for the economic comparison of the components is the manufacturing cost of the hypothetical prepreg composite rib post. This manufacturing cost was estimated using the commercial cost estimation software SEER-DFM.

7.1 Autoclave prepreg rib post manufacturing cost estimation

All aspects of the prepreg rib post manufacturing cost other than equipment and energy costs were estimated in SEER-DFM, which does not include this information. The major pieces of equipment used in the prepreg/autoclave process consist of the autoclave itself and the vacuum pump used for de-bulking and applying a vacuum to the part during the autoclave process. Freezers were not accounted for as their usage is assumed to be the same for all of the studied manufacturing processes (Being used in the RTM process for the storage of the one part resin). The capital cost of the autoclave

used in this process was published in a recent study by Witik et al [113], where an economic evaluation of a variety of composite material production methods was performed. The autoclave used in this study was standard and the same as that which would be required for the hypothetical prepreg rib post. The internal volume of the autoclave was 0.75m^3 , a suitable size for an individual rib post. The cost of the autoclave was provided by the manufacturer. It was given as £140k (2011). The implemented vacuum pump was assumed to be the same model as that used during the RTM of the tufted and non-tufted composite rib posts, therefore the same capital cost (£2458) was also assumed.

The energy rating of the autoclave, was also provided by Witik et al [113]. During heating, using the estimates and validations of Witik et al [113] and Scelsi et al [136], the autoclave was assumed to use 60% of this rating. During dwell and cooling, the autoclave was assumed to use 20% of its documented rating. The times of the stages of the autoclave cure cycle were estimated from the recommendations provided by the prepreg material's datasheet [141]. The energy rating of the vacuum pump was provided by its specifications and it was assumed to run at its documented rating. The duration of the vacuum pump's use was determined with the use of recommendations made by the material's processing guidelines (each debulking vacuum lasting 10 minutes) and the assumption that the material was held under vacuum throughout the cure cycle. Once energy consumption was determined, the energy rate documented in Chapter 5 was used to estimate of the consumed energy cost. All of the discussed values of the prepreg rib post manufacturing equipment are noted in Table 7-1.

Table 7-1. The power rating, usage time, energy consumption and energy cost/part of the prepreg rib post manufacturing equipment

Equipment	Power rating (kW)	Usage time (h)	Energy consumption (kW.h)	Energy cost/part (£)
Autoclave	27.000	4.17 (1.3 heating, 2 dwell, 0.87 cooling)	36.558	2.74
Vacuum pump	0.550	6	3.300	0.25

The material feedstock, consumable and tooling material cost input data required by SEER-DFM were updated with values obtained from manufacturers. The consumable material input costs are shown in (Table 7-2).

Table 7-2. Consumable input costs assumed for the prepreg rib post manufacturing cost estimates

Consumable	Cost
Tygavac DPT1000 bagging material (£/m²)	1.50
Tygavac MR1 release film (£/m²)	5.30
Tygavac AWN4 breather fabric (£/m²)	0.90
Tygavac VBS 750 sealant tape (£/m)	4.17

The manufacturing cost estimate of the prepreg composite rib post makes the assumption that the tooling for the process is manufactured internally rather than purchased. Making this assumption, labour rates and raw material costs are required in order to estimate the costs of the manufacture of the tool. The tool manufacturing labour rate was set at £50/hour, remaining the same as the labour rates used elsewhere within the rib post manufacturing cost estimate. The raw material cost of the tooling was dependent on the chosen material. Commonly used within the manufacture of prepreg components [4], steel was selected as the tooling material. Its raw cost was established to be £0.22 /kg [142] (18/10/12). Again tool replacement was not

considered due to its predicted lack of impact on the relative manufacturing cost estimates. The cost of the prepreg material used to manufacture the component was determined through contact with the manufacturer of the material. The prepreg was a 300mm wide uni-directional carbon/epoxy tape with a typical cured ply thickness of 0.191mm (Cycom 997 UD). The price of this prepreg was given as £31.14/m² (08/11/12).

The manufacturing cost estimates of the prepreg composite rib post were generated using the detailed composites facility of SEER-DFM. In order to generate the estimates a number of parameters were defined. These parameters and their defined qualitative or quantitative values are provided in Table 7-3.

Table 7-3. SEER-DFM parameters for the prepreg rib post manufacturing cost estimate

Estimate parameter	Value
PRODUCT DESCRIPTION	
Production Quantity	10, 100, 1000, 1000, 100000
Direct Hourly Labor Rate (£/hr)	50.00
Setup Hourly Labor Rate (£/hr)	50.00
Production Experience/Optimization	VHi
Product Classification	VHi
ENGINEERING DESCRIPTION	
Part Complexity	
Least	Nom+
Likely	Hi-
Most	Hi
Overall Length (mm)	185
Shape/Dimensions (mm)	T Channel
Width	100
Height	65
Thickness	8
Vertices	6
PROCESS TYPE	HLU
MATERIALS	
Prepreg Material Type	Cycom 997 UD
Material Cost (£) Per Kg.	105.88
Roll/Tape Width (mm)	300
Fabric Waste Factor	20.00%
PROCESS DESCRIPTION	
Cutting Type	hand cutting
Layup Type	Manual
BAGGING/TOOL CLOSING	YES
Operator Attendance Factor	20.00%
Debulk	YES
Debulk Interval	4
CONSUMABLES	
Bagging Material	Tygavac DPT1000

Release Agent	Tygavac MR1
Breather	Tygavac AWN4
Sealant Tape	Tygavac VBS 750
CURE	YES
Cure Method	Autoclave
Cure Temp. (°C)	177.00
Final Cure Duration (min)	120.00
Initial Temp. Cure Duration (min)	0.00
Operator Attendance Factor	10.00%
Resin Port Couple Time (min)	5.00
Infusion Time (min)	0.00
Heat-up Rate (°C/min)	2.00 (from 21°C)
Cool-down Rate (°C/min)	3.00 (to 21°C)
MANUFACTURING DESCRIPTION	
Set-up Complexity	
Least	Low
Likely	Nom-
Most	Nom+
Tooling Complexity	Low
TOOL DESCRIPTION	
Clean Tool	YES
Initial Tool Fabrication	YES
Tool Material	steel (18/10/12)
Tool Cost (£/m3)	1717.07 [142]
Tool Construction	Machined
Tool Manufacture Hourly Rate	50.00

A number of parameters within the detailed composites model can be defined as qualitative, requiring the choice of expressive terms best describing the case for which the estimate is being made. With these qualitative parameters, SEER-DFM is able to apply a fuzzy logic approach to the cost estimate, considering uncertainty with regard to aspects of the product design and the manufacturing process. Within the prepreg

composite rib post cost estimate, these parameters include: production experience/optimisation, product classification, part complexity, and set-up complexity. These refer to the manufacturer's experience in producing the part, the application of the part, the complexity of the part (curvature and other features), and the complexity of the tooling respectively. For each of these parameters, descriptive terms ranging from 'Very high' to 'Low' are chosen for minimum, likely and maximum circumstances, which define the level of uncertainty by bounding a probability distribution defined for the parameter. According to the chosen terms SEER-DFM then applies factors determined from statistical distributions relating to the defined parameter range to the relevant cost drivers. The effect of the variation of these factors within the statistical distribution is accounted for using Monte Carlo iteration, which also allows uncertainty with regard to more specific dimensional parameters of parts and tools, and also waste and operator attendance factors to be considered.

The estimates provided by SEER-DFM with and without the addition of equipment costs are summarised in Figure 7-1 for production quantities of 10 to 100,000 parts, in increments increasing by a factor of 10.

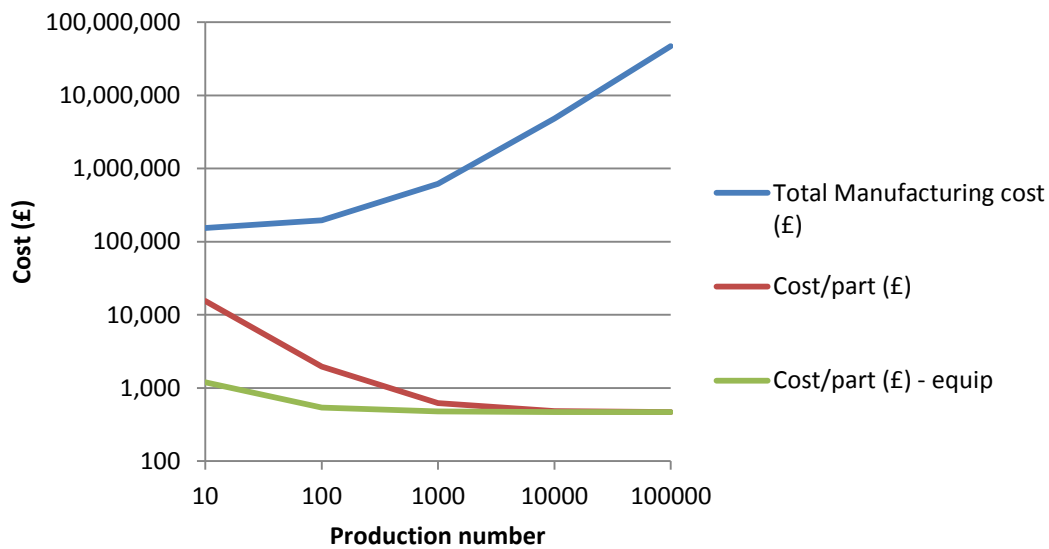


Figure 7-1. SEER-DFM manufacturing cost estimates for the prepreg rib post. The standard deviation of the total manufacturing cost is 3%, and that of the cost/parts is £24

A similar pattern to that seen with the estimated cost/part of the tufted rib post can also be seen here, with the cost/part including the cost of the equipment reaching its practical minimum at a production quantity of approximately 100,000 parts. However, as stated in Chapter 5, a much more realistic production quantity for this component is 1000 parts. Breakdowns of the cost/part of the prepreg rib post at a production quantity of 1000, both considering and excluding equipment costs are shown in Figure 7-2 and Figure 7-3.

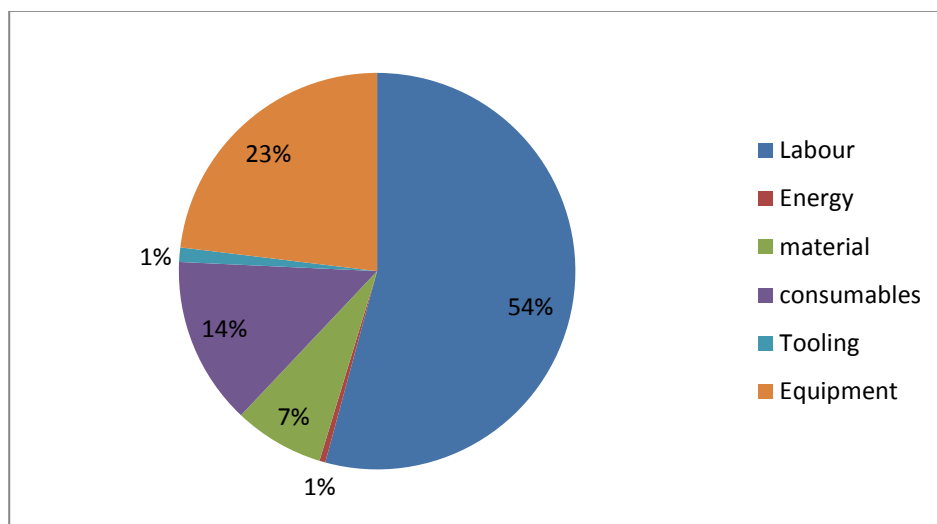


Figure 7-2. Prepreg rib post manufacturing cost breakdown with a production quantity of 1000 parts

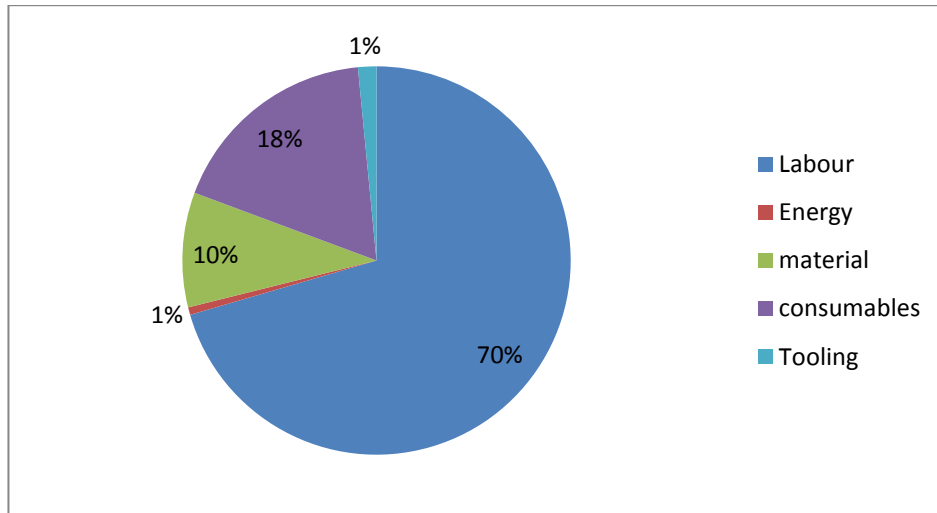


Figure 7-3. Prepeg rib post manufacturing cost breakdown with a production quantity of 1000 parts, excluding equipment costs

As can be seen from the division of the cost/part of the prepeg rib post, including and excluding equipment costs, labour is the greatest contributor. This is similarly the case with the tufted and non-tufted components as shown in Figure 5-5 and Figure 5-6. The contribution of the consumable materials is also considerably high. This is mainly the result of the de-bulking steps required during the lay-up of the prepeg material and the use of additional consumable materials during these steps. Within the manufacturing cost estimate, the prepeg layup was assumed to be de-bulked after every 4 plies laid, as recommended by SEER-DFM (and also prepeg processing guidelines).

7.1.1 Cost/part comparison of the considered composite rib posts

The costs/part of the tufted and non-tufted composite rib posts estimated in Chapter 5 and also the prepeg rib post, each with a production quantity of 1000 parts are shown in Table 7-4. Here the error values represent the standard deviations of the estimates iterated using Monte Carlo simulations.

Table 7-4. Costs/part of the prepreg, tufted, and non-tufted composite rib posts

Component	Cost/part (£)	Cost/part excl. Equip (£)
Prepreg	620 ± 19	477 ± 19
Tufted (Industrial extrapolation)	592 ± 3	349 ± 2
Non-tufted (Industrial extrapolation)	232 ± 3	207 ± 2

Comparing the values it can be seen that the non-tufted component has a far lower manufacturing cost than both the prepreg and tufted components when considering equipment costs and when excluding them. The origins of these differences are shown in Figure 7-4, where the manufacturing cost drivers of each of the manufacturing processes are compared.

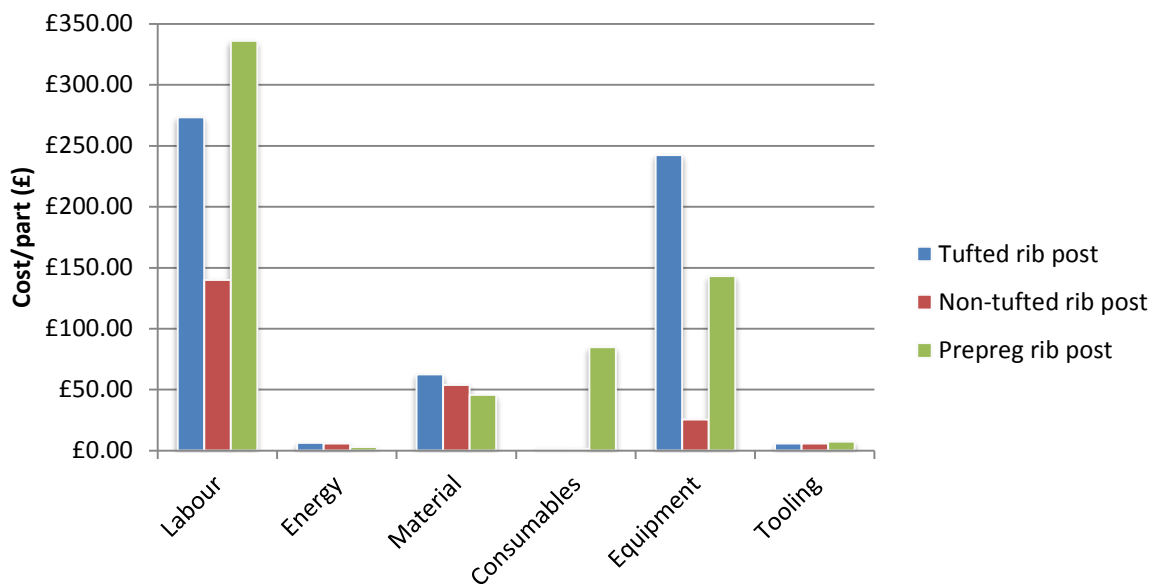


Figure 7-4. Manufacturing cost driver comparison of the tufted, non-tufted and prepreg components at a production quantity of 1000 parts

Analysing Figure 7-4 it is quite clear that the main sources of the tufted and prepreg rib posts' higher manufacturing cost/part are their approximate doubling of labour costs compared to the non-tufted component, their far greater equipment costs, and in the case of the prepreg component its consumption of substantially more consumable materials. The prepreg component's manufacturing costs are greater than those of the tufted

component mainly as a result of its higher labour and consumable costs, which are somewhat counterbalanced by the tufted rib post's greater material and equipment costs. This counterbalancing effect is the reason that there is a larger difference between the prepreg and tufted component cost/part when the equipment costs are excluded from the estimates (Table 7-4). The difference in manufacturing cost/part between the two components is only £35 ± 20 when including equipment costs, but £134 ± 19 when excluding them from the estimate.

7.2 Relative component economy

Using the performance indices developed in Chapter 6 it is possible to define how the weights of the components vary when normalised to achieve the same maximum strain in the modelled pull off load case. It is then possible to calculate the resultant variation in the estimated manufacturing cost by altering the material costs and costs of the labour directly associated with the quantity of material accordingly. Using these corrected manufacturing cost estimates, the economy of each component is established in terms of its trade-off between manufacturing cost and lifetime aircraft fuel consumption resulting from its weight in a similar calculation to that of DOC (Direct Operating Cost) [143].

The weight of each rib post is calculated by scaling up the test section to full size. The calculated weights of the various rib posts are provided in Table 7-5 alongside their calculated performance indices.

Table 7-5. Estimated rib post weight and component performance index

Rib post material	Component weight (kg)	Performance index (M£) ⁻¹
Non-tufted composite	0.179	2623
Tufted composite	0.185	2758
Prepreg composite	0.185	2730

As can be seen from the performance indices, the performance of the tufted composite rib post is 5% greater than that of the non-tufted composite rib post and 1% greater than the prepreg composite rib post. In order to normalise the performance of the non-tufted and prepreg rib posts to the same maximum strain as the tufted component, their weights are increased by the same proportion. The corrected component weights are provided in Table 7-6.

Table 7-6. Corrected component weights for performance normalised to tufted rib post maximum strain

Rib post material	Corrected component weight (kg)
Non-tufted composite	0.188
Tufted composite	0.185
Prepreg composite	0.187

As discussed earlier, the increases to the weight of the non-tufted and prepreg components required to achieve the same maximum strain as the tufted component in the pull off load case, must also be accounted for in their manufacturing cost estimates. This is achieved by calculating the additional material required for this weight increase, and subsequently the additional labour and consumable materials.

To calculate the cost of the additional material required for the non-tufted rib post, the weight fractions of the carbon fibre and epoxy resin making up the component are required. The weight fractions of the component's constituent materials are calculated with their known volume fractions and densities using Equation 7-1 [138].

$$W_{fr} = \frac{V_f \rho_f}{V_f \rho_f + V_m \rho_m}$$

Equation 7-1

The weight fraction of the matrix (W_m) is then simply $1-W_{fr}$. The weight fractions of the non-tufted rib post's constituent materials, and their subsequent weights within the component before normalisation are given in Table 7-7.

Table 7-7. Original non-tufted rib post constituent material weight fractions and subsequent weights within the component

Constituent material	Weight fraction	Weight of component material (kg)
Carbon Fibre	0.703	0.132
Epoxy resin	0.297	0.056

As the weight increase required for the normalisation of the non-tufted rib post's performance will occur with no change in the respective weight fractions, the weight fractions stated in Table 7-7 are used to determine the weight increase attributed to each material, and subsequently the additional material costs. Of the 9g weight increase, 0.6g is attributed to the carbon fibre (approximately one bi-axial ply) and 0.3g is attributed to the epoxy resin matrix. As the fibre content is split equally between $\pm 45^\circ$ bi-axial NCF fabric and $0/90^\circ$ bi-axial NCF fabric, the fibre weight is split equally between them. This assumes that the noodle material remains unchanged.

Using these additional constituent material weights in conjunction with the material unit costs provided in Chapter 5, the additional material costs of the non-tufted rib post required to normalise its performance to that of the tufted component were calculated and are provided in Table 7-8.

Table 7-8. The additional material costs of the non-tufted rib post with normalised performance

Constituent material	Additional cost for normalised performance (£)
Carbon $\pm 45^\circ$ bi-axial NCF fabric	0.10
Carbon $0/90^\circ$ bi-axial NCF fabric	0.09
Epoxy resin	0.20
Total	0.39

The additional labour cost required to process the additional material is calculated by increasing the fibre cutting and lay-up labour cost estimated by SEER-DFM for the industrial extrapolation of the non-tufted rib post manufacturing cost, also by 5%. This percentage increase in the fibre cutting and lay-up labour cost equates to an increase of £2.00. Summing the increased material costs with the necessary additions to labour cost, the additional weight required to normalise the non-tufted rib post's performance leads to a cost/part increase of £2.39 (new total cost/part of non-tufted rib post at 1000 parts incl equip = £234.42 \pm 1.82).

To determine the increased cost/part associated with the 1% weight increase of the prepreg rib post required to normalise its performance (equating to approximately one ply), the same process was completed for the material and labour costs of this component. The additional material cost of the normalised prepreg component was calculated to be £0.43. The additional labour cost required for this material increase was determined to be £0.31. The small material increase was assumed not to contribute to additional consumable material costs or labour with respect to their use. The modified costs/part and weight of the non-tufted and prepreg rib posts for a maximum through-thickness strain normalised to that of the tufted component are provided in Table 7-9.

Table 7-9. The costs/part and weights of the various rib posts when normalised to achieve the same maximum through-thickness strain as the tufted rib post, at a production quantity of 1000 parts

Component	Weight (kg)	Cost/part (£)	Cost/part excl. Equip (£)
Prepreg	0.187	620 ± 19	478 ± 19
Tufted (Industrial extrapolation)	0.185	592 ± 3	349 ± 3
Non-tufted (Industrial extrapolation)	0.188	234 ± 2	209 ± 2

Taking these modified values into account, the lifetime fuel consumption attributed to the weight of each component can be calculated to compare the economies of the components. The lifetime fuel consumption of each of the components is calculated assuming the lifetime fuel burn/kg of the Airbus A380, estimated within the introduction of the thesis to be €2000 or £1620 (Chapter 1). Using this value indiscriminately does not account for the positive feed-back created by the reduction of structural weight, where fuel consumption is reduced not only because less weight is transported but also because the aircraft becomes more fuel efficient. Table 7-10 provides the costs/part of the components considering both their manufacturing cost and lifetime fuel consumption.

Table 7-10. Rib post cost/part considering manufacturing cost at a production quantity of 1000 parts and component lifetime fuel consumption

Component	Cost/part (£)	Cost/part excl. Equip (£)
Prepreg	923 ± 19	781 ± 19
Tufted (Industrial extrapolation)	892 ± 3	649 ± 3
Non-tufted (Industrial extrapolation)	539 ± 2	514 ± 2

The final cost/part estimates of the three rib posts considering lifetime fuel consumption and manufacturing cost (Table 7-10) highlight that the non-tufted rib post is the most economic component for the studied case, providing a lifetime saving of £384 ±20 per

part compared to the prepreg rib post and $\text{£}343 \pm 4$ per part compared to the tufted rib post.

Despite the weight savings of the prepreg and tufted rib posts over the non-tufted component, their larger manufacturing costs outweigh the savings resulting from their reduced fuel consumption. In fact it is impossible for the tufted and the prepreg component to be considered more economic than the non-tufted rib post when taking lifetime fuel consumption as the weight penalty and accounting for equipment costs, as their manufacturing costs (Table 7-9) are greater than the total costs of the non-tufted rib post (lifetime fuel consumption + manufacturing costs) (Table 7-10). However, when excluding equipment from the calculation of cost/part, greater economy than the non-tufted component could be achieved with further improvements to the through-thickness elastic modulus. Taking the tufted component as an example and referring to Figure 6-10, it can be seen that, hypothetically, doubling the through-thickness elastic modulus reduces the maximum strain experienced by the component by 47%, which equates to a 47% reduction in weight for the same maximum strain as the non-tufted component, and therefore a 47% reduction to lifetime fuel consumption, reducing the tufted component cost/part excluding equipment to $\text{£}508 \pm 2$.

It is evident from the costs/part calculated excluding equipment investment (Table 7-10) that the larger manufacturing costs of the tufted and prepreg components also outweigh the savings resulting from their reduced fuel consumption in this case. The reason for this being that the recurring cost of labour is the main driver of the manufacturing cost of each component at this production quantity, with tooling making insignificant contributions (Figure 7-5).

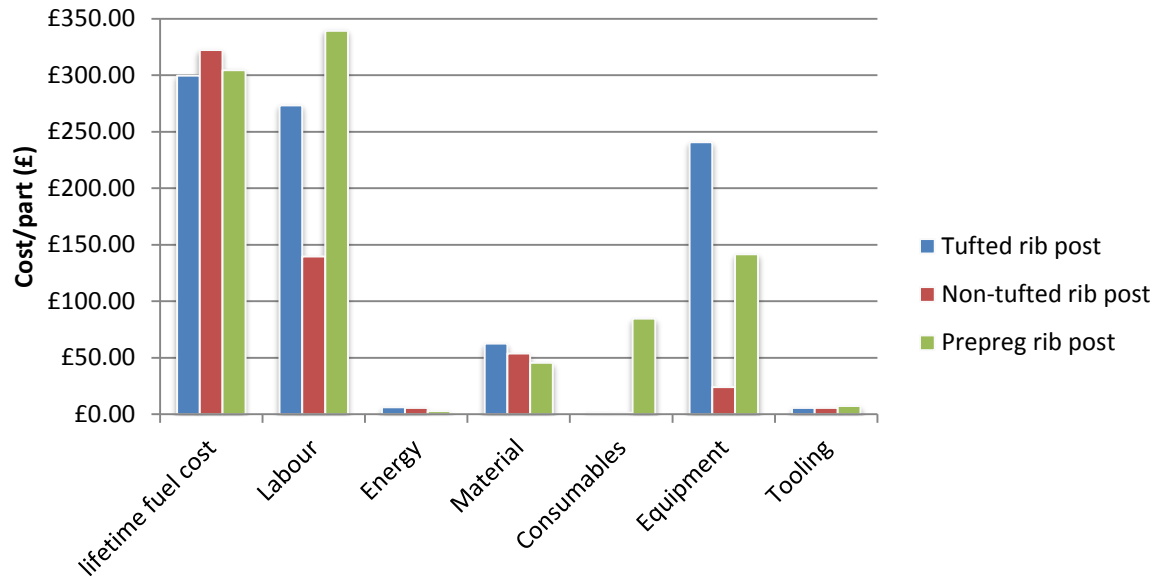


Figure 7-5. A breakdown of rib post manufacturing cost/part when performance is normalised, including lifetime fuel cost

Evaluating the results within Table 7-10 it can also be seen that the tufted composite rib post provides an economic advantage over the prepreg component, facilitating a reduction in manufacturing cost as well as lifetime fuel cost. The reduced manufacturing costs attributed to labour and consumable materials are the main drivers of this saving. The overall lifetime cost/part reduction achieved by the tufted composite rib post is $\text{£}31 \pm 19$, which in a single aircraft would generate a saving of $\text{£}1364 \pm 858$ assuming the use of 44 identical wing rib posts per aircraft.

7.2.1 Weight penalty variation

In order to provide an economic advantage over the non-tufted rib post, an increased weight penalty would need to be experienced in combination with a reduction to the labour consumed during the manufacture of the tufted rib post. In addition, the manufacturing process would require the use of pre-amortised equipment or a production quantity large enough to minimise its cost/part contribution ($\sim \geq 100,000$ parts). The larger labour costs of the tufted component result from the additional sub processes within its production and also its increased RTM mould fill time (7.2mins \pm 1.25) established by the flow modelling completed in Chapter 4, resulting from the

decreased permeability of the material suggested by the experiments carried out in Chapter 3.

It is expected that the labour time generated by the additional sub processes of the tufted rib post production (robotic tufting and preform de-moulding) can be reduced. Within the current tufting sub process a technician supervises the automated robotic tufting activities, creating an additional labour cost of £79 per part. Assuming that the automated tufting activities will become independent of supervision, this labour cost can be removed from the manufacturing cost estimate. In addition, it can also be conceived that the current labour intensive preform de-moulding sub process will become much more efficient with the development of more specialised mould materials. It is speculated that a three quarter reduction in the labour time consumed by this de-moulding process could be achieved, reducing the manufacturing cost by £19 ± 1. Making these adjustments to the manufacturing cost/part excluding equipment (Table 7-9), a lower value of £252 ± 2 is estimated. Increasing the weight penalty associated with the components by assuming the cost of jet fuel to double, which is not unprecedented considering the six fold increase in the price of jet fuel from the year 2000-2009 [11], the cost/part of the tufted rib post including lifetime fuel consumption and excluding equipment costs becomes £852 ± 2, becoming almost as economic as the non-tufted component whose cost/part is estimated be £819 ± 2 under the same conditions.

A condition in which the tufted component would be considered economically favourable using pre-amortised equipment is with an alternative, more significant weight penalty rather than exclusively fuel cost/kg. As stated within the introduction to this thesis Kaufmann [11] suggests that a commercial aircraft could earn €30,000 (£24,300) of additional revenue per kg of reduced structural weight during its life. This

value is based on an aircraft completing a single transatlantic return trip per day, 300 days a year for 25 years, with a ticket price of €500. This results in a lifetime revenue of €3.75M per seat, for which Kaufmann also assumes a passenger weight allocation of 125 kg. Applying this additional revenue value to the weight saving made by the tufted rib post results in a potential additional lifetime revenue of £73 compared to the non-tufted component. When assuming the labour reductions to the tufted rib post manufacturing process discussed earlier (£97 ± 1), the additional revenue offsets the component's manufacturing cost per part excluding equipment costs (Table 7-9), reducing it to £179 ± 3 ((349-97)-73), producing a saving of £30 ± 4 compared to the non-tufted component.

Applying this reasoning to the prepreg component shows that it would generate an increased lifetime revenue of £24/part compared to the non-tufted component. However this value does not offset the component's higher manufacturing cost/part enough to create a net saving over that of the non-tufted rib post. With the increased revenue, the prepreg rib post manufacturing cost/part is offset to £454 ± 19, a cost/part £245 ± 20 greater than that of the non-tufted part (Table 7-9).

In summary of the overall findings of this project, the use of the non-tufted carbon NCF/epoxy composite material within the studied rib post application produces the lowest combination of manufacturing cost and lifetime fuel cost (considering current jet fuel cost). The novel composite rib post, though proving to be more expensive than the non-tufted benchmark, does provide a cost advantage over the prepreg version processed using the hand lay-up/autoclave manufacturing route. Considering likely reductions to the labour of the novel composite rib post manufacturing process and potential increases to the price of jet fuel, the tufted component becomes almost as economic as the non-tufted component. The novel composite rib post becomes the most

economic choice when the considered weight penalty is a decrease in lifetime revenue rather than increased lifetime fuel consumption.

The conclusions made about the economy of the components studied within this project are limited to the case in which they are loaded in direct pull-off, emulating tests performed on the novel composite rib post within the NGCW project. Additional limitations are also present in the fact that the mechanical properties of the composites were estimated using a combination of the rule of mixtures approach and laminate design software, resulting from the lack of access to the results of the material characterisation tests completed at QinetiQ. Due to the insensitivity of the pull-off load case to the in-plane mechanical properties of the composite material, the structural modelling required to estimate the performance of the component under this load case could be completed using estimated values and relative through-thickness properties based on the composite's fibre volume fraction, matrix mechanical properties and through-thickness fibre alignment.

The absence of absolute in-plane mechanical properties for the tufted composite is the reason why structural modelling was not completed considering the mixed load case the component is expected to experience in service, which will have a greater sensitivity to these characteristics. In order to develop a complete appreciation of the economy of the considered materials within the mixed load case of the novel composite rib post application, results from the testing of the tufted composite and also the tufted rib post under the expected mixed loading conditions are required. Despite the absence of these data it may be hypothesised that as a result of the shear/peeling load case generated by the expected in-service load, the benefits provided by tufting to shear and delamination performance, documented by the literature reviewed in Chapter 2, would theoretically provide the tufted rib post with the greatest performance in terms of strength and

stiffness. However, to determine whether the tufted component is the most economic option requires detailed examination to establish the increase in performance in the mixed loading case and also the consideration of a more appropriate failure criterion such as delamination toughness, which the results from material and structural testing would allow. It is during delamination, which is the common failure mode of composite T-joints under a pull-off load, that the greatest benefits of tufting would be seen. Despite this fact, considering failure by delamination alongside the current assembly of the tufted rib post (the component itself consisting of three separate tufted preforms which are not connected by tufting), it is likely that the tufted-rib post would not experience the benefits to delamination toughness associated with the addition of tufting due to the tufted rib post assembly creating a resin rich layer at the meeting point of each of the preforms. The resin rich layer would cause a susceptibility to crack initiation and propagation.

To maximise the benefits to performance provided by the addition of tufting, it is recommended that a more appropriate assembly of the tufted rib post preform is also considered. This assembly would entail the tufting of the three fabric preforms together in the form of the rib post rather than individually, removing the resin rich layer formed by the assembly of the three separate preforms. Though it is probable that this change in assembly will increase manufacturing costs due to added complexity, it is hypothesised that the increase to performance would result in an overall increase in economy. In this circumstance the tufted rib post is expected to show greater superiority in performance to that of the non-tufted and prepreg components and therefore also a superior economy.

The overall findings of this project are pertinent for advanced carbon fibre prepreg composite applications where the critical structural response is experienced through the

thickness of the material. In these applications, the use of tufted carbon fibre reinforcements is likely to reduce manufacturing costs and decrease component weight, increasing economy.

Chapter 8. Discussion and future work

The drive from the aircraft industry to reduce the cost and weight of aircraft and attain high volume production [22-25] has led to increased interest in the 3D fibre reinforcement process of tufting, amongst others, which offers the potential to reduce the weight and manufacturing costs of composite components in certain applications traditionally manufactured using the prepreg/autoclave process.

The focus of this project has been to establish if the potential cost and weight benefits of the robotic tufting process can be realised. The study uses the novel composite rib post application of the NGCW project as an example case for this assessment. Through detailed analyses of the tufted composite rib post manufacturing process, relationships between manufacturing activities and consumed resources have been determined. In addition, novel data regarding the permeability of the tufted preform have been generated, facilitating the simulation of the liquid composite manufacturing process. Combining the findings of these studies, a manufacturing cost model for the novel composite rib post has been formed, including algorithms defining the cost generated by the robotic tufting process, which may be adapted for different geometries and tuft parameters. With the generated cost model, structural analyses and adapted manufacturing cost estimates for a prepreg/autoclave rib post generated with commercial software, the study establishes the manufacturing route providing the most economic component.

8.1.1 Rib post manufacturing cost

In generating estimates for the manufacturing cost of the tufted composite rib post, the project has characterised the robotic tufting process and the additional manufacturing activities required compared to the production of a non-tufted component.

Providing previously undocumented detail of the manufacturing process, the analysis is limited only in that it does not consider the programming of the tufting robot or additional manufacturing activities resulting from needle or thread breakage. This is the result of neither of these events being observed during the process recording. The significance of these omissions is arguable due to the amortisation of the programming time which is likely to become insignificant compared to the repeated manufacturing activities and the low likelihood of thread or needle breakage occurring at the tufting speed used.

Experimental investigation of preform permeability was also carried out to determine the effect of the tufting on manufacturing costs. The experiments considered the primary directions of resin flow during the component's RTM, assuming through-thickness resin flow to be negligible. The results of this investigation have provided an insight into the effect of tufting on the average in-plane permeability of fibre reinforcement. The limitations of the liquid permeability experiments were due mainly to the difficulty in minimising experimental error, however, this did not reach a level that endangered the experiment's precision, remaining well within the standard deviation of the data.

The occurrence of race-tracking is likely to have contributed to the scatter within the permeability results. For the calculations of permeability, the average propagated distance of the fluid was used as a representative linear flow front length. Caused by poor sample fit, the accuracies of the material cutting techniques are likely to be

responsible for the race-tracking. Interestingly this is supported by the fact that the permeability results of the non-tufted material cut by hand, ply by ply, show a greater degree of scatter than those of the tufted material cut as a preform using a computer controlled cutting machine with a greater degree of accuracy. An additional possibility for the reduced scatter within the permeability results of the tufted material is that additional stability is provided by the tufts, making the preform structure much less sensitive to variation from handling and insertion into the mould than the non-tufted material.

The investigations and theoretical calculations carried out in Chapter 3 and Chapter 4 show that, in agreement with the theories of Lundstrom [86], Hu and Liu [89] tufting decreases permeability in the plane of the material. The completed investigation shows that the in-plane permeability of the studied preform is reduced by approximately a factor of 3.5 perpendicular to the alignment of the tuft seams, and a factor of 2 parallel to their alignment. In the case of the novel composite rib post the decrease in permeability leads to an increase in the manufacturing cost/part compared to the non-tufted rib post by a somewhat trivial sum of £6. This permeability decrease could act as more of an issue in larger components with mould fill times in the range of an order of magnitude greater than the investigated component.

Ultimately the difference between the permeabilities of the tufted and non-tufted preforms is likely to result from the increased local fibre volume fraction caused by tufting such as the 9% increase within NCF fabric documented by Treiber [58].

The findings of these studies have been used to create a novel new manufacturing cost model for the investigated component, using new algorithms to define labour, energy and material consumption. The modular nature in which the model has been built allows it to also estimate the manufacturing cost of the component without tufting. The

cost model is sensitive to tufting parameters, feedstock material, preform layup, and preform number, a condition being that the effect of these parameters on the in-plane permeabilities of the final preform is known and that the facility for the modelling of RTM mould fill time is available. The cost model is also sensitive to production quantity and rate. Due to the omission of overhead costs and some equipment costs from the considerations (resulting from their assumed constancy through the studied manufacturing processes) the generated estimates are of a relative rather than definitive nature. It should be noted that this does not restrict the capability of the study to determine whether the use of tufting provides an economic advantage in the studied application.

Using the novel composite rib post manufacturing cost model to estimate the component's costs and also those of a non-tufted rib post, the study has compared estimates with those formed by the commercial manufacturing cost estimation software SEER-MFG for a prepreg composite rib post of the same dimensions. These comparisons have shown that the tufted component has lower manufacturing costs than the hypothetical prepreg component producing a reduction to cost/part of ~5% ($\pm 3\%$). However, they have also asserted that the use of the non-tufted material generates the lowest manufacturing costs, being approximately 62% lower than the costs of the prepreg component and approximately 60% lower than those of the novel composite rib post at a production quantity of 1000 parts.

8.1.2 Rib post performance and economy

The structural modelling completed within this research was used to establish the relative performance of the components considering the fibre orientations and volume fractions of their constituent material. The elastic properties of the composite materials were estimated using a combination of rule of mixtures calculations and laminate design

software. Component performance (defined in this case as the maximum experienced strain) was analysed simulating the pure pull-off load case used during the testing program of the NGCW novel composite rib post.

The numerical analyses found that the novel composite rib post achieved the lowest maximum strain and therefore the greatest stiffness considering the identical load used in the simulated test cases. The reduction in maximum strain experienced by the novel composite rib post was approximately $8.0 \pm 0.1\%$ and $1.3 \pm 0.5\%$ compared to the non-tufted and prepreg components respectively. Having an estimated component weight, a performance index was created to quantify the efficiency of each of the composite materials within the studied application. The index values were calculated as $(M\varepsilon)^{-1}$, the inverse of component mass multiplied by its maximum strain, with the largest value indicating the best performance per unit weight. Comparing these values the study determined the novel composite rib post to be most efficient in terms of structural weight, though the performance index of the prepreg component suggested that it was almost as efficient.

Within this study the economy of each component was based on the assumption of a weight penalty, attributing a cost to the structural weight of each component. The performance of the components were normalised to that of the tufted component, altering their weights accordingly. Their economy was considered by combining component manufacturing cost with an additional cost defined by the weight penalty. Initially, the weight penalty considered was lifetime fuel consumption/kg, specifically that estimated for the Airbus A380. The component with the smallest combination of lifetime fuel cost and manufacturing cost was considered most economic. Under the assumed conditions this component was deemed to be the non-tufted rib post, its estimated combined lifetime fuel cost and manufacturing cost being the lowest of all of

the components both when including and excluding equipment costs. In each case its cost was ~ 20-40% less than those of the other components. This outcome indicates that the fuel savings resulting from the reduced weight of the tufted and prepreg components were not significant enough to offset the increased manufacturing cost required to generate their improved through-thickness performance.

Under the assumed conditions the study has nevertheless established that the tufted component provides an economic advantage over the prepreg rib post, having not only a lower manufacturing cost but also reduced lifetime fuel consumption. The overall cost saving/part is approximately 3% when considering equipment costs and 17% when assuming these to have been amortised previously. It can be argued that this saving has a great potential to increase growth. Considering expected savings to the labour cost of the novel composite rib post from the development of the manufacturing process for more industrial production (estimated to be in the region of £100 per part), and also the potential for increased fuel prices, the overall cost/part saving of the tufted rib post over the prepreg component becomes more significant. In fact, when assuming a factor of two increase in fuel price, and also the use of pre-amortised equipment, the novel composite rib post becomes almost as economic as the non-tufted rib post.

The novel composite rib post was shown to be most economic when additional lifetime revenue was considered as an alternative weight penalty (Chapter 7), the value/kg based on transatlantic ticket price and passenger weight allowance. In this case the theoretical saving over the cost/part of the non-tufted component was approximately 14%. The effect of the value of the weight penalty on the relative economy of the components is shown in Figure 8-1, where the lifetime cost/part of the components is calculated as the sum of the estimated manufacturing costs and an additional cost calculated as a function of component weight and the assumed weight penalty/kg.

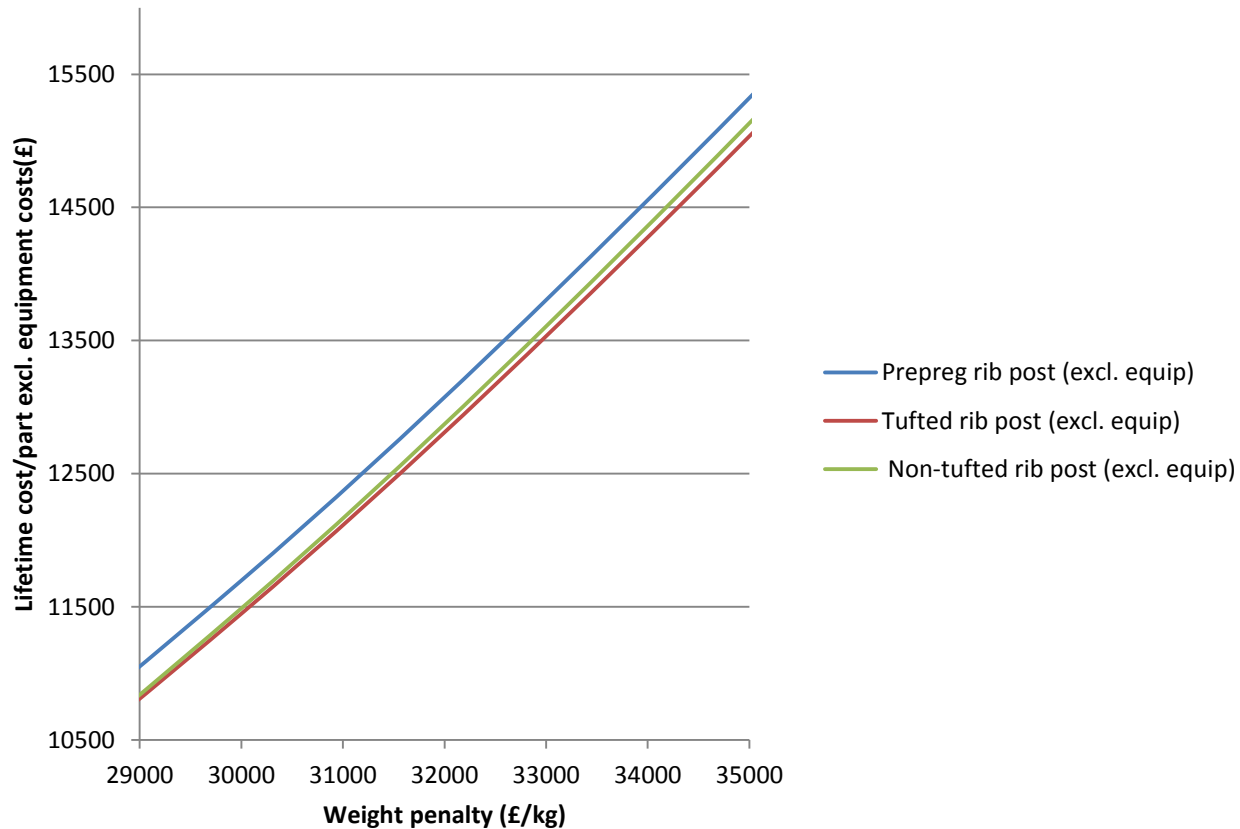


Figure 8-1. Comparison of component economies with increasing weight penalty

The lifetime cost/part of each component is shown plotted with an incrementally increasing weight penalty. When lower weight penalties are considered the lifetime costs are dominated by the manufacturing costs of the components, leading to the heaviest rib post with the lowest manufacturing cost being considered most economic. However, as more significant weight penalties are considered, the lighter components become increasingly more economic until finally a cross-over point is reached. At this point the higher manufacturing costs of the lighter components are outbalanced by their reductions to the cost resulting from the weight penalty. This leads to the novel composite rib post eventually being considered the most economic component.

Though limited to the specific component and load case studied within this project, the findings have pertinent implications for composite components whose performance are dictated by through-thickness mechanical properties, and which are currently manufactured using autoclave processed carbon fibre/epoxy prepreg. Depending on the

value associated with the reduction of weight, it may be more economical to manufacture these components with carbon/epoxy composites using RTM, or indeed RTM processed tufted carbon preforms.

8.2 Future work

To further understand the influence of tufting on component costs, this study has analysed the economy of the NGCW's novel composite rib post relative to its manufacture with different composite materials. Having focused on a pure pull-off load case, further data are required to facilitate conclusions about the novel composite rib post's economy, considering its expected mixed loading in-service. This information could be provided by the results of the structural testing completed within the NGCW project and it would also facilitate validations of the completed work. However, as has been the case during the completion of this project, access to these data is highly restricted. Considering this constraint, to enable further work regarding the validation of the completed structural modelling and the consideration of the novel composite rib post's in-service load case, a test program including both material and structural testing is required. In addition to making this further work possible the proposed test program will also determine the various strengths of the material and the component, making it possible to create additional component performance indices based on the induced maximum stresses, providing further means by which to assess relative component economy.

It is also recommended that within future structural modelling, a more suitable failure criterion such as delamination toughness should be considered to provide a greater understanding of the effect of tufting on performance. In addition to this failure criterion, a more appropriately tufted rib post should also be studied to give a true appreciation of the potential benefits to performance and therefore economy provided

by tufting. Rather than the discontinuous through-thickness tufting of the considered case, resulting from the rib post manufacture consisting of the assembly of three individually flat fabric preforms (creating an inter-preform resin rich layer susceptible to delamination), a more appropriate tufting strategy would be to tuft through the thickness of the rib post limbs. This strategy would create a preform of the rib post itself and also produce continuous through-thickness reinforcement more capable of tolerating delamination within the final composite.

The study would also benefit from an appreciation of the effect of the novel composite rib post's tufting on the maintenance costs of the component. Conceivably this could be achieved by fatigue testing the various composite rib posts investigated within this study using the expected in-service load. Assuming the form of maintenance required within this application to be part replacement, the point at which this would be necessary could be defined within the proposed fatigue testing as the point at which the applied factor of safety load generates greater deflection than the component's design limit. The number of fatigue cycles required to reach this point could then be recorded and used in conjunction with an estimate of the number of cycles the part would experience in-service, determining the number of replacements required during the lifetime of the aircraft. Subsequently these figures could be used with the estimated manufacturing costs to determine the relative costs associated with the maintenance/replacement of the components.

It would also be of great interest to perform further investigation of the tufted preform's permeability. It is proposed that this could be completed using CFD techniques in conjunction with a representative unit cell model created with the aid of Micro-CT. Micro-CT scanning facilities such as the Skyscan 1174 housed at the University of Plymouth, which has been experimented with during the project (Appendix 4), could be

used to generate a stacked array of 2D scan images of a unit cell sample of the tufted preform, compressed to its final thickness. It would then be possible to produce a mesh for CFD simulation from the image data, using software produced by Simpleware Ltd [144]. The image segmentation platform Scan IP v5.1 could be used to process the data, creating a voxel based 3D model. The fully integrated +FE module would then allow the creation of the numerical model for simulation. The +FE module is able to generate meshes in numerous formats for simulation in FE or CFD solvers, including ANSYS CFX [145], which would be used in this case due to its availability at the University of Plymouth. Exporting the required inlets, outlets and boundary conditions with the generated mesh, the permeability of the unit cell and therefore the tufted preform could be investigated within the solver.

As well as facilitating the validation of the experimentally investigated in-plane permeabilities of the tufted preform, the use of CFD would also allow the investigation of through-thickness permeability, assumed within this study to have no significant effect on the processing of the material due to the dominance of in-plane resin flow during the component's RTM. Using the investigated through-thickness permeability in conjunction with LCM processing simulation software such as PAM-RTM, and the determined in-plane permeabilities, the validity of the assumption of the insignificance of the through-thickness processing characteristic in this application may be tested.

The completion of this validation study will naturally lead to an additional investigation of the effect of varying tuft parameters on the permeability of the investigated preform, and conceivably additional fibre reinforcements using the same methods. Comparing the results of the validation study with results generated using an idealised unit cell, created with fibre reinforcement geometry generation packages such as Wisetex [146] or Texgen [147], or indeed the facilities of Scan IP to integrate CAD based data,

significant differences between the use of the two techniques will be highlighted. If it can be established that the two techniques give similar results, this investigation can be carried out using fibre reinforcement geometry generation packages, significantly reducing time and physical material requirements. Otherwise, the investigation will require the analysis of material samples using Micro-CT facilities.

In order to broaden the considerations of this project it would also be of interest to investigate the economy of the composite rib post manufactured using 3D woven preforms. This would facilitate conclusions to be made about whether in such an application the initial purchasing costs of the preforms are outweighed by their final component economies. It would also provide an opportunity to evaluate whether the component economy is significantly affected by the global volume fraction limitations of the 3D weaving process. Such an investigation would require both material and structural testing, and also analyses of the component manufacture using the 3D woven preforms.

In future work it is also conceivable that the cost model generated within this project could be integrated with the commercial manufacturing cost model SEER-MFG, using its ability to integrate sub routines and custom calculations. This integration would provide the facility to estimate the manufacturing costs of different components using robotically tufted materials. With the provision of test data documenting the mechanical properties of the studied tufted composite, this would allow the evaluation of the relative economy of components using the tufted material, but additional material testing would be required to facilitate similar evaluations for material variations.

Chapter 9. Conclusions

This PhD thesis has focused on providing an understanding of the effect of manufacturing costs, performance and weight on the economy of a tufted composite component, in relation to the use of different types of fibre reinforcement and manufacturing techniques. Of particular interest has been its comparison to the prepreg/autoclave method, due to the frequent use of this technique within the aerospace industry. The work completed throughout this study has delivered:

- Detailed documentation of the tuft reinforced composite manufacturing process using RTM as the manufacturing method.
- Novel investigations of the effect of the studied tufting on 1D permeability, finding reductions of a factor of 3.5 in the direction perpendicular to the alignment of the tuft seams, and 1.8 in the direction parallel to the seams.
- Findings that the alignment of tuft seams result in anisotropy, affecting both processing and in-plane mechanical properties.
- A novel manufacturing cost model for the NGCW project's novel composite rib post, including new algorithms defining the costs generated by the robotic tufting process. The proposed algorithms are one of the major contributions to knowledge in this thesis.

- Definition of the manufacturing cost drivers of the novel composite rib post at a production quantity of 1000 parts, showing labour and equipment costs to have the greatest influence.
- Findings that the manufacturing cost of the novel composite rib post is ~5% lower than the production of an autoclaved processed carbon fibre/epoxy prepreg version of the component, and that with expected reductions to labour this saving is estimated to increase to ~20%.
- The finding that under the pure pull-off load case, considering lifetime fuel consumption as the weight penalty, the novel composite rib post is more economic without tufting in its considered form (discontinuous through the thickness of the rib post limbs) due to its lower manufacturing costs. Without tufting the three flat fabric preforms assembled to form the rib post, the lifetime cost/part of the component is ~40% lower than its costs with tufting, and ~42% less than the lifetime cost/part of the prepreg rib post.
- The conclusion that with the consideration of a more significant weight penalty, such as potential increased lifetime revenue, the use of the novel composite rib post results in greater economy, its lifetime cost/part excluding equipment costs estimated to be 14% less than the component without tufting and 61% less than the lifetime cost/part of the prepreg component excluding equipment.

The future aim of the work of this project is to contribute to a strategy by which the economic implications of the robotic tufting process may be considered at the early design stage of any component where its use may be beneficial. To make such a contribution it is recommended that in addition to the consideration of delamination

toughness within the performance index, a more appropriately tufted component with tufts which pass through the entire thickness of the component limbs should be analysed, allowing for an appreciation of the maximum possible structural benefit of tufting.

With additional detailed studies of the various other forms of 3D fibre reinforced composites, a similar strategy may be formed by which the most economic form of through-thickness reinforcement may be selected at an equally early stage during component design. This PhD has begun this process, investigating the effect of robotic tufting on the manufacturing costs, performance and subsequently weight and economy of the novel composite rib post of the NGCW project, finding that tufting is able to provide increased economy in components whose through-thickness performance is critical.

Evaluation of the project's methodologies has highlighted the assumptions made due to the limitations of available information. Accordingly, these assumptions are believed to be the best representations of what is experienced in reality. However, errors resulting from their possible inaccuracy have been accounted for as far as possible in rigorous error analyses, to establish their propagation through the various calculations performed. These analyses have provided confidence in the results of the study, ensuring the significance of the determined economical differences between the investigated components.

Appendix 1 - Differential pressure gauge adaption

Designed to measure the differential pressure of air, it was necessary to adapt the Digitron 2022P gauge to measure the pressure differential between the pressure of the liquid at the injection point and the pressure at the liquid flow front. The simple adaptation consisted of attaching the differential gauge to the mould with a length of pipe, as shown in Figure 9-1. This allowed the injected liquid to move up the pipe, compressing the air trapped within it.

The assumption was made that as the liquid injection pressure increased to maintain a constant flow rate, equilibrium was instantaneously experienced by the trapped air and the liquid. With the liquid and the trapped air continuously equalising, the pressure gauge was able to measure the pressure of the liquid at injection by measuring that of the compressed air inside the pipe.

With the mould being open ended, the liquid flow front was assumed to have a pressure equal to that of atmosphere. Thus the differential pressure gauge was able to measure the differential pressure between the injection point and the dry side of the liquid flow front by measuring atmospheric pressure in addition to the injection pressure. This was achieved simply by keeping one of the pressure sensor inlets open to atmospheric pressure. The arrangement can be seen in Figure 9-1, with the right sensor inlet on top of the differential pressure gauge being open and un-attached to the mould.

The required length of pipe was estimated using Boyles law and an estimated worst case scenario inlet pressure. The estimate of the maximum inlet pressure was based upon the

use of Darcy's law in conjunction with estimates of minimum permeability from process records of the RTM of the material completed by QinetiQ.



Figure 9-1. Differential pressure gauge arrangement

Appendix 2 – Corn oil dynamic viscosity measurement and thermometer calibration

In order to calculate the permeability of a material using Darcy's law, the dynamic viscosity of the liquid employed to infiltrate the material must be determined. Within this research corn oil was used as the experimental liquid. Its dynamic viscosity was measured with the use of a Brookfield RS Rheometer (Figure 9-2)



Figure 9-2. The RS Brookfield Rheometer employed to measure the dynamic viscosity of the experimental liquid.

The rheometer was fitted with a C-50 cone, and 7ml of the corn oil was placed on the rheometer's temperature controlled baseplate. The cone was then lowered allowing a distance of 50 μ m between its apex and the baseplate, spreading the liquid within this space (Figure 9-3). Any excess liquid appearing at the edge of the cone was removed to avoid edge effects interfering with the dynamic viscosity measurement.

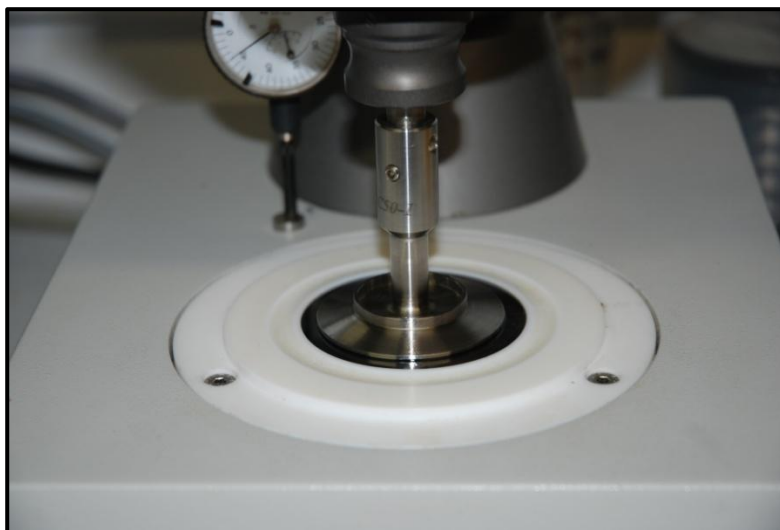


Figure 9-3. Lowered C-50 rheometer cone

Following the arrangement of the cone, the dynamic viscosity measurement was started. The dynamic viscosity of the liquid was measured at 15, 20, 25 and 30°C in order to determine the liquids dynamic viscosity / temperature profile. Each temperature was maintained by the rheometer's temperature controlled baseplate for ten minutes whilst dynamic viscosity measurements were made, ensuring that the temperature of the liquid stabilised. The final five measurements of dynamic viscosity at each temperature were then averaged.

This method was repeated for ten samples from the single bottle of 'off the shelf' corn oil used. The average dynamic viscosities of these samples at each temperature can be seen in Figure 9-4 .

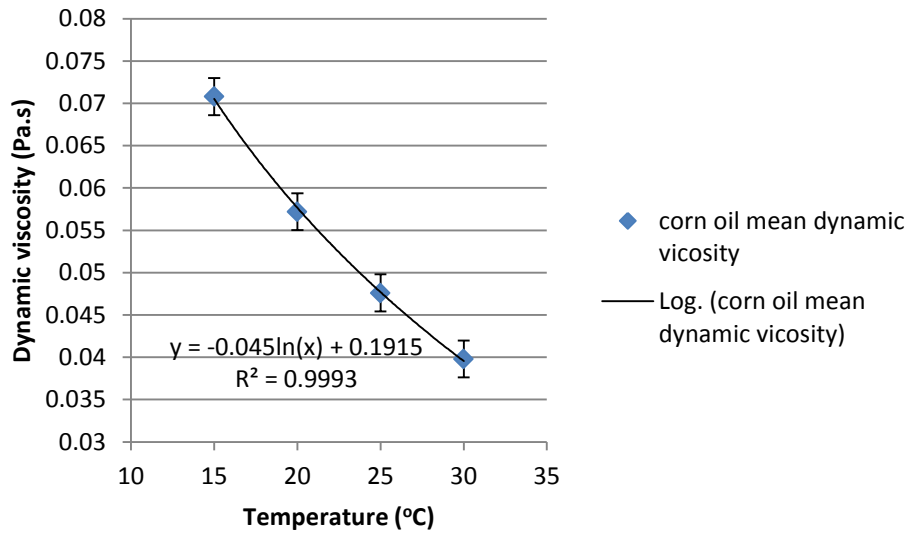


Figure 9-4. Corn oil dynamic viscosity / temperature profile

Using the dynamic viscosity / temperature profile (Figure 9-4), the dynamic viscosity of the corn oil during the experiment could be determined by measuring its temperature. This required the thermometer used to measure the corn oil temperature during the experiment to be calibrated with the temperature controlled baseplate of the rheometer. This was achieved by taping the K-series thermocouple of the thermometer to the temperature controlled baseplate and then bringing it to the required temperature (Figure 9-5).

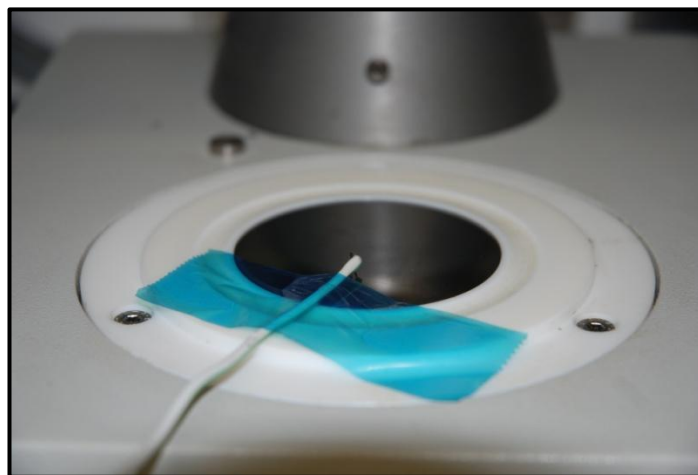


Figure 9-5. Thermometer calibration

Once the baseplate temperature had stabilised the thermometer reading was logged. This was completed five times for each of the temperatures used within the corn oil

dynamic viscosity measurement, allowing for representative means to be calculated.

The thermometer calibration graph is presented in Figure 9-6.

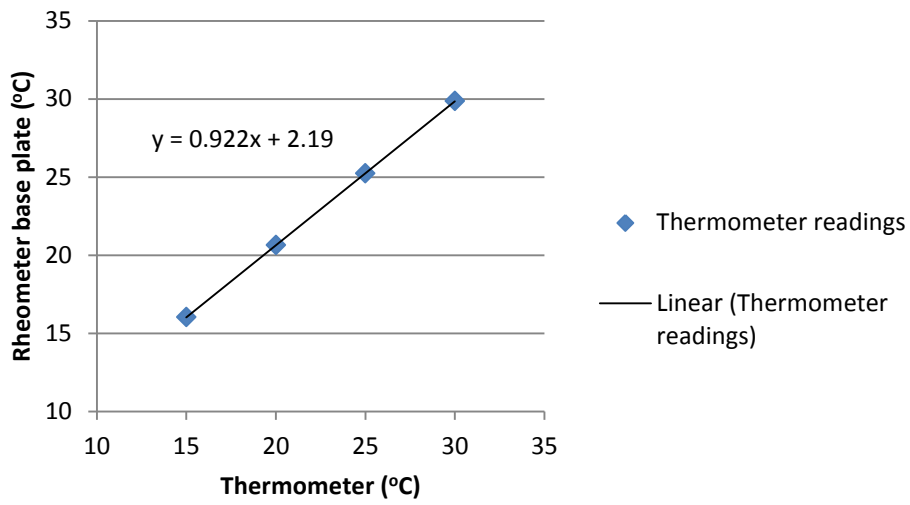


Figure 9-6. Thermometer calibration with rheometer base plate

Appendix 3 – Calculation of volumetric flow rate

As a result of adaptations made to the differential pressure gauge used within the permeability experiments allowing it to measure the pressure of the liquid at injection, the constant volumetric flow rate provided by the pump was not equal to that of the flow of liquid through the material sample.

The adaptation of the differential pressure gauge primarily consisted of the addition of a length of pipe by which to attach the gauge to the mould. This length of pipe ensured that the liquid used within the experiment did not reach the sensor of the pressure gauge and subsequently cause damage.

The pressure gauge adaptation worked on the basis that air trapped in the pipe would compress and equalise with the pressure of the liquid entering the pipe from the mould inlet cavity. This allowed the pressure of the liquid at the materials injection point to be determined by measuring the pressure of the trapped compressed air (Figure 9-7).

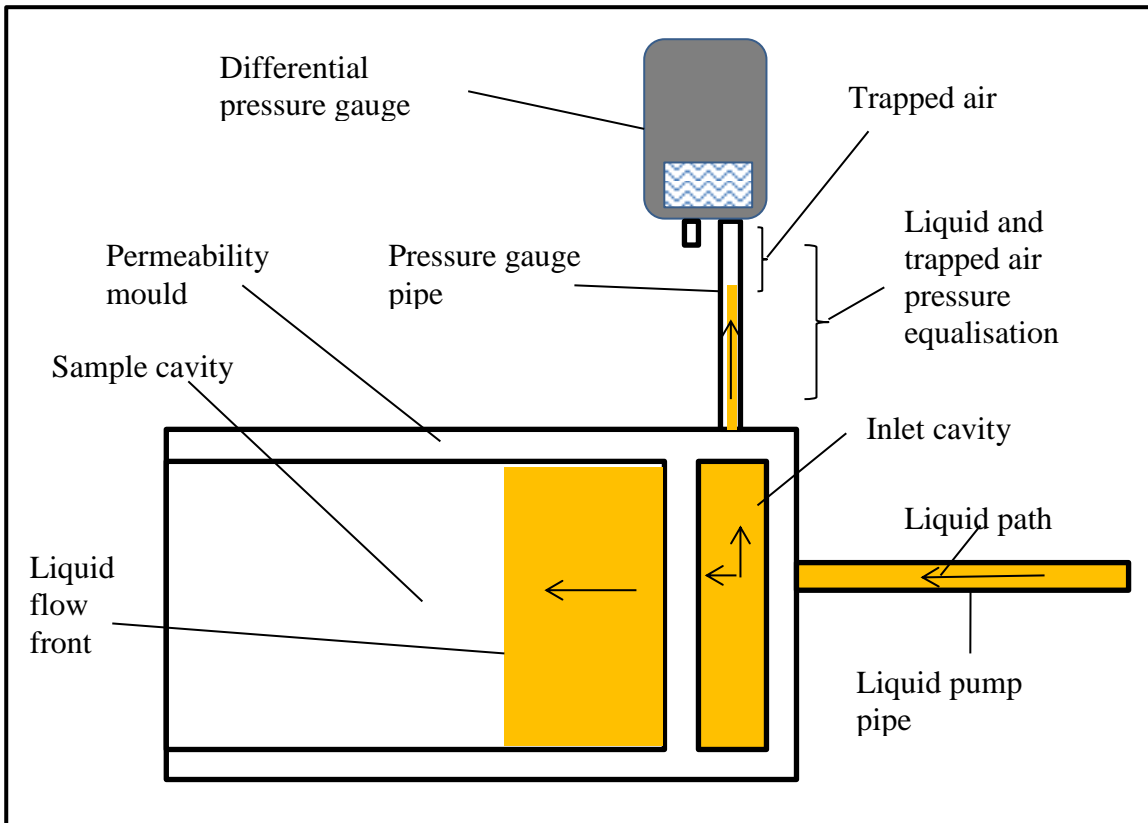


Figure 9-7. The separation of liquid flow into the sample cavity and the pressure gauge pipe

Maintaining a constant flow rate within the experiment, the pressure of the liquid entering the mould was constantly increasing. As a consequence of this, the air trapped inside the pressure gauge pipe was under constant compression and was therefore constantly reducing in volume. To maintain this situation, the volume of incompressible liquid inside the pipe had to increase. This resulted in a reduction of the volumetric flow of liquid through the material sample from that entering the inlet cavity directly from the pump.

In order to determine the volumetric flow rate of liquid through the material sample, calculations had to be made based on the observation of the liquid flow front propagation with time.

For each sample, the time required for the liquid flow front to reach each 10mm increment along the mould's length was recorded. With this information, the

volumetric flow rates required to fill the specific lengths in the recorded time were calculated using the following equation [82]:

$$Q = \frac{Vol \phi}{t}$$

Equation 9-1

For each sample the calculated volumetric flow rates were averaged to provide a sample specific value to be used in the calculation of each sample's permeability. Table 9-1 provides the average volumetric flow rate calculated for each sample.

Table 9-1. Mean volumetric flow rates

Sample	Mean volumetric flow rate (m³/s)
NCF1	2.12x10 ⁻⁰⁸
NCF2	1.78 x10 ⁻⁰⁸
NCF3	1.25 x10 ⁻⁰⁸
NCF4	1.26 x10 ⁻⁰⁸
Tufted 1	8.85x10 ⁻⁰⁹
Tufted 2	7.68 x10 ⁻⁰⁹
Tufted 3	7.34 x10 ⁻⁰⁹
Tufted 4	1.2 x10 ⁻⁰⁸
Tufted 5	8.89 x10 ⁻⁰⁹

With the volumetric flow rate supplied to the mould being constant in all cases, variations to the volumetric flow rate through each sample would not be expected. The variations observed in Table 9-1 may be a result of error in the observed filled length or the presence of small leaks causing sample to sample variations.

Appendix 4 – 3D fibre preform internal architecture analysis with the Skyscan 1174 micro-CT scanner

Introduction

The Skyscan 1174 micro-CT scanner, lent to the University of Plymouth through the EPSRC equipment pool, provided the opportunity to begin an investigation of the processing characteristics of a variety of 3D fibre reinforcements. The Skyscan 1174 micro-CT scanner is shown in Figure 9-8 with the Thermo Fisher Scientific Mini 900 rate meter used to perform regular leak rate checks. The investigation will evaluate the significance of the processing characteristics of the materials to the processing cost and the total cost of the manufacturing cycle. This will help determine whether the processing characteristics of 3D fibre reinforcements are cost drivers and give insight into how, and in what detail these factors should be accounted for within a cost model. The micro-CT scanner was successfully used to scan two types of 3D fibre reinforcement; 3Tex 3D woven fabric and Saertex NCF quasi 4x4 tufted fabric, and a variety of 3D and 2D fibre reinforced composites. Among these scans were those conducted with a variety of magnifications and also those conducted with the material testing stage. The material testing stage was capable of the controlled and recorded compression and release of the samples.



Figure 9-8. The Skyscan 1174 micro-CT scanner and the Thermo Fisher Scientific Mini 900 rate meter

With software provided with the Skyscan 1174 and that already in use at the University of Plymouth, the 3D structures of the samples will be modelled. From these models and recorded data of the compression and release of the samples, processing characteristics of the dry fibre reinforcements such as permeability and compressibility will be determined. By considering these figures in conjunction with the processing cost data of the two materials, it will be possible to evaluate the effect of the processing characteristics on the processing cost and the total cost of the manufacturing cycle. The following report describes the methods used to analyse the internal architectures of the samples with the micro-CT scanner and presents the results obtained.

Analysis Methodologies

Sample preparation

To remove the detrimental effects to scan image quality associated with a varying sample diameter, cylindrical specimens were used. During the rotation of the specimen for 360° scanning, a specimen with an irregular diameter would cause interference to the

captured images and decrease the accuracy of the subsequent computer model. The methods used to form cylindrical samples of the materials analysed are described below.

- *Dry Fabric*

In order to form cylindrical specimens of the two types of dry fibre 3D reinforcements provided by QinetiQ, 3Tex 3D woven fabric and Saertex NCF quasi 4x4 tufted fabric, a WAD hole punch No.1000-05 with a 16mm diameter die was used.

In the case of both fabric types; the specimens were cut, taken to the micro-CT scanner inside the die and then removed onto the Micro-CT scanner stage. This brought the handling of the specimen and therefore fabric disturbance to a minimum. It was found in previous attempts that if this method was not adopted, rovings would come loose of the fabric and the sample would begin to fall apart.

- *Composite*

Preparation of composite specimens was completed with a hole saw fitted to a Pacera Pillar drill. Cylindrical specimens with a diameter of 16mm were cut. During the specimen preparation it was observed that panels with through-thickness reinforcement resisted much delamination, whereas those without suffered some delamination at the bottom of the sample.

Micro-CT Scanning Methodology

Within this study the Skyscan 1174 micro-CT scanner was used to conduct scans with two different sample stages. The use of these stages will allow the analysis of different processing characteristics of the materials studied. The stages consisted of a circular platform and a more advanced material testing stage capable of loading samples in compression and tension. The use of the different specimen stages required two different scanning methods, these are described below

Scan method with the circular platform stage

To facilitate a view of the whole specimen when using the circular platform stage, which is pictured in Figure 9-9 and Figure 9-10, a spacer was placed on the stage surface. The spacer elevated the material specimen above the height of a brass flange on the surface of the stage, which was obstructing the passage of the x-rays through the material specimen. Adherence of the spacer to the stage and the specimen to the spacer was provided by a thin layer of white tack on either side of the spacer. Following the placement of the specimen on to the stage and the insertion of the stage into the micro-CT scanner, the Skyscan1174 control program was used to; move the stage into the required position, set the magnification (6-33 μ m), choose X-ray source settings, finalise the scan parameters and start the scan. The scan was then completed automatically, with the specimen being rotated and scan images being collated.



Figure 9-9. The circular platform stage for the Skyscan 1174 micro-CT scanner, with and without spacer



Figure 9-10. The circular platform stage fixed inside the Skyscan 1174 micro-CT scanner

Scan method with the material testing stage

The material testing stage was used to carry out micro-CT scans of material samples under compression. The information obtained will help to determine the compressibility of the materials studied. These materials consisted of the dry 3Tex 3D woven fabric and the dry Saertex NCF quasi 4x4 tufted fabric.

The material testing stage is able to carry out the controlled compression of samples and allow scans to be completed at any point during the compression. The stage is pictured in Figure 9-11 where it is shown fixed inside the micro-CT scanner with the specimen already inserted. To insert the material sample into the material testing stage, the stage has to first be fixed inside the micro-CT scanner. The stage has to then be carefully dismantled. The cylindrical specimen is then placed on top of the lower compression plate in as central position as possible and the stage is reassembled. The specimen chamber and upper compression plate are replaced over the material sample, assuring a small gap between the top surface of the specimen and the upper compression plate. A scan is then completed with the specimen unloaded.

Following the completion of the unloaded scan, the compression of the specimen is started. The compression is halted at chosen increments of the compression stage height, with scans being completed at each. Throughout the compression and also each time the compression is halted, the load and displacement are logged by the material testing stage software. This process is continued until either maximum load (222.4N) or maximum travel (6mm) is reached by the test stage. Once this has occurred a scan is completed at full compression and then the specimen is released. The release is halted at the same stage heights as during the compression, again a scan is completed each time it is halted and load and displacement data are collected throughout. Once zero load is reached a final scan is completed.

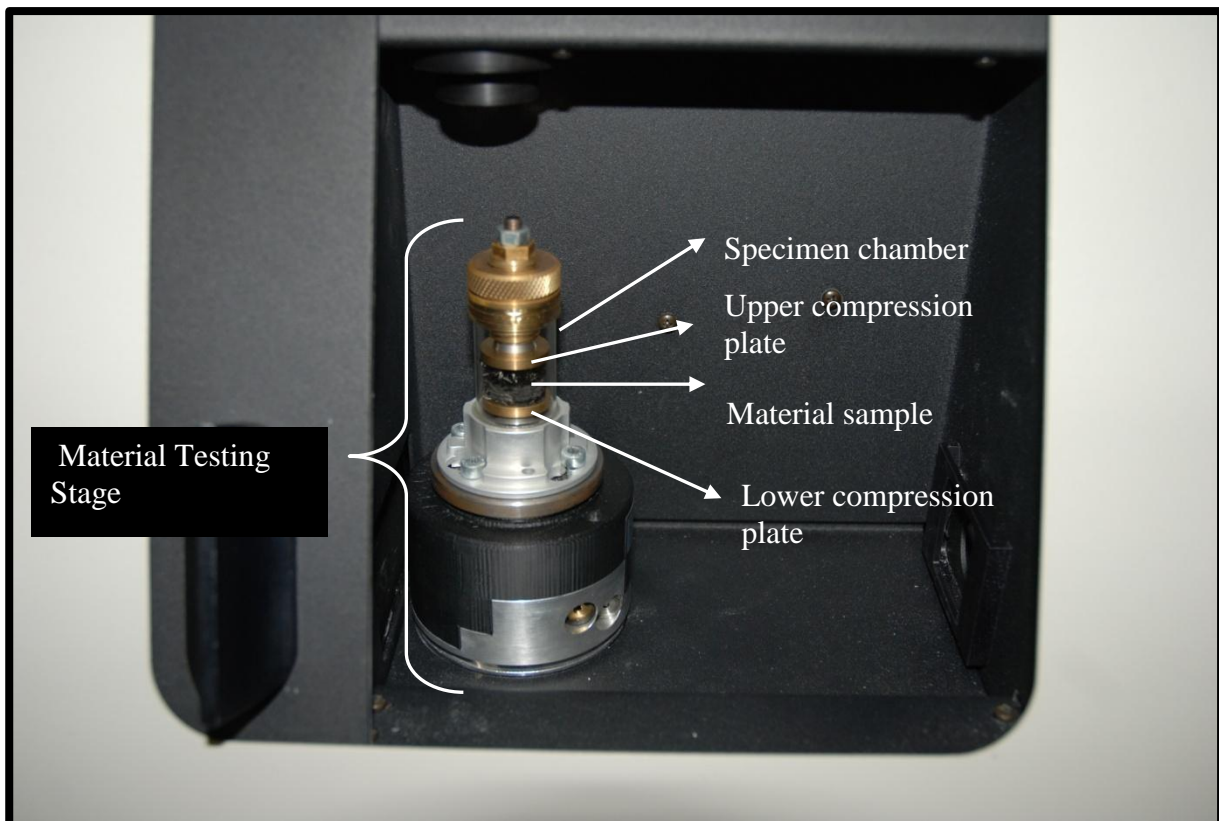


Figure 9-11. The material testing stage fixed inside the Skyscan 1174 micro-CT scanner with the dry Saertex NCF quasi 4x4 tufted fabric inserted

Results

Selections of the micro-CT scan images for each of the studied materials, captured when using the circular platform stage, are presented below. The small selection of images will aid in the assessment of the quality of the computer models that will be produced. Clear images will facilitate the production of more accurate models than those that appear grainy and undefined.

Circular Platform Stage Scans

- Dry Fabric Samples

With the analysis of the selections of micro-CT scans shown in Figure 9-12 and

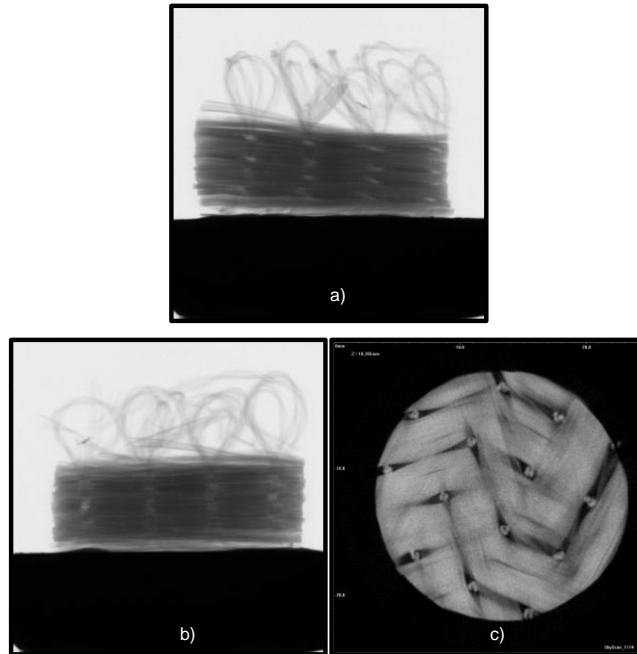


Figure 9-13, it can be seen that the scan images obtained for the dry fibre 3Tex 3D woven fabric and the dry fibre Saertex quasi NCF 4x4 tufted fabric are relatively clear. Due to the clarity of the micro-CT scan images obtained for these specimens, it can be presumed that the computer models produced for the dry fibre 3Tex 3D woven fabric and the dry fibre Saertex quasi NCF 4x4 tufted fabric will be effective in the investigation of their processing characteristics.

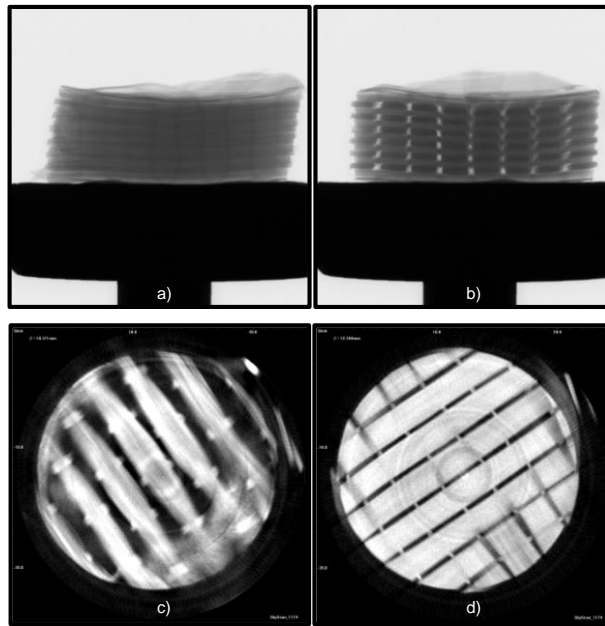


Figure 9-12. Micro-CT scans of dry fibre 3Tex 3D woven fabric a) view of warp binder b) view in warp direction c) visible distortion to surface weft rovings due to binder yarn d) through-thickness view of fabric's internal architecture

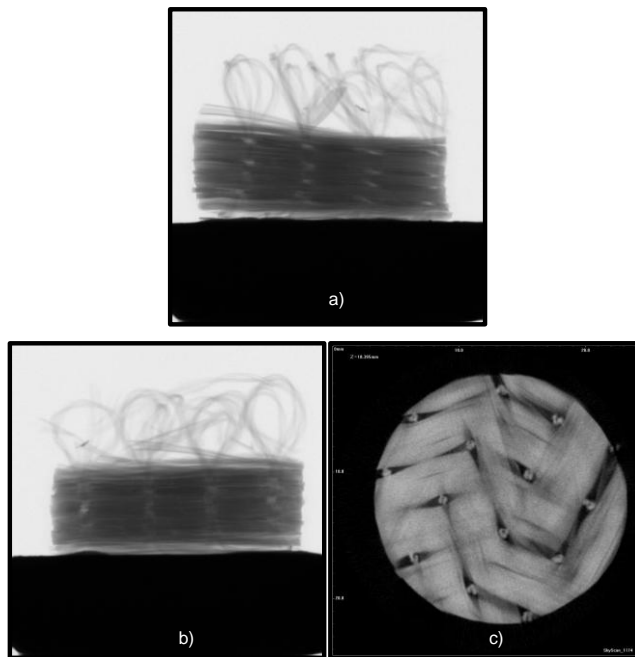


Figure 9-13. Micro-CT scans of dry fibre Saertex quasi NCF, 4x4 tufted fabric a) view in tuft row direction b) view perpendicular to tuft row direction c) through-thickness view of the fabric's internal architecture

- Composite Samples

Comparing the clarity of the scan images of the composite samples, Figure 9-14 to Figure 9-22, to those of the fabric samples, the composite scan images can be seen to be much less clear. This is a result of the much lower difference in density between the

carbon fibre and the matrix compared to carbon fibre and air. The effect is most apparent with the through-thickness slice images of the samples. As a result of the lack of clarity of the through-thickness slice images, known as the reconstructed images, it is likely that the accuracy of the computer models produced for these samples will be questionable. This is due to the fact that the reconstructed images play a large part in the formation of the computer models of the scanned materials. If internal architecture detail is not captured in the reconstructed images, it will not be accounted for within the computer models produced. Although the micro-CT scan images obtained may not be ideal for the production of computer models of the composite samples, they will aid in the characterisation of the materials.

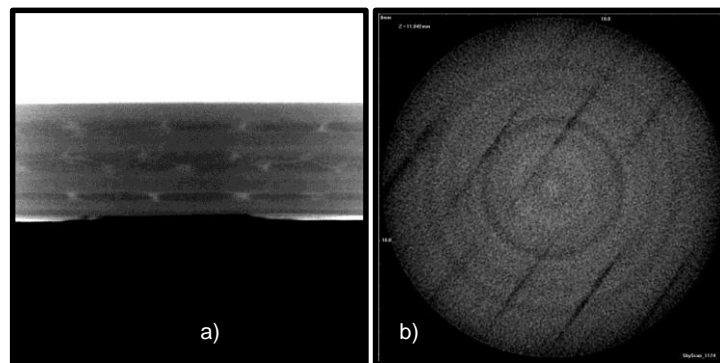


Figure 9-14. Micro-CT scans of panel 12 – unstitched Saertex NCF quasi carbon and epoxy. a) a view of the internal architecture of the composite along y axis b) a through- thickness slice of the composite along the z axis

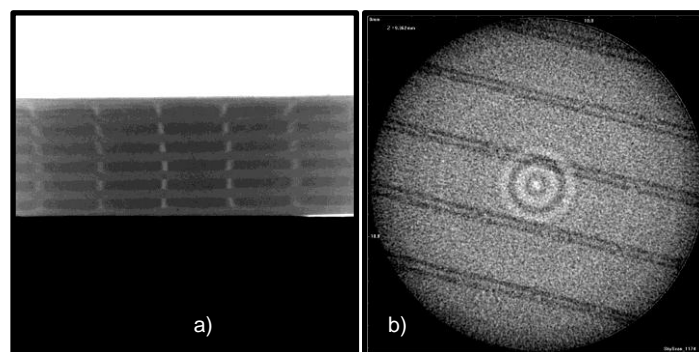


Figure 9-15. Micro-CT scans of panel 13 – 0,90 3Tex 3D woven carbon and epoxy. a) a view of the internal architecture of the composite along y axis b) a through-thickness slice of the composite along the z axis

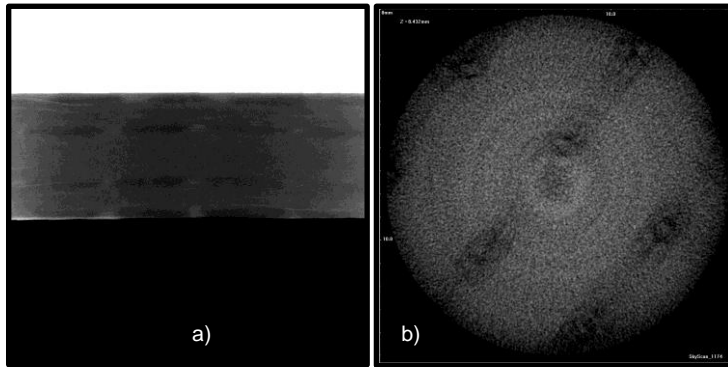


Figure 9-16. Micro-CT scans of panel 15 – baseline 4x4 tufted Saertex quasi NCF carbon and epoxy. a) a view of the internal architecture of the composite along y axis b) a through- thickness slice of the composite along the z axis

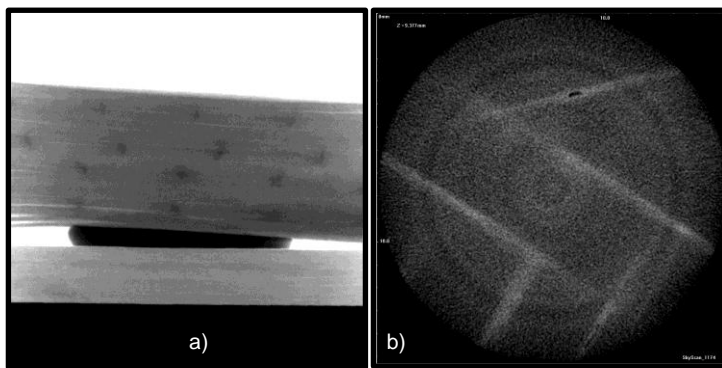


Figure 9-17. Micro-CT scans of panel 29 – Carbon/Priform soluble fibre and epoxy a) a view of the internal architecture of the composite along y axis b) a through-thickness slice of the composite along the z axis

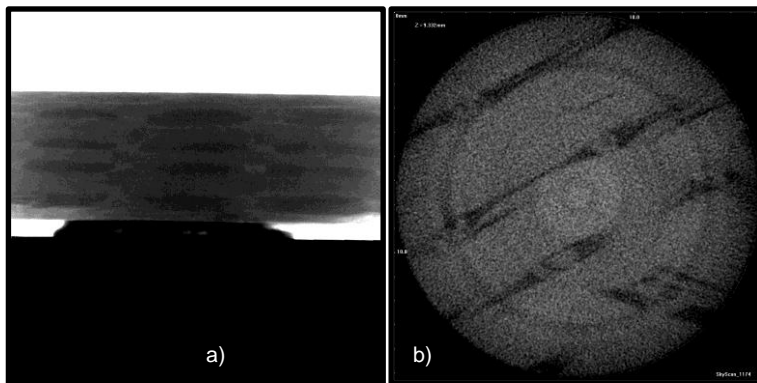


Figure 9-18. Micro-CT scans of panel 36 – 4x4 tufted Saertex quasi NCF carbon with 45o tuft angle, and epoxy. a) a view of the internal architecture of the composite along y axis b) a through- thickness slice of the composite along the z axis

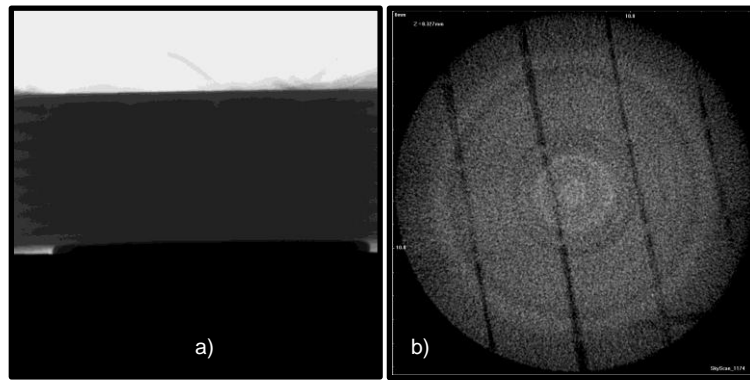


Figure 9-19. Micro-CT scans of panel 46 – 1k Sigmatex orthogonal 3D woven carbon and epoxy. a) a view of the internal architecture of the composite along y axis b) a through-thickness slice of the composite along the z axis

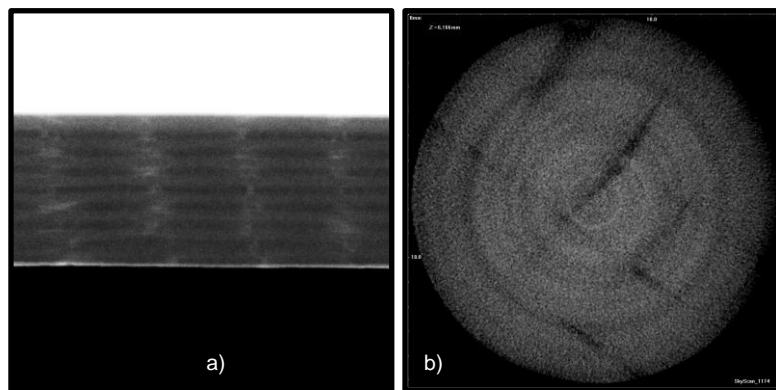


Figure 9-20. Micro-CT scans of panel 49 – 1k Sigmatex angle interlock 3D woven carbon and epoxy. a) a view of the internal architecture of the composite along y axis b) a through-thickness slice of the composite along the z axis

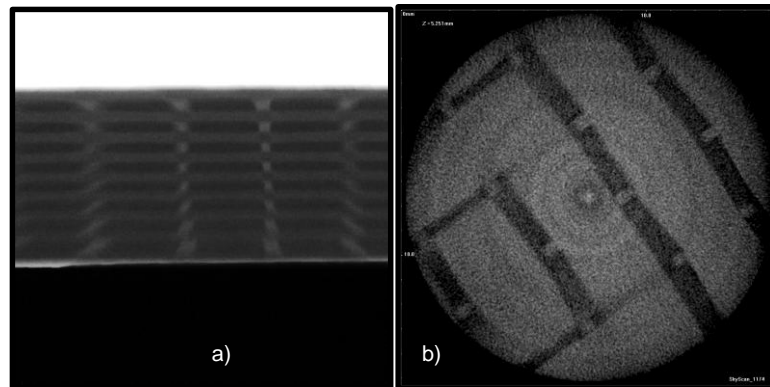


Figure 9-21. Micro-CT scans of panel 53 – 3k Sigmatex orthogonal 3D woven carbon and epoxy. a) a view of the internal architecture of the composite along y axis b) a through-thickness slice of the composite along the z axis

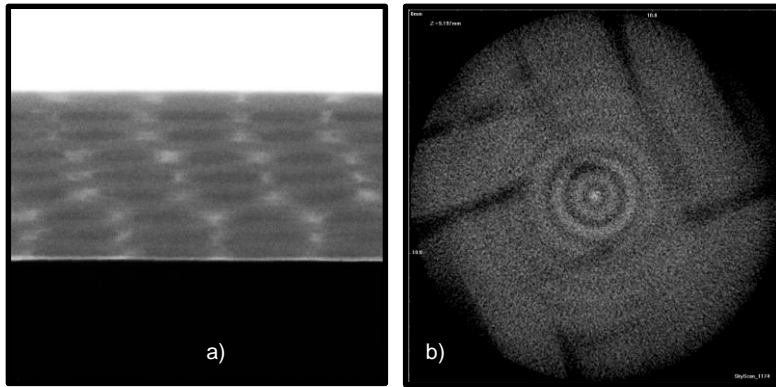


Figure 9-22. Micro-CT scans of panel 58 – 3k Sigmalex angle interlock 3D woven carbon and epoxy. a) a view of the internal architecture of the composite along y axis b) a through-thickness slice of the composite along the z axis

Material Testing Stage Compression and Release Scans

Figure 9-23 and Figure 9-24 show a selection of micro-CT scans chosen from those captured when using the material testing stage to compress, and subsequently, release the dry fibre 3Tex 3D woven fabric and the dry fibre Saertex quasi NCF 4x4 tufted fabric respectively. When completing the compression and release scans, the material testing stage and corresponding computer software facilitated the collation of load and displacement data. The load and displacement data gathered during the compression and release of the dry fibre 3Tex 3D woven fabric is shown plotted in graph form in Figure 9-25. That of the compression and release of the dry fibre Saertex quasi NCF 4x4 tufted fabric is again plotted in graph form in Figure 9-26.



Figure 9-23. Micro-CT scans of the compression and release of the dry fibre 3Tex 3D woven fabric. a) the compression of the fabric specimen shown with cross section scans along the y axis and reconstructed images of a single point along the z axis b) the release of the fabric specimen shown with cross section scans along the y axis and reconstructed images of a single point along the z axis

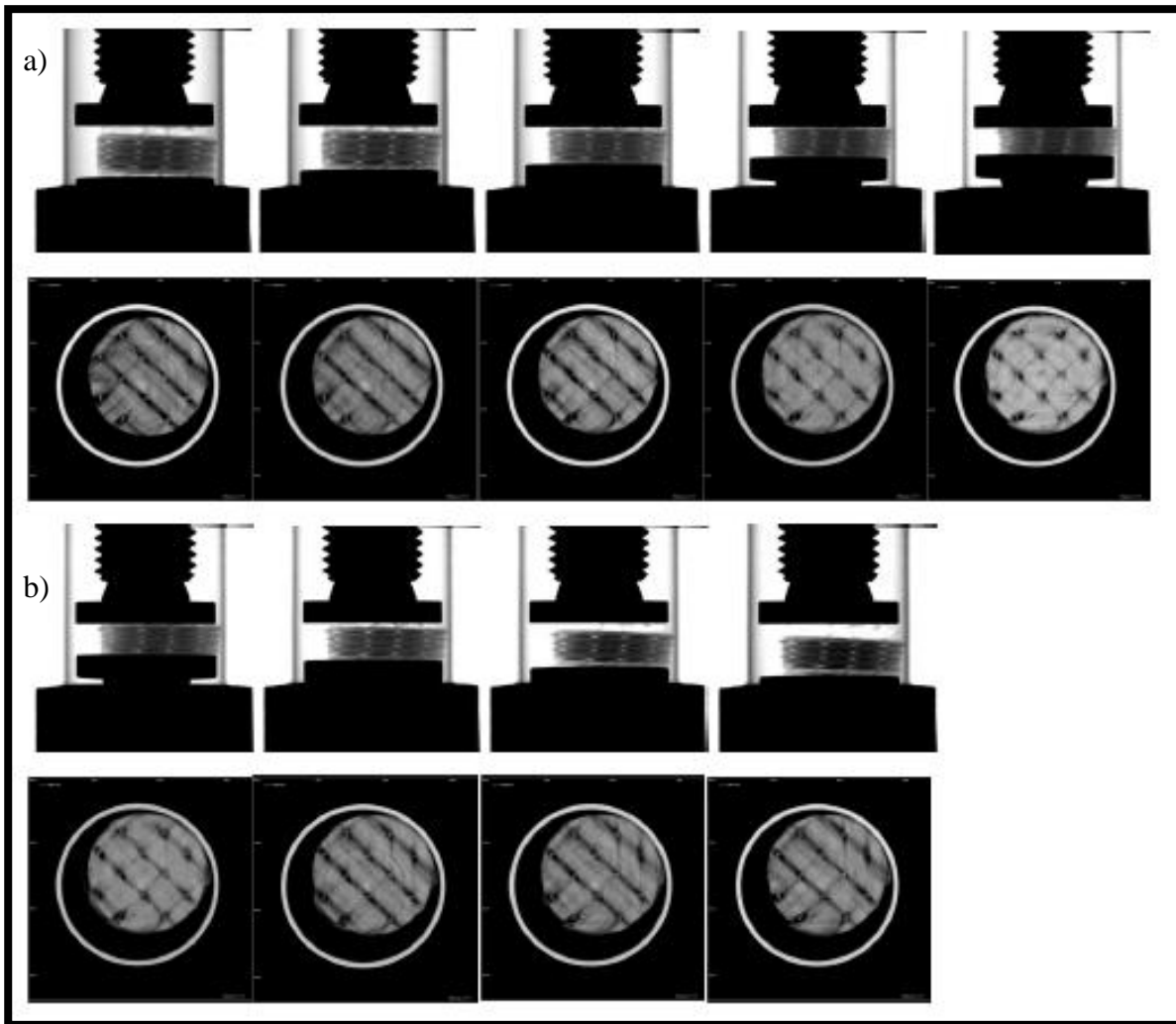


Figure 9-24. Micro-CT scans of the compression and release of the dry fibre Saertex quasi NCF 4x4 tufted fabric. a) the compression of the fabric specimen shown with cross section scans along the y axis and reconstructed images of a single point along the z axis b) the release of the fabric specimen shown with cross section scans along the y axis and reconstructed images of a single point along the z axis

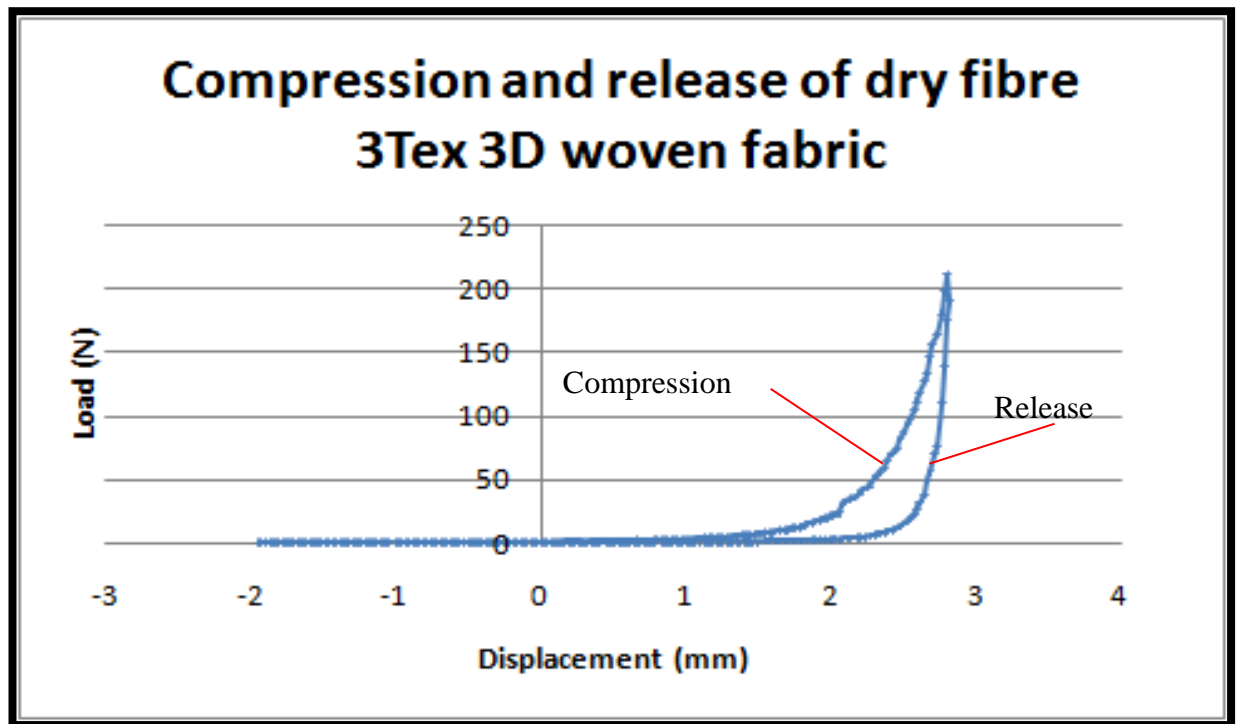


Figure 9-25. A graph plotting the load (N) and displacement (mm) data collated during the compression and release of the dry fibre 3Tex 3D woven fabric

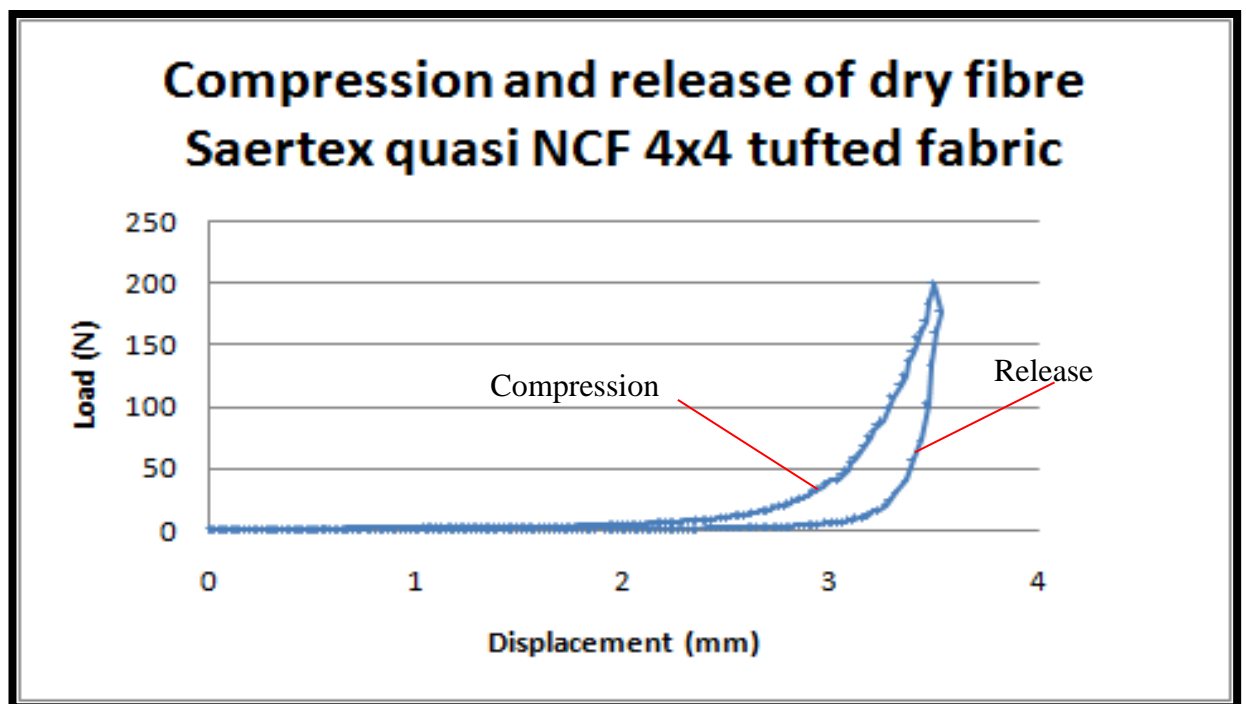


Figure 9-26. A graph plotting the load (N) and displacement (mm) data collated during the compression and release of the dry fibre Saertex quasi NCF 4x4 tufted fabric

Discussion and Conclusions

With the use of the Skyscan 1174 micro-CT scanner, lent to the University of Plymouth through the EPSRC equipment pool, various analyses have been successfully completed on a number of dry 3D fibre reinforcements, 3D and 2D fibre reinforced composites. These analyses mark the beginning of an investigation into the processing characteristics of 3D fibre reinforcements.

The analyses completed using the Skyscan 1174 micro-CT scanner have consisted of micro-CT scans of dry 3D fibre reinforcement specimens, 3D and also the 2D fibre reinforced composite specimens. In the case of the micro-CT scans of the dry 3D fibre reinforcement specimens, in addition to the more general scans that were also completed for both the 3D and 2D fibre reinforced composite specimens, the scans completed consisted of; compression and release scans. For each of the dry 3D fibre reinforcement specimens the compression and release scans consisted of the completion of a micro-CT scan at various points during the specimen's controlled compression and release. As well as micro-CT scans at these various points of the specimen's compression, which can be used for the creation of computer models, load and displacement data was also collated. With further analysis of the load and displacement data, which is presented in Figure 9-25 and Figure 9-26, information of the compressibility of the materials, an important processing characteristic which may later be verified with the completed computer models may be determined.

The micro-CT scans of the 3D and 2D fibre reinforced composite samples, presented in Figure 9-14 to Figure 9-22, as opposed to the micro-CT scans of the dry 3D fibre reinforcement samples; do not possess the clarity that is required for the formation of accurate computer models of this architecture. This is due to the lack of contrast between the fibre and the matrix of the composite resulting from their similar densities.

Problems with the internal analysis of composite samples with the use of a micro-CT scanner have also been experienced by Mahadik and Hallett [148]. The authors [148] found a lack of sufficient contrast between the reinforcement and matrix within the images produced and had to use image manipulation techniques to provide definition. Fortunately, in the case of the present study, the most effective models for investigating the processing characteristics of the 3D fibre reinforcements are those created with the scans of 3D fibre reinforcement specimens. The clarity of these scans facilitates the formation of more accurate computer models than capable of the micro-CT scans of the composite specimens.

For the continuance of the investigation into the processing characteristics of 3D fibre reinforcements, it is recommended that the collated load and displacement data for the dry fabric specimens be further analysed and the collated micro-CT scans used to generate computer models. With the analyses of the models of the material specimens, compressibility values obtained through the further analysis of collated load and displacement data can be validated and various other processing characteristics such as material permeabilities can be determined computationally to validate experimental values. Further sub investigations incorporating gathered processing cost data could also be carried out to determine the effect of the processing characteristics of stitched reinforcements on process costs. The results of these sub investigations would then provide the means by which to determine how the material's processing costs are influenced by the presence of stitches, allowing novel estimates of the material's infusions times and therefore processing costs.

A record of the specimens scanned with the Skyscan 1174 micro-CT scanner is presented in Table 9-2. The table documents the type and number of scans completed for each specimen and the type of image files collated during each scan.

Table 9-2. The specimens scanned with the Skyscan 1174 micro-CT scanner, the types of scan completed for each specimen and the type of image files collated during each scan

Specimen Material	Material Type	Scan Type and Number Completed	Image File Types
Fibre Reinforcement	3Tex 3D Woven Fabric	Circular platform stage scan x 2	Scan Images – tif Reconstructions – bmp
		Material testing stage scan x 1	Scan Images – tif Reconstructions – bmp
	NCF Quasi 4x4 Tufted Fabric	Circular platform stage scan x 2	Scan Images – tif Reconstructions – bmp
		Material testing stage scan x 2	Scan Images – tif Reconstructions – bmp
Composite	Panel 12 – Saertex Unstitched Quasi/Epoxy	Circular platform stage scan x 2	Scan Images – tif Reconstructions – bmp
	Panel 13 – 3Tex 3D Woven Fabric/Epoxy	Circular platform stage scan x 2	Scan Images – tif Reconstructions – bmp
	Panel 15 – Saertex Baseline 4x4 Tufted Quasi/Epoxy	Circular platform stage scan x 2	Scan Images – tif Reconstructions – bmp
	Panel 29 – Priform Soluble Fibre/Epoxy	Circular platform stage scan x 2	Scan Images – tif Reconstructions – bmp
	Panel 36 - Saertex NCF 45o Angle Tufts 4x4 Quasi/Epoxy	Circular platform stage scan x 3	Scan Images – tif Reconstructions – bmp
	Panel 46 – 1k Sigmatex Orthogona/Epoxy	Circular platform stage scan x 2	Scan Images – tif Reconstructions – bmp
	Panel 49 – 1k Sigmatex Angle Interlock/Epoxy	Circular platform stage scan x 2	Scan Images – tif Reconstructions – bmp
	Panel 53 – 3k Sigmatex Orthogonal/Epoxy	Circular platform stage scan x 2	Scan Images – tif Reconstructions – bmp
	Panel 58 – 3k Sigmatex Angle Interlock/Epoxy	Circular platform stage scan x 2	Scan Images – tif Reconstructions – bmp

Future Work

It is recommended that the collated micro-CT scan images are used in conjunction with available software to create solid models of each specimen. The solid modelling software available consists of CT analyser (CTan), provided with the micro-CT scanner, and Simpleware Ltd.'s ScanIP and ScanFE, solid modelling software already possessed by the University. Following the construction of the solid models, a computer based analysis of the processing characteristics of the various materials will be possible. Below, shown in Figure 9-27 and Figure 9-28, are some examples of solid models formed with captured micro-CT scan images.

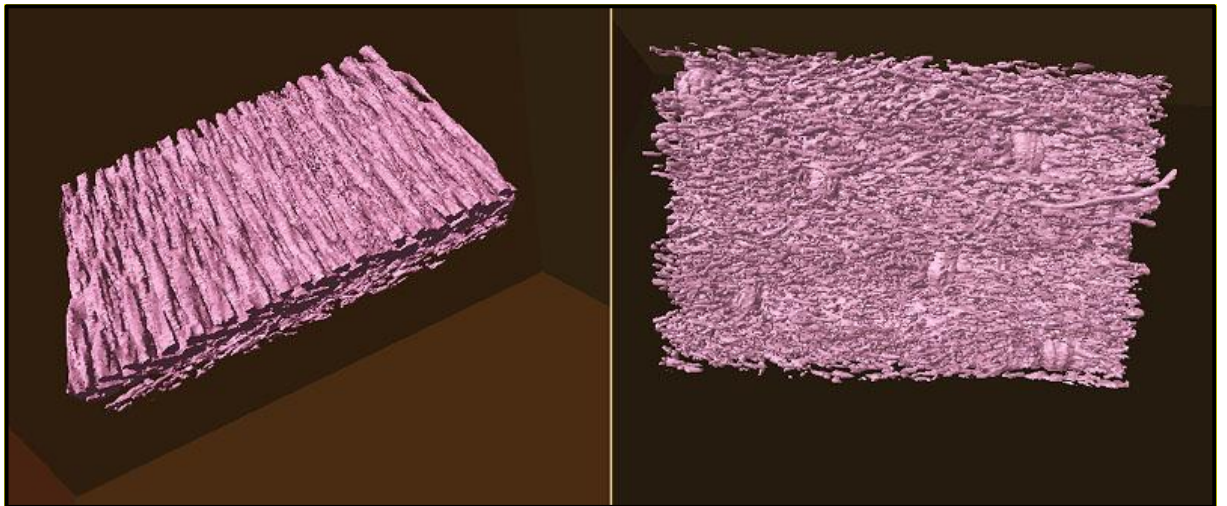


Figure 9-27. 3D visualization of the sample microstructure of a double layer fabric with two different types of glass fibre [149]

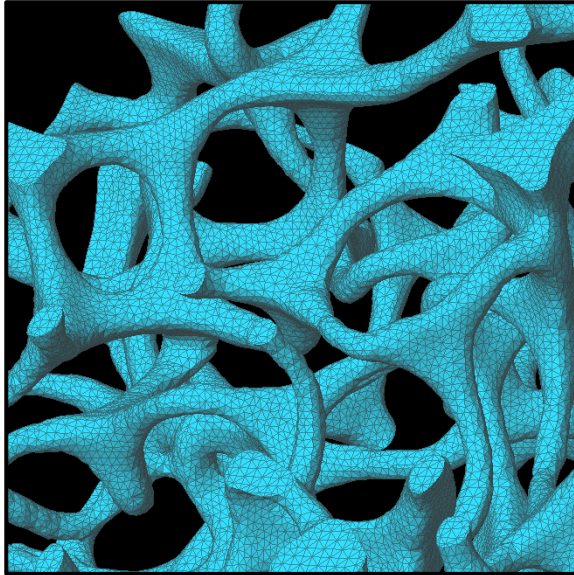


Figure 9-28. A 3D smooth volumetric mesh of an Aluminium auxetic foam, generated within the +ScanFE meshing module of Simpleware [150]

References

1. Airbus, *Global Market Forecast 2009-2028*, 2009, Airbus.
2. Boeing. *787 Dreamliner - Program fact sheet*. 2011 [cited 2011 12/09/11]; Available from: <http://www.boeing.com/commercial/787family/programfacts.html>.
3. Vosteen, L.F., *Composite Structures for Commercial Transport Aircraft*, N.L.R. Center, Editor 1978, National Aeronautics and Space Administration: Washington, DC. p. 27.
4. Mazumdar, S.K., *Composites Manufacturing - Materials, Product, and Process Engineering*. 2002, New York: CRC Press. 392.
5. Bouhicha, M., F. Aouissi, and S. Kenai, *Performance of composite soil reinforced with barley straw*. *Cement & Concrete Composites*, 2005. **27**(2005): p. 617-621.
6. Goodhew, S. and R. Griffiths, *Sustainable earth walls to meet the building regulations*. *Energy and Buildings*, 2005. **37**(2005): p. 451-459.
7. Middleton, D., *A technology revolution - Composite materials*. *Aircraft Engineering and Aerospace Technology*, 1989. **61**(7): p. 14-15.
8. Galán-Marín, C., C. Rivera-Gómez, and J. Petric, *Clay-based composite stabilized with natural polymer and fibre*. *Construction and Building Materials*, 2010. **24**(8): p. 1462-1468.
9. Soutis, C., *Fibre reinforced composites in aircraft construction*. *Progress in Aerospace Sciences*, 2005. **41**(2): p. 143-151.
10. Marsh, G., *Composites lift off in primary aerostructures*. *Reinforced Plastics*, 2004. **48**(4): p. 22-27.
11. Kaufmann, M., *Cost optimization of aircraft structures*, in *Department of Aeronautical and Vehicle Engineering 2009*, KTH: Stockholm. p. 50.
12. (ATAG), A.T.A.G. *Airbus and the A380*. 2011 [cited 2011 30/08/11]; Available from: <http://www.enviro.aero/A380casestudy.aspx>.
13. Airbus. *A380 Family/A380-800/Dimensions & key data*. 2011 [cited 2011 30/08/11]; Available from: <http://www.airbus.com/aircraftfamilies/passengeraircraft/a380family/a380-800/specifications/>.

References

14. Airbus. *A380 Family - New generation, new experience*. 2012 [cited 2013 02/01/13]; Available from: <http://www.airbus.com/aircraftfamilies/passengeraircraft/a380family/innovation/>.
15. (IATA), T.I.A.T.A. *Jet Fuel Price Development*. 2011 [cited 2011 31/08/11]; Available from: http://www.iata.org/whatwedo/economics/fuel_monitor/Pages/price_development.aspx.
16. Times, F. *ft.com/markets*. 2011 [cited 2011 31/08/11]; Available from: <http://www.ft.com/markets>.
17. Kaufmann, M., D. Zenkert, and M. Akermo, *Cost/weight optimization of composite prepreg structures for best draping strategy*. *Composites: Part A*, 2010. **41**(2010): p. 464-472.
18. Marx, W.J., D.N. Marvis, and D.P. Schrage, *A knowledge-based system integrated with numerical analysis tools for aircraft life-cycle design*. *Artificial intelligence for engineering design, analysis and manufacturing* 1998. **12**(3): p. 211-229.
19. Kruckenberg, T. and R. Paton, eds. *Resin Transfer Moulding for Aerospace Structures*. 1998, Kluwer Academic Publishers: Dordrecht. 522.
20. ALCAS. *ALCAS - Advanced low cost aircraft structures*. 2007 [cited 2011 15/09/11]; Available from: <http://alcas.twisoftware.com/>.
21. Kaye, A. *ALCAS - WPI Airliner wing*. in *ALCAS final review*. 2011. Airbus, Toulouse.
22. Vockings, N., *Delivering business through high performance products - experience from airbus UK*, 2010, Airbus UK: Nottingham.
23. KeyNote, *Aerospace Market Report 2003*, J. Baxter, Editor 2003, Key Note Ltd.
24. House of Commons, T.a.I.C., *Recent developments with Airbus*, D.o.T.a. Industry, Editor 2007, The Stationery Office Limited: London.
25. Bradley, S. *Boeing to boost 737 production rate to 42 airplanes per month in 2014*. 2011 [cited 2011 24/06/2011]; Available from: <http://boeing.mediaroom.com/index.php?s=43&item=1781>.
26. Tong, L., A.P. Mouritz, and M.K. Bannister, *3D Fibre Reinforced Polymer Composites* 2002, Oxford: Elsevier Science Ltd. 241.
27. Potter, K., *Resin Transfer Moulding*. 1997, London: Chapman & Hall. 246.

References

28. Bannister, M.K., *Development and application of advanced textile composites*. Journal of Materials: Design and Applications, 2004. **218**(3): p. 253-260.
29. Mouritz, A.P., K.H. Leong, and I. Herszberg, *A review of the effect of stitching on the in-plane mechanical properties of fibre-reinforced polymer composites*. Composites Part A: Applied Science and Manufacturing, 1997. **28A**: p. 979-991.
30. Tai, N.H., C.C.M. Ma, J.M. Lin, and G.Y. Wu, *Effects of thickness on the fatigue-behavior of quasi-isotropic carbon/epoxy composites before and after low energy impacts*. Composites Science and Technology, 1999. **59**(11): p. 1753-1762.
31. Cantwell, W.J. and J. Morton, *The impact resistance of composite materials - A review*. Composites, 1991. **22**(5): p. 347-362.
32. Bibo, G.A. and P.J. Hogg, *The role of reinforcement architecture on impact damage mechanisms and post-impact compression behaviour* J. Mat. Sci, 1996. **31**(5): p. 1115-1137.
33. Chou, T.W., *Microstructural design of fiber composites*. 1992, Cambridge: Cambridge University Press.
34. Santuiste, C., S. Sanchez-Saez, and E. Barbero, *Residual flexural strength after low-velocity impact in glass/polyester composite beams*. Composite Structures, 2010. **92**(1): p. 25-30.
35. Cottone, A., T. Turetta, and G. Giambanco, *Delamination study of through-thickness reinforced composite laminates via two-phase interface model*. Composites Part A: Applied Science and Manufacturing, 2007. **38**(9): p. 1985-1995.
36. Jain, L.K. and Y. Mai, *Determination of mode II delamination toughness of stitched laminated composites*. Composites Science and Technology, 1995. **55**(1995): p. 241-253.
37. Gude, M.R., S.G. Prolongo, T. Gomez-del Rio, and A. Urena, *Mode-I adhesive fracture energy of carbon fibre composite joints with nanoreinforced epoxy adhesives*. International Journal of Adhesion, 2011.
38. Garcia, E.J., B.L. Wardle, and A. John Hart, *Joining prepreg composite interfaces with aligned carbon nanotubes*. Composites Part A: Applied Science and Manufacturing, 2008. **39**(6): p. 1065-1070.
39. Mouritz, A.P. and B.N. Cox, *A mechanistic interpretation of the comparative in-plane mechanical properties of 3D woven, stitched and pinned composites* Composites Part A: Applied Science and Manufacturing, 2010. **41**(6): p. 709-728.

References

40. Mitschang, P. and A. Ogale. *Quality aspects of and thread selection for stitched preforms*. in *ICCM-17*. 2009. Edinburgh.
 41. Brandt, J., K. Drechsler, and J. Filsinger. *Advanced Textile Technologies for the Cost Effective Manufacturing of High Performance Composites*. 2001 [cited 2012 18/11/12]; Available from: [ftp://ftp.rta.nato.int/PubFullText/RTO/MP/RTO-MP-069-II/MP-069\(II\)-\(SM1\)-20.pdf](ftp://ftp.rta.nato.int/PubFullText/RTO/MP/RTO-MP-069-II/MP-069(II)-(SM1)-20.pdf).
 42. Colin de Verdiere, M., A.K. Pickett, A.A. Skordos, and V. Witzel, *Evaluation of the mechanical and damage behaviour of tufted non crimped fabric composites using full field measurements*. *Composites Science and Technology*, 2009. **69**(2): p. 131-138.
 43. Mouritz, A.P., M.K. Bannister, P.J. Falzon, and K.H. Leong, *Review of applications for advanced three-dimensional fibre textile composites*. *Composites: Part A*, 1999. **30**(1999): p. 1445-1461.
 44. Vinchery, J.A.J., *Reinforcement of composite aircraft structures using tufting*, in *School of Applied Sciences Advanced Materials 2007*, Cranfield University: Milton Keynes. p. 109.
 45. Mouritz, A.P. and B.N. Cox, *A mechanistic approach to the properties of stitched laminates*. *Composites Part A: Applied Science and Manufacturing*, 2000. **31**(2000): p. 1-27.
 46. Sickinger, C. and A. Herrmann, *Structural stitching as a method to design highperformance composites in future*, 2001, Institute of Structural Mechanics, German Aerospace Centre: Brunswick, Germany.
 47. Wittig, J. *In-mold-reinforcement of preforms by 3-dimensional tufting in 47th International SAMPE Symposium*. 2002. Society for the Advancement of Material and Process Engineering
 48. KSL. *Composites - Stitching Heads*. 2005 [cited 2009 27th May]; Available from: http://www.kse-export.de/ksl-lorsch/frame_eng.html.
 49. Dell'Anno, G., D.D.R. Cartié, I.K. Partridge, and A. Rezai, *Exploring mechanical property balance in tufted carbon fabric/epoxy composites*. *Composites Part A: Applied Science and Manufacturing*, 2007. **38**(2007): p. 2366-2373.
 50. Scarponi, C., A.M. Perillo, L. Cutillo, and C. Foglio, *Advanced TTT composite materials for aeronautical purposes: Compression after impact (CAI) behaviour*. *Composites Part B: Engineering*, 2007. **38**(2): p. 258-264.
 51. Beier, U., F. Fischer, J.K.W. Sandler, V. Altstädt, C. Weimer, and W. Buchs, *Mechanical performance of carbon fibre-reinforced composites based on stitched*
-

References

- preforms*. Composites Part A: Applied Science and Manufacturing, 2007. **38**(2007): p. 1655-1663.
52. Zhao, N., H. Rödel, C. Herzberg, S.-L. Gao, and S. Krzywinski, *Stitched glass/PP composite. Part I: Tensile and impact properties*. Composites Part A: Applied Science and Manufacturing, 2009. **40**(5): p. 635-643.
53. Heß, H. and N. Himmel, *Structurally stitched NCF CFRP laminates. Part 1: Experimental characterization of in-plane and out-of-plane properties*. Composites Science and Technology, 2011. **71**(5): p. 549-568.
54. Yoshimura, A., S. Yashiro, T. Okabe, and N. Takeda, *Characterization of tensile damage progress in stitched CFRP laminates*. Advanced Composite Materials, 2007. **16**(3): p. 223-244.
55. Kamiya, R. and T.-W. Chou, *Strength and failure behavior of stitched carbon/epoxy composites*. Metallurgical and Materials Transactions A, 2000. **31**(13): p. 899-909.
56. Zheng, Y., X. Cheng, and B. Yasir, *Effect of Stitching on Plain and Open-hole Strength of CFRP Laminates*. Chinese Journal of Aeronautics, 2012. **25**(3): p. 473-484.
57. Yudhanto, A., N. Watanabe, Y. Iwahori, and H. Hoshi, *Effect of stitch density on tensile properties and damage mechanisms of stitched carbon/epoxy composites*. Composites Part B: Engineering, 2012(0).
58. Treiber, J.W.G., *Performance of tufted carbon fibre/epoxy composites*, 2011, Cranfield University: Cranfield. p. 300.
59. Mouritz, A.P., *Flexural properties of stitched GRP laminates*. Composites Part A: Applied Science and Manufacturing, 1996. **27**(7): p. 525-530.
60. Koissin, V., J. Kustermans, S.V. Lomov, I. Verpoest, B. Van den Broucke, and V. Witzel, *Structurally stitched NCF preforms: Quasi-static response*. Composites Science and Technology, 2009. **69**(2009): p. 2701-2710.
61. Larsson, F., *Damage tolerance of a stitched carbon/epoxy laminate*. Composites Part A: Applied Science and Manufacturing, 1997. **28**(11): p. 923-934.
62. Tan, K.T., N. Watanabe, and Y. Iwahori, *Effect of stitch density and stitch thread thickness on low-velocity impact damage of stitched composites*. Composites Part A: Applied Science and Manufacturing, 2010. **41**(12): p. 1857-1868.
63. Yudhanto, A., N. Watanabe, Y. Iwahori, and H. Hoshi, *The effects of stitch orientation on the tensile and open hole tension properties of carbon/epoxy plain weave laminates*. Materials & Design, 2012. **35**(0): p. 563-571.
-

References

64. Kang, T.J. and S.H. Lee, *Effect of stitching on the mechanical and impact properties of woven laminate composite*. Journal of Composite Materials, 1994. **28**(16): p. 1574-1587.
65. Yoshimura, A., T. Nakao, S. Yashiro, and N. Takeda, *Improvement on out-of-plane impact resistance of CFRP laminates due to through-the-thickness stitching*. Composites Part A: Applied Science and Manufacturing, 2008. **39**(9): p. 1370-1379.
66. Beier, U., J.K.W. Sandler, V. Altstädt, H. Spanner, and C. Weimer, *Mechanical performance of carbon fibre-reinforced composites based on stitched and bindered preforms*. Composites Part A: Applied Science and Manufacturing, 2009. **40**(11): p. 1756-1763.
67. Dransfield, K.A., L.K. Jain, and Y.-W. Mai, *On the effects of stitching in CFRPs—I. mode I delamination toughness*. Composites Science and Technology, 1998. **58**(6): p. 815-827.
68. Jain, L.K., K.A. Dransfield, and Y. Mai, *On the effects of stitching in CFRPs - II. Mode II delamination toughness*. Composites Science and Technology, 1997. **58**(1998): p. 829-837.
69. Tan, K.T., N. Watanabe, Y. Iwahori, and T. Ishikawa, *Understanding effectiveness of stitching in suppression of impact damage: An empirical delamination reduction trend for stitched composites*. Composites Part A: Applied Science and Manufacturing, 2012. **43**(6): p. 823-832.
70. Tan, K.T., N. Watanabe, Y. Iwahori, and T. Ishikawa, *Effect of stitch density and stitch thread thickness on compression after impact strength and response of stitched composites*. Composites Science and Technology, 2012. **72**(5): p. 587-598.
71. Plain, K.P. and L. Tong, *An experimental study on mode I and II fracture toughness of laminates stitched with a one-sided stitching technique*. Composites Part A: Applied Science and Manufacturing, 2011. **42**(2): p. 203-210.
72. Schiebel, P. and A.S. Herrmann. *Textile preform technologies in the aviation sector – chances and challenges for the automotive sector, in IFAI Advanced Textiles '08*. 2008. Berlin.
73. Treiber, J.W.G., D.D.R. Cartié, and I.K. Partridge. *Determination of crack bridging laws in tufted composites*. in *ICCM-17*. 2009. Edinburgh.
74. Cartié, D.D.R., G. Dell'Anno, E. Poulin, and I.K. Partridge, *3D reinforcement of stiffener-to-skin T-joints by Z-pinning and tufting*. Engineering Fracture Mechanics, 2006. **73**(2006): p. 2532-2540.

References

75. Koh, T.M., M.D. Isa, S. Feih, and A.P. Mouritz, *Experimental assessment of the damage tolerance of z-pinned T-stiffened composite panels*. Composites Part B: Engineering, 2013. **44**(1): p. 620-627.
76. Preau, M., J.W.G. Treiber, and I.K. Partridge. *Comportement et endommagement d'un raidisseur Ω carbone/époxy renforcé par tufting*, in *17èmes Journées Nationales sur les Composites (JNC17)*. 2011. Poitiers-Futuroscope : France.
77. *Saertex - Reinforcing your ideas*. 2012 [cited 2012 11/11/12]; Available from: <http://www.saertex.com/home/>.
78. *TORAYCA - T700S DATA SHEET*. [cited 2012 28/05/12]; Available from: <http://www.toraycfa.com/pdfs/T700SDataSheet.pdf>.
79. *Delivery programme and characteristics for Tenax HTA filament yarn*. 2011 [cited 2012 28/05/12].
80. Koissin, V., A. Ruopp, S.V. Lomov, I. Verpoest, V. Witzel, and K. Drechsler, *On-surface fiber-free zones and irregularity of piercing pattern in structurally stitched NCF preforms*. Advanced Composite Letters, 2006. **15**(3): p. 87-94.
81. *Composite Integration ltd*. 2012 [cited 2012 11/11/12]; Available from: <http://www.composite-integration.co.uk/>.
82. Rudd, C.D., A.C. Long, K.N. Kendall, and C.E. Mangin, *Liquid moulding techniques: resin transfer moulding, structural reaction injection moulding, and related processing techniques*. 1997, Cambridge: Woodhead Publishing.
83. Summerscales, J. and T.J. Searle, *Low-pressure (vacuum infusion) techniques for moulding large composite structures*. Proceedings of the Institution of Mechanical Engineers, Part L: Journal of Materials: Design and Applications, 2005. **219**(1): p. 45-58.
84. Summerscales, J., *Resin Infusion Under Flexible Tooling (RIFT)* in *Encyclopedia of Composites - Second ed*. 2012, John Wiley & Sons. p. 2648-2658.
85. Williams, C., S.M. Grove, and J. Summerscales, *Resin Infusion Under Flexible Tooling (RIFT): a review* Composites Part A: Applied Science and Manufacturing, 1996. **A27**(7): p. 517-524.
86. Lundström, T.S., *The permeability of non-crimp stitched fabrics*. Composites Part A: Applied Science and Manufacturing, 2000. **31**(12): p. 1345-1353.
87. Nedanov, P.B. and S.G. Advani, *A method to determine 3D permeability of fibrous reinforcements*. Journal of Composite Materials, 2002. **36**(2): p. 241-254.

References

88. Abrate, S., *Resin flow in fiber preforms*. Applied Mechanics Reviews, 2002. **55**(6): p. 579-599.
89. Hu, J. and Y. Liu, *Effect of stitches on the permeability of interbundle channels in stitched fabrics*. Textile Research Journal, 2003. **73**(8): p. 691-699.
90. Talvensaaari, H., E. Ladstätter, and W. Billinger, *Permeability of stitched preform packages*. Composite Structures, 2005. **71**(3-4): p. 371-377.
91. Drapier, S., A. Pagot, A. Vautrin, and P. Henrat, *Influence of the stitching density on the transverse permeability of non-crimped new concept (NC2) multiaxial reinforcements: measurements and predictions*. Composites Science and Technology, 2002. **62**(15): p. 1979-1991.
92. Han, N.L., S.S. Suh, J.M. Yang, and H.T. Hahn, *Resin film infusion of stitched stiffened composite panels*. Composites Part A: Applied Science and Manufacturing, 2003. **34**(3): p. 227-236.
93. Scholz, S., J.W. Gillespie Jr, and D. Heider, *Measurement of transverse permeability using gaseous and liquid flow*. Composites Part A: Applied Science and Manufacturing, 2007. **38**(9): p. 2034-2040.
94. Loendersloot, R., *The structure-permeability relation of textile reinforcements*, 2006, University of Twente: Enschede, Netherlands. p. 248.
95. Wu, X., J. Li, and R.A. Sheno, *A New Method to Determine Fiber Transverse Permeability*. Journal of Composite Materials, 2007. **41**(6): p. 747-756.
96. Papathanasiou, T.D., *A structure-oriented micromechanical model for viscous flow through square arrays of fibre clusters*. Composites Science and Technology, 1996. **56**(9): p. 1055-1069.
97. Binétruy, C., B. Hilaire, and J. Pabiot, *The interactions between flows occurring inside and outside fabric tows during rtm*. Composites Science and Technology, 1997. **57**(5): p. 587-596.
98. Pomeroy, R.A.H., *Permeability characterisation of continuous filament mats for resin transfer moulding*, in *School of Engineering 2009*, University of Plymouth: Plymouth. p. 435.
99. Summerscales, J. *The effect of permeant on the measured permeability of a reinforcement*, in *The 7th International Conference on Flow Processes in Composite Materials*. 2004. Newark, Delaware, USA.

References

100. *Pipex px - Producing excellence*. 2012 [cited 2012 11/11/12]; Available from: <http://www.pipexp.com/home/>.
101. Gurit. *Gurit guide to composites*. 2012 [cited 2013 03/01/13]; Available from: [http://www.gurit.com/files/documents/Gurit_Guide_to_Composites\(1\).pdf](http://www.gurit.com/files/documents/Gurit_Guide_to_Composites(1).pdf).
102. Michaud, V. and A. Mortensen, *Infiltration processing of fibre reinforced composites: governing phenomena*. Composites Part A: Applied Science and Manufacturing, 2001. **32**(8): p. 981-996.
103. Massey, B.S., *Mechanics of Fluids*. 6th ed. 1989, London: VNR (International). 599.
104. Taylor, J.R., *An introduction to error analysis: The study of uncertainties in physical measurements*. 2nd ed. 1982, California: University Science Books. 327.
105. *Composites & Plastics - PAM-RTM*. 2010 [cited 2012 26/02/12]; Available from: <http://www.esi-group.com/products/composites-plastics/pam-rtm>.
106. *Resin Transfer Moulding - RTM-Worx*. 2007 [cited 2012 12/03/12]; Available from: <http://www.polyworx.com/pwx/rtm/>.
107. *LIMS(Liquid injection molding simulation)*. 2004 [cited 2012 12/03/12]; Available from: <http://www.ccm.udel.edu/Pubs/techbriefs/102.html>.
108. *myRTM - Software for simulating the RTM process*. 2012 [cited 2012 12/03/12]; Available from: <http://iwk.hsr.ch/myRTM.3575.0.html?&L=4>.
109. Geuzaine, C. and J.F. Remacle, *Gmsh: a three-dimensional finite element mesh generator with built-in pre- and post-processing facilities*. International Journal for Numerical Methods in Engineering 2009. **79**(11): p. 1309-1331.
110. *HexFlow RTM 6*. 2012 [cited 2012 28/05/12]; Available from: http://www.hexcel.com/Resources/DataSheets/RTM-Data-Sheets/RTM6_global.pdf.
111. *MVR444 - Matrix for liquid resin infusion processes*. [cited 2012 28/05/12]; Available from: http://www.advanced-composites.co.uk/data_catalogue/catalogue%20files/pds/PDS1190_MVR444_Issue1a.pdf.
112. Soutis, C., *Carbon fiber reinforced plastics in aircraft construction*. Materials Science and Engineering: A, 2005. **412**(1-2): p. 171-176.
113. Witik, R.A., F. Gaille, R. Teuscher, H. Ringwald, V. Michaud, and J.-A.E. Månson, *Economic and environmental assessment of alternative production methods for*

References

- composite aircraft components*. Journal of Cleaner Production, 2012. **29–30**(0): p. 91-102.
114. Monroy Aceves, C., M.P.F. Sutcliffe, M.F. Asby, A.A. Skordos, and C. Rodriguez Roman. *Design selection of a wind turbine blade using prepreg materials*. in *ICCM-17*. 2009. Edinburgh.
115. Bader, M.G., *Selection of composite materials and manufacturing routes for cost-effective performance*. Composites: Part A, 2002. **33**(2002): p. 913-934.
116. Cheung, J.M.W., J.P. Scanlan, and S.S. Wiseall. *An aerospace component cost modelling study for value driven design*, in *CIRP IPS2 Conference 2009: Industrial Product-Service Systems*. 2009. Cranfield, UK.
117. Curran, R., A. Kundu, J. Wright, S. Crosby, M. Price, S. Raghunathan, and E. Benard, *Modelling of aircraft manufacturing cost at the concept stage*. The International Journal of Advanced Manufacturing Technology, 2006. **31**(3): p. 407-420.
118. Niazi, A., J.S. Dai, S. Balabani, and L. Seneviratne, *Product cost estimation: Technique classification and methodology review*. Journal of Manufacturing Science and Engineering, 2006. **128**: p. 563-575.
119. Rush, C. and R. Roy. *Analysis of cost estimating processes used within a concurrent engineering environment throughout a product life cycle*, in *Seventh ISPE international conference on concurrent engineering: research and applications*. 2000. Lyon, France: Technomic.
120. Curran, R., S. Raghunathan, and M. Price, *Review of aerospace engineering cost modelling: The genetic causal approach*. Progress in Aerospace Sciences, 2004. **40**(8): p. 487-534.
121. Geiger, T.S. and D.M. Dilts, *Automated design-to-cost: integrating costing into the design decision*. Computer-Aided Design, 1996. **28**(6/7): p. 423-438.
122. Scanlan, J., T. Hill, R. Marsh, C. Bru, M. Dunkley, and P. Cleevely, *Cost modeling for aircraft design optimization* J. ENG. DESIGN, 2002. **13**(3): p. 261-269.
123. Esawi, A.M.K. and M.F. Ashby, *Cost estimates to guide pre-selection of processes*. Materials & Design, 2003. **24**(8): p. 605-616.
124. Weiland, F., C. Weimer, C.V. Katsiropoulos, S.G. Pantelakis, M. Asareh, D.D.R. Cartié, A.R. Mills, A.A. Skordos, L. Dufort, P. De Luca, and A.K. Pickett. *Manufacture of a rotor blade pitch horn using novel binder yarn fabrics*. in *ICCM-17*. 2009. Edinburgh.
-

References

125. Galorath, *SEER for Manufacturing (SEER-MFG)*, 2008, Galorath Inc.
126. PRICE Systems, L.L.C. *Price Products*. 2008 [cited 2010 08/12/10]; Available from: http://www.pricystems.com/products/price_trueplanning.asp.
127. Zhao, W., J. Li, C. Zhang, Z. Liang, and B. Wang, *Feature-based cost estimation for composite structures with Fuzzy Multi-Attribute Utility Theory*. Int. J. Industrial and Systems Engineering, 2006. **1**(1/2): p. 284-300.
128. Xu, Y., F. Elgh, J.A. Erkoyuncu, O. Bankole, Y. Goh, W.M. Cheung, P. Baguley, Q. Wang, P. Arundachawat, E. Shehab, L. Newnes, and R. Roy, *Cost Engineering for manufacturing: Current and future research*. International Journal of Computer Integrated Manufacturing, 2011. **25**(4-5): p. 300-314.
129. Hollmann, J. *The monte-carlo challenge: A better approach*, in *AACE International Transaction*. 2007. Nashville, TN, USA: AACEI.
130. Bao, H.P. and J.A. Samareh. *Affordable design - A methodology to implement process-based manufacturing cost models into the traditional performance-focused multidisciplinary design optimization*. in *AIAA/USAF/NASA/ISSMO Symposium on Multidisciplinary Analysis and Optimization*. 2000. Long Beach, California: AIAA.
131. Barton, A.C., *Integrating manufacturing issues into structural optimization*, in *School of Aerospace, Mechanical and Mechatronic Engineering 2002*, The University of Sydney: Sydney. p. 173.
132. LeBlanc, D.J., *Advanced composite cost estimating manual*, 1977, Northrop Corporation: Hawthorne, California. p. 54.
133. Zaloom, V. and C. Miller, *A review of cost estimating for advanced composite materials applications*. Engineering Costs and Production Economics, 1982. **7**(1982): p. 81-86.
134. Mitchell, S., D. LaChapelle, R. Ufkes, and K. Sargent. *Benefits of using cost models to guide composite frame designs*. [cited 2012 22/09/12]; Available from: www.galorath.com/images/uploads/Real-Time-Cost1.pdf.
135. *Edwards - A34310940 E1M18 2012* [cited 2012 08/12/12]; Available from: <http://www.edwardsvacuum.com/Products/View.aspx?sku=A34310940>.
136. Scelsi, L., M. Bonner, A. Hodzic, C. Soutis, C. Wilson, R. Scaife, and K. Ridgway, *Potential emissions savings of lightweight composite aircraft components evaluated through life cycle assessment*. eXPRESS Polymer Letters, 2011. **5**(3): p. 209-217.
137. *Quarterly Energy Prices - June 2012*, D.o.E.C. Change, Editor 2012, National Statistics.

References

138. Hull, D. and T.W. Clyne, *An Introduction to Composite Materials*. 2nd ed. Cambridge Solid State Science Series. 1996, Cambridge: Cambridge University Press. 326.
139. *Component Design Analysis (CoDA)*. 2012 [cited 2012 14/05/12]; Available from: <http://www.anaglyph.co.uk/CoDA.htm>.
140. *Solidworks*. 2013 [cited 2013 11/01/13]; Available from: <http://www.solidworks.com/>.
141. *CYCOM 997 epoxy resin system - Technical data sheet*. 2012 [cited 2012 12/12/12]; Available from: http://www.cemselectorguide.com/pdf/CYCOM_997_031912.pdf.
142. *Steel*. 2012 [cited 2012 02/11/12]; Available from: <http://www.metalprices.com/metal/steel/lme-steel-billet-cash-official>.
143. Park, C.H. and W.I. Lee, *Manufacturing: Economic Consideration*. Wiley Encyclopedia of Composites, 2012.
144. Simpleware. *Software*. 2010 2010 [cited 2010 30th April]; Available from: <http://www.simpleware.com/software.php>.
145. ANSYS. *ANSYS CFX*. 2013 [cited 2013 13/01/13]; Available from: <http://www.ansys.com/Products/Simulation+Technology/Fluid+Dynamics/Fluid+Dynamics+Products/ANSYS+CFX>.
146. Lomov, S. *WiseTex suite*. 2011 [cited 2012 28/01/12]; Available from: <http://www.mtm.kuleuven.be/Onderzoek/Composites/software/wisetex>.
147. *TexGen*. 2011 [cited 2012 28/01/12]; Available from: http://texgen.sourceforge.net/index.php/Main_Page.
148. Mahadik, Y. and S.R. Hallett. *Characterisation of 3D woven composite internal architecture and effect of compaction*. in *ICCM-17*. 2009. Edinburgh.
149. Skyscan. *Applications: material science (5) / SkyScan1174*. 2009 [cited 2010 15th January]; Available from: <http://www.skyscan.be/applications/materials/materials005.htm>.
150. Simpleware. *MicroCT scan of auxetic foam*. 2010 [cited 2010 15th January]; Available from: <http://www.simpleware.com/applications/casestudies/foam.php>.